Functionalized Carbon Surfaces for Clean Electrochemical Energy Systems

by

Holly M. Fruehwald

A thesis submitted to the
School of Graduate and Postdoctoral Studies in partial
fulfillment of the requirements for the degree of

Doctor of Philosophy in Materials Science

Facutly of Science

University of Ontario Institute of Technology

Oshawa, Ontario, Canada

March 2022

ABSTRACT

The development and implementation of clean energy technologies is the way to overcome the global energy crisis and reduce pollution. Therefore, new energy solutions are rapidly needed. Fuel cells (FCs) may become one such solution. FCs are devices that utilize chemical reactions to directly produce electric energy. While these devices are ideal clean energy sources for the transportation industry, conventional FCs are based on expensive materials that implement platinum catalysts on a carbon support (Pt/C). The high cost and limited availability of platinum hinders the applicability of FCs. Nitrogen and metal-doped carbon supports have been investigated as a non-precious metal replacement for costly precious metal-based materials in various electrochemical energy applications. However, the design of non-precious metal materials (NPMMs) involves high temperature pyrolysis treatments, which leads to an almost random distribution of nitrogen atoms on the surface and therefore can limit efficiency. In this work, a method to graft only the most active nitrogenous groups and/or transition metals on the surface of carbon supports was developed. Specifically, diazonium coupling chemistry to covalently attach molecularly defined moieties bearing a terpyridine (tpy) group onto the surface of carbon supports, followed by the introduction of Fe (or other transition metal) centers into anchored tpy groups. Pyridinic nitrogenous groups, which are the basis of tpy, are believed to be required for high activity in the oxygen reduction reaction (ORR) in FC applications and are thought to increase capacitance in SC applications. Upon metal coordination into the tpy sites, the metal-N$_3$/C catalyst shows promising activity for the ORR and SC applications and opens the door for molecularly controlled, inexpensive, and efficient materials. Importantly, upon an energy intensive heat-treatment, the material's activity does not improve. Confirming that this system's properties are dictated by the molecularly defined tpy-Fe units, new efficient NPMMs can be fabricated using energy-saving conditions. This design can be applied and optimized to create a family of NPMMs for various clean energy applications. Modifying carbon-based materials opens the way for new low-cost materials for clean energy systems such as FCs, SC, and water oxidation.

Keywords: non-precious metals; electrochemistry; energy; fuel cells; supercapacitors

AUTHOR'S DECLARATION

I hereby declare that this thesis consists of original work of which I have authored. This is a true copy of the thesis, including any required final revisions, as accepted by my examiners.

I authorize the University of Ontario Institute of Technology to lend this thesis to other institutions or individuals for the purpose of scholarly research. I further authorize University of Ontario Institute of Technology to reproduce this thesis by photocopying or by other means, in total or in part, at the request of other institutions or individuals for the purpose of scholarly research. I understand that my thesis will be made electronically available to the public.

Holly M. Fruehwald

STATEMENT OF CONTRIBUTIONS

Part of the work described in Chapter 2 has been published as:

Fruehwald, H. M.; Ebralidze, I. I.; Zenkina, O. V.; Easton, E. B., Fe-N3/C Active Catalytic Sites for the Oxygen Reduction Reaction Prepared with Molecular-Level Geometry Control through the Covalent Immobilization of an Iron-Terpyridine Motif onto Carbon. ChemElectroChem. **2019**, *6*, 1350-1358. doi: 10.1002/celc.201801842.

I performed the majority of the synthesis, physical and electrochemical testing of the materials, and writing of the manuscript. I. I. Ebralidaze collected and analyzed the X-ray photoelectron spectroscopy (XPS) of the V-tpy-Fe and V-tpy-Fe24 catalysts, along with the collection, analysis and write-up of the TofSIMS analysis of the V-tpy-Fe. R. B. Moghaddam assisted in collecting the SEM image of V-tpy-Fe. L. Zhang from the University of Waterloo performed the TEM measurements of the catalysts.

Part of the work described in Chapter 3 has been published as:

Fruehwald, H. M.; Ebralidze, I. I.; Melino, P. D.; Zenkina, O. V.; Easton, E. B., Probing the Influence of the Carbon support on the Activity of Fe-N$_3$/C Model Active Sites for the Oxygen Reduction Reaction. *J. Electrochem. Soc.* **2020,** *167*, 084520. doi: 10.1149/1945-7111/ab92b9

I performed the majority of the synthesis, physical and electrochemical testing of the materials, and writing of the manuscript. I. I. Ebralidze collected, analyzed, and drafted the X-ray photoelectron spectroscopy (XPS) of all the catalysts. P. D. Melino performed TGA and BET on some of the catalysts.

Part of the work described in Chapter 4 has been published as:

Fruehwald, H. M.; Ebralidze, I. I.; Melino, P. D.; Zenkina, O. V.; Easton, E. B., Effect of Transition Metals on the Oxygen Reduction Reaction Activity at Metal-N$_3$/C Active Sites. *ChemElectroChem.* **2021,** *8*, 53-61. doi: 10.1002/celc.202000954

I performed the majority of the synthesis, physical and electrochemical testing of the materials and writing of the manuscript. I.I. Ebralidze collected and analyzed the X-ray photoelectron spectroscopy (XPS) of the catalysts. C. Andrei collected the TEM measurements of the catalysts.

Part of the work described in Chapter 5 has been published as:

Fruehwald, H. M.; Melino, P. D.; Zenkina, O. V.; Easton, E. B., Hybrid Supercapacitor Electrode Materials via Molecular Imprinting of Nitrogenous Ligands and Iron Complexes into Carbon Support. *J. Electrochem. Soc.* **2021**, *168*, 120527. doi: 10.1149/1945-7111/ac4058 .

I performed the majority of the synthesis, physical and electrochemical testing of the materials, and writing of the manuscript. P. D. Melino performed some TGA and BET of the materials.

Part of the work described in Chapter 6 has been published as:

Fruehwald, H. M.; Melino, P. D.; MacLean, B. J.; Zenkina, O. V.; Easton, E. B., Dual Role of the Carbon Materials Functionalized by Nitrogenous Ligands for Energy Storage and Production: Fuel Cells and Supercapacitors. *Electrochim. Acta*. **2022**, 414, 140209.

I performed the majority of the synthesis, physical and electrochemical testing of the materials, and writing of the manuscript. P. D. Melino performed the BET, Raman, and Dunn analysis of the materials. B. J. MacLean synthesized the ligand and performed the characterization of the ligand used.

Part of the work described in Chapter 7 has been published as:

Fruehwald, H. M.; Moghaddam, R. B.; Zenkina, O. V.; Easton, E. B., High-performance water oxidation catalysts based on the spontaneous deposition of ruthenium on electrochemically exfoliated graphene oxide. *Catal. Sci. Technol.* **2019,** *9*, 6547-6551. doi: 10.1039/c9cy02017a

I performed the majority of the synthesis, physical and electrochemical testing of the materials, and writing of the manuscript. R. B. Moghaddam had the original idea and assisted with the editing of the manuscript. I.I. Ebralidze collected and analyzed the x-ray photoelectron spectroscopy (XPS) of the Ru@EGO catalysts. C. Andrei performed the HRTEM measurements.

Part of the work described in Chapter 8 has been published as:

Fruehwald, H. M.; Moghaddam, R. B.; Melino, P. D.; Ebralidze, I. I.; Zenkina, O. V.; Easton, E. B., Ni on graphene oxide: a highly active and stable alkaline oxygen evolution catalyst. *Catal. Sci. Technol.* **2021,** *11*, 4026-4033. doi: 10.1039/d1cy00297j

I performed the majority of the synthesis, physical and electrochemical testing of the materials, and writing of the manuscript. R. B. Moghaddam had assisted with the editing and idea for the manuscript. P. D. Melino synthesized the graphene oxide used. I.I. Ebralidze collected and analyzed the X-ray photoelectron spectroscopy (XPS) of the Ni@EGO catalyst. C. Andrei performed the TEM measurements.

Part of the work described in Chapter 9 has been submitted as:

Fruehwald, H. M.; Zenkina, O. V.; Easton, E. B., Carbon-Nitrogen-Metal Material as a High Performing Oxygen Evolution Catalyst. *Catal. Sci. Technol.* Submitted.

I performed the majority of the synthesis, physical and electrochemical testing of the materials, and writing of the manuscript.

ACKNOWLEDGEMENTS

I would like to dedicate my thesis to my late Grandmother, Theresa Beaugrand who passed away during the end of my thesis. She was a very important support for me throughout my graduate degree and taught me to be a strong, kind, and resilient person. When I thought about finishing my PhD I always envisioned her there and proud of me at my graduation, so this thesis is for her.

It is hard to express in words how thankful I am to have had such wonderful supervisors throughout my PhD. I would like to thank Dr. Olena Zenkina for giving me a chance to learn about research in her lab in 2016, working for her developed and inspired my passion for research. I would like to thank Dr. Brad Easton for teaching me patience and so much electrochemistry. Doing a PhD with Dr. Brad Easton and Dr. Olena Zenkina has been one of the best decisions I have made. I cannot thank them enough for all the support both personally and academically they have showed me over the past 7 years I have worked with them. They have taught me how to be a resilient and more confident scientist and helped my personal growth and have incredibly supportive of my future career goals.

I would like to thank all past and present members of both the Zenkina and Easton Lab groups for all their constant support with reading scholarships, watching presentations, and being and ear to listen. I would especially like to thank Rana Ahmad and Keenan Black-Araujo who were a constant support to me while trying to complete this thesis in the middle of a pandemic. I would like to thank Dr. Nadia Laschuk and Jakki Egan who started this degree with me and were there to join in through all the laughs and tears. They have unconditionally supported me throughout this degree, and I couldn't be more thankful to

call them friends. The friends I have made throughout this degree made my time here so much fun from working with them in the labs to learning new hobbies like how to golf outside the lab.

I would like to thank the chemistry department at Ontario Tech for the support that they gave me throughout my time here. To all the people who I interacted with, who taught me, and who supported me, it means so much and you have all shaped my journey here. A special thank you goes out to Dr. Richard Bartholomew and Michael Allison. They so kindly let me borrow chemicals, glassware, and instrumentation to complete some of my work. They were there to be a listening ear and gave my helpful advice for both research and teaching. I would like to thank Dr. Kevin Coulter for involving me in the SEAL program where I got to foster my creativity and passion for outreach. I enjoyed every moment being able to lead this activity and mentor and teach high school students about electrochemistry.

I would like to thank all my friends and family for their unwavering support throughout my degree. It has been challenging and when things got tough, they were the first to motivate me and remind me that I am supported no matter what. My parents, sister, and friends gave me the confidence, and support to fulfill my dreams doing a PhD.

TABLE OF CONTENTS

LIST OF TABLES

LIST OF FIGURES

CHAPTER 4

CHAPTER 5

CHAPTER 6

CHAPTER 7

CHAPTER 8

LIST OF ABBREVIATIONS AND SYMBOLS

FC	Fuel Cells
SC	Supercapacitors
NPMM	Non-precious metal materials
tpy	terpyridine
ORR	Oxygen reduction reaction
PEMFC	proton exchange membrane fuel cell
Pt	platinum
OER	Oxygen evolution reaction
Pt/C	Platinum on carbon
HOR	hydrogen oxidation reaction
Co	Cobalt
NPMC	non-precious metal catalyst
MOFs	metal-organic frameworks
HER	hydrogen evolution reaction
GO	graphene oxide
Ru	ruthenium
Ni	nickel
EDLCs	electric double layer capacitors

Chapter 1. Introduction

1.1 Energy Crisis

The modern socioeconomic demand for fossil fuels has had, and will continue to have, a detrimental effect on Canada's environment and the entire planet. Replacing these fossil fuels with renewable energy technologies is one of the major scientific challenges faced today[1]. With rapid advancements in technology, the implementation of environmentally friendly energy systems has become prevalent. A promising way to overcome some issues with the burning of fossil fuels is to use the energy stored in chemical bonds[2]. Currently, many clean energy systems operate by using expensive and rare metals such as platinum, ruthenium, and iridium, which is disadvantageous due to the high cost and scarcity of these precious metals. To overcome these issues, cost-efficient and abundant alternatives are being explored for the replacement of the high-cost materials in many clean energy systems. One commonality between low-cost clean energy systems is that they rely on very similar materials design, but there is rarely any intersection in using materials for more than one application. For example, heat-treated carbon, nitrogen, and iron materials are often used in sustainable fuel cells (FCs) (efficient chemical-to-electrical energy conversion devices) and in supercapacitor (SC) applications to prepare more sustainable electrodes with enhanced charge storing capabilities[3-5]. However, the materials used for FCs are rarely examined for their charge storing applications in SCs. Clean energy materials design must combine the ability to manipulate nature on the molecular level in order to fine-tune the properties and still result in inexpensive materials. Indeed, high processing costs are not beneficial for the widespread commercialization of these inexpensive alternatives. To produce the most economical materials and designs, sustainable materials must be used to their full potential in both FC and SC applications. It is imperative that cost-efficient materials are being used to their full advantage as it is likely the materials for FCs could be beneficial in SC applications as well. Current renewable technologies that are being rapidly developed (wind, solar) energy sources suffer from highly intermittent power and the efficiency to store charge is lower[6]. Hydrogen represents a promising form of energy storage because it is easier to store than electrons

and can be generated from any energy source through water electrolysis, then can be later used in hydrogen fuel cells to reform water[6-7].

1.2 Proton Exchange Membrane Fuel Cells

The use of hydrogen has been of particular interest as renewable fuel as it holds vast amounts of chemical energy to be utilized for the formation of large amounts of electrical energy. Therefore, there is a need for appropriate and efficient devices to utilize the potential of hydrogen fuel to produce the energy output that is desired to power various stationary and portable devices.

Hydrogen gas is widely used in Proton Exchange Membrane Fuel cells (PEMFC). PEMFCs are of great interest for clean energy technologies as it relies on the usage of chemical energy, in the form of hydrogen and oxygen gas, and converts it to electrical energy[8]. They are a promising alternative in automotive applications by replacing the combustion engine[9]. The only product of this reaction is water and heat, thus making it an ideal clean energy source in applications such as stationary, portable, and transportation. A diagram of a PEMFC is shown in Figure 1.1. Fuel cells operate by flowing hydrogen gas at the anode and oxygen gas at the cathode. At the anode hydrogen is split into protons and electrons[10]. The electrons travel through the external load and create the electrical energy delivered to the device, while the protons cross an electrolyte. This electrolyte in fuel cells is a polymer membrane, typically Nafion®, that is sandwiched between the anode and cathode. At the cathode, the electrons and protons react with the oxygen gas to produce water. Within the anode and cathode there is a catalyst layer that performs these reactions. Historically, noble metals are the most effective catalysts used to perform these reactions, most commonly a platinum-coated carbon (Pt/C) catalyst is often used at a variety of Pt loadings from 20-40% or higher[11].
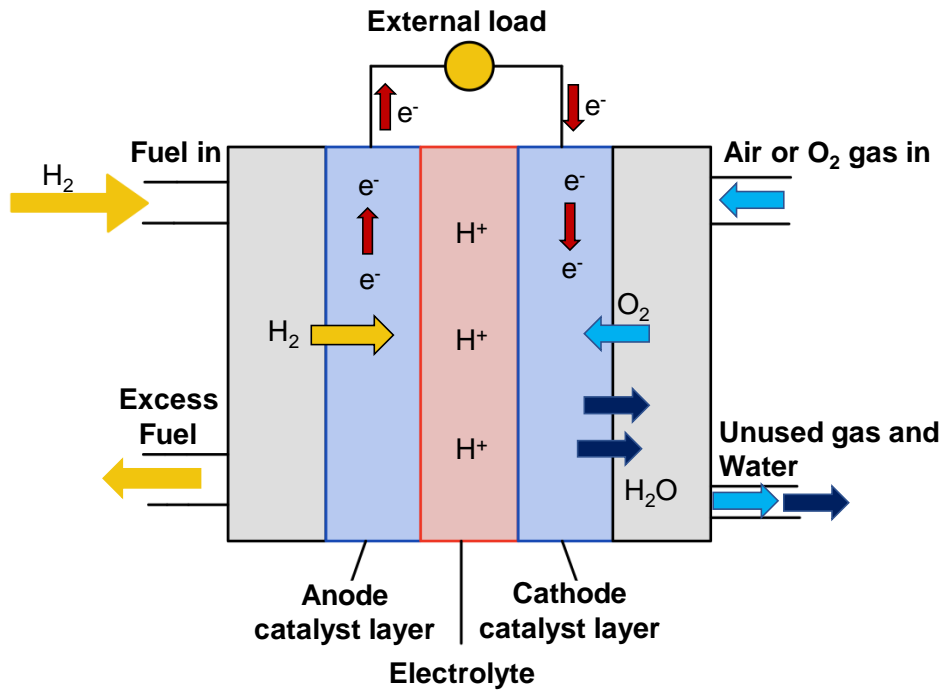
Figure 1.1) Schematic of a Proton exchange membrane fuel cell.

The two electrochemical processes in the FC that take place at the catalyst layer are the oxidation of hydrogen to protons (anode) named the hydrogen oxidation reaction (HOR) and the reduction of oxygen or air at the cathode to produce water named the oxygen reduction reaction (ORR)[12]. The half cell reactions at the anode and cathode in acidic media are[13]:

$$HOR: \qquad H_2 \rightarrow 2\,H^+ + 2e^- \qquad\qquad (1.1)$$

$$ORR: \qquad O_2 + 4\,H^+ + 4\,e^- \rightarrow 2H_2O \qquad (1.2)$$
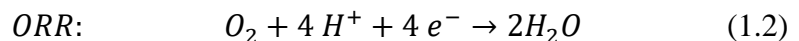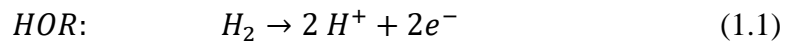
1.2.1 Main Limitations of Fuel cells

The main limitation of the PEMFC is the use of the Pt/C catalyst at both the anode and the cathode, which hinder its large scale commercialization of the devices[8]. It is estimated that nearly 30% of the cost of PEMFCs is due to the use of Pt/C catalysts[8-9]. In fuel cells, HOR is very fast, but ORR is kinetically hindered[13], thus the sluggish ORR often produces high overpotentials[14-15]. Thus, to mitigate this and improve the efficiency of the FC, often times higher loadings of the Pt catalyst are used at the cathode[8]. This is highly

disadvantageous due to the cost and scarcity of Pt. Commercialization is then hindered by high costs in addition to the hydrogen fuel-related technologies[16]. Therefore, to create sustainable PEMFCs, using inexpensive and non-precious metals to replace the Pt/C catalysts are necessary and essential for the future commercialization of PEMFCs[15].

1.2.2   Non-precious metal catalysts

Seminal work on non-precious metal catalysts (NPMCs) began in 1960 by Jasinski who reported the first non-precious metal catalyst for the ORR based on porphyrins and/or phthalocyanines[17]. This cobalt (Co)-based catalyst demonstrated high activity for the ORR in a basic electrolyte but was not stable in acidic media[10].
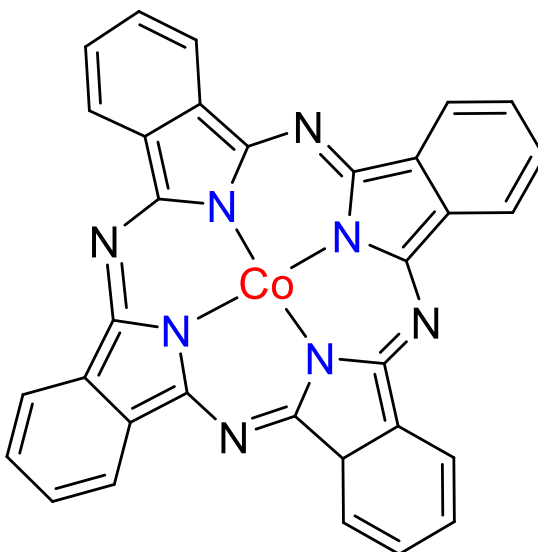
Figure 1.2) Image of the Jasinski catalyst developed in 1964.

Later, various metal-N_4 supported on carbon catalysts demonstrated significant activity for ORR in acidic media[15]. The next breakthrough was the report of Yeager published in 1989 that showed that the expensive porphyrin units could be replaced by using a nitrogen containing molecule and cobalt individually to create ORR catalysts[18]. Then, in 2009 Dodelet and co-workers created a new catalytic system by impregnation iron acetate on a microporous carbon as a support. This was further heat-treated in the presence of argon and ammonia gas[8]. The pyrolysis of the catalysts resulted in improved activity and stability of the catalysts, especially in acidic media[13, 19]. Until now, there had been little evidence of what the precise active sites on the catalyst were, so the exact nature of the

4

active sites has been debated for a long time[20-21]. However, Dodelet et al, were able to hypothesize a predicted active site for the catalyst that is still the most commonly believed active site for NPMCs to this day[8]. The predicted active catalytic site is shown in Figure 1.3. This model states that iron acetate could fit within the micropores of the carbon support and upon high-temperature heat treatment (>800 °C) in the presence of NH_3 forming a bridging structure between two graphene sheets of the carbon support with basal nitrogen's functionality coordinated to the Fe. The active sites of the ORR catalysts are predicted to be nitrogens coordinated to a transition metal either embedded into the basal plane or bridging two graphene layers together to form either $Fe-N_4/C$ or $Fe-N_{2+2}/C^{[22]}$.
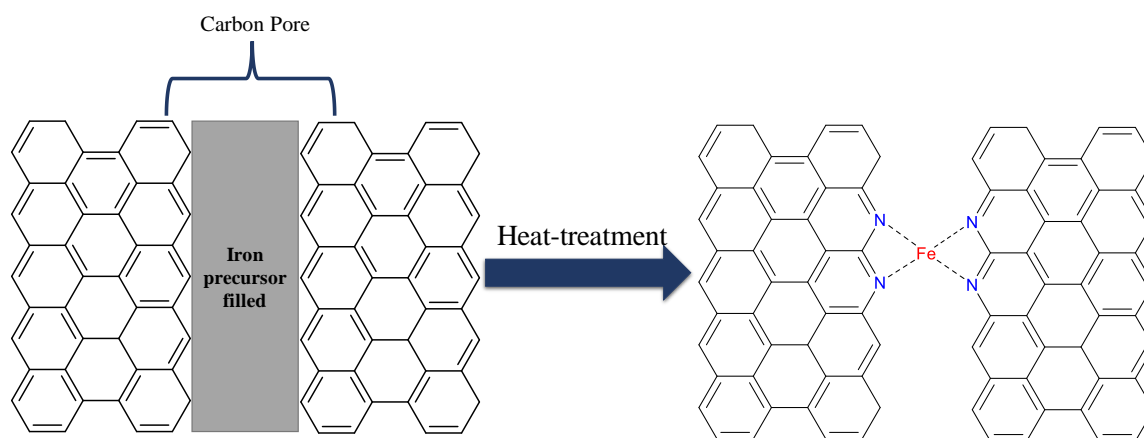
Figure 1.3) Schematic of Dodelet's predicted active site for a $Fe-N_X/C$ catalyst.

Newer generations of NPMCs heavily rely on carbon materials enriched by nitrogen and a non-precious transition metal, commonly iron[8, 14]. More recently, new iterations employ metal-organic frameworks (MOFs) to provide more porous structures that lead to better mass transport and higher performance[8]. While this area is rapidly evolving and new exciting catalytic materials designed and manufactured, there are still a lot of debates in literature with regards to the nature of active sites of the catalysts[23].

NPMCs can produce current and power densities that are similar to the state-of-the-art Pt/C catalysts[9]. The catalyst activity is directly related to the structure which can vary due to synthetic conditions, synthesis, carbon support, metal, and/or nitrogen ligands[24]. The carbon support can greatly influence the activity of the catalyst, as more microporous supports are better capable to host the active sites[4]. Of importance for these catalysts are

the concentration and the chemical state of the nitrogen functionalities on the surface (Figure 1.4)[8]. For example, specific nitrogen groups such as pyridinic nitrogens result in higher activity while pyrrolic nitrogens result in lower activity due to protonation[8]. The nitrogen functionalities are important as the pyridinic nitrogens lower the Lewis basicity of the carbon atoms located on the surface where they are easily reachable by O_2 gas[8, 25]. The pyridinic nitrogens are Lewis bases, which increases the electron-donor properties of the nitrogen-doped carbon material. This helps to weaken the O-O bond and increase the catalytic activity of the N-doped carbon[23]. Lastly, the presence of the transition metal will facilitate the coordination and incorporation of the nitrogen functionalities into the carbon support. The role of the metal is not fully understood, but it is widely believed that the metal center actively participates in the ORR and is crucial for creation of the most active catalytic sites. However, some researchers believe that metal just aids in the formation of the active site, but does not actively participate in the catalytic transformation[26]. Regardless, the addition of a transition metal is important for the creation of these materials. Iron, cobalt, or manganese are metals commonly used to create effective NPMCs[22].

Typical production procedures of NPMCs include high-temperature heat treatments exceeding 900 ℃[9, 22] in the presence of Fe with N-containing molecules, chalcogenides, metal oxides/carbides, nitrides, enzymatic compounds[27]. One of the major disadvantages of this method to synthesize the NPMCs is that it leads to a wide range of different sites on the surface such as various nitrogen functionalities coordinated to the iron including iron nitrides, and iron carbides; some of which are not beneficial to ORR activity of the system and could reduce the efficiency of the cataylst[8]. For example, pyridinic sites are more favourable for the ORR since they facilitate fast 4-electron transfer from O_2 gas to H_2O[16]. During the heat treatment process, the carbon usually contains at least 4-types of nitrogen functionalities on the surface: pyridinic, pyrrolic, nitrile, and graphitic[16]. Furthermore, if pyrolyzation occurs in the presence of metal, this can create heterogeneous structures with at least 5 different iron-nitrogen interactions[28]. Thus, this method results in higher degrees of disorder and is hardly possible to use it for the creation of materials with a narrow distribution of specific structural active sites[20].
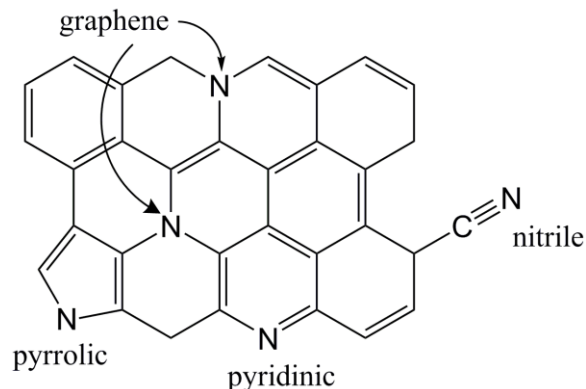
Figure 1.4) Schematic of the 4 types of nitrogen functionalities that can form on the carbon support during heat treatment.

Finally, NPMCs still suffer from stability issues and could follow various degradation mechanisms, of which one is the deactivation of the active sites due to anion binding from the electrolyte that reduces the activity of the highly active pyridinic nitrogens[9]. Next, carbon corrosion can occur as the catalysts are used at potentials greater than 1.2 V vs RHE for prolonged periods. One of the major degradation pathways of the active sites is catalyst poisoning via by-products including H_2O_2[14, 22, 24]. Many other complications arise from the leaching of metallic sites due to corrosion in acidic environments and the resulting loss in metal particles that could react with H_2O_2 by-products to produce Fenton's reagent which subsequently oxidizes the carbon support[10]. Many of these degradation mechanisms are more pronounced in acidic environments which have further issues such as protons reacting with the basic pyridinic sites, effectively deactivating them[12, 23]. While the NPMCs are a very promising route to replace the costly Pt-based catalyst, further work needs to address the stability issues along with the determination of the active sites, so to maximize the activity of the catalysts for future commercialization and use.

1.3 Electrolyzers

The production of hydrogen gas as a fuel is important as hydrogen is considered a clean fuel with great properties as an energy carrier[29-30]. The hydrogen economy is rapidly expanding, however, one of the major issues is that a majority of the hydrogen gas produced comes from fossil fuel burning processes such as coal gasification and steam reforming[2]. A minor producer of hydrogen is through water electrolysis (the splitting of water), this method is preferred as there is no greenhouse gases produced throughout the

process[2]. Over 65 million tons of H_2 are produced yearly and electrolysis of water only accounts for 4%[31]. Large-scale water splitting to produce hydrogen and oxygen fuels is an emerging research topic due to this[32] and thus the hydrogen economy will depend on a stable and low-cost method to produce the fuel[33]. Polymer electrolyte membrane electrolysis cells are devices that are used to perform the reaction to create hydrogen gas[31]. The water-splitting reaction is comprised of two half-reactions known as the hydrogen evolution reaction (HER) to release H_2 gas and the oxygen evolution reaction (OER) releasing O_2 gas[34-35].
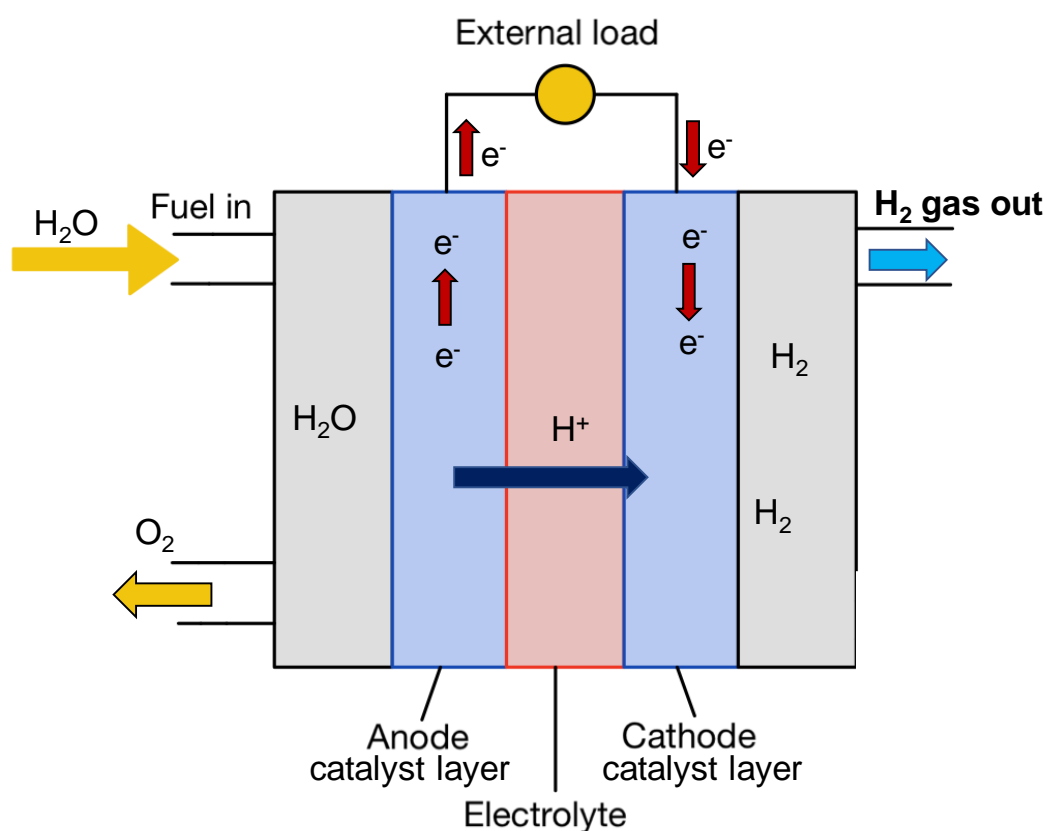
Figure 1.5) Schematic of a polymer electrolyte membrane electrolyzer.

The OER is one of the main areas of interest due to slow kinetics and high overpotentials[35-37]. This is due to the high number of electrons (4) and oxidative conditions to evolve oxygen[37]. The most common materials to perform this reaction are precious metals such as platinum or metal oxides such as iridium and ruthenium[1, 38-39]. Thus,

widespread use of these catalysts is hindered by scarcity and cost[38]. The OER reaction mechanism is presented below[40-41].

$$2H_2O \rightarrow O_2 + 4e^- + 4H^+ \qquad\qquad E^o = 1.23\ V\ vs\ RHE$$

An advantage of the electrolysis of the water is that it will yield hydrogen gas which can be converted back into the water in a PEM fuel cell[10, 42]. To perform this reaction efficiently, an ideal catalyst material will require low-cost synthesis, large abundance of catalyst materials, and stability in acidic electrolyte environments[33]. Finding efficient electrocatalysts using earth-abundant materials for OER is essential for the development of modern electrolyzer devices[43].

1.3.1 Non-precious metal oxygen evolution catalysts

Promising non-precious metal catalysts should have low overpotentials, high stability, and high specific capacity[43-44]. An approach to make this new generation of catalyst involves supporting metals on earth-abundant 2D carbon materials[38], such as depositing metal particles on a highly porous carbon will ensure a significant exposure of active sites on the surface[32]. To date, long term stability and low operating potentials remain a challenge for the non-precious metal catalysts[41]. Sluggish kinetics, aggregation of active sites are some other causes of low efficiency[45]. To create a high-performing catalyst for the OER, understanding the catalyst composition and activity is essential[39]. To improve the activity of these catalysts much research has gone into increasing the active sites on the 2D materials to provide more efficient charge transfer, along with having larger electrode/electrolyte areas and shorter diffusion lengths to enhance the redox reactions[46-47].

Combining metals with carbon is becoming quite popular in the production of OER catalysts, especially oxygen-rich carbon supports[33, 46, 48]. The carbon support can provide a surface facilitating uniform distributions of catalytically active sites[49]. Graphene is ideal to use based on the high electrical conductivity from strong conductive networks, surface area, and mechanical properties it possesses[50-52]. The shape of the graphene sheets allows them to orient parallel to each other which provides channels for efficient mass transport[50]. This 2D material shows exceptional electrochemical properties due to the high density of active sites on the surface when doped for electrocatalysis and allows easy release of the

oxygen and hydrogen gas[45, 53]. In general, a larger surface area of the support is beneficial since it allows for an increase in the number of active sites in the catalyst. This will in turn increase the catalyst's activity[54]. Having abundant functional groups allows the graphene oxide (GO) to strongly adsorb metals via electrostatic attraction[55]. Producing graphene can be quite extensive with harsh chemical agents and complex workups[47]; By far the most common method of graphene production is through Hummer's method involving strong acids and oxidants[52, 56-57]. Using these strong acids and oxidants can severely damage the sp^2 structure and deteriorates its performance[57]. Graphene oxide (GO) is a 2D material composed of sp^2 and sp^3 hybridized carbon atoms, along with surface oxygen functionalities such as carboxyl, phenolic and epoxide groups[58]. GO is commonly synthesized through the oxidation of graphite with acid, followed by exfoliation[56]. The electrochemical methods of exfoliation take graphite and intercalate molecules between the layers[59]. This allows for the mass production of high-quality graphene without the use of harsh chemicals[59]; In addition to a simpler work up in the materials.
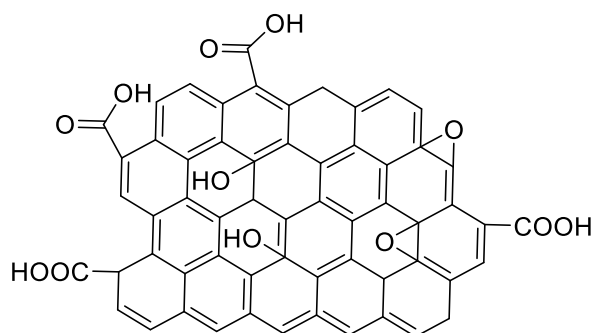
Figure 1.6) Schematic of graphene oxide.

1.3.1.1 Ruthenium (Ru)

A cheaper alternative to platinum or iridium is ruthenium metal[32]. Ruthenium is used for oxygen evolution due to its high stability in acidic media and better performance[37]. Low oxidation state (III) Ru is generally preferred as higher oxidation states usually lead to lower OER performance[37]. However, Ru-catalysts often suffer from corrosion at high potentials. To mitigate this, it is now being explored in a mixture with other high surface area materials, like carbon to stabilize the matrix due to increased access of reactants and the subsequent release of the products[1,54].

10

1.3.1.2 Nickel (Ni)

Even though Ru oxides are commonly used, they are relatively expensive, so to further improve these catalysts, low-cost materials need to be explored[60]. Nickel is ideal to use as a replacement due to the theoretically high activity and low cost of the material[50]. Ni has desirable redox properties and the surface defects make it an ideal candidate for OER[45]. One such approach to use Ni is to couple metal nanoparticles onto carbon. This approach yields a material with high electrocatalytic properties that significantly decreased the tendency to corrode the surface at the high oxidative potentials[60]. The preparation of most Ni catalysts for OER require a high-temperature carbonization process, which is disadvantageous in the large scale-up synthesis of the materials[60]. Ni still has some issues involving lower activities, poor kinetics and durability[50]. Thus, Ni is combined with other metals such as Fe[61].

1.4 Supercapacitors

The wide implementation of clean electrochemical technologies will then require significant developments of fuel cells (to generate energy), and charge storage devices (to store and release energy). For example, electric double-layer capacitors (EDLCs), are devices capable of storing and releasing large amounts of energy very quickly. These devices are made up of two current collectors that are typically coated with porous carbon. There is a separator in the middle that allows for the movement of charge. These devices work by simply forming electric double layers at the electrode/electrolyte interfaces (Figure 1.7). These devices are similar to batteries, however, they are lower in cost and have longer cycle life when compared to a typical lithium-ion battery[62]. Therefore, they are a more effective, and environmentally friendly way to store charge in materials.
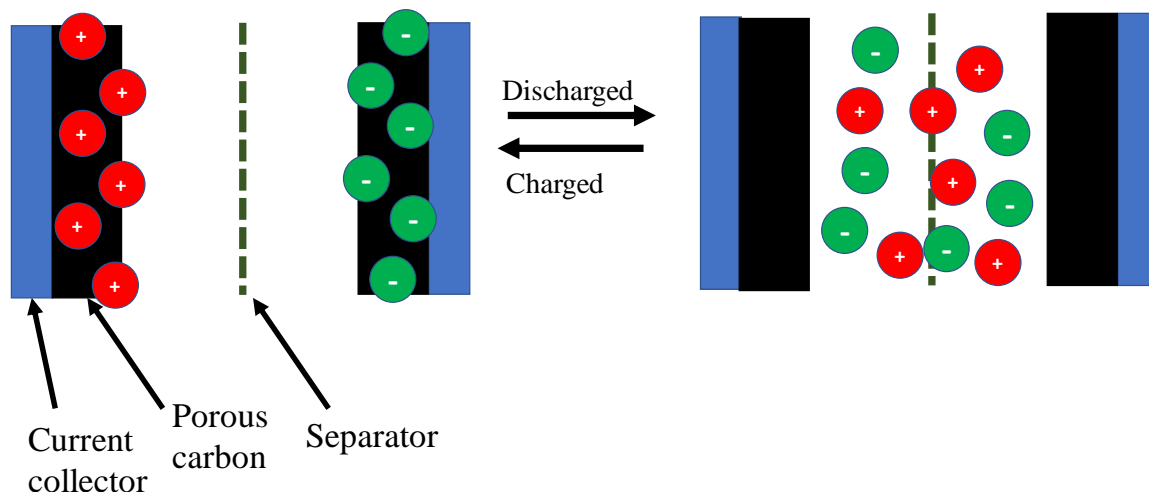
Figure 1.7) Schematic of a supercapacitor.

EDLCs are made from carbon-based materials due to carbon's abundance, mechanical stability, surface area, and high electric conductivity[63-64]. The main limitation of carbon-based EDLCs is that they have relatively low energy and power density[65-66]. To combat this, supercapacitors have been developed that combine the electrostatic interactions from the carbon electrodes and Pseudofaradaic or Faradaic (redox) processes from the suitable dopant(s). The addition of the Faradaic processes could aid to resolve the EDLCs limitation and offer increased charge storing capability and energy density[67-69].

Rare earth transition metal-oxides such as Ru oxide are often used as dopants for supercapacitor materials due to the ability of the metal center to adopt multiple valence states and support multiple redox processes that are elevating charge transfer and energy storage properties of the materials, however high cost of the dopant hindering large scale application of the materials[70-73].

1.4.1 Non-precious metal materials for SCs

To mitigate the high cost of the Ru oxide, doping of carbon materials with heteroatoms (i.e. nitrogen, phosphorus, sulfur, boron) is an affordable alternative strategy for enhancing the EDLCs performance due to the additional electronic effects caused by the heteroatom dopant(s)[66]. Nitrogen is the most common heteroatom used to dope carbon materials. This is achieved by embedding nitrogen functionalities into a porous carbon backbone via high-temperature pyrolysis of the carbon with a nitrogen source. The use of

high-temperature treatments to synthesized these materials can be very energy-demanding which hinders the wide applications of the resulting materials. In addition, pyrolysis results in the formation of different heteroatom-containing moieties non-homogeneously distributed on the surface of the carbon that will result in vastly different properties across the material.

The procedure to synthesize these materials is lacking reproducibility and scalability and it is difficult to tune the performance of the materials due to uncertainty with the functional groups caused by the heat treatment. Another method to add nitrogen functionalities to the carbon surface is through the addition of electroactive molecules. Using nitrogenous ligands, attached to the surface, aids in the fast transfer of one or more electron(s)[74]. The chemical attachment of molecules (especially covalent bonding to carbon) can enhance electronic effects as well as improve the amount and homogeneity of nitrogen functionalities on the surface, assist in ion adsorption, and aid in wettability[63, 75]. Polymers (such as polyaniline (PANI)) have also been used for supercapacitor design, however, they are not useful in aqueous capacitors due to oxidative degradation upon testing in prolonged exposure in the aqueous electrolyte[76]. Better control on what nitrogen groups form on the surface by using a molecularly defined method might open more avenues on how to better build these materials for the future of supercapacitor electrodes to get the most energy and power out of the materials.

1.5 Electrochemical Testing

1.5.1 Rotating disk Voltammetry

One of the most important techniques used in this thesis is rotating ring disk electrode (RRDE) analysis. This 3-cell electrode test is used to determine how well a material will catalyze the ORR by using hydrodynamic voltammetry. This is a technique that uses an electrode rotating at high speeds to measure the kinetic and diffusion-limited reactions at the catalyst layer on the surface of the electrode. In a typical redox reaction, oxidized species O, is reduced to R at the surface of the WE as the potential at the WE is scanned towards more negative potentials (more negative than the $E_{1/2}$ of the redox reaction-where the O species would be reduced). This is the fundamental process that takes place when using a RDE. However, as this is occurring a constant rotation rate is applied

(typically in RPM) while the potential at the disk is swept to more negative potentials than the $E_{1/2}$ (reduction). This continues until a limiting current is reached (Figure 1.9). In other words, the potential is sufficient enough to immediately reduce any species that come in contact with the WE. For example, oxidized species, O, reaches the electrode surface through convection processes during rotation where upon contact with the disk O is converted to reduced species, R. Then R will be diffused away from the disk back to the bulk electrolyte. The addition of the ring (separated from the disk by a Teflon sheath) creates a second working electrode that can monitor both the oxidation and reduction processes at both electrodes[77]. In this mode the ring is held at a more positive potential so that any reduced species that come into contact with the ring will immediately be oxidized. The oxidation current is then measured and plotted at as a function of potential.

For example, the direct conversion of oxygen to water is a 4-electron process and is the desired product for a potential FC catalyst candidate. However, there is often a by-product, hydrogen peroxide, formed via a 2-electron process due to the incomplete conversion of oxygen to water (Figure 1.8).

4-electron transfer process

$$O_2 + 4e^- + 4H^+ \longrightarrow 2\ H_2O$$

2-electron transfer process

$$O_2 + 2e^- + 2H^+ \longrightarrow H_2O_2$$
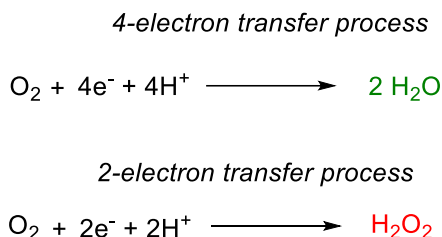
Figure 1.8) Equations for the different pathways that can occur during the oxygen reduction reaction

The production of hydrogen peroxide is undesirable, leads to efficiency losses in FCs, and can poison the catalyst. Thus, determining the amount of hydrogen peroxide produced during the course of the ORR is a direct measure of the reaction efficiency (the affinity of the system to produce the ideal product for the ORR, water) of new catalysts for FCs. In RRDE, obtaining the ring and disk current data as the potential is scanned provides a reliable method to determine the product distribution, H_2O vs H_2O_2[77]. An example of this plot is shown below in Figure 1.9. More information on this technique can be found in Fruehwald et. al[77].
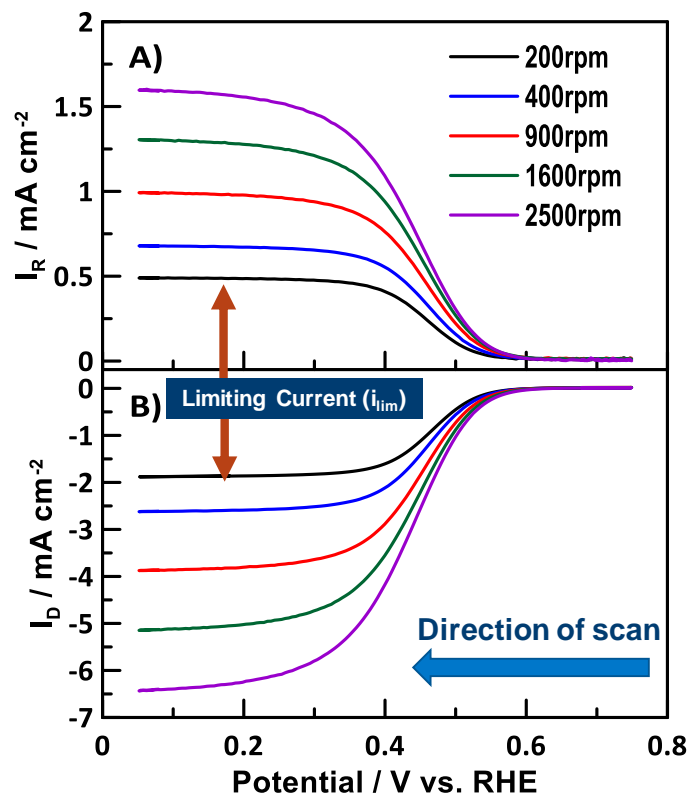
Figure 1.9) Example of an RRDE curve to monitor the ORR reaction.

1.5.2   Electrochemical Impedance Spectroscopy

In this thesis, electrochemical impedance spectroscopy (EIS) is used mainly in Chapters 5,6,8. EIS was used in these chapters to determine the capacitance of the materials at a specific potential to determine the capacitance of the double layer and Faradic processes and using that to determine the pseudocapacitance of the materials. Briefly, EIS works by altering the frequency perturbation using a selected direct current (DC) potential. The response from the impedance of a circuit is recorded as a function of the time at the changing frequencies. A Nyquist plot can be made by plotting the real impedance (Z') versus the imaginary impedance (Z"). Using this plot a variety of important information about a reaction can be gathered such as the charge transfer resistance, solution resistance, electronic resistance, electrolyte resistance. The majority of the EIS used in this work is in regard to making capacitance plots. These plots are made by calculating the series capacitance using the transmission line model[80]. The transmission model is used when analyzing porous electrodes to determine how charge can be stored at the electrode

15

interface (Figure 1.10). In this model the DC bias is chosen where there is no charge transfer resistance at the electrode and thus the double layer can be addressed[81].

GDL catalyst layer   Electrolyte
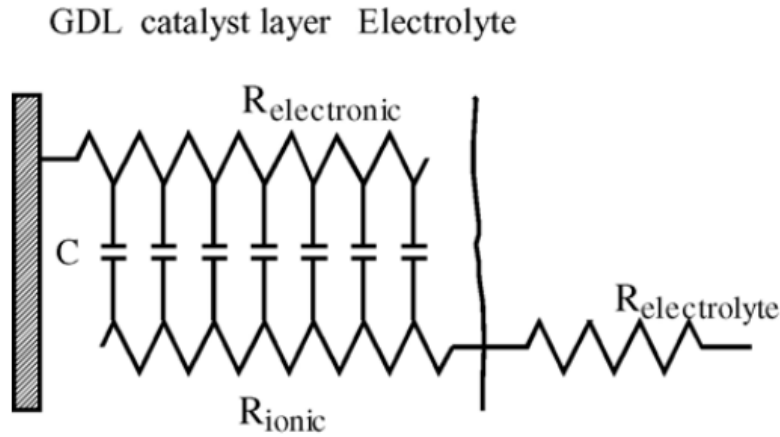
Figure 1.10) Transmission Line Model reproduced from Ref. 81[81]

The calculated series capacitance is plotted versus the real impedance[78]. The series capacitance can be calculated using:

$$C = -\frac{1}{\omega Z''}$$

Where ω is the angular frequency. The capacitance plots give rise to the electrochemical storage due to Faradaic processes. In chapters 5,6, and 8 by running EIS at different potentials, the double layer, and Pseudofaradaic processes can be perturbed by using a DC potential in the double layer region (0.4 V for this work, C_{dl}) and a DC bias where surface redox properties are observed ($Fe^{3+/2+}$ at 0.7 V, C_F). Using the follow expression[80]:

$$C_T = C_{dl} + C_F$$

We can assume that at the double layer no Faradaic processes are occurring and thus $C_T=C_{dl}$ and thus this gives a tool to determine the pseudocapactiance[80].

1.5.3   Tafel plots

One important figure of merit for OER catalysts is the overpotential that is necessary to drive the reaction, or the current density per area at 10 mA[43]. Tafel slopes are obtained by using the slope of the line in the linear region of the Tafel plot[60]. This is used for the determination of activity in OER analysis that is presented in Chapter 8. In the Tafel

analysis, a plot of the log of the current is plotted versus the overpotential. The slope of the linear line will give the Tafel slope that is used to compare catalysts in the OER. More detail about this technique can be found in Bard and Faulkner[79].

1.6 Thesis Objectives

The objective of this thesis was to create a surface modification approach which will be used to modify carbon materials with nitrogen containing molecules. In this work we use a N_3 type coordination on the surface as this active site is rarely used in applications in ORR. The investigation if this type of configuration on the surface is active in chapters 2-4. In addition, using this modification approach will allow for specific active sites to be present on the surface, classically in the typical synthesis of these materials a heat treatment procedure is used and it leads to unwanted side effects such as carbides or metal oxides, various forms of nitrogen which are inactive for the ORR[27], as well as uncontrollable discrepancies[28]. By using a surface modification approach the aim is to increase the Fe-pyridinic nitrogen site density which in turn can improve the ORR activity[27]. Then, tuning the properties of both the carbon support (Chapter 3) and the metal center used (Chapter 4). Finally, the goal of this thesis will be to use the C-N-transition metal-doped materials as a multi-functional electrode for electrochemical energy systems including supercapacitor applications (Chapters 5,6) and as an electrode material for oxygen evolution (Chapters 7-9).

1.7 References

[1]   S. Haschke, D. Pankin, V. Mikhailovskii, M. K. S. Barr, A. Both-Engel, A. Manshina, J. Bachmann, *Beilstein J Nanotechnol* **2019**, *10*, 157-167.

[2]   J. M. Kamdar, D. B. Grotjahn, *Molecules* **2019**, *24*.

[3]   M. Lefevre, E. Proietti, F. Jaouen, J. P. Dodelet, *Science* **2009**, *324*, 71-74.

[4]   F. Charreteur, F. Jaouen, S. Ruggeri, J.-P. Dodelet, *Electrochim. Acta* **2008**, *53*, 2925-2938.

[5]   F. Jaouen, F. Charreteur, J. Dodelet, *J. Electrochem. Soc.* **2006**, *153*, A689-A698.

[6]   D. Banham, T. Kishimoto, Y. Zhou, T. Sato, K. Bai, J. I. Ozaki, Y. Imashiro, S. Ye, *Sci. Adv.* **2018**, *4*, eaar7180.

[7]   A. Zitolo, N. Ranjbar-Sahraie, T. Mineva, J. Li, Q. Jia, S. Stamatin, G. F. Harrington, S. M. Lyth, P. Krtil, S. Mukerjee, E. Fonda, F. Jaouen, *Nat. Commun* **2017**, *8*, 957.

[8]   U. I. Kramm, M. Lefevre, N. Larouche, D. Schmeisser, J. P. Dodelet, *J. Am. Chem. Soc.* **2014**, *136*, 978-985.

[9]   U. I. Kramm, M. Lefevre, P. Bogdanoff, D. Schmeisser, J. P. Dodelet, *J. Phys. Chem. Lett* **2014**, *5*, 3750-3756.

[10]   D. Banham, S. Ye, K. Pei, J.-i. Ozaki, T. Kishimoto, Y. Imashiro, *J. Power Sources* **2015**, *285*, 334-348.

[11]   H. Tan, Y. Li, X. Jiang, J. Tang, Z. Wang, H. Qian, P. Mei, V. Malgras, Y. Bando, Y. Yamauchi, *Nano. Ener.* **2017**, *36*, 286-294.

[12]   G. Zhang, R. Chenitz, M. Lefèvre, S. Sun, J.-P. Dodelet, *Nano. Ener.* **2016**, *29*, 111-125.

[13]   A. Janßen, I. Martinaiou, S. Wagner, N. Weidler, A. Shahraei, U. I. Kramm, *Hyperfine Interact.* **2018**, *239*.

[14]   M. Kübler, S. Wagner, T. Jurzinsky, S. Paul, N. Weidler, E. D. Gomez Villa, C. Cremers, U. I. Kramm, *Energy Technology* **2020**, *8*, 2000433.

[15]   Z. Chen, D. Higgins, A. Yu, L. Zhang, J. Zhang, *Energy Environ. Sci.* **2011**, *4*, 3167-3192.

[16]   L. Zhang, D. P. Wilkinson, Y. Liu, J. Zhang, *Electrochim. Acta* **2018**, *262*, 326-336.

[17]   R. Jasinski, *Nature* **1964**, *201*, 1212-1213.

[18]   S. Gupta, D. Tryk, I. Bae, W. Aldred, E. Yeager, *J. Appl. Electrochem.* **1989**, *19*, 19-27.

[19]   L. Osmieri, R. Escudero-Cid, M. Armandi, P. Ocón, A. H. A. Monteverde Videla, S. Specchia, *Electrochim. Acta* **2018**, *266*, 220-232.

[20]   U. I. Kramm, I. Herrmann-Geppert, J. Behrends, K. Lips, S. Fiechter, P. Bogdanoff, *J. Am. Chem. Soc.* **2016**, *138*, 635-640.

[21]   A. Sarapuu, L. Samolberg, K. Kreek, M. Koel, L. Matisen, K. Tammeveski, *Journal of Electroanalytical Chemistry* **2015**, *746*, 9-17.

[22] N. R. Sahraie, U. I. Kramm, J. Steinberg, Y. Zhang, A. Thomas, T. Reier, J. P. Paraknowitsch, P. Strasser, *Nat. Commun* **2015**, *6*, 8618.

[23] G. Liu, X. Li, P. Ganesan, B. N. Popov, *Appl. Catal. B. Eniv* **2009**, *93*, 156-165.

[24] C. W. Bezerra, L. Zhang, K. Lee, H. Liu, A. L. Marques, E. P. Marques, H. Wang, J. Zhang, *Electrochim. Acta* **2008**, *53*, 4937-4951.

[25] M. Rauf, Y.-D. Zhao, Y.-C. Wang, Y.-P. Zheng, C. Chen, X.-D. Yang, Z.-Y. Zhou, S.-G. Sun, *Electrochem. Commun.* **2016**, *73*, 71-74.

[26] M. Lefèvre, J.-P. Dodelet, *Electrochim. Acta* **2008**, *53*, 8269-8276.

[27] L. Wang, L. Zhang, J. Zhang, *Electrochim. Acta* **2011**, *56*, 5488-5492.

[28] M. Sun, D. Davenport, H. Liu, J. Qu, M. Elimelech, J. Li, *J. Mat. Chem. A* **2018**, *6*, 2527-2539.

[29] L. Duan, F. Bozoglian, S. Mandal, B. Stewart, T. Privalov, A. Llobet, L. Sun, *Nat Chem* **2012**, *4*, 418-423.

[30] J. Creus, L. Mallón, N. Romero, R. Bofill, A. Moya, J. L. Fierro, R. Mas-Ballesté, X. Sala, K. Philippot, J. García-Antón, *Eur. J. Inorg. Chem.* **2019**, *2019*, 2071-2077.

[31] D. S. Hall, C. Bock, B. R. MacDougall, *J. Electrochem. Soc.* **2013**, *160*, F235-F243.

[32] T. Qiu, Z. Liang, W. Guo, S. Gao, C. Qu, H. Tabassum, H. Zhang, B. Zhu, R. Zou, Y. Shao-Horn, *Nano. Ener.* **2019**, *58*, 1-10.

[33] S. S. Zance, S. Ravichandran, *Appl. Phys. A* **2019**, *125*, 456.

[34] M. Gil-Sepulcre, M. Bohler, M. Schilling, F. Bozoglian, C. Bachmann, D. Scherrer, T. Fox, B. Spingler, C. Gimbert-Surinach, R. Alberto, R. Bofill, X. Sala, S. Luber, C. J. Richmond, A. Llobet, *ChemSusChem* **2017**, *10*, 4517-4525.

[35] N. Govindarajan, A. Tiwari, B. Ensing, E. J. Meijer, *Inorg. Chem.* **2018**, *57*, 13063-13066.

[36] Y. Gao, Y. Wei, Z. Lu, X. Chen, D. Wang, *J. Energ. Chem.* **2019**, *35*, 49-54.

[37] S. Laha, Y. Lee, F. Podjaski, D. Weber, V. Duppel, L. M. Schoop, F. Pielnhofer, C. Scheurer, K. Müller, U. Starke, K. Reuter, B. V. Lotsch, *Adv. Ener. Mater.* **2019**, *9*.

[38]   X. Gao, Y. Zhou, Y. Tan, S. Liu, Z. Cheng, Z. Shen, *Appl. Surf. Sci.* **2019**, *492*, 8-15.

[39]   L. Trotochaud, J. K. Ranney, K. N. Williams, S. W. Boettcher, *J. Am. Chem. Soc.* **2012**, *134*, 17253-17261.

[40]   R. Matheu, M. Z. Ertem, C. Gimbert-Surinach, X. Sala, A. Llobet, *Chem. Rev.* **2019**, *119*, 3453-3471.

[41]   A. Shatskiy, A. A. Bardin, M. Oschmann, R. Matheu, J. Benet-Buchholz, L. Eriksson, M. D. Karkas, E. V. Johnston, C. Gimbert-Surinach, A. Llobet, B. Akermark, *ChemSusChem* **2019**, *12*, 2251-2262.

[42]   R. B. Moghaddam, C. Wang, J. B. Sorge, M. J. Brett, S. H. Bergens, *Electrochem. Commun.* **2015**, *60*, 109-112.

[43]   C. C. McCrory, S. Jung, I. M. Ferrer, S. M. Chatman, J. C. Peters, T. F. Jaramillo, *J. Am. Chem. Soc.* **2015**, *137*, 4347-4357.

[44]   L. Sévery, S. Siol, S. Tilley, *Inorganics* **2018**, *6*.

[45]   M. Ramadoss, Y. Chen, Y. Hu, W. Li, B. Wang, X. Zhang, X. Wang, B. Yu, *J. Power Sources* **2020**, *451*, 227753.

[46]   X. Meng, J. Han, L. Lu, G. Qiu, Z. L. Wang, C. Sun, *Small* **2019**, *15*, 1-10.

[47]   K. K. Upadhyay, N. Bundaleska, M. Abrashev, N. Bundaleski, O. M. N. D. Teodoro, I. Fonseca, A. M. de Ferro, R. P. Silva, E. Tatarova, M. F. Montemor, *Electrochim. Acta* **2020**, *334*, 135592.

[48]   X. Li, H. Wang, J. T. Robinson, H. Sanchez, G. Diankov, H. Dai, *J. Am. Chem. Soc.* **2009**, *131*, 15939-15944.

[49]   M. Zhang, J. Chen, H. Li, P. Cai, Y. Li, Z. Wen, *Nano. Ener.* **2019**, *61*, 576-583.

[50]   S. Chen, J. Duan, J. Ran, M. Jaroniec, S. Z. Qiao, *Energy Environ. Sci.* **2013**, *6*, 3693-3699.

[51]   H. Lim, J. S. Lee, H. J. Shin, H. S. Shin, H. C. Choi, *Langmuir* **2010**, *26*, 12278-12284.

[52]   W. Tu, J. Lei, S. Zhang, H. Ju, *Chemistry* **2010**, *16*, 10771-10777.

[53]   S. N. Faisal, E. Haque, N. Noorbehesht, H. Liu, M. M. Islam, L. Shabnam, A. K. Roy, E. Pourazadi, M. S. Islam, A. T. Harris, *Sustain. Energy Fuels* **2018**, *2*, 2081-2089.

[54]   G. Chen, Y. Zhu, H. M. Chen, Z. Hu, S. F. Hung, N. Ma, J. Dai, H. J. Lin, C. T. Chen, W. Zhou, Z. Shao, *Adv. Mater.* **2019**, *31*, e1900883.

[55]   P. Li, R. Chen, S. Tian, Y. Xiong, *ACS Sustain. Chem. Eng.* **2019**, *7*, 9566-9573.

[56]   K. Krishnamoorthy, M. Veerapandian, K. Yun, S.-J. Kim, *Carbon* **2013**, *53*, 38-49.

[57]   J. Liu, C. K. Poh, D. Zhan, L. Lai, S. H. Lim, L. Wang, X. Liu, N. Gopal Sahoo, C. Li, Z. Shen, J. Lin, *Nano. Ener.* **2013**, *2*, 377-386.

[58]   D. Long, W. Li, L. Ling, J. Miyawaki, I. Mochida, S. H. Yoon, *Langmuir* **2010**, *26*, 16096-16102.

[59]   P. Yu, S. E. Lowe, G. P. Simon, Y. L. Zhong, *Current Opinion in Colloid & Interface Science* **2015**, *20*, 329-338.

[60]   L. Ai, T. Tian, J. Jiang, *ACS Sustain. Chem. Eng.* **2017**, *5*, 4771-4777.

[61]   C. Wang, R. B. Moghaddam, M. J. Brett, S. H. Bergens, *ACS Sustain. Chem. Eng.* **2016**, *5*, 1106-1112.

[62]   N. H. Basri, M. Deraman, R. Daik, M. T. M. Ayob, M. I. Sahri, N. S. M. Nor, B. N. M. Dolah, S. Soltaninejad, *Advanced Materials Research* **2015**, *1112*, 236-240.

[63]   G. Pognon, C. Cougnon, D. Mayilukila, D. Belanger, *ACS Appl Mater Interfaces* **2012**, *4*, 3788-3796.

[64]   P. J. Hall, M. Mirzaeian, S. I. Fletcher, F. B. Sillars, A. J. R. Rennie, G. O. Shitta-Bey, G. Wilson, A. Cruden, R. Carter, *Energy Environ. Sci.* **2010**, *3*.

[65]   S. Zhang, N. Pan, *Adv. Ener. Mater.* **2015**, *5*.

[66]   Z. Ji, N. Li, M. Xie, X. Shen, W. Dai, K. Liu, K. Xu, G. Zhu, *Electrochim. Acta* **2020**, *334*, 135632.

[67]   T. Brousse, D. Bélanger, J. W. Long, *J. Electrochem. Soc.* **2015**, *162*, A5185-A5189.

[68]   M. Toupin, D. Bélanger, I. R. Hill, D. Quinn, *J. Power Sources* **2005**, *140*, 203-210.

[69]   S. Mallakpour, A. Abdolmaleki, M. Mahmoudian, A. A. Ensafi, M. M. Abarghoui, *Journal of Materials Science* **2017**, *52*, 9683-9695.

[70]   X. Liu, T. A. Huber, M. C. Kopac, P. G. Pickup, *Electrochim. Acta* **2009**, *54*, 7141-7147.

[71]   X. Liu, P. G. Pickup, *J. Electrochem. Soc.* **2011**, *158*, A241-A249.

[72]   X. Liu, P. G. Pickup, *J. Power Sources* **2008**, *176*, 410-416.

[73]   H. M. Fruehwald, R. B. Moghaddam, O. V. Zenkina, E. B. Easton, *Catal. Sci. Technol.* **2019**, *9*, 6547-6551.

[74]   G. Pognon, T. Brousse, D. Bélanger, *Carbon* **2011**, *49*, 1340-1348.

[75]   J. Zhou, S. Xu, L. Ni, N. Chen, X. Li, C. Lu, X. Wang, L. Peng, X. Guo, W. Ding, *J. Power Sources* **2019**, *438*, 227047.

[76]   F. Fusalba, P. Gourec, D. Villers, D. Belanger, *J. Electrochem. Soc.* **2001**, *148*, A1-A6.

[77]   H. M. Fruehwald, O. V. Zenkina, E. B. Easton, *Chemistry Teacher International* **2021**.

[78]   N. O. Laschuk, E. B. Easton, O. V. Zenkina, *RSC Adv.* **2021**, *11*, 27925-27936.

[79]   A. J. Bard, L. R. Faulkner, *Electrochemical Methods: Fundamentals and Applications, Vol. 2*, Wiley, **2001**.

[80]   O. R. O. Reid, F. S. Saleh, E. B. Easton, *ECS Transactions* **2014**, *61*, 25-32.

[81]   E. B. Easton, P. G. Pickup, Electrochim. Acta 2005, 50, 2469-2474.

Chapter 2. Fe-N$_3$/C Active Catalytic Sites for the Oxygen Reduction Reaction Prepared with Molecular-Level Geometry Control through the Covalent Immobilization of an Iron-terpyridine Motif onto Carbon

2.0 Preface

Part of the work described in this chapter has been previously published as Fruehwald, H. M.; Ebralidze, I. I.; Zenkina, O. V.; Easton, E. B., Fe-N$_3$/C Active Catalytic Sites for the Oxygen Reduction Reaction Prepared with Molecular-Level Geometry Control through the Covalent Immobilization of an Iron-Terpyridine Motif onto Carbon. *ChemElectroChem.* **2019,** *6*, 1350-1358. doi: 10.1002/celc.201801842 with permission from Wiley-VCH Verlag GmbH & Co.

In this chapter, the exploration of the design of a nitrogen modified carbon support using a surface modification approach as a model N$_3$ active site for the oxygen reduction reaction. I used a covalent diazonium coupling chemistry method to attach only the most active forms of nitrogen to the resulting Vulcan carbon surface. The resulting catalyst was prepared under ambient temperatures and conditions, lowering the cost to synthesize these materials. The synthetic procedure showed a unique and simple way to produce a high performing model catalyst for the oxygen reduction reaction. As a result, this synthetic methodology to modify terpyridine-based molecules was performed using other nitrogen-containing molecules on Vulcan carbon, as well as other carbon supports. This methodology will be explored again in Chapters 3-6, and 9.

2.0 Abstract

A model for a non-precious metal catalyst for the oxygen reduction reaction (ORR) in aqueous media has been prepared by functionalizing a commercial Vulcan XC-72 carbon support with a terpyridine-based nitrogenous ligand. The terpyridine ligand geometry allows the formation or active catalytic sites by selectively embedding a N_3/C structural motif into the carbon support confirmed by using thermogravimetric analysis (TGA) and X-ray photoelectron spectroscopy (XPS) measurements. Room-temperature metal-ligand coordination results in the desired $Fe-N_3/C$ moieties on the surface. This model system was used to demonstrate the catalytic activity of the surfaces containing mainly $Fe-N_3$ sites for the ORR in acidic and basic media. Importantly, we demonstrate that the system could be prepared under mild reaction conditions, does not require high-temperature treatments, and shows catalytic activity for the ORR. Interestingly, when the system was pyrolyzed in an N_2 atmosphere at 700 ºC the resulting activity declined. The non-heat-treated $Fe-N_3/C$ surface demonstrates comparable activity in acidic electrolyte medium when compared to most literature catalysts that are typically heat treated to produce four nitrogen atoms coordinated to one iron center ($Fe-N_{2+2}/C$). Interestingly, despite the fact that many systems reported so far in the literature exhibit enhanced activity after heat treatment, our system showed an increase in activity when the material was not pyrolyzed.

2.1 Introduction

Fuel cells (FCs) are devices that utilize chemical reactions to directly produce electrical energy. These devices are ideal as clean energy sources in various electrochemical systems such as transportation, and portable energy devices[1-3]. The main drawback of conventional FCs is the use of a platinum catalyst on a carbon support (Pt/C) used to achieve high activity. There are many concerns with this catalyst material such as the cost and the limited availability of platinum (Pt)[4]. Therefore, developing non-precious metal catalysts (NPMC) that involve cost efficient materials and/or abundant metals is essential for the development of modern commercial fuel cell devices.

NPMCs are typically prepared from a microporous carbon support, nitrogen precursor (nitrogen source), and a non-precious metal such as Fe or Co[5-6]. The development of NPMCs is continually advancing, however, the exact nature of the active site(s) remains ambiguous. Furthermore, many reported catalysts were prepared via

24

methods that have very limited control over the final active site geometry, yielding catalysts with randomly distributed nitrogen-enriched domains with unknown/mixed geometry and as a result diverse activity in the ORR. Molecularly precise systems based on a single type of catalytic site are rare but are essential in order to gain a better understanding of the mechanism and rational design of the best catalytic systems. Dodelet's group has done extensive research on the active site of an M-N/C catalyst (where M=Fe) design and has reported that the most likely active site is one where Fe is coordinated to four nitrogens[7]. Further developing Dodelet's pivotal investigation, most research has gone into synthesizing materials using various nitrogen precursors and non-precious metals which generally adopt an M-N_{2+2}/C site, M=Fe, to mimic predicted M-N_{2+2} active site. To the extent of our knowledge, only few attempts were made to explore alternative conformation motifs of the active catalytic sites.

The most common method of synthesizing non-precious metal ORR catalysts involves pyrolysis of the carbon support and iron precursor in the presence of either NH_3 gas or a nitrogenous ligand, at optimal temperatures to produce the desired catalytic materials[8-11]. The challenge is that this approach results in a wide distribution of nitrogen functionalities on the carbon surface, which give poor control over the geometry of catalytic sites, types of nitrogen functionalities present, and homogeneity of the distribution on the surface[12-13]. It is commonly believed that the most active nitrogen functional groups that enhance ORR activity are pyridinic nitrogens[14]. However, when these materials are heat-treated it is difficult to control the amount of pyridinic nitrogen present on the surface to maximize catalytic activity. High temperature pyrolysis treatments can be beneficial and enable one to tune the reactivity of the catalyst material based on temperature[3, 9, 15-18]. Nonetheless, this is still undesirable due to the generally higher temperatures (900 ºC or greater) involved, which is highly energy demanding and thus the molecular design of the surface will be governed by uncertainty from the distribution of functional groups on the surface. For example, when a phenanthroline ligand was used as a precursor to maximize the formation of the active catalytic sites during high temperature heat treatment, control was lost due to the significant breakdown and major structural changes of the molecules at very high temperatures[10].

On the other hand, the high-temperature heat treatment in the presence of nitrogen can be beneficial for the carbon support since it can etch the surface and create micropores that could help enhance the performance of the catalyst material[16, 19]. Thus, it is challenging to design a catalytic material that has a high density of a single active site geometry when conventional synthetic methods are employed. Furthermore, for the commercial development of NPMCs, it is highly desirable to exclude energy demanding and expensive high temperature heat treatment procedures out of the conventional synthetic process. Therefore, novel synthetic methodologies should be developed for the creation of catalytically active materials at mild reaction conditions.

Many studies have reported exceptional activity for NPMCs synthesized via high temperature heat treatment procedures[16]. However, the resulting materials are often unstable due to a variety of reactions that can be involved in the destruction of the active sites of the catalysts, of which are not completely understood. These degradation mechanisms can include metal leaching in acidic solution and peroxide poisoning of the active sites[20]. Thus, operational stability remains a current challenge for NPMCs. Therefore, to synthesize a material candidate for real practical applications requiring long lifetimes, like transportation, the material needs to not only have exceptional activity but also have superior durability for long operational times[21]. Recently, some stability improvements have been seen when there is not only a high quantity of pyridinic nitrogen, but also quaternary nitrogen present on the surface[16, 22]. The method to produce quaternary nitrogen sites normally relies on high temperature heat treatment steps that leaves a high level of uncertainty of the resulting nature and geometry of the active sites due to the harsh conditions of the synthetic process[16, 22]. Using a bottom-up approach where the attachment of nitrogen-iron moieties involves a more defined chemical linkage method, this could allow for more robust linkages to the surface that could give rise to longer lifetimes of the materials.

Our group has previously reported a method that utilized a pre-defined structure of a nitrogenous aromatic ligand (1,10-phenanthroline-5,6-diamine) with high affinity to iron that allows controlled and highly selective incorporation of Fe-N_{2+2}/C active sites onto the carbon surface. As a result, good catalytic activity for Fe-N_{2+2}/C was demonstrated for these systems in acidic media when the material was heat-treated[23]. In this work, we use

a similar synthetic approach to introduce novel Fe-N$_3$/C active sites into the materials. We employ diazonium coupling chemistry to covalently functionalize the surface of the carbon support with terpyridine-based metal coordination sites. Chemical deposition of 4'-(4-aminophenyl)-2,2':6',2"-terpyridine (tpy) results in selective grafting of the terpyridine unit to the surface, shown in Scheme 2.1. Then, unique iron-metal coordination motifs were created on the surface by treatment of the materials at room temperature with a 10 mM solution of FeCl$_3$ in methanol[23].
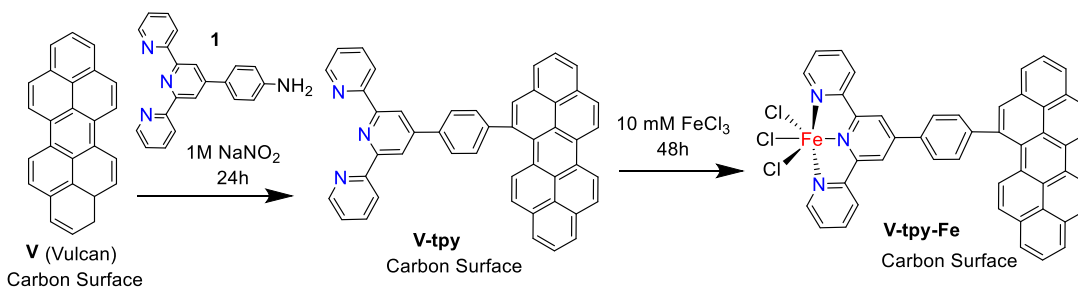
Scheme 2.1) Synthetic methodology for the surface modification. Diazonium coupling reaction used to incorporate terpyridine moiety onto the carbon surface. The material was further reacted with iron chloride in the solution.

We report here the synthesis of a nitrogen-enriched catalyst for ORR which featured a unique pre-designed Fe-N$_3$/C catalytic active site. To our knowledge, this is the first evidence in the literature where distinctive Fe-N$_3$ sites were selectively incorporated onto the carbon surface. Majority of previously reported literature procedures for the preparation of nitrogen-enriched surfaces were suited to simply get increased nitrogen content in the materials. Methods that allow for the fine control of the processes on a molecular level and/or allow for the incorporation of predesigned active sites with particular geometries are rare and limited by the Fe-N$_{2+2}$/C concept only.

2.2 Experimental

2.2.1 Materials

Commercial carbon black (Vulcan XC-72) was purchased from Cabot. Methanol, acetone, isopropyl alcohol, iron(III)chloride, sulfuric acid, potassium hydroxide, sodium nitrite, and Nafion© perfluorinated resin solution were purchased from Sigma-Aldrich.

2.2.2   Synthesis of the Catalysts

Vulcan XC-72 was utilized as a carbon support in this study and was not purified prior to synthesis. The catalyst preparation was adapted from literature procedures[23-24]. Briefly, a 10 mM solution of 4'-(4-aminophenyl)-2,2':6',2''-terpyridine (tpy) prepared via previously published literature procedure[25] and 1 M $NaNO_2$ was added to 1.16 g of commercial carbon black. After 24 hours, the solution was vacuum filtered and washed with methanol, acetone, and water before being placed in an oven at 100 ℃ overnight (V-tpy). A 10 mM solution of iron(III)chloride was added to the tpy modified carbon. After 48 hours, the tpy-Fe modified carbon was washed with methanol, acetone, and water before being placed in an oven at 100 ℃ overnight (V-tpy-Fe). A portion of the V-tpy-Fe catalyst was heat treated in a Barnstead International type F21100 tube furnace at 700 ℃ using a ramp of 50 ℃ min^{-1} for 2 hours under an N_2 atmosphere, this material is denoted as V-tpy-Fe-700.

2.2.3   Physical Characterization

Commercial and the modified carbons were characterized by thermogravimetric analysis (TGA) using a TA instruments Q600 SDT thermal analyzer. The samples were heated at 5 ℃ min^{-1} from room temperature to 1000 ℃ while flowing air and argon (50 mL min^{-1}). Brunauer-Emmett-Teller (BET) was measured using a Quantachrome NOVAe 1200 pore size analyzer. Scanning electron microscopy was measured using a HITACHI FlexSEM 1000. Beam was 10 kV and the distance was 5 mm with a spot size of 50. XPS measurements were performed using a Thermo Scientific K-Alpha Angle-Resolve C-ray photon spectrometer equipped with monochromated Al Kα (1486.7 eV) X-ray source and 180º double focusing hemispherical analyzer with 128 channel detector with effective charge compensation. A Shirley fit algorithm was used for background subtraction and Powell peak-fitting algorithm for data analysis. TEM measurements were performed on a Zeiss Libra 200MC Transmission Electron Microscope system operating at 200 kV using a slit width of 10 eV and a spot size of 1 nm. Magnification of the sample was 100 kX. Time-of-Flight Secondary Ion Mass Spectrometry was performed using an IonTof TOF-SIMS V (IonToF Gmbh-Münster, Germany) located at the Ontario Centre for the Characterization of Advanced Materials (OCCAM), University of Toronto. The Bi Cluster ion sources was utilized; with Bi_3^{2+} ion chosen for the primary ions. High resolution mass

spectra were obtained on the surfaces of V-tpy-Fe. Both positive and negative ion spectra were collected utilizing Bi_3^{2+} primary ions (25 keV, 0.3 Pa) from the Bi cluster source over an area of 500 x 500 µm. Instrument operation was performed with the system software (SURFACE LAB 6). Data processing was performed using ION TOF spectra program.

2.2.4 Electrochemical Characterization

The oxygen reduction reaction was studied using rotating ring disk electrode (RRDE) in O_2 saturated 0.1 M H_2SO_4 or 0.1 M KOH. A catalyst ink was made by sonicating 10 mg of catalyst, 400 µL of a 50:50 deionized water/isopropyl alcohol mixture, and 100 µL of Nafion® for 30 minutes then the ink was stirred overnight. 3 µL of catalyst ink was dropped onto a 0.19625 cm^{-2} glassy carbon rotating disk electrode (305 µg cm^{-2} loading of material or ca. 6.1 µg cm^{-2} per Fe loading) and during the deposition the electrode was rotated and dried with heat. The ring potential was held as 1.2 V versus SHE and the calibrated collection efficiency of the ring was N=0.24 at 900 rpm. The electrode was placed in a cell with 0.1 M H_2SO_4 of 0.1 M KOH. A mercury/mercury sulfate reference electrode was used along with a platinum wire counter electrode. The electrochemical measurements were performed using a Pine Instrument model AFCP2 with corresponding aftermath software. Data was obtained at 10 mV s^{-1} for both the CVs and the RRDEs in the presence and absence of oxygen. Durability tests were performed in N_2 saturated 0.1 M H_2SO_4 for 10,000 cycles at 50 mV s^{-1}. RDE was performed in O_2 saturated 0.1 M H_2SO_4 solution after every 5000th cycle.

2.3 Results and Discussion

A model system for the material based solely on N_3/C active site was prepared[23-24]. The commercial Vulcan XC-72 carbon surface, V, was used due to the stability of the material and it is a well-defined and characterized carbon. This carbon surface was functionalized by the terpyridine ligand receptor using diazonium coupling chemistry. Resulting nitrogen-enriched support (V-tpy) was further reacted with an aqueous solution of $FeCl_3$ at room temperature (V-tpy-Fe). Strong affinity between nitrogenous ligand and iron ion resulted in quantitative coordination of iron metal to N_3 (tpy) binding sites on the surface. Both V-tpy and V-tpy-Fe surfaces were fully characterized by combination of TGA, differential thermogravimetry (DTG), Brunauer-Emmett-Teller pore size analysis (BET), XPS, Secondary Ion Mass Spectrometry (SIMS), scanning electron microscopy

(SEM), and transmission electron microscope (TEM). Electrochemical characterization techniques such as cyclic voltammetry (CV), and rotating ring disk voltammetry (RRDE) were used to evaluate the catalytic abilities of the material for the ORR.

2.3.1 Physical Characterization

We used TGA to track changes in the nature of the carbon-based material through the various stages of the surface modification process. Due to significant changes in the carbon structure upon modification with the functionalities bearing solely nitrogenous ligand or metal complex, we saw significant changes in the decomposition temperature and weight percent losses of the modified materials when compared to the unmodified commercial Vulcan carbon material. Figure 2.1 shows the TGA curves obtained in air for the starting and modified V-tpy, V-tpy-Fe, V-tpy-Fe-700 carbon materials. These results indicate that the iron content in the V-tpy-Fe sample was quite low (2 wt%). This Fe content is similar to other NPMCs that have been reported in literature[6, 11, 26-27]. The DTG shows a peak around 450 ℃ with a small shoulder indicating the combustion of the carbon and tpy, respectively. Through the various stages of modification, the combustion temperature of the material begins to shift to lower temperatures when compared to the unmodified carbon support. This is most likely due to the changes in the carbon structure upon modification with both the tpy moiety and the iron. As expected, introducing organic terpyridine functionalities into the Vulcan carbon support results in the overall lowering of the combustion temperature for the materials. Formation of the typ-Fe complex on the surface support, slightly altered the combustion temperature of the resulting carbon material. Interestingly, metal—enriched surface V-tpy-Fe combusted at lower temperatures than the metal-free nitrogen-enriched carbon surface (V-tpy). This distinct change of properties indicates a chemical modification of the surface by iron. Finally we demonstrated that the surface of V-tpy-Fe-700 material after standard heat-treatment (pyrolysis at 700 ℃ in N_2 atmosphere[23]) demonstrates a lower stability (decomposes at a lower temperature) when compared to the non-heat treated V-tpy-Fe system.

In order to further probe how surface modification affects the decomposition process of the material, we performed TGA under argon atmosphere (Figure 2.1B and D). After modification with the tpy moiety, the decomposition temperature lowered significantly (150-200 ℃). Further modification with Fe led to a decomposition process

beginning at considerably low temperatures (200-350 ℃), though significant mass losses did not occur until the temperature exceeded 650 ℃.
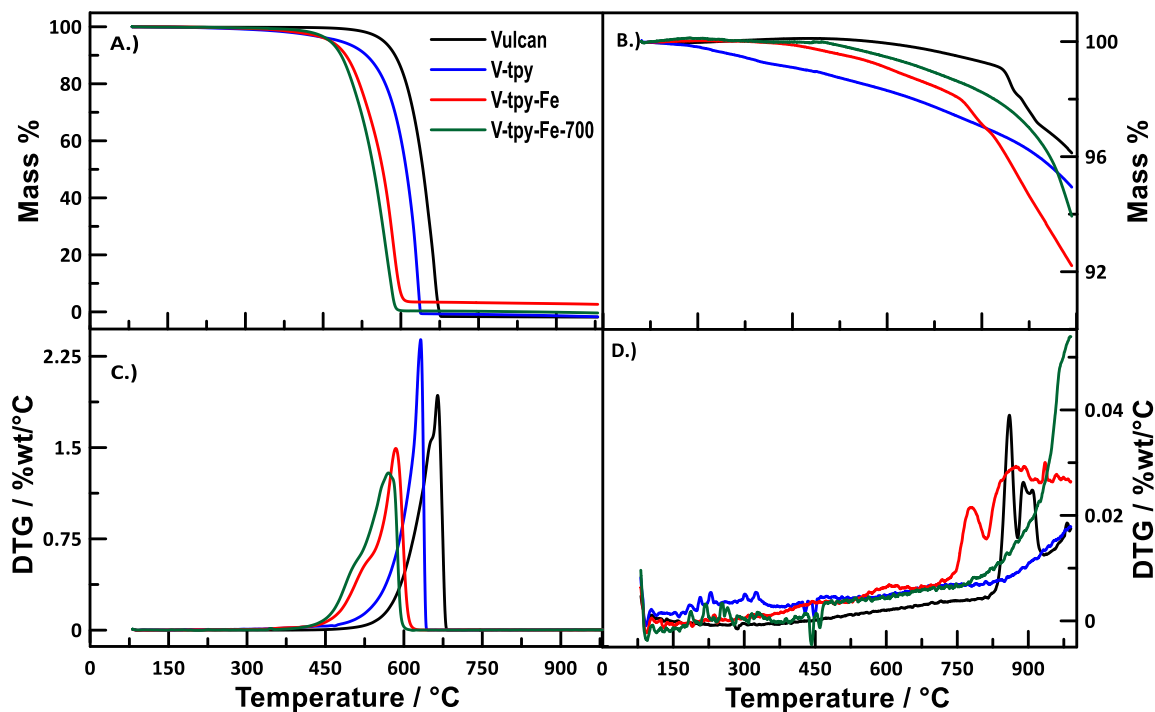
Figure 2.1) TGA analysis of the Vulcan-modified catalysts (A) in air and (B) under argon. DTG of the catalysts (C) in air and (D) under argon.

The BET surface area was determined for the nitrogen enriched carbon surfaces functionalized with iron-tpy sites and is reported in Table 2.1 (See Figure S2.1 for N_2 adsorption isotherms). Upon modification of the carbon with both the terpyridine-moiety and iron, the surface area slightly lowered from 220 m^2 g^{-1} to 197 m^2 g^{-1}. The lowering of the surface area can be explained by the fact that the relatively bulky iron-tpy moieties can physically block access to some of the pores within the material, which can lower the measured surface area. The heat-treated V-tpy-Fe sample showed an increase in surface area. This is likely caused by the tpy coordinated to Fe becoming embedded into the structure of the carbon, creating more pores in the material.

XPS was performed on the V-tpy-Fe sample and the measured spectra are displayed in Figure 2.2. Figure 2.2A shows the Fe 2p region of the V-tpy-Fe spectrum which contains two characteristic peaks for Fe^{3+}: Fe 2$p_{3/2}$ at 711 eV and Fe 2$p_{1/2}$ at 724.5 eV[28]. The nitrogen N1s peak appears at 399.9 eV which is a characteristic peak for pyridinic

nitrogen[9]. This was expected due to the synthetic method that was used to modify the carbon surface (Scheme 2.1). Using diazonium coupling chemistry results in a carbon-carbon bond to the surface, which should leave the pyridinic tpy nitrogens free and easily accessible on the surface. Deconvoluting the C1s signal results in 3 peaks with a full width at half max (FWHM) of 1.8 eV at 284.6 eV corresponding to aliphatic carbon[29], 286 eV for aromatic carbon, and 289 eV for carbonyl or carboxyl groups[30]. The peak area normalization for V-tpy-Fe using relative XPS sensitivity factors as determined by Wagner[31] suggests that the amount of iron is insufficient to react with nitrogen atom in expected 3:1 stoichiometry.
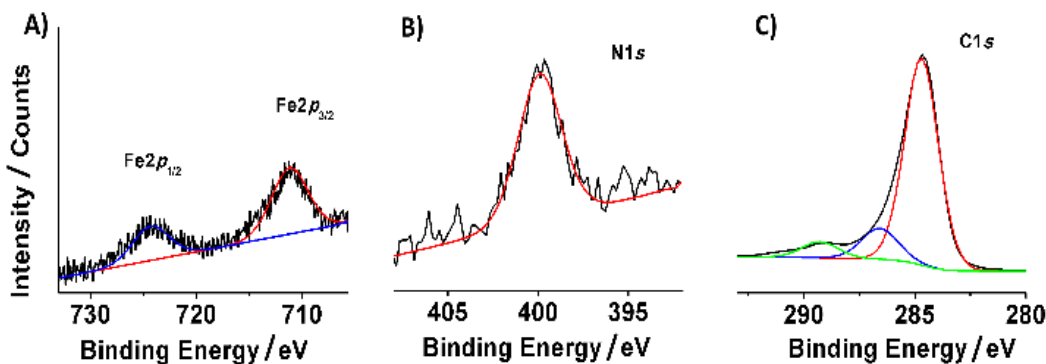
Figure 2.2) XPS spectra for V-tpy-Fe: (A) Fe 2p region, (B) N1s region, and (C) C1s region. Black lines show the experimental data, while the red, blue, and green lines represent corresponding spectrum deconvolution.

Due to the relatively low Fe content (~2wt%, confirmed by TGA), the effect of Fe deposition time was investigated. It was found that after only 24 hours of stirring, and dissolving the Fe solution in water, (to get V-tpy-Fe24) the N:Fe ratio calculated from the XPS areas of the peaks applying Wagner sensitivity factors becomes 3.00:0.69 (Figure 2.3). While the wt% of Fe increases to reach ~2.7%, it still remains relatively low. It was also observed that the iron redox peak seen in CV measurements has increased. However, the increase in iron coordination did not show a significant improvement on the activity of the V-tpy-Fe24 sample for the ORR (Figure S2.3), thus the 48hr Fe deposition was kept as the optimal for this system.

32
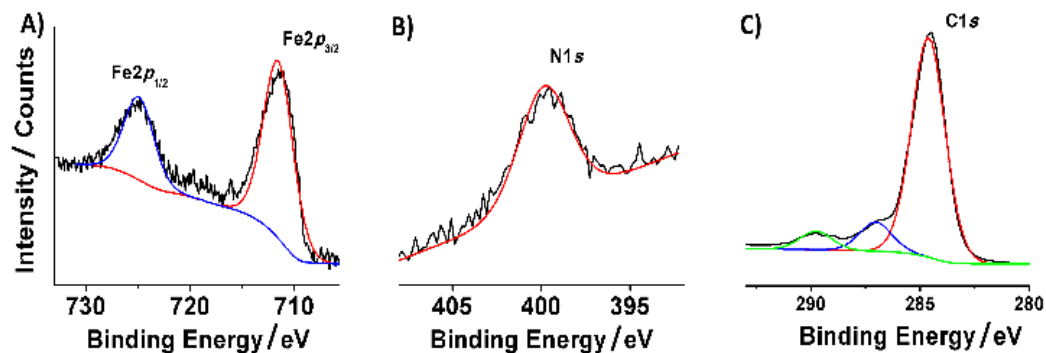
Figure 2.3) XPS spectra of V-tpy-Fe24: (A) Fe 2p region, (B) N1s region, and (C) C1s region. Black lines show the experimental data, while the red, blue, and green lines represent corresponding spectrum deconvolution.

Figure 2.4 displays a SEM image acquired for the V-tpy-Fe material along with high resolution TEM images of the novel model system. The images show that the catalyst material has porosity and grain sizes expected for the Vulcan carbon. The TEM shows no visible Fe particles/agglomerates, which indicate that this modification process produces a smooth layer (close to monolayer) of the catalyst on the support. This indicates that the modification process has a minimal change on the morphology of the carbon support. V-phen and V-phen-Fe was also analyzed by TEM and results are reported in the SI (Figure S2.4).
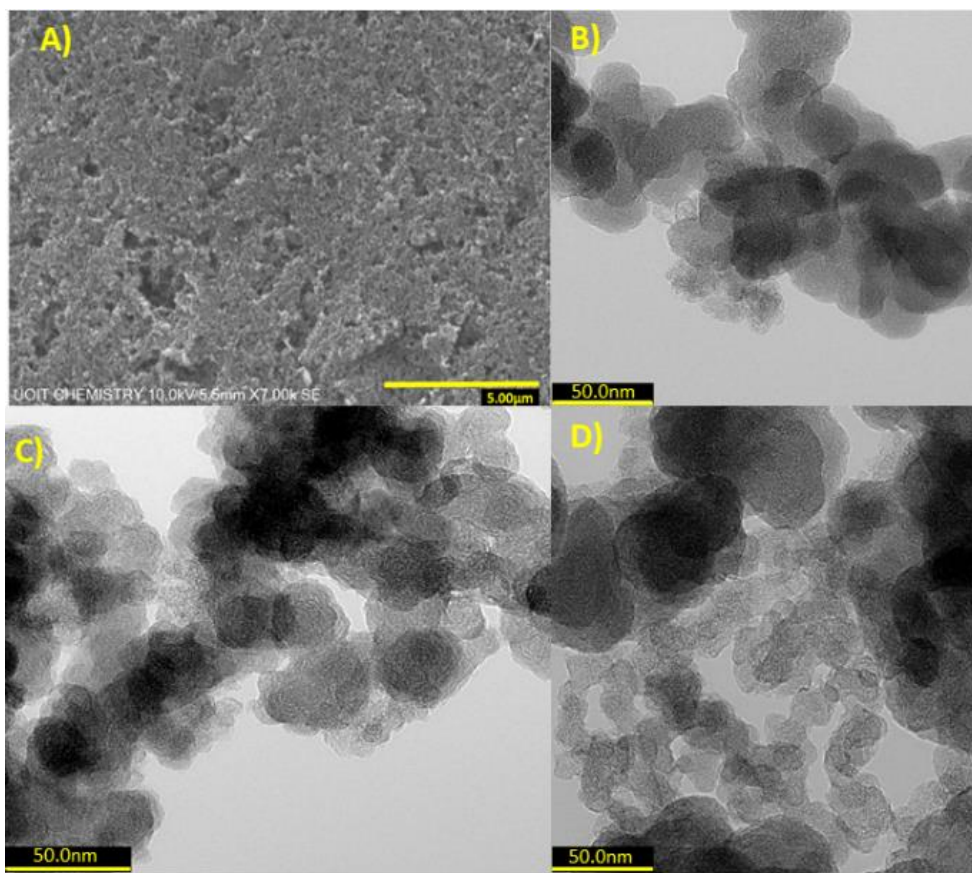
Figure 2.4) (A) SEM image of the morphology of the catalyst V-tpy-Fe; TEM images of (B) V-tpy catalyst, (C) the V-tpy-Fe catalyst, and (D) the V-tpy-Fe-700 catalyst.

Time-of-Flight Secondary Ion Mass Spectrometry (ToF-SIMS) was used to identify functional $Fe-N_3$ active sites. During these measurements, a pulse of Bi_3^{2+} primary ions impacted the sample surface and induced a fragmentation leading to the formation of positively and negatively charged species. The measurements were performed in a way that the emitted particles originate from the uppermost one or two monolayers. Figure 2.5 shows a typical positive secondary ion mass spectrum.
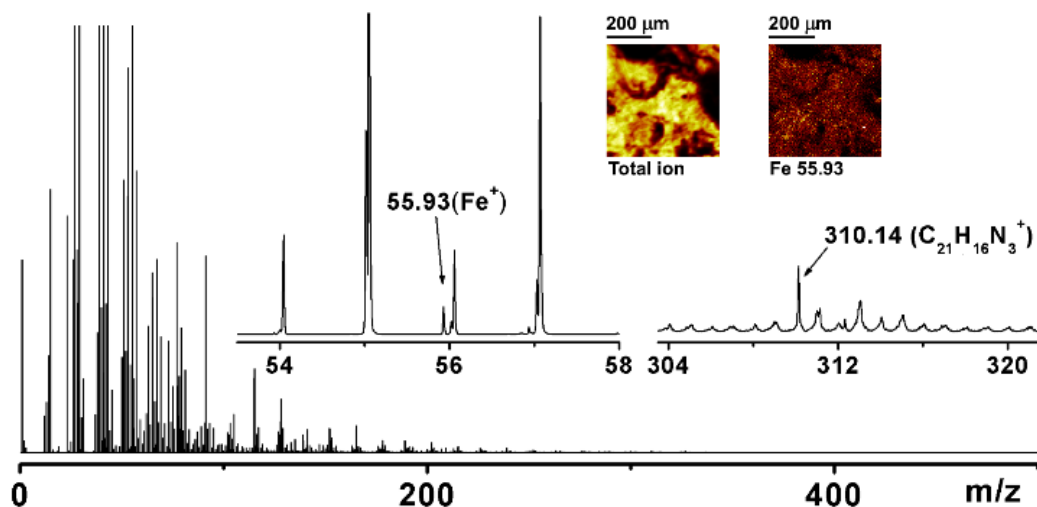
Figure 2.5) Positive-ion mass spectra of V-tpy-Fe. Regions demonstrating the presence of Fe^+ and tpy moiety ($C_{21}H_{16}N_3^+$) are enlarged for clarity. Inserts demonstrate chemical image maps of V-tpy-Fe surface: the topography based on the total ion and the distribution of iron over the surface.

The peaks of high intensity mostly correspond to fragments of the ligand: 1.01 (H^+), 27.02 ($C_2H_3^+$), 29.04 ($C_2H_5^+$), 43.05 ($C_3H_7^+$), and 115.05 ($C_8H_5N^+$). The tpy-Fe moiety is chemically grafted to the Vulcan support, which is formed of the several graphene-like layers. Therefore, the bond cleavage and fragmentation is expected. The small intensity peak corresponding to protonated tpy ligand unit ($C_{21}H_{16}N_3^+$) is observed at m/z 310.14. The small intensity peak at m/z 55.93 corresponding to Fe^+ is also observed. Lower sensitivity of the method to double and especially triple charged species does not allow a clear determination of the tpy-Fe(III) species. Nevertheless, when the pulsed primary ion beam was rastered across several points within a given surface area to determine the lateral distribution of Fe^+ (Figure 2.5 insert), it shows the uniform distribution of iron on the surface that is in good agreement with the formation of a tpy-Fe monolayer.

2.3.2   Electrochemical Characterization

Figure 2.6 compares the CV results in acidic electrolyte for each material prepared in this study through various stages during the synthesis of the catalyst. The CVs in Figure 2.6 show that when tpy is first grafted onto the surface, a small redox wave appears at ca. 0.6 V, which we attribute to the redox behaviour of the tpy ligand[23]. After the addition of Fe, a peak appears at ca. 0.7 V. This second peak we attribute to the oxidation/reduction of $Fe^{2+/3+}$ coordinated to the N_3 site on the tpy. The capacitance of the material was slightly increased upon the modification of the carbon with the tpy and further increased upon

addition of Fe due to pseudocapactive behaviour[32]. After heat treatment at 700 ℃, the low potential peak was effectively removed, possibly due to structural rearrangement of free tpy, while the high potential peak was reduced in size.
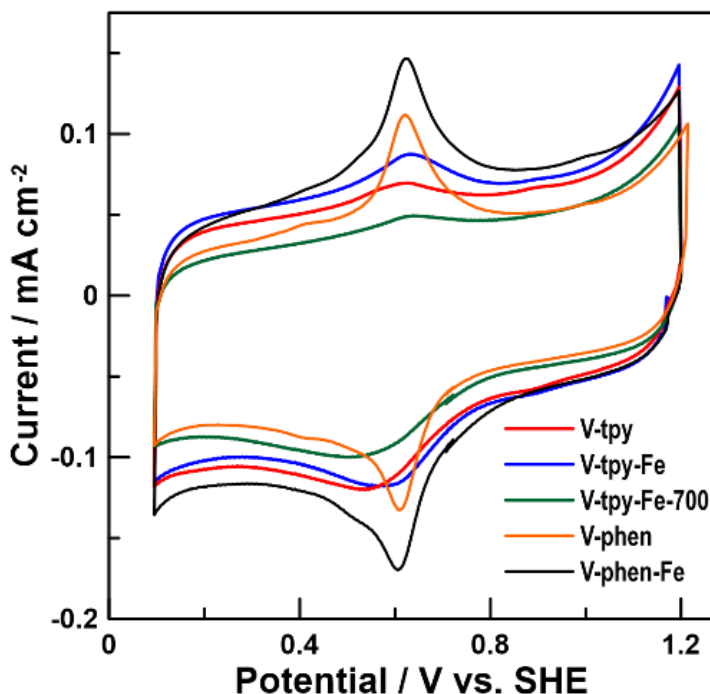
Figure 2.6) CVs of commercial Vulcan XC-72 and modified carbon support through various stages of synthesis at a scan rate of 10 mV s^{-1} in N_2 purged 0.1 M H_2SO_4.

We compared our results to a commonly used phenanthroline-based N_2/C motif embedded on a Vulcan support via the same procedure, Scheme 2.2[23]. With respect to the V-phen CV, a redox wave appeared at ca. 0.6 V which is attributed to the redox activity of the phen ligand. When iron was introduced in the system another peak appeared at ca. 0.7 V which is characteristic of the $Fe^{2+/3+}$ redox couple. The iron peak appears to have some small shouldering at lower potential (ca. 0.6 V) which can be due to the phen and iron in the CV which contained the metal complex (V-phen-Fe). The larger peaks for the V-phen and V-phen-Fe system compared to the tpy system indicated that there are more electrochemically accessible redox sites in the phen system compared to the tpy system.
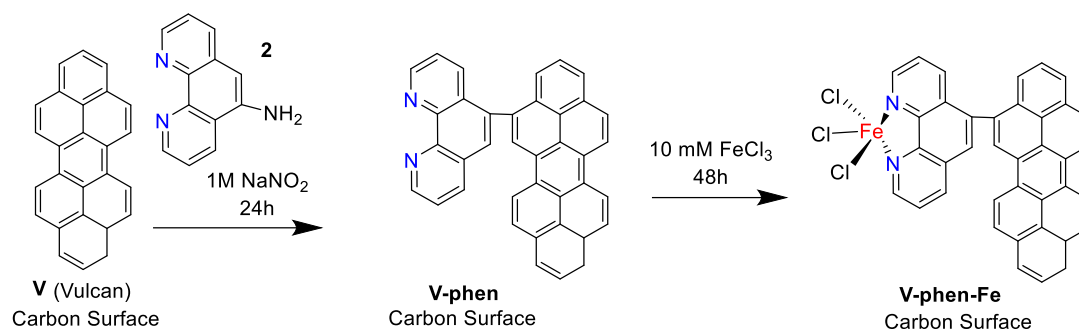
Scheme 2.2) Scheme for the preparation of V-phen-Fe.

Figure 2.7 compares the ORR activity of each catalyst measured using a rotating ring disk electrode (RRDE) for both the disk and the ring. Onset potentials for ORR for each catalyst are listed in Table 2.1. The V-tpy catalyst began to show ORR activity at ca. 0.85 V, indicating that even the metal-free tpy site is quite active. The V-tpy-Fe catalyst shows a slightly different profile, though it did have a similar onset potential to that observed for the V-tpy sample, the addition of Fe into the tpy allowed the catalyst to reach higher current densities. The shape of the curve appears to indicate that the catalyst material is undergoing a two-step process in catalyzing the ORR. Perhaps this is caused from the cooperative activity of the iron free sites and the metal-ligand coordinated sites. However, heat-treatment resulted in a significant change in the shape of the curve, with the onset potential shifting to lower potential and current densities (ca. 0.84 V). This decline in ORR activity is attributed to the reduction in the number of N_3 sites after heat treatment. The $E_{1/2}$ of all the catalysts are tabulated in Table 2.1. The model system, V-tpy-Fe, was compared to literature $E_{1/2}$ values for similar catalysts. The value obtained for the tpy-Fe system was 0.62 V compared to 0.82 V of a similar Fe-N_{2+2}/C catalyst reported in literature[33]. While the V-tpy-Fe system in its current stage is not as active as current NPMCs reported in literature, future valuable knowledge that we receive from studies of our model catalytic system(s) will allow effective rational design, modification and future optimizations of the actual catalytic material to reach superior performance and stability. Remarkably, even with a lower amount of electrochemically active available sites in the V-tpy-Fe system the ORR proved to be comparable to the activity of the V-phen-Fe system.
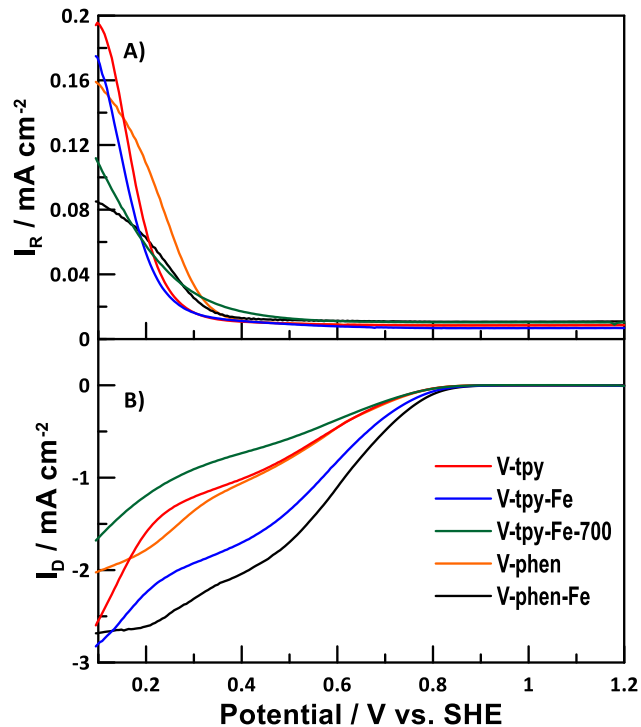
Figure 2.7) RRDE ring currents at 900 rpm comparing the catalysts in O_2 saturated 0.1 M H_2SO_4 (A) holding the ring potential at 1.2 V vs hydrogen and (B) at a scan rate of 10 mV s^{-1}.

Table 2.1) Onset potentials of the different materials in an N_2 purged 0.1 M H_2SO_4 electrolyte at 10 mV s^{-1} with the BET surface areas.

Material	Onset potential /V	i_k / mA cm^{-2}	$E_{1/2}$	Number of electrons transferred		BET surface area / m^2 g^{-1}
				Peroxide	KL	
V-phen	0.84 ± 0.16	1.89 ± 0.88	0.55 ± 0.04	3.6	3.8	-
V-phen-Fe	0.86 ± 0.11	4.75 ± 2.64	0.65 ± 0.03	3.8	3.9	-
V-tpy	0.85 ± 0.02	1.67 ± 0.03	0.55 ± 0.04	3.7	3.8	197
V-tpy-Fe	0.87 ± 0.04	3.34 ± 1.18	0.62 ± 0.06	3.8	4.0	206
V-tpy-Fe-700	0.84 ± 0.07	1.49 ± 0.38	0.48 ± 0.09	3.5	2.0	305
Vulcan	-	-	-	-	-	220

It has been shown through literature that most prominent NPMC activities towards ORR show surfaces that are rich in pyridinic nitrogens[2, 19]. Our XPS results confirm that

the surface nitrogen is mainly in pyridinic form, thus this is likely the reason why our non-heat-treated V-tpy-Fe catalyst demonstrates good activity. The diazonium coupling reaction allows selective embedding of pyridinic source of nitrogen due to the terpyridine core aligned exclusively in the N_3 geometry (Scheme 2.1).

Interestingly, upon heat treatment at 700 ºC, the V-tpy-Fe catalyst did not seem to show any positive effects on the activity. Dodelet et al. have done extensive work to optimize the heat treatment procedure for the Fe-N_{2+2}/C aimed to increase activity without being detrimental to the catalysts[8, 19]. However, in this study we observe opposite behaviour for the Fe-N_3/C system in acidic electrolyte, the heat treatment resulted in lowering of the catalytic activity. We attribute this to possible change of the conformation of the catalytically active Fe-N_3/C to catalytically inert Fe-N_{3+3}/C. Similar type of conformation change was reported with the Fe-N_2 catalytic sites that transform to another active Fe-N_{2+2}/C catalysts[34]. Thus, heat-treatment could cause some of the active Fe-N_3/C to adopt inactive Fe-N_{3+3}/C site geometry. In Fe-N_{3+3} configuration, we expect two terpyridine ligands coordinating to one iron center[35]. This is a stable fully saturated 18 electron configuration with no empty coordination site and significant steric hindrance preventing coordination of the oxygen molecule to the iron center. Thus, catalytic activity at this site is being turned off.

Kinetic currents and an estimate of the number of electrons transferred for all materials in acidic medium was calculated using Koutecky-Levich analysis (KL) (plots shown in Figure S2.4 and the detailed calculation shown in section 2.5). The slope of the plot of $1/i_{lim}$ versus $1/\omega^{1/2}$ determines the number of electrons transferred in the ORR and the intercept determines the kinetic currents. The kinetic current (i_k) values for V-tpy-Fe and V-tpy-Fe-700 were 3.38 mA cm^{-2} and 1.49 mA cm^{-2}, respectively. The significant decrease in the kinetic current for the heat-treated sample could be attributed to the structural rearrangement caused by the heat treatment procedure. This could produce Fe-N_{3+3}/C sites which lowers the activity of the catalyst due to the limited availability for the O_2 reaction to take place, due to close shell configuration and the steric hindrance of the Fe-N_{3+3}/C complex. The peroxide collection experiment was performed to provide a more accurate determination of the number of electrons transferred[36]. The determination of the number of electrons (n) and %H_2O_2 were calculated via the following equations where I_D

is the disk current, I_R is the ring current, and N is the collection efficiency of the ring [Eqs. (2.1) and (2.2)]:[37]

$$n = \frac{4I_D}{\left(I_R + \left(\frac{I_R}{N}\right)\right)} \qquad (2.1)$$

$$\%H_2O_2 = \frac{200 \times \left(\frac{I_R}{N}\right)}{\left(I_D + \left(\frac{I_R}{N}\right)\right)} \qquad (2.2)$$

The number of electrons calculated for the V-tpy-Fe and V-tpy-Fe-700 are 3.8 and 3.5 respectively. This indicates that the V-tpy-Fe is mainly undergoing a 4-electron process and the V-tpy-Fe-700 is mainly undergoing a 3-electron transfer process. For the ORR, the 4 electron process is more favourable since it avoids formation of the undesirable H_2O_2 intermediate observed from a 3 electron process[15]. A 3-electron process refers to the catalysts going through both the 2 and 4 electron processes. Thus, this shows that after the heat treatment procedure the catalyst loses activity as it moves from a primarily 4 electron process to a 3-electron process. Figure 2.8 shows the peroxide yield of each catalyst and the number of electrons transferred at different potentials. This shows that the V-tpy-Fe material has a constant n throughout the various potentials identical to the V-phen-Fe material. Similarly, the percent H_2O_2 calculated for the materials show that both the V-tpy-Fe and V-phen-Fe material are generating almost identical amounts of hydrogen peroxide (ca. 5%). However, after heat treatment n drops significantly and H_2O_2 begins to increase which is expected and correlates with results presented in Table 2.1 and Figure 2.7.
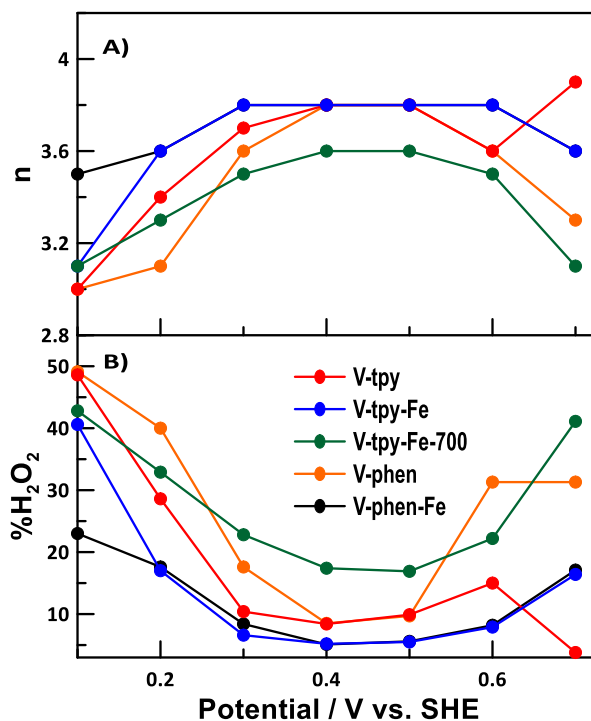
Figure 2.8) (A) Number of electrons transferred calculated from the H_2O_2 collection experiment at various potentials at 900 rpm in 0.1 M H_2SO_4. (B) %H_2O_2 generated at the ring for the various catalyst materials at 900 rpm in 0.1 M H_2SO_4.

Finally, we subjected the V-tpy-Fe to a durability protocol suggested by the DOE to determine the stability and durability of our novel Fe-N$_3$/C material[25, 38]. We assessed the activity of the material for ORR after 1000, 5000, 10,000 cycles and the results are shown in Figures S2.7-2.8. The V-tpy-Fe material was shown to be unstable after 10,000 cycles. While this structural motif is unique, the system is still prone to degradation issues. This is not uncommon in literature, as non-precious metals are not as stable, particularly in acid when compared to their noble counterparts[38].

The ORR performance of all materials were also evaluated in O$_2$ saturated 0.1 M KOH using RRDE and CV. Figure 2.9 shows the CVs of the different materials and Table 2.2 reports the onset potentials of each material tested.

Comparing the disk and ring currents of the V-tpy-Fe catalyst at different stages of synthesis (modification with tpy alone and then after the addition of iron), it can be seen that the onset potentials for the catalysts are very similar (Figure 2.10 and Table 2.2). In basic electrolyte, the V-tpy-Fe-700 catalyst has a similar onset potential compared to the V-tpy-Fe catalyst. However, a small difference in current density values were observed between two catalysts, where non-heat-treated sample achieves a slightly higher current

density. In acidic electrolyte, the onset potential or the V-tpy-Fe catalyst was higher than the heat-treated catalyst (non-heat treated 0.87 V vs 0.84 V heat-treated). However, in the basic electrolyte the current density of the non-heat-treated V-tpy-Fe is still comparable to the V-tpy-Fe-700 since the overall activity of the catalyst is normally attributed to both the high current density and higher more positive onset potential. The ring currents increased dramatically for all samples as the potential decreased, indication there was a significant rise in peroxide production till it hit a maximum at a ca. 0.5-0.6 V then the ring current began to decay again. The $E_{1/2}$ of the catalysts are tabulated in Table 2.2. The model system, V-tpy-Fe, was directly compared to a similar NPMC system in basic electrolyte. The $E_{1/2}$ value for the tpy-Fe system was 0.66 V compared to 0.87 V of a similar Fe-N$_{2+2}$/C catalyst reported in literature[39]. We believe this shows that the model system has potential for competing with the highest activity NPMCs upon further optimization.
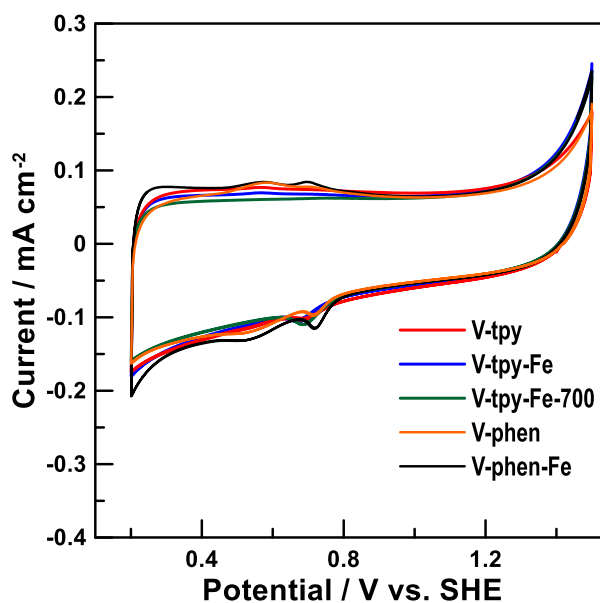
Figure 2.9) CV comparing the synthesized catalysts to commercial Vulcan XC-72 in an N$_2$-saturated 0.1 M KOH at a scan rate of 10 mV s^{-1}.
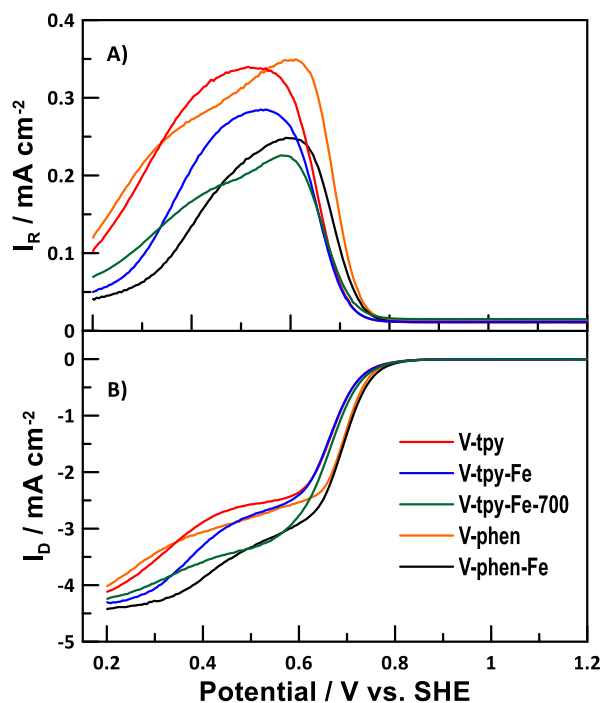
Figure 2.10) (A) RRDE ring currents at 900 rpm comparing the catalysts in O_2 saturated 0.1 M KOH holding the ring potential at 1.2 V vs hydrogen. (B) RRDE disk currents at 900 rpm comparing the catalysts in an O_2 saturated 0.1 M KOH at a scan rate of 10 mV s^{-1}.

KL analysis (see Figure S2.5) was performed on the catalyst materials in basic 0.1 M KOH in a similar way to the acidic electrolyte. Kinetic currents were determined to be 24.81 mA cm^{-2} and 33.26 mA cm^{-2} for the V-tpy-Fe and V-tpy-Fe-700, respectively. Kinetic currents in literature for similar Fe-N/C catalysts produced current that appear to be on the order of 14 mA cm^{-2}[40-42]. The V-tpy-Fe catalyst shows significant kinetic currents and performance for the ORR while the V-tpy-Fe-700 sample had an i_k value double what has been reported in literature for Fe-N$_{2+2}$/C type catalysts. On the other hand, the V-phen showed similar results to reported literature on Fe-N$_{2+2}$/C catalysts, however, upon addition of iron (V-phen-Fe) the kinetic activity increased to about double of that without the Fe showing the important role that iron plays in the catalyst design. In fact, relatively small amount of iron that was incorporated into the film (2% for the V-tpy-Fe catalyst) leads to a drastic difference in catalytic activity of the materials.

Table 2.2) Onset potentials of the different materials in an N_2 purged 0.1 M KOH electrolyte at 10 mV s^{-1} with the BET surface areas.

Material	Onset potential / V	i_k / mA cm^{-2}	$E_{1/2}$	Number of electrons transferred	
				Peroxide	KL
V-phen	0.82 ± 0.02	20.71 ± 4.23	0.69 ± 0.06	3.1	3.7
V-phen-Fe	0.82 ± 0.01	45.23 ± 0.05	0.69 ± 0.03	3.7	4.2
V-tpy	0.79 ± 0.03	20.25 ± 3.28	0.66 ± 0.03	3.2	3.8
V-tpy-Fe	0.79 ± 0.02	24.81 ± 0.23	0.66 ± 0.02	3.6	4.2
V-tpy-Fe-700	0.80 ± 0.02	33.26 ± 0.17	0.67 ± 0.04	3.5	4.0

The number of electrons transferred were calculated for this material and compared to KL analysis (Table 2.2). The number of electrons calculated for V-tpy-Fe and V-tpy-Fe-700 are 3.6 and 3.5 respectively. This indicates that both catalysts are mainly undergoing a 3-electron transfer process. This can be observed in the disk current measurement where it appears that there is a 2-step process occurring from the two plateaus seen in Figure 2.10B curves. Figure 2.11 shows the peroxide yield and the number of electrons transferred at different potentials. It can be explained by the number of electrons transferred (Figure 2.11A) and the disk current observed for the samples (Figure 2.10B). As the potential decreases, the number of electrons transferred increases and the %H_2O_2 decreases. Thus, as the ORR is beginning the catalysts is undergoing mainly 2 electron process and as the potential is decreased it moves towards a 3 or 4 electron process[37]. This same trend is seen with the V-phen and the V-phen-Fe sample. Again, comparing the V-tpy-Fe and the V-phen-Fe samples both of these materials behave similarly; they have the same onset potentials, produce similar amounts of peroxide, and both catalysts go through similar number of electron transfer process. Overall, we could conclude that the Fe-N_3/C based catalyst shows good activity towards ORR in both acidic and basic electrolyte.
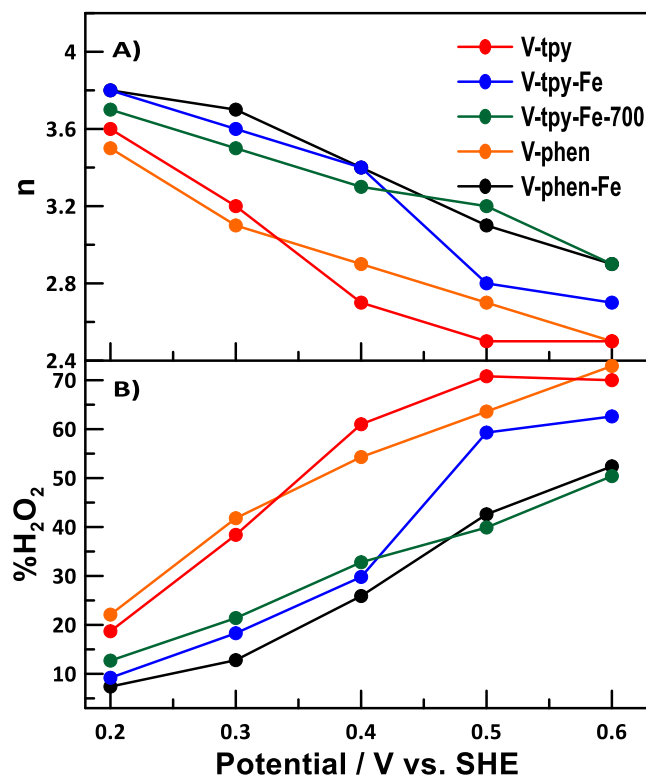
Figure 2.11) (A) Number of electrons transferred calculated from the H_2O_2 collection experiment at various potentials at 900 rpm in 0.1 M KOH (B) %H_2O_2 generated at the ring for the various catalysts at 900 rpm in 0.1 M KOH.

2.4 Conclusion

In this work we demonstrate a rational approach to create molecularly defined ORR active catalysts by using well-defined geometry of the nitrogenous (terpyridine) ligand to artificially create specific active catalytic sites on the commercial Vulcan XC-72 carbon support. This strategy is a promising example of a systematic surface modification aimed to graft onto the surface most catalytically active species. Moreover, for the first time it was demonstrated prominent activity of the Fe-N_3/C active catalytic site that is a fundamentally new concept in the area. We showed that the model system based on Fe-N_3/C active sites covalently embedded into Vulcan XC-72 carbon show ORR catalytic activity that opens up new methodologies for rational design and development of novel active, stable and affordable NPMCs with molecular precision.

Interestingly, conversely to previously published methodologies that all require high temperature treatment to activate the catalyst, our catalytic system does not require heat-treatment. We demonstrated that the heat treatment of our catalysts did not increase the activity of the ORR in the Fe-N_3/C catalyst. On the contrary, better performance from

45

the non-heat-treated sample was achieved. This study shows the importance of in-depth understanding of the catalytic process on the molecular scale, on the scale of single catalytic site, and taking this invaluable knowledge toward achievement of the high standing goal to create low-cost alternatives to modern platinum-based fuel cell catalysts. The results of this study prove that a Fe-N$_3$/C geometry of the catalytic site has potential in the ultimate goal to create active inexpensive and robust, NPM-based catalytic materials for ORR.

2.5 Supporting Information
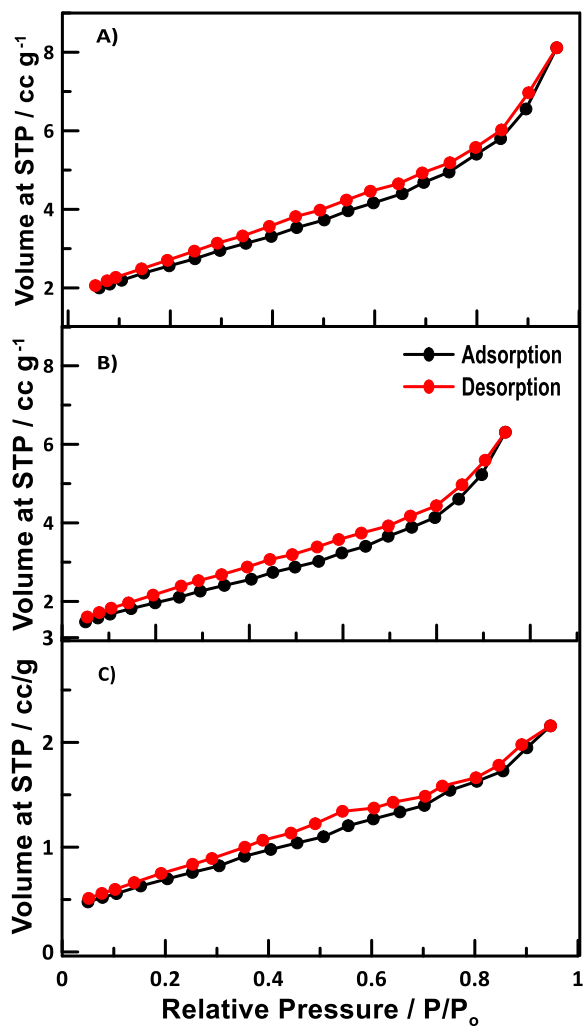
Supporting Information Figure S2.1) (A) BET analysis of the V-tpy catalyst with N$_2$ as the adsorbate (B) BET analysis of the V-tpy-Fe catalyst with N$_2$ as the adsorbate (C) BET analysis of the V-tpy-Fe-700 catalyst with N$_2$ as the adsorbate.

The surface area of V-tpy, V-tpy-Fe, and V-tpy-Fe-700 was determined using the BET equation in the range of 0.05-0.3 P/P$_0$. Samples were degassed for 3h at 200 ºC and no significant mass loss occurred.
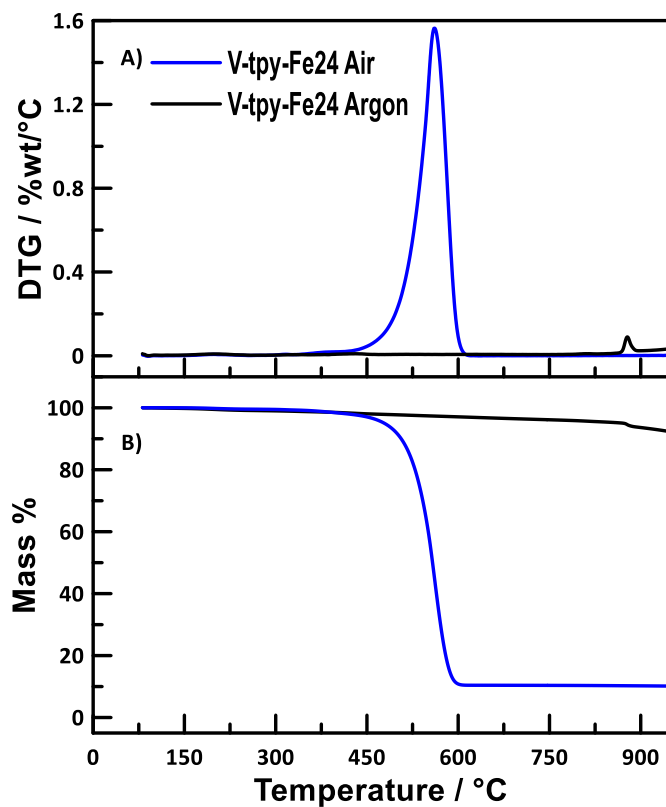
Supporting Information Figure S2.2) (A) TGA analysis of the V-tpy-Fe24 catalyst in air and argon (B) DTG of the catalyst in argon and air.
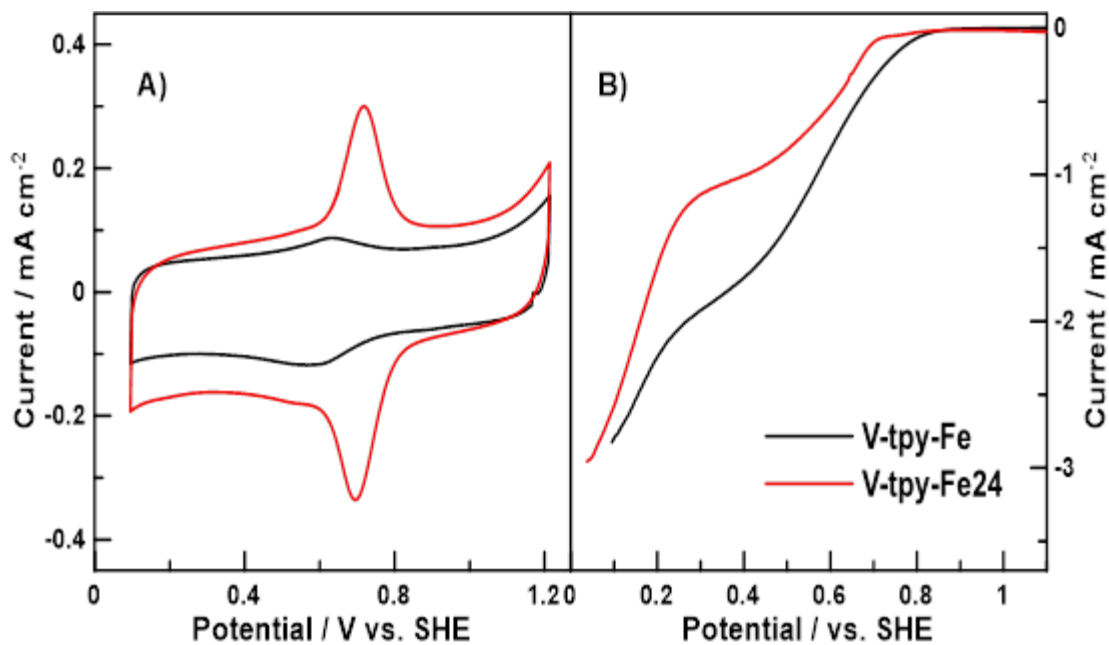
Supporting Information Figure S2.3) A) CVs of V-tpy-Fe and V-tpy-Fe24 at a scan rate of $10mVs^{-1}$ in N_2 purged 0.1 M H_2SO_4. B) Linear sweep voltammetry at 900rpm comparing the synthesized catalysts in an O_2 saturated 0.1 M H_2SO_4 at a scan rate of $10mVs^{-1}$.
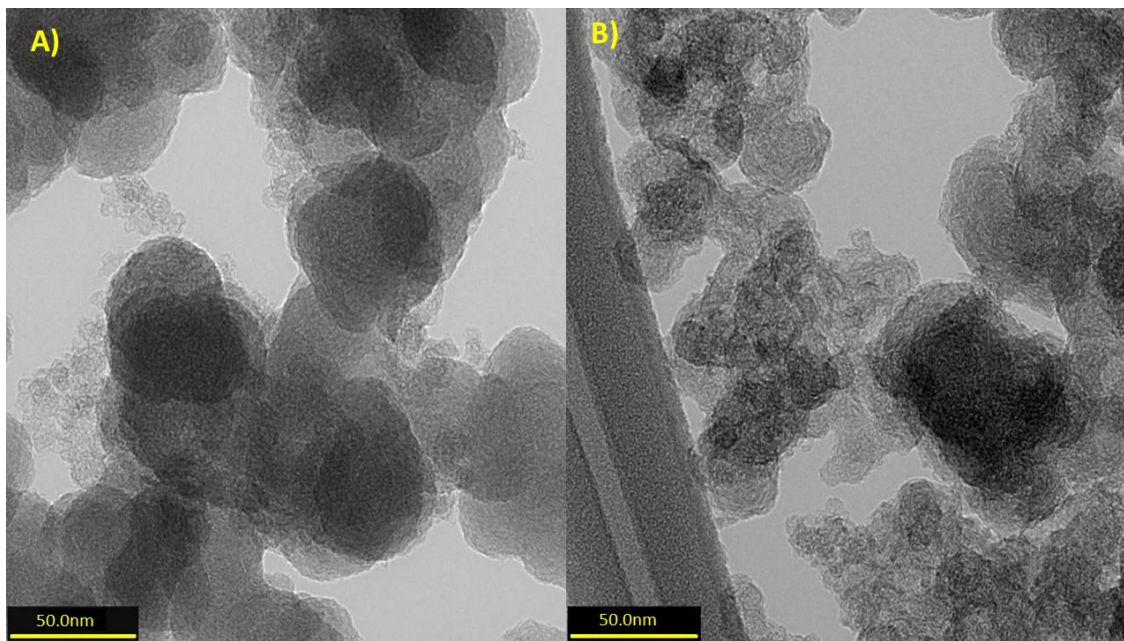
Supporting Information Figure S2.4) (A) TEM image of the morphology of V-phen (B) TEM image of the morphology of V-phen-Fe.
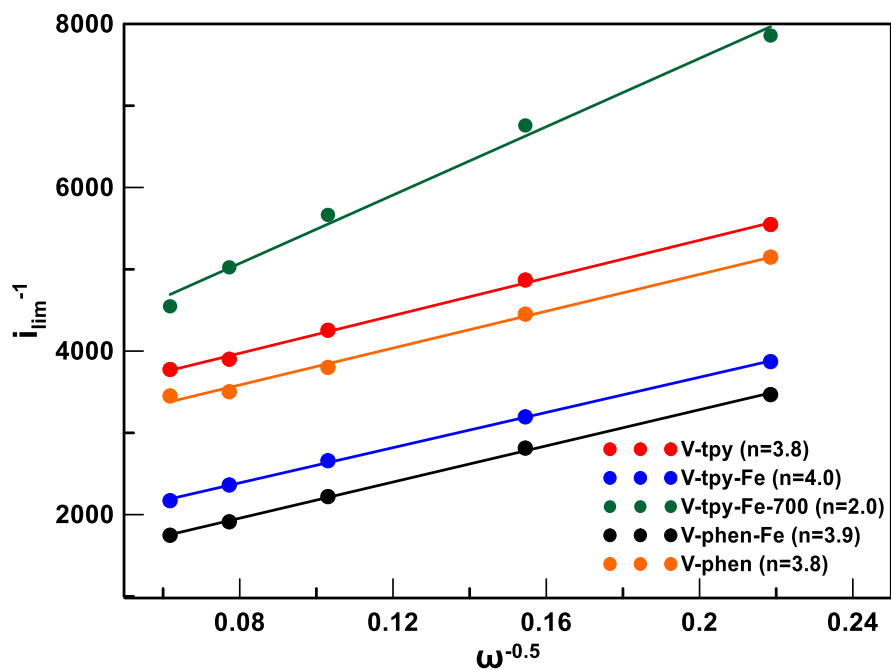
Supporting Information Figure S2.5) Koutecky-Levich analysis of the synthesized catalysts in 0.1 M H_2SO_4 at 0.3 V versus hydrogen.
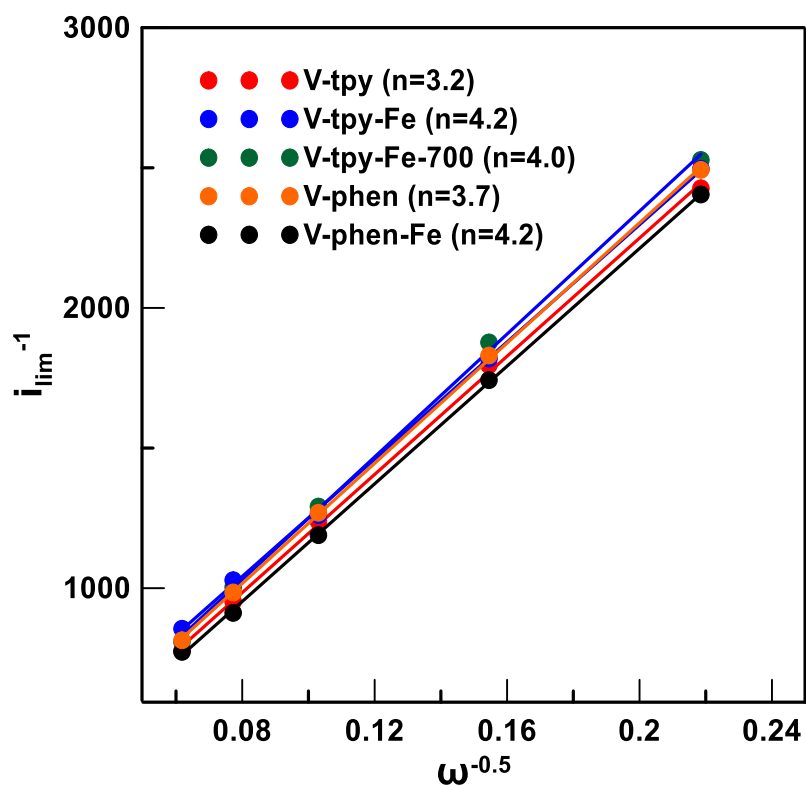
Supporting Information Figure S2.6) Koutecky-Levich analysis of the synthesized catalysts in 0.1 M KOH at 0.3 V versus hydrogen.

According to the Koutecky-Levich equation[34]:

$$\frac{1}{i_d} = \frac{1}{i_{lev}} + \frac{1}{i_k}$$

Where i_{lev} is given as: $0.62nFD_o^{\frac{2}{3}}v^{-\frac{1}{6}}C_o^*\omega^{\frac{1}{2}}$

$$D_o = in\ 0.1M\ KOH\ \left(1.93 \times 10^{-5}\frac{cm^2}{s}\right), in\ 0.1M\ H_2SO_4\ \left(1.67 \times 10^{-5}\frac{cm^2}{s}\right)$$

$$v = 0.01\frac{cm^2}{s}$$

$$F = 96485\frac{C}{mol}$$

$$A = 0.19625\ cm^2$$

$$C_o = 1.26 \times 10^{-3}\frac{mol}{L}\ in\ 0.1M\ KOH, 1.38 \times 10^{-3}\frac{mol}{L}\ in\ 0.1M\ H_2SO_4$$

The data was obtained from the Fe-N_x/C catalysts on a glassy carbon electrode rotated over a range of rotation rates (200-2500rpm) in O_2 saturated 0.1M H_2SO_4 and data was chosen at 0.3V vs. SHE. Similarly, the 0.1M KOH was saturated with O_2 and the catalysts were tested over the same range of rotation rates (200-2500rpm).
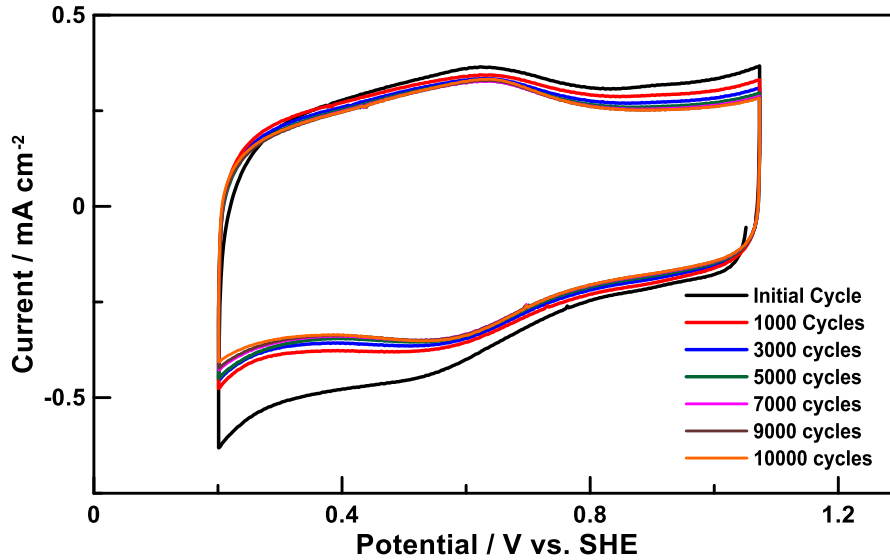
Supporting Information Figure S2.7) CVs of the V-tpy-Fe in 0.1 M H_2SO_4 at 50mVs^{-1} at various points throughout the durability test.
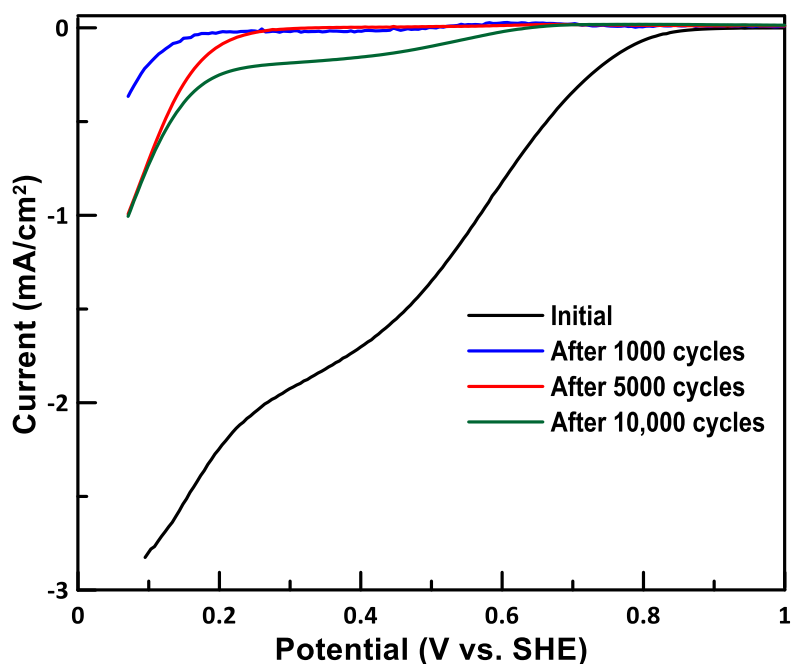
Supporting Information Figure S2.8) ORR activity at 900rpm of the V-tpy-Fe catalyst in O_2 saturated 0.1 M H_2SO_4 10mVs^{-1} through various stages in the 10,000 cycle durability test.

After the first 1000 cycles there is a significant decay in the original activity of the V-tpy-Fe material. This can be attributed to significant loss in the active sites, i.e. loss of Fe, H_2O_2 attack or protonation of the tpy nitrogens[20]. After 5000 cycles some activity is revived and further activity is revived after 10,000 cycles. Due to the increase in activity, what is likely occurring is that Fe is being leached or the break-down of most of the active sites is occuring. The increase in activity could be due to contributions from the nitrogen groups on the surface giving rise to increased ORR activity. Future studies will aim to address the degradation mechanism and improve the durability of this novel site.

2.6 Acknowledgements

2.7 References

[1]   D. Banham, T. Kishimoto, T. Sato, Y. Kobayashi, K. Narizuka, J.-i. Ozaki, Y. Zhou, E. Marquez, K. Bai, S. Ye, *J. Power Sources* **2017**, *344*, 39-45.

[2]   F. Jaouen, S. Marcotte, J. P. Dodelet, G. Lindbergh, *J. Phys. Chem. B* **2003**, *107*, 1376-1386.

[3]   B. Liu, W. Dai, Z. Liang, J. Ye, L. Ouyang, *Int. J. Hydrog. Energy* **2017**, *42*, 5908-5915.

[4]   U. I. Kramm, M. Lefevre, P. Bogdanoff, D. Schmeisser, J. P. Dodelet, *J. Phys. Chem. Lett* **2014**, *5*, 3750-3756.

[5]   D. Higgins, G. Wu, H. T. Chung, U. Martinez, S. Ma, Z. Chen, P. Zelenay, *ECS Transactions* **2014**, *61*, 65.

[6]   Y. Zheng, D.-S. Yang, J. M. Kweun, C. Li, K. Tan, F. Kong, C. Liang, Y. J. Chabal, Y. Y. Kim, M. Cho, J.-S. Yu, K. Cho, *Nano. Ener.* **2016**, *30*, 443-449.

[7]   M. Lefevre, E. Proietti, F. Jaouen, J. P. Dodelet, *Science* **2009**, *324*, 71-74.

[8]   M. Lefèvre, J.-P. Dodelet, *Electrochim. Acta* **2008**, *53*, 8269-8276.

[9]   G. Liu, X. Li, P. Ganesan, B. N. Popov, *Appl. Catal., B. Eniv* **2009**, *93*, 156-165.

[10]   H. Meng, F. Jaouen, E. Proietti, M. Lefèvre, J.-P. Dodelet, *Electrochem. Commun.* **2009**, *11*, 1986-1989.

[11]   J. Li, S. Ghoshal, W. Liang, M.-T. Sougrati, F. Jaouen, B. Halevi, S. McKinney, G. McCool, C. Ma, X. Yuan, Z.-F. Ma, S. Mukerjee, Q. Jia, *Energy Environ. Sci.* **2016**, *9*, 2418-2432.

[12]   K. M. Palanivelu, V. Prabhakaran, V. K. Ramani, K. Ramanujam, *J. Electrochem. Soc.* **2015**, *162*, F475-F482.

[13]   L. Osmieri, R. Escudero-Cid, M. Armandi, A. H. A. Monteverde Videla, J. L. García Fierro, P. Ocón, S. Specchia, *Appl. Catal. B. Eniv* **2017**, *205*, 637-653.

[14]   M. Rauf, Y.-D. Zhao, Y.-C. Wang, Y.-P. Zheng, C. Chen, X.-D. Yang, Z.-Y. Zhou, S.-G. Sun, *Electrochem. Commun.* **2016**, *73*, 71-74.

[15]   C. W. B. Bezerra, L. Zhang, K. Lee, H. Liu, A. L. B. Marques, E. P. Marques, H. Wang, J. Zhang, *Electrochim. Acta* **2008**, *53*, 4937-4951.

[16]   G. Liu, X. Li, P. Ganesan, B. N. Popov, *Electrochim. Acta* **2010**, *55*, 2853-2858.

[17]   H. Tan, Y. Li, X. Jiang, J. Tang, Z. Wang, H. Qian, P. Mei, V. Malgras, Y. Bando, Y. Yamauchi, *Nano. Ener.* **2017**, *36*, 286-294.

[18]   L. Osmieri, R. Escudero-Cid, M. Armandi, P. Ocón, A. H. A. Monteverde Videla, S. Specchia, *Electrochim. Acta* **2018**, *266*, 220-232.

[19]   F. Charreteur, F. Jaouen, S. Ruggeri, J.-P. Dodelet, *Electrochim. Acta* **2008**, *53*, 2925-2938.

[20]   D. Banham, S. Ye, K. Pei, J.-i. Ozaki, T. Kishimoto, Y. Imashiro, *J. Power Sources* **2015**, *285*, 334-348.

[21]   E. F. Holby, P. Zelenay, *Nano. Ener.* **2016**, *29*, 54-64.

[22]   H. R. Byon, J. Suntivich, Y. Shao-Horn, *Chemistry of Materials* **2011**, *23*, 3421-3428.

[23]   A. D. Pauric, A. W. Pedersen, T. Andrusiak, E. B. Easton, *J. Electrochem. Soc.* **2010**, *157*, B370-B375.

[24]   F. J. Rawson, C. L. Yeung, S. K. Jackson, P. M. Mendes, *Nano Lett* **2013**, *13*, 1-8.

[25]   G. Wu, K. L. More, C. M. Johnston, P. Zelenay, *Science* **2011**, *332*, 443-447.

[26]   D. Malko, A. Kucernak, T. Lopes, *Nat. Commun* **2016**, *7*, 13285.

[27]   G. Zhang, R. Chenitz, M. Lefèvre, S. Sun, J.-P. Dodelet, *Nano. Ener.* **2016**, *29*, 111-125.

[28]   J. T. S. Allan, S. Quaranta, Ebralidze, II, J. G. Egan, J. Poisson, N. O. Laschuk, F. Gaspari, E. B. Easton, O. V. Zenkina, *ACS Appl. Mater. Interfaces* **2017**, *9*, 40438-40445.

[29]   N. Graf, E. Yegen, T. Gross, A. Lippitz, W. Weigel, S. Krakert, A. Terfort, W. E. S. Unger, *Surf. Sci.* **2009**, *603*, 2849-2860.

[30]   C. Y. Tang, Y.-N. Kwon, J. O. Leckie, *Desalination* **2009**, *242*, 149-167.

[31]   C. D. Wagner, L. E. Davis, M. V. Zeller, J. A. Taylor, R. H. Raymond, L. H. Gale, *Surf. Interface Anal.* **1981**, *3*, 211-225.

[32]   G. Pognon, C. Cougnon, D. Mayilukila, D. Belanger, *ACS Appl. Mater. Interfaces* **2012**, *4*, 3788-3796.

[33]   X. Wang, H. Zhang, H. Lin, S. Gupta, C. Wang, Z. Tao, H. Fu, T. Wang, J. Zheng, G. Wu, X. Li, *Nano. Ener.* **2016**, *25*, 110-119.

[34]   Z. Chen, D. Higgins, A. Yu, L. Zhang, J. Zhang, *Energy Environ. Sci.* **2011**, *4*, 3167-3192.

[35]   N. O. Laschuk, I. I. Ebralidze, D. Spasyuk, O. V. Zenkina, *Eur. J. Inorg. Chem.* **2016**, *2016*, 3530-3535.

[36]   P. Matter, L. Zhang, U. Ozkan, *J. Catal.* **2006**, *239*, 83-96.

[37]   G. Zhang, Q. Wei, X. Yang, A. C. Tavares, S. Sun, *Appl. Catal. B. Eniv* **2017**, *206*, 115-126.

[38]   X. Li, G. Liu, B. N. Popov, *J. Power Sources* **2010**, *195*, 6373-6378.

[39]   Q. Wei, G. Zhang, X. Yang, R. Chenitz, D. Banham, L. Yang, S. Ye, S. Knights, S. Sun, *ACS Appl. Mater. Interfaces* **2017**, *9*, 36944-36954.

[40]   S. Wang, M. Zhu, X. Bao, J. Wang, C. Chen, H. Li, Y. Wang, *ChemCatChem* **2015**, *7*, 2937-2944.

[41]   A. Sarapuu, L. Samolberg, K. Kreek, M. Koel, L. Matisen, K. Tammeveski, *J. Electroanal. Chem* **2015**, *746*, 9-17.

[42]   Z. Chen, D. Higgins, H. Tao, R. S. Hsu, Z. Chen, *J. Phys. Chem. C* **2009**, *113*, 21008-21013.

Chapter 3. Probing the Influence of the Carbon Support on the Activity of Fe-N$_3$/C Model Active Sites for the Oxygen Reduction Reaction.

3.0 Preface

Part of the work described in this chapter has been published as: Fruehwald, H. M.; Ebralidze, I. I.; Melino, P. D.; Zenkina, O. V.; Easton, E. B., Probing the Influence of the Carbon support on the Activity of Fe-N$_3$/C Model Active Sites for the Oxygen Reduction Reaction. *J. Electrochem. Soc.* **2020,** *167*, 084520. doi: 10.1149/1945-7111/ab92b9 with permission from IOP Publishing Limited.

In this chapter, the exploration of the effect that altering the carbon support has on the novel N$_3$/C site from Chapter 2 for the oxygen reduction reaction. I used diazonium coupling chemistry to chemically attach only the most active forms of nitrogen from the terpyridine molecule to the carbon supports, which ranged in porosity and surface area. The resulting general synthetic procedure showed a unique and simple way to produce high-performing materials for the oxygen reduction reaction using a variety of supports. As a result, the more microporous support used, the lower the activity for the oxygen reduction reaction was observed. This work is continued in Chapter 4 where I explore using the optimal carbon support (Vulcan) and terpyridine ligand while altering the nature of the transition metal center. The role of the various carbon supports on the performance of the materials is further explored again in Chapter 6 with an alternative nitrogenous ligand for energy storage applications.

3.0 Abstract

We report here an investigation of the role that various carbon supports have on a model non-precious metal catalyst for the oxygen reduction reaction (ORR) prepared through a molecularly defined terpyridine moiety covalently embedded onto various high surface area carbons (Black Pearls 2000, Ketjen Black 600, Multi-Walled Carbon Nanotubes). A terpyridine modified catalyst has been previously prepared and allowed for the controlled deposition of one specific and unique N_3/C active site on the surface of the support. The effect of changing the porosity and surface area of the carbon was analyzed for its oxygen reduction reaction activity and characterized using thermogravimetric analysis, pore size determination, and rotating disk measurements. This system showed that when a more microporous support was used the activity for the oxygen reduction reaction was significantly decreased in acidic media, this could be explained by the differences in the formation and overall accessibility of the active sites on the high surface area supports.

3.1 Introduction

Fuel cells (FCs) are devices that convert chemical energy, in the form of hydrogen gas or alcohols, to electrical energy[1]. They are ideal in many clean energy systems such as transportation, portable, and stationary devices. The reactions that take place in the FC catalysts occur at the interface of both the anode and the cathode. Typically, a platinum on carbon (Pt/C) catalyst is required to facilitate the reactions occurring at both electrodes. However, the oxygen reduction reaction (ORR) that occurs at the cathode, is quite sluggish and often requires higher loadings of Pt to make the reaction more efficient due to significant overpotentials[2-3]. This becomes disadvantageous due to the cost and limited availability of Pt[4-5]. Thus, it becomes essential to alter the catalyst materials such that they do not rely on the use of precious and rare metals such as Pt[6-9].

Non-precious metal catalysts (NPMC) are considered to be a promising potential replacement for Pt/C catalysts at the cathode. NPMCs are typically synthesized from a carbon source, nitrogen precursor, and an iron salt[2, 10-12]. There has been abundant literature in recent years in this area due to a pivotal investigation by Dodelet et. al that proposed the most commonly believed model active site for the ORR catalyst. Their active site predicted model was synthesized via the pyrolysis of the carbon support and iron salt under the nitrogen atmosphere at elevated temperatures that lead to a bridged crystallite

model active site[11]. Thus, the most common method of production of NPMCs involves high-temperature pyrolysis steps (above 700 °C) which are believed to form the active site(s) of the catalyst in the micropores of the carbon support[6, 13-16]. However, this method of production itself can be disadvantageous as pyrolysis leads to a variety of nitrogen functional groups on the surface, where pyridinic nitrogens are widely believed to be one of the more active groups for the ORR[17-20]. While it is believed that the formation of the active sites happens upon pyrolysis, other less-desirable nitrogen functionalities, such a pyrrolic, are just as likely to form. Thus, it is difficult to design a surface rich in only one kind of active site with specific geometry for the desired application. While NPMCs are considered a promising alternative to Pt/C based catalysts, there are still issues that need to be addressed such as stability and activity of the materials[21].

Another important factor to consider in catalyst design is the effect carbon support has on the material[22-24]. Dodelet and coworkers have previously investigated the effect of altering the carbon support on the active site density and activity of the resulting catalysts[20, 25]. It was found that the microporosity is an important factor to consider when designing a catalyst as it is considered the most likely host for the active sites[20]. Improvements in the activity were observed when a more microporous carbon support was used which was correlated to a high density of active sites forming[25]. Thus, choosing appropriate carbon support will have significant impacts on the activity of the material towards the ORR.

Previously, we had reported a model catalyst synthesized from unique molecularly defined N_3 sites on a commercial Vulcan XC-72 carbon support[26]. Using diazonium coupling chemistry[27-29] followed by room temperature addition of Fe allowed for the creation of exclusively desirable catalytically active in ORR metal-ligand coordination motifs on the surface. Remarkably, the highest ORR activity was reached without the use of high-temperature pyrolysis treatment in out model catalyst. Building on this, we wanted to investigate if there are significant changes in activity when using out chemical modification approach to create active sites with predefined geometry.

Here we have investigated the role that different carbon supports play on the ORR catalytic activity of our model N_3 active site geometry. A majority of reported work in NPMCs observes enhancements in the activity upon the usage of more microporous support[13, 30]. We report here how changes in the activity of catalysts in ORR correlate with

the nature of carbon support that was altered from Vulcan XC-72 to Black Pearls 2000, Ketjen Black 600, and multi-walled carbon nanotubes.

3.2 Experimental

3.2.1 Materials

Sodium nitrite, methanol, iron(III) chloride, isopropyl alcohol, acetone, sulfuric acid, potassium hydroxide and Nafion® perfluorinated resin solution were purchased from Sigma Aldrich. Commercial Vulcan XC-72 and Black Pearls 2000 was purchased from Cabot. Commercial Ketjen Black 600 was purchased from Fuel Cell Earth.

3.2.2 Synthesis of the Catalysts

Commercial Black Pearls 2000 (BP), Ketjen Black 600 (KB), or multi-walled carbon nanotubes (MWCNTs) were modified with 4'-(4-aminophenyl)-2,2':6'2"-terpyridine (tpy) ligand via previously published procedures[15, 26, 31]. Briefly, 5 mL of 10 mM solution of tpy was added to 5 mL of 1 M $NaNO_2$ and allowed to react for 3 min before adding it to 700 mg of carbon support and stirring overnight. The resulting mixture was filtered and washed with methanol, acetone, and deionized water 3 times before being placed in the oven to dry producing BP-tpy, KB-tpy, or M-tpy. Fe-tpy coordination motifs were synthesized by reacting an excess of 10 mM $FeCl_3$, ca. 3-fold with respect to the stoichiometry of the ligand, with the materials for 48 h at room temperature. Materials were vacuum filtered and dried in the oven overnight to afford BP-tpy-Fe, KB-tpy-Fe, or M-tpy-Fe catalysts. A pre-made tpy_2-Fe complex in solution was synthesized to achieve a 2:1 ligand to metal stoichiometry for the BP system. Following the same procedure, the resulting molecular motif was attached to the surface through a diazonium coupling linkage (Scheme 3.1). Portions of the materials were heat-treated in a Barnstead International type F21100 tube furnace at a 10 ℃ min^{-1} ramp from room temperature to 700 ℃ while flowing N_2 atmosphere at 60 mL min^{-1} for 2 h, these samples are denoted as BP-tpy-Fe-700, KB-tpy-Fe-700, M-tpy-Fe-700, and BP-tpy_2-Fe-700. The materials were compared to our previously published V-tpy-Fe material that was synthesized in the same manner as these catalysts.
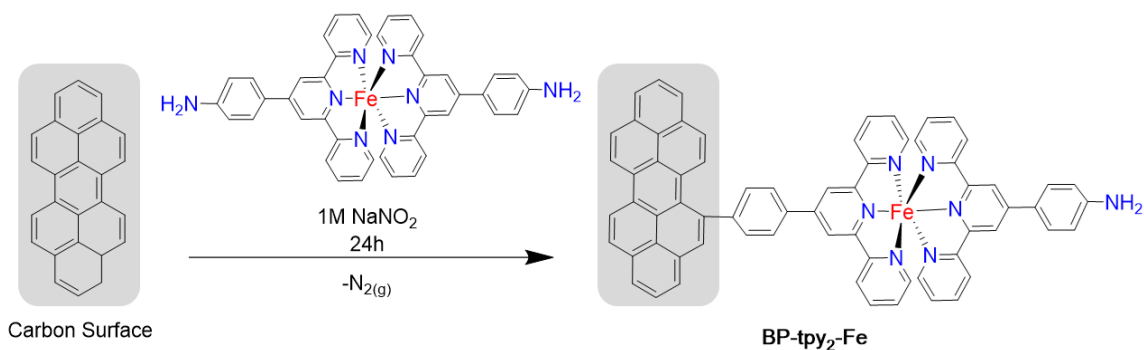
Scheme 3.2) Schematic diagram of the synthesis of the BP-tpy$_2$-Fe.

3.2.3 Physical Characterization

Modified carbons were characterized by Brunauer-Emmett-Teller pore size analyzer using a Quantachrome NOVAe 1200 pore analyzer. 60-point isotherms were recorded using N_2 as an adsorbate. Thermogravimetric analysis (TGA) was performed using a TA instruments Q600 SDT thermal analyzer. The materials were heated at a heating ramp of 5 ℃ min^{-1} from room temperature to 1000 ℃ while under an air atmosphere flowing at 10 mL min^{-1}. Raman spectra were obtained using a Renishaw inVia confocal Raman microscope with a 2400 l mm^{-1} (vis) grating and a Renishaw Centrus OMCN39 CCD detector. Excitation wavelength of the Nd:YAG laser (Renishaw) was 532 nm with a power output of 50 mW. Measurements were performed with an exposure time of 30 s per scan at 1% laser power at a 50 x objective (Lecia DM2700 M). X-ray photoelectron spectroscopy (XPS) analysis was performed using Thermo Scientific K-alpha XPS system equipped with a monochromated Al Kα (1486.7 eV) X-ray source and charge compensating flood gun. The data was analyzed using Avantage software. The spectra were baselined using Smart algorithm. The Smart background algorithm is based on the Shirley approximation method with the additional constraint that the background should not be of greater intensity than the actual data at any point in the region. The elemental ratio for each material was calculated from the XPS data using Wagner sensitivity factors[32]. The fitting of Fe 2p area was performed according to classical Lin et al. methodology[33]. Briefly, initially, the fitting was performed using Powel algorithm starting with delta between Fe 2p$_{3/2}$ and Fe 2p$_{1/2}$ of 13 eV and unfixed Fe 2p$_{3/2}$ shake-up peaks. Then the value of delta was unfixed and binding energy, full width at half maximum (FWHM), and height of all peaks were free to vary. Scanning electron microscopy (SEM) was performed using a

HITACHI FlexSEM 1000. The beam was 5 kV with a working distance of 5 mm and a spot size of 30 Å.

3.2.4 Electrochemical Characterization

Oxygen reduction reaction activity was studied using linear sweep voltammetry (LSV) in O_2 saturated 0.1 M H_2SO_4 and 0.1 M KOH. Catalyst inks were prepared by adding 10 mg catalyst, 200 µL deionized water, 700 µL isopropyl alcohol, 100 µL Nafion® (to afford 95%-to-5% catalyst-to-Nafion® ratio in the ink) and sonicating for 15 min. The inks were stirred overnight prior to use. 6 µL of catalyst ink was deposited on the 0.196 cm^2 glassy carbon electrode (302 µg cm^{-2} catalyst loading) and was rotated and dried under heat. The electrode was placed in a cell containing either 0.1 M H_2SO_4 or 0.1 M KOH with a mercury/mercury sulfate reference electrode and a platinum wire counter. N_2 sparged electrolyte was used to collect cyclic voltammograms at 20 mV s^{-1} prior to ORR measurements. Rotating-ring disk measurements were performed with the same catalyst ink formation and loading. A collection experiment was performed by holding the platinum ring at 1.2 V vs RHE. The collection efficiency was calibrated using 0.1 M NaOH with 10 mM $K_3Fe(CN)_6$. The calibrated collection efficiency was 0.24 at 900 rpm[34]. Measurements were made on a Pine Instruments model AFPC2 and Pine WaveDriver 20 with corresponding Aftermath software. LSV's were recorded in the absence of oxygen at 10 mV s^{-1} and then in the presence of oxygen to subtract the background currents.

3.3 Results and Discussion

3.3.1 Physical Characterization

We characterized our materials using TGA to analyze the effect the modification with tpy had on catalysts with different supports (Figure 3.1). In all the modified samples there was a significant change in the combustion temperature of the carbon when compared to the unmodified sample. This is due to changes in the carbon support upon modification of the material with tpy, and Fe. Similar results were seen in our previous work on this surface modification approach on a commercial Vulcan XC-72 support[26]. Differential thermogravimetric (DTG) analysis of the modified material shows two decomposition peaks at ca. 400 ℃ and ca. 450 ℃ for the BP system and ca. 500 ℃ and 600 ℃ for the KB system. The first peak is assigned to the combustion of the tpy group on the carbon support and the second is related to the combustion of the carbon support. The combustion peak of

the tpy is clearly present throughout all the tpy modified supports which is indicative of the presence of the ligand. In the case of the MWCNTs materials there were no apparent two peaks in the DTG. An estimated Fe loading was determined from the TGA for all samples (Table 3.1). The majority of our synthesized materials had Fe loadings ca. 2% comparable to literature and our previous work[8, 14, 16, 26, 35-37]. The TGA data for the BP-tpy$_2$-Fe sample is presented in the SI (Figure S3.1).
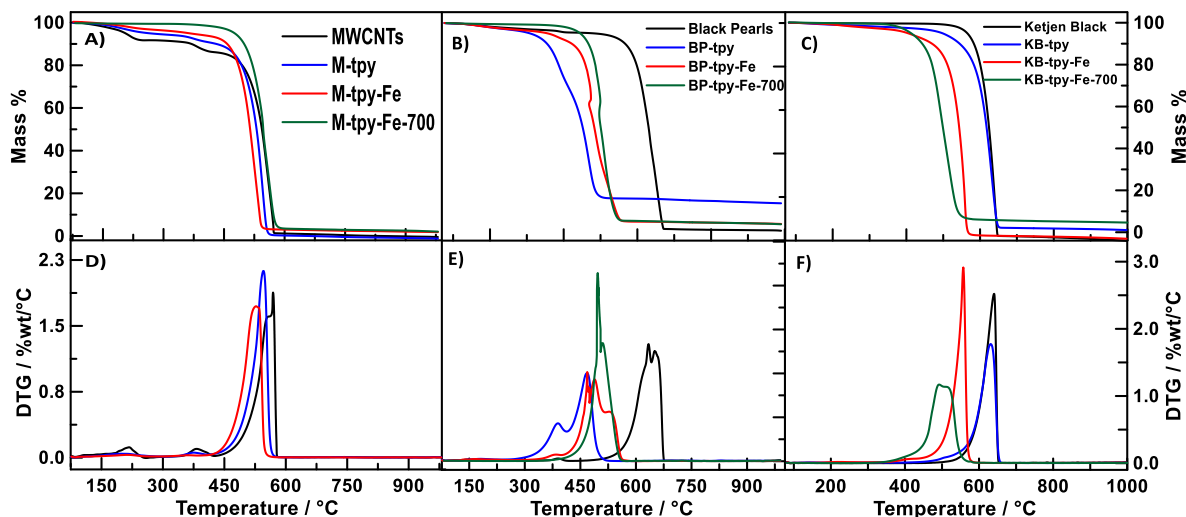
Figure 3.1) (A-C) Thermogravimetric analysis (TGAs) of the MWCNTs, BP, KB materials in an air atmosphere ran at a ramp of 10°C min^{-1}, respectively. (D-F) Differential thermograms (DTGs) of the MWCNTs, BP, and KB materials ran at a ramp of 10°C min^{-1}, respectively.

Table 3.1) TGA Fe wt% remaining, BET surface areas, and I_D/I_G ratios of the materials.

Catalyst	Wt% Remaining	Fe At% from XPS	N at% from XPS	SA$_{BET}$ (m^2 g^{-1})	I_D/I_G
MWCNTs	-			344.0	2.13
M-tpy	-			275.9	0.69
M-tpy-Fe	2.1%	0.24	0.47	266.8	1.37
M-tpy-Fe-700	-			315.4	1.45
Black Pearls	-			1431.9	1.63
BP-tpy	-			1154.2	1.48
BP-tpy-Fe	3.2%	0.52	0.17	1198.7	1.68
BP-tpy-Fe-700	-			1535.0	1.77
Ketjen Black	-			1658.4	2.35
KB-tpy	-			814.0	2.09
KB-tpy-Fe	1.7%	0.59	0.22	854.1	2.24
KB-tpy-Fe-700	-			967.0	2.10
V-tpy-Fe[26]	2.1%			206.0	-

Pore size analysis was performed on all the materials to analyze changes in the surface area upon modification with the tpy and in the BP, the tpy$_2$-Fe complex (Figure S3.2). The Brunauer-Emmett-Teller (BET) isotherms and Barrett-Joyner-Halenda (BJH) pore size distributions are shown in Figure 3.2 and surface areas are presented in Table 3.1. In all samples, upon addition of the tpy molecule the surface area decrease can be attributed to the bulky tpy molecules filling or blocking access to the pores, which decreases the surface area of the material[38]. Upon heat-treatment of the samples the surface area increases due to evolution of physisorbed molecules and the partial decomposition of the tpy groups, exposing more of the pores[13, 25].
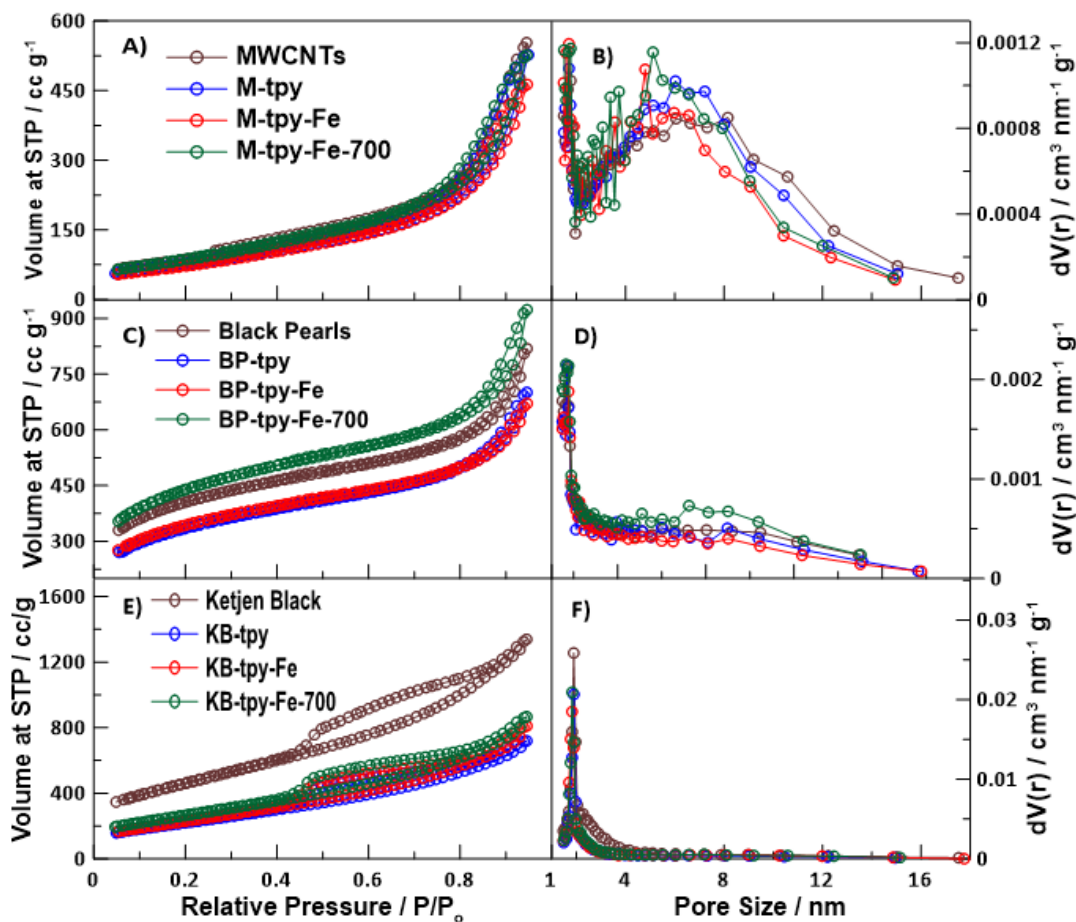
Figure 3.2) (A) BET isotherm of MWCNT materials using N_2 as the adsorbate (B) BJH pore size analysis of MWCNT materials (C) BET isotherms of BP materials using N_2 as the adsorbate (D) BJH pore size analysis of BP materials (E) BET isotherms of KB materials using N_2 as an adsorbate (F) BJH pore size analysis of KB materials.

Raman analysis was performed on the materials to analyze further changes in the carbon support upon modification with the tpy and the Fe (Figure 3.3). We calculated the I_D/I_G ratios of the D (1350 cm^{-1}) and the G (1500cm^{-1}) bands in the spectra to determine the degree of defects on the carbon structure upon modification (Table 3.1). Upon addition of the tpy molecule we saw that the I_D/I_G ratio decreased indicating that there is an increase in graphitization of the material[39-40]. When Fe was added to the materials there was an increase in the I_D/I_G ratio indicating that the addition of iron causes some disturbances in the carbon lattice[40-42]. After the heat treatment procedure there were further increases in the I_D/I_G ratios due to some etching of the carbon support and further disturbances in the carbon lattice as a result of the heat treatment process.
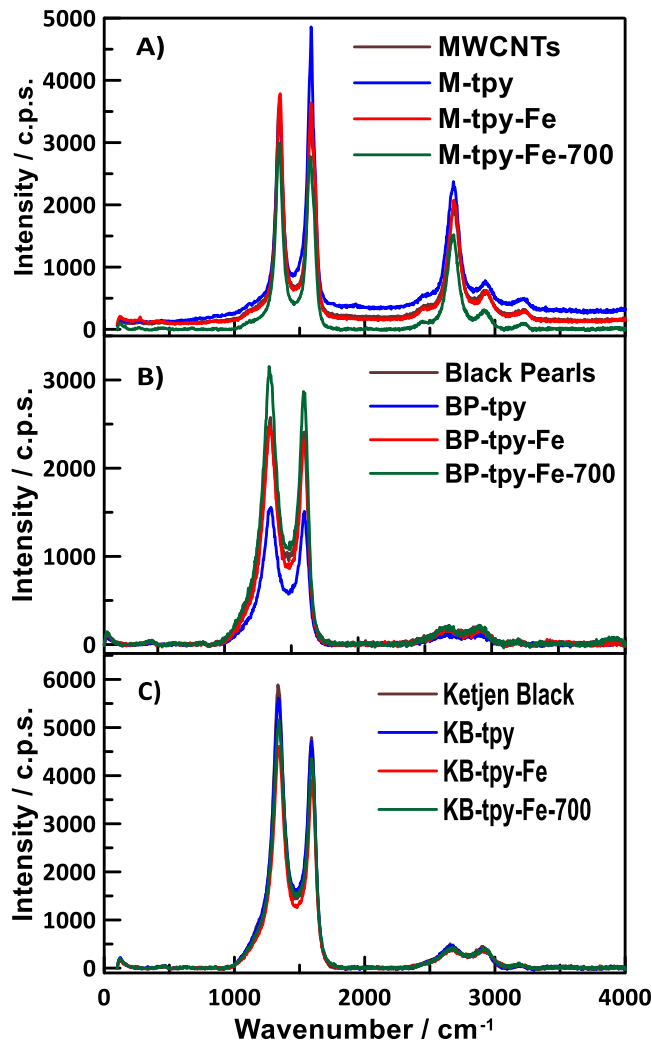
Figure 3.3) (A) Raman spectra of MWCNT materials (B) Raman spectra of BP materials (C) Raman spectra of KB materials.

SEM analysis was performed on M-tpy-Fe, BP-tpy-Fe, and KB-tpy-Fe catalysts and compared to the bare carbon supports (Figure 3.4). The SEM images of the bare carbon show morphology and pore sizes expected for each carbon support used. Upon modification with the tpy and Fe in each sample there were minimal changes to the carbon structure indicating that the modification approach does not change the morphology of the carbon support significantly.
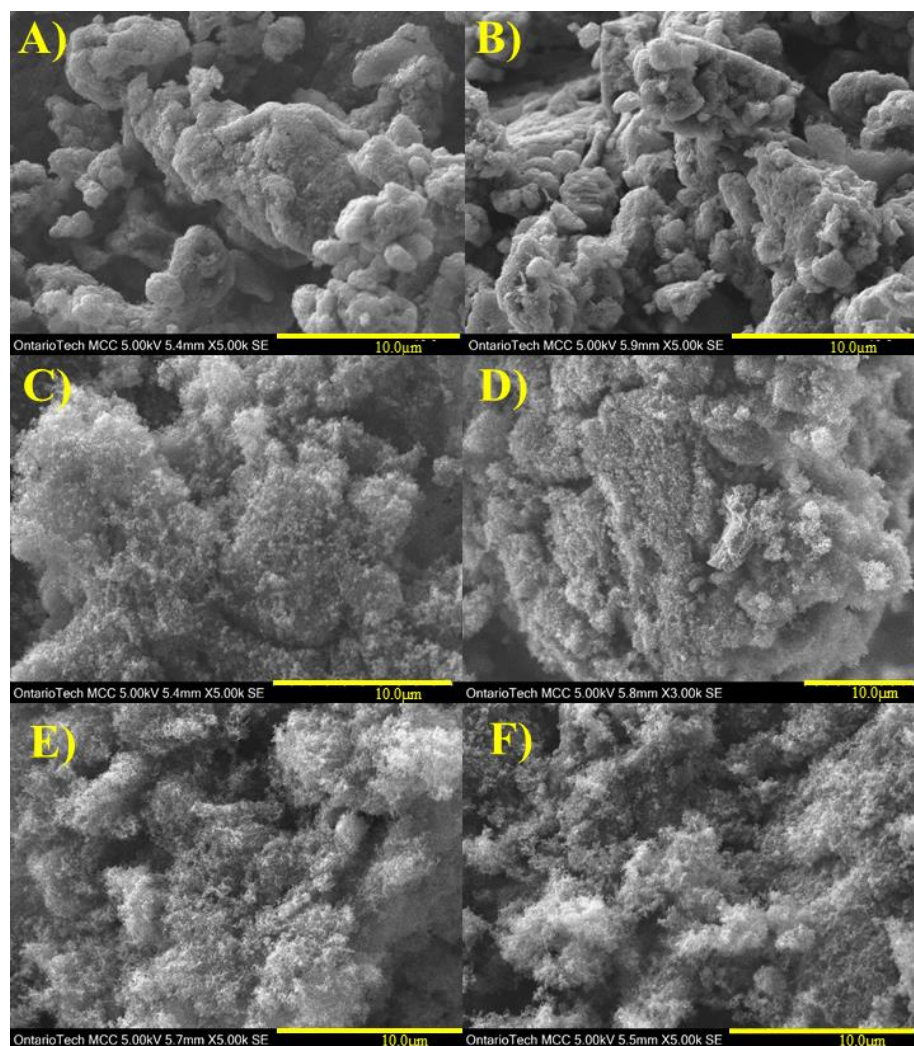
Figure 3.4) (A) SEM images of MWCNTS (B) M-tpy-Fe (C) Black Pearls (D) BP-tpy-Fe (E) Ketjen Black (F) KB-tpy-Fe.

XPS analysis confirms that carbon is the main component of all three materials. Thus KB-tpy-Fe contains 98.9 At% of carbon, while BP-tpy-Fe and M-tpy-Fe contain 99.1 At% and 99.24 At% carbon, respectively. C 1s peaks of all three materials are centered at 284.5 eV, Figure 3.5A. Moreover, C KLL Auger spectra of these materials are similar suggesting that carbon in the materials has a similar electronic structure. The separation value between the maxima and minima of the first derivatives of the C KLL Auger peaks, known as D parameter, allows the determination of the hybridization states of carbon atoms[43]. Lascovich et al.[44] have proposed a linear approximation, starting from D=14.2 eV for the sp$_3$ diamond and going up to D=22.5 eV for the sp$_2$ graphite, which permitted to extrapolate the D values for other compounds[45]. D parameters of KB-tpy-Fe, BP-tpy-

Fe, and M-tpy-Fe are 22.0, 20.5, and 21.2 eV, respectively (Figure 3.5B), confirming that all carbon supports have predominantly sp_2 graphitic nature.

XPS spectra of KB-tpy-Fe (Figures 3.5C-D) confirm the presence of iron and nitrogen in the material. Fe 2p region contains two main peaks: Fe $2p_{1/2}$ at 724.5 and Fe $2p_{3/2}$ at 711.7 eV, which is characteristic of Fe^{3+} ions[26]. Further deconvolution allows allocating Fe $2p_{3/2}$ satellite peak at 718.5 eV, which is in good agreement with Fe^{3+}[33]. As expected, the satellite feature of Fe $2p_{1/2}$ is obscured by the inelastic background. Interestingly, N 1s region shows the presence of three types of nitrogen atoms. Thus the peak at 406.2 eV corresponds to some remaining starting nitrate ($N_{nitrate}$), while deconvoluted peaks at 400.2 eV and 398.8 eV belong to iron-complexed (N_{pyr}^{Fe}) and free pyridinic nitrogen atoms (N_{pyr}), respectively[46]. The ratio between iron and nitrogen species Fe:$N_{nitrate}$:N_{pyr}^{Fe}:N_{pyr} is 1.0:1.4:3.5:5.0. This confirms that all iron atoms in the material are in the complexed form (Fe:N_{pyr}^{Fe} ratio is close to the expected stoichiometric 1:3 ratio). Moreover, there is excess of non-reacted pyridinic groups on the surface.

BP-tpy-Fe (Figures 3.5E-F) also contains iron and nitrogen atoms on the graphitic carbon support. Fe 2p peaks are located at 725.2 and 711.9 eV, while the shake-up satellite is located at 718.7 eV, respectively. The position of peaks unambiguously confirms the iron in the material is situated in Fe^{3+} oxidation state. The nitrogen area contains only pyridinic peaks. N_{pyr}^{Fe} peak is centered at 400.5 eV while N_{pyr} is located at 398.7 eV. It should be pointed out that N 1s peak of related iron-tpy complex deposited on indium tin oxide (ITO) support was observed at 400.0 eV[46]. When comparing these spectra (Figure S3.11), the slight shift of N_{pyr}^{Fe} peak in BP-tpy-Fe into higher binding energy area can be explained by the different support nature and more prominent electron-withdrawing properties of Fe^{3+} in BP-tpy-Fe. Similar position of N_{pyr}^{Fe} in both carbon-supported and ITO-supported materials confirms that our grafting methodology results in the formation of similar complex architectures on the carbon support. Further analysis of the Fe:N_{pyr}^{Fe}:N_{pyr} ratio at the surface of BP-tpy-Fe-gives 1.0:1.7:3.0. This suggests that only a part of the iron atoms is present on the surface in complexed form. Even though there is an excess of iron ions, not all of the pyridinic nitrogen species are involved in the complex formation.

Similarly, to the above forementioned materials, M-tpy-Fe contains iron and nitrogen atoms on carbon support (Figures 3.5G-H). Relatively high (up to 0.3 atomic %) amount of iron on the surface of this catalyst allows deconvolution of two iron species similarly to recently observed at related carbon catalyst[47]. The first pair of Fe 2p peaks are centered at 724.1 and 711.1 eV with the satellite peak at 718.3 eV. The second pair of Fe 2p peaks is located at 727.1 eV and 713.4 eV, the satellite peaks are found at 719.7 and 718.3 eV. Nitrogen atoms are represented by N_{pyr}^{Fe} located at 400.6 eV and N_{pyr} centered at 398.7 eV. Analyzing the position of the peaks and iron-to-nitrogen ratios, the iron species with the Fe $2p_{3/2}$ peak centered at 713.4 eV fit the best to the complexed nitrogen species. This is in good agreement with the allocation of complexed N-Fe^{3+} species in a previously reported nitrogen-doped porous carbon catalyst[48]. Overall, M-tpy-Fe contains about 0.08 At% of complexed iron and 0.22 At% of complexed nitrogen as well as 0.25% of non-complexed pyridinic nitrogen and 0.16 At% of non-complexed iron. Thus, we see increases in activity when the non-complexed nitrogens are on the support, due to the pyridinic core exposed on the surface. When the iron is complexed, the activity increases due to the structure on the surface creating active sites that correspond to sites that are related to high activity.
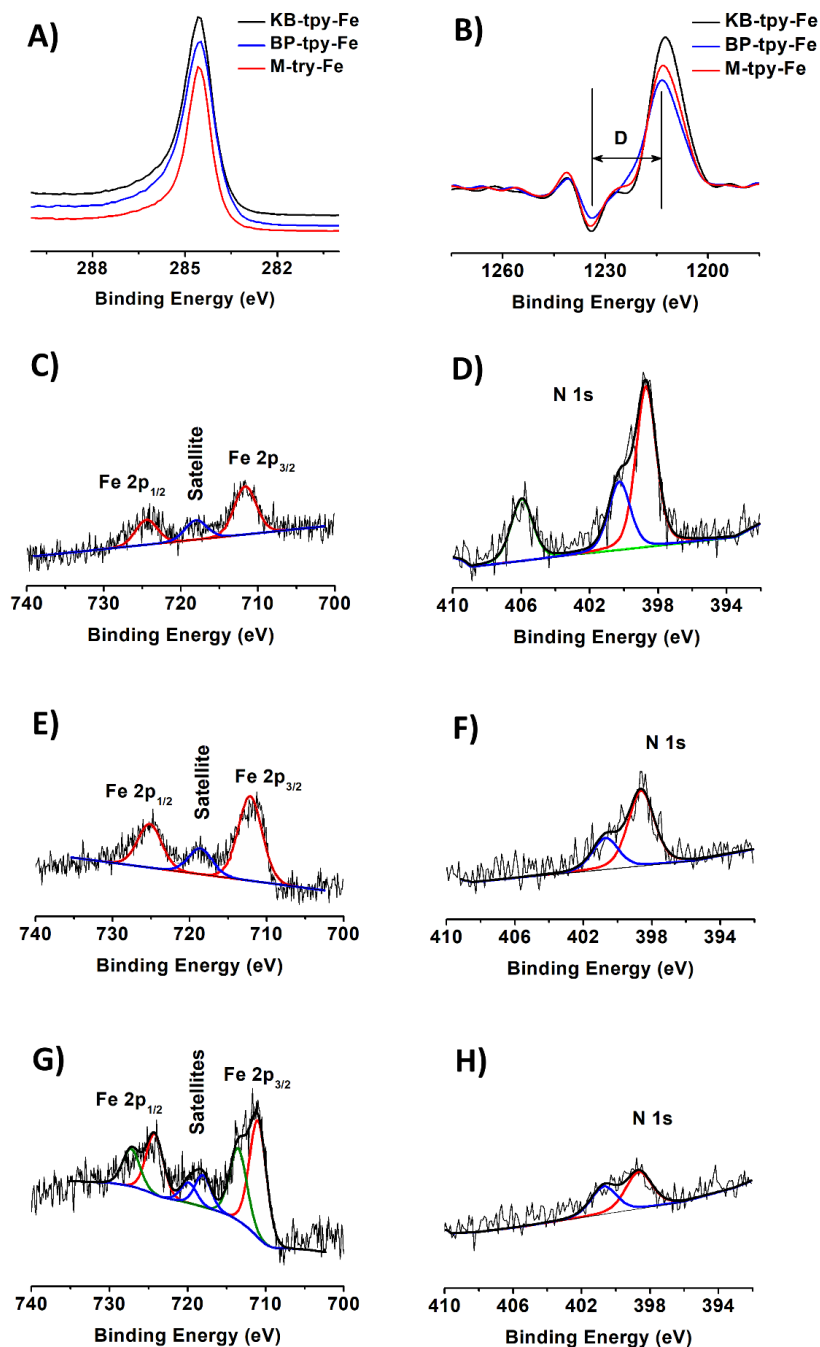
Figure 3.5) Representative (A) C 1s and (B) first-derivative C KLL Auger spectra recorded for all three materials. Representative XPS spectra of KB-tpy-Fe: (C) Fe 2p region and, (D) N 1s region, Black lines show the experimental data, the red, blue, and green lines represent corresponding spectrum deconvolution. Representative XPS spectra of BP-tpy-Fe: (E) Fe 2p region, (F) N 1s region. Representative XPS spectra of M-tpy-Fe: (G) Fe 2p region, (H) N 1s region.

3.3.2 Electrochemical Characterization

Figure 3.6 shows the CVs of our materials in 0.1 M H_2SO_4. Upon modification of the tpy ligand, two peaks appear at ca. 0.5 V and 0.8 V. The first peak can be attributed to the quinone/hydroquinone redox peak that is typically observed in acidic media. The second peak has been attributed to the electrochemistry of the pyridinic nitrogens in the tpy ligand. Previously, it has been observed that higher potential peaks correlate to nitrogen functional groups on the surface[15]. Incorporation of Fe shows a redox peak that appears at ca. 0.7 V which is indicative of $Fe^{2+/3+}$ redox couple[11, 49-50].
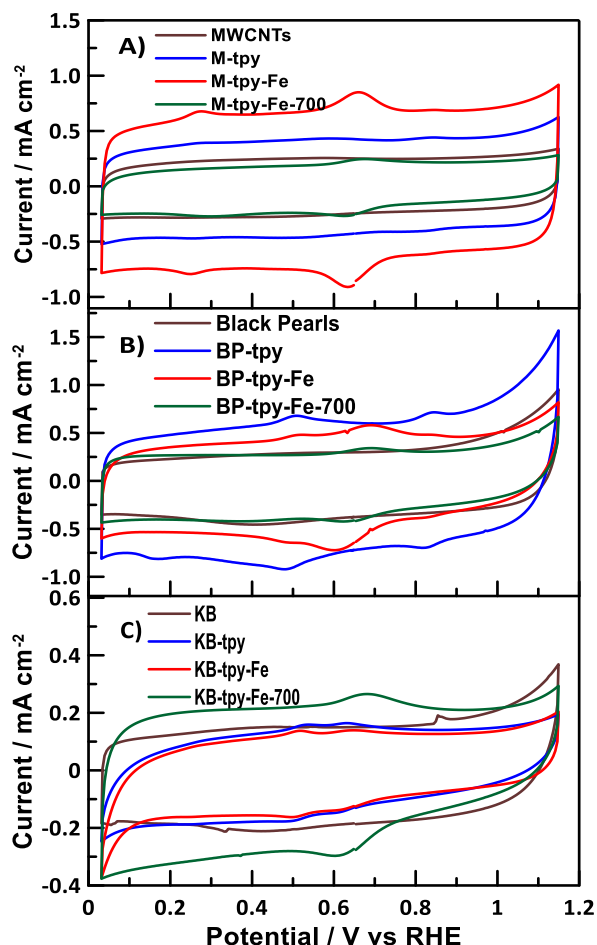
Figure 3.6) (A) CVs of MWCNT materials in N_2 saturated 0.1 M H_2SO_4 at a sweep rate of 20 mV s^{-1}. (B) CVs of BP materials in N_2 saturated 0.1 M H_2SO_4 at a sweep rate of 20 mV s^{-1}. (C) CVs of KB materials in N_2 saturated 0.1 M H_2SO_4 at a sweep rate of 20 mV s^{-1}.

The ORR activity of these materials in acidic media is shown in Figure 3.7. The onset potential determined at 0.1 mA cm^{-2} was monitored and tabulated in Table 3.2 as it is a good indication of how active our catalysts are for the ORR[51]. We compared our results to our previously published V-tpy-Fe catalyst, which was our best system to date

using our surface modification approach with the tpy ligand. In all cases the ORR activity of the material was quite poor in comparison to the V-tpy-Fe. However, for most of the catalysts, the activity dramatically increased after heat-treatment, which was not observed for the V-tpy-Fe material. For the surface modification approach without heat-treatment, altering the carbon support to more microporous carbons changed the onset potential from 0.87 V to 0.27 V, while after heat-treatment the onset potential greatly increased. The dramatic changes in the ORR activity are likely due to the location where the tpy group is grafting onto the support, which is different in comparison to the less microporous Vulcan model system[26]. We observed minor gains in the activity upon addition of Fe in the M-tpy and BP-tpy case. This is expected due to the role that the iron plays in the catalyst design, increasing the activity of the NPMCs[2, 19, 42, 52].
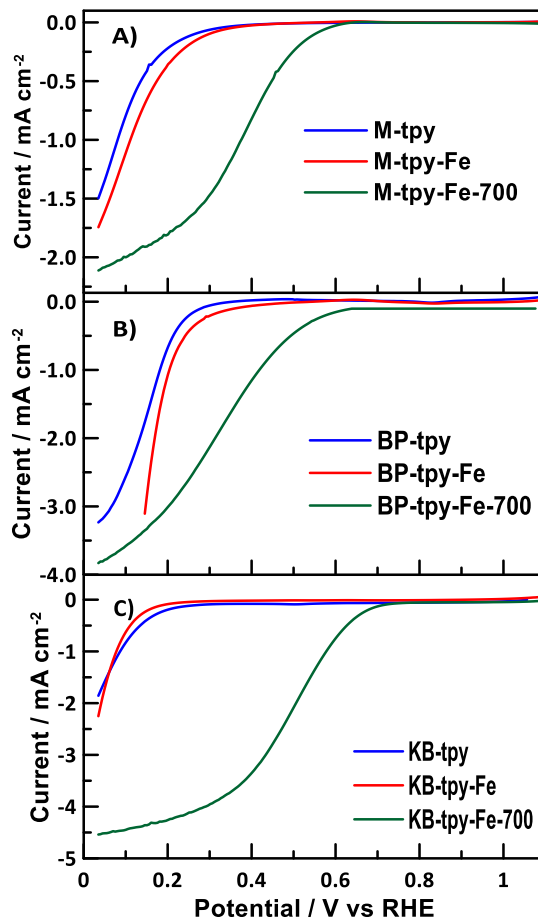
Figure 3.7) (A) LSV of the MWCNT materials in O_2 saturated 0.1 M H_2SO_4 at 900 rpm with a sweep rate of 10 mV s^{-1} (B) LSV of the BP materials in O_2 saturated 0.1 M H_2SO_4 at 900 rpm with a sweep rate of 10 mV s^{-1} (C) LSV of the KB materials in O_2 saturated 0.1 M H_2SO_4 at 900 rpm with a sweep rate of 10 mV s^{-1}.

We had previously hypothesized that if a bis-complex formed on the surface that the activity of the material would essentially be turned off due to the formation of a fully saturated 18 electron Fe-tpy$_2$ complex, with no open coordination sites for O$_2$. This was seen for the activity of the BP-tpy$_2$-Fe material which is quite low (Figure S3.6) supporting our initial hypothesis that the bis-complex may almost completely turn off activity for ORR. Notably, heat-treatment of the sample resulted in only minor improvements in the onset potential of this bis-complex and negligible gains in the activity. Moreover, based on the size of the molecule and typical pore size of the commercial Black Pearls 2000, the complex is larger than the average pore size (Scheme 3.2)[13, 53-54]. Comparing this to the size of Dodelet's model of the active site in which the Fe-N$_{2+2}$/C sites are bridged between the two crystallites of the carbon support, it is reported to be about 13 Å in diameter[30]. With this in mind, we could expect that the bis-complex is too large to enter the micropores of the support and to form active catalytic sites or it would enter the micropores and block them from making active sites accessible for the ORR. However, after heat-treatment of the material the tpy molecule will decompose into smaller fragments and thus some of the active nitrogen functionalities might be forming in the micropores which is enhancing the activity of the material. However, even though improvements were seen for the BP-tpy$_2$-Fe-700 for the ORR activity, it still demonstrated poorer performance than the BP-tpy-Fe-700.
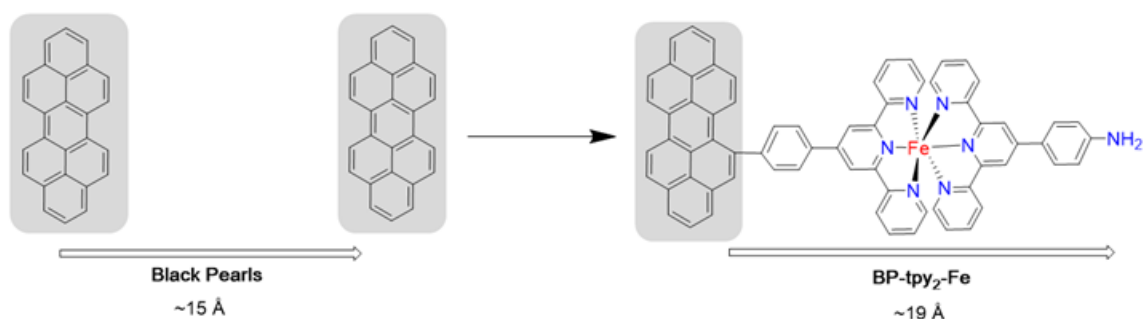
Scheme 3.2) Comparison of the size of the BP-tpy$_2$-Fe to the pore size of the commercial Black Pearls 2000 support.

It is commonly believed that with the higher surface area carbons their ORR performance of the catalysts increases due to an increase in the active site density[19]. As we altered the less microporous support (Vulcan) to more microporous carbon support (Black Pearls), we believe this support could be producing active sites that are not the same

as the V-tpy-Fe material, based on the differences in the activity for ORR. Thus, by changing the supporting material, the activity of the catalyst has significantly decreased owing to the effect of the proper choice in carbon support for our surface modification approach. The lesser microporosity of the carbon results in the formation of the more uniform active sites on the surface of the material as was seen with the V-tpy-Fe material.

Koutecky-Levich (KL) analysis was performed at 0.15 V_{RHE} to determine the number of electrons transferred and the kinetic currents (Table 3.2). For all the catalyst materials the number of electrons transferred was quite low, only ca. 2 electrons were transferred, indicating that the product of this reaction is mainly hydrogen peroxide[55]. This is in stark contrast to the results reported for the V-tpy-Fe model system where 4-electron process was dominant. This indicates that the active site(s) formed on the surface of microporous BP, MWCNTS, and KB carbon materials are different and not active without heat treatment in comparison to our V-tpy-Fe catalyst on lower surface area carbon support, which activity has deteriorated after heat-treatment.

Table 3.2) Onset potentials and Koutecky-Levich analysis of the catalysts in 0.1M H_2SO_4

Catalyst	Onset Potential at 0.1 mA cm^{-2} (V)	Half-Wave Potential (V)	Koutecky-Levich Analysis	
			Number of electrons transferred	i_k (mA cm^{-2})
M-tpy	0.26	N/A	1.9	1.32
M-tpy-Fe	0.29	N/A	2.2	2.26
M-tpy-Fe-700	0.54	0.39	2.0	20.18
BP-tpy	0.27	N/A	2.8	3.49
BP-tpy-Fe	0.32	N/A	2.7	2.03
BP-tpy-Fe-700	0.63	N/A	4.1	18.92
KB-tpy	0.27	N/A	2.4	2.23
KB-tpy-Fe	0.18	N/A	3.4	1.48
KB-tpy-Fe-700	0.71	0.50	4.2	68.90
V-tpy-Fe[26]	0.87	0.62	4.0	3.34

To study further the effect of the microporosity of the carbon support, we also subjected the BP, M, and KB materials to the ORR in basic media (Figure 3.8). In this case the ORR activity was remarkably improved in basic media as opposed to acidic media and performed similarly or better than our V-tpy-Fe model catalyst. It is well known that NPMCs perform better in basic media as the surface nitrogen atoms are not as easily

protonated as they are in acidic media. In acidic media, the pyridinic nitrogens can become easily protonated and thus attract anion binding[6, 56-57]. This will lead to lower activity as the Lewis basicity of the site is lowered upon the protonation of the nitrogen functional groups[19].
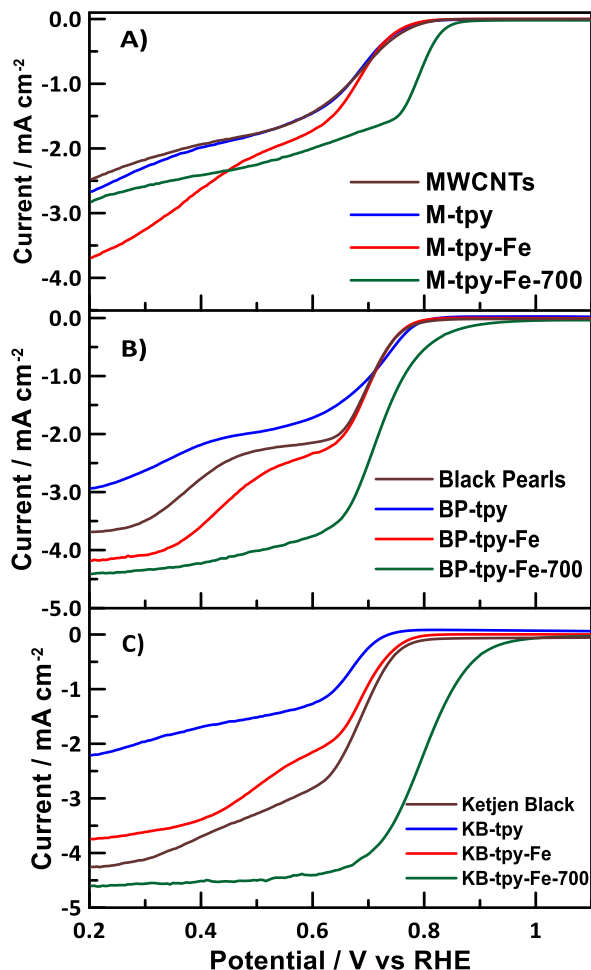
Figure 3.8) (A) LSV of the MWCNT materials in O_2 saturated 0.1 M KOH at 900 rpm with a sweep rate of 10 mV s^{-1} (B) LSV of the BP materials in O_2 saturated 0.1 M KOH at 900 rpm with a sweep rate of 10 mV s^{-1} (C) LSV of the KB materials in O_2 saturated 0.1 M KOH at 900 rpm with a sweep rate of 10 mV s^{-1}.

KL analysis at 0.3 V was performed on these materials in basic media as well (Table 3.3). The number of electrons transferred for most of the materials was 3.5 or higher indicating that the materials are going through 4 electron transfer process to directly produce water[55]. The KB-tpy, and M-tpy showed the poorest activity with mainly 2 electron transfer processes occurring. Interestingly, MWCNT catalysts had relatively high onset potentials but reached a significantly lower limiting current density, which is a result of the 2-electron reduction being more dominant. However, upon the incorporation of Fe

73

into those materials, the number of electrons transferred increases to 4 indicating again the importance of iron in catalyst design. The 2:1 ligand to metal complex had the lowest number of electrons transferred, however, still showed some activity towards the ORR. This could be due to the carbon showing some activity for ORR in basic media, as carbon alone has some activity in the basic electrolyte[55]. After heat treatment, the activity for the ORR catalysts has enhanced especially for more microporous BP-tpy-Fe-700 and KB-tpy-Fe-700. A comparison of the ORR onset potentials in both acidic and alkaline media are shown in Figure 3.9.

Table 3.3) Onset potentials and Koutecky-Levich analysis of all the catalysts in 0.1 M KOH.

Catalyst	Onset Potential at 0.1 mA cm^{-2} (V)	Half-Wave Potential (V)	Koutecky-Levich Analysis	
			Number of electrons transferred	i_k (mA cm^{-2})
M-tpy	0.77	0.68	2.7	8.98
M-tpy-Fe	0.76	0.68	3.8	12.97
M-tpy-Fe-700	0.84	0.79	2.9	13.83
BP-tpy	0.78	0.72	3.6	7.63
BP-tpy-Fe	0.77	0.70	4.0	38.08
BP-tpy-Fe-700	0.90	0.72	4.1	29.82
KB-tpy	0.71	0.67	1.9	18.25
KB-tpy-Fe	0.76	0.69	3.2	20.65
KB-tpy-Fe-700	0.96	0.81	3.9	112.5
V-tpy-Fe[26]	0.79	0.66	3.6	24.81
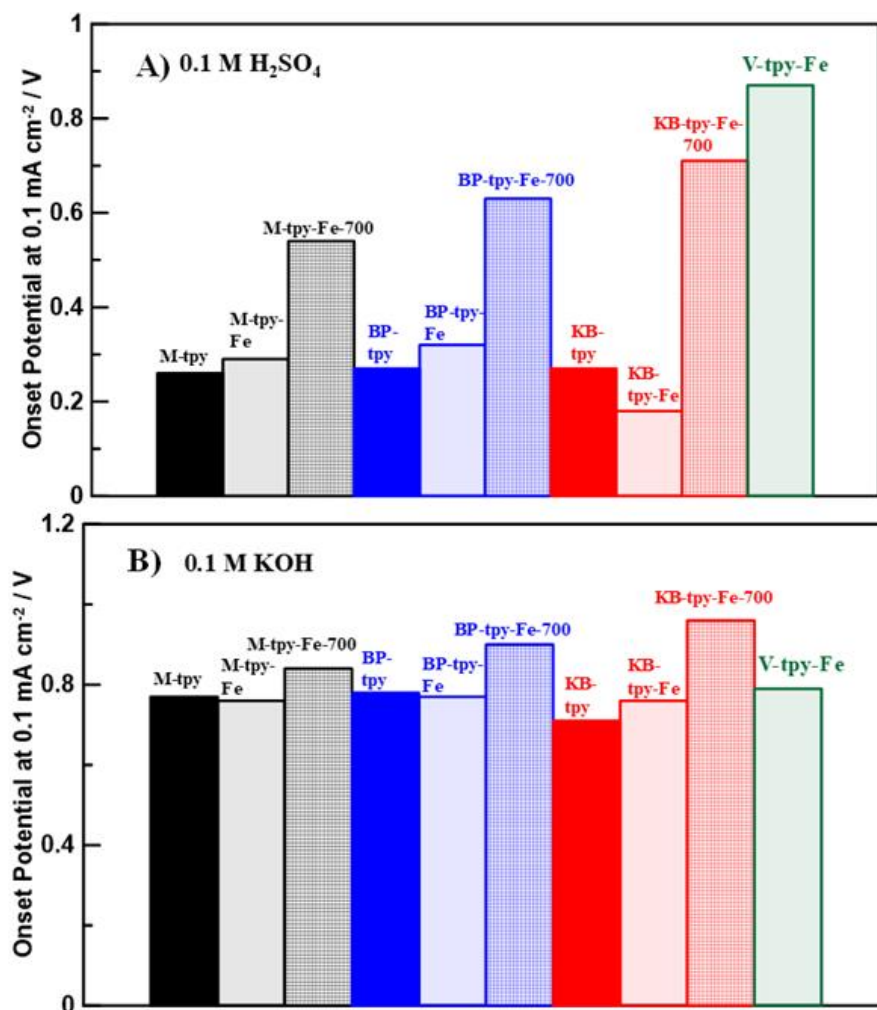
Figure 3.9) (A) Comparison of the ORR onset potential in 0.1 M H$_2$SO$_4$ of the catalysts during different stages in the synthesis (B) Comparison of the ORR onset potential in 0.1 M KOH of the catalysts during different stages in the synthesis.

Due to the high activity of the KB-tpy-Fe-700 for the ORR reaction in basic media, we performed rotating ring disk analysis on this material to gain more mechanistic information about the peroxide production (Figures S3.9-3.10). It was seen that upon heat treatment of the KB-tpy-Fe-700 material the amount of H$_2$O$_2$ produced was quite low, less than 10% over the course of the reaction and the number of electrons transferred was very high, approximately 4 electrons. The KB-tpy-Fe had a low number of electrons transferred and a large amount, >70%, of peroxide generated. We compared this to our V-tpy-Fe material analyzed in the same conditions and we saw that from the disk currents V-tpy-Fe and the KB-tpy-Fe materials appeared to perform similarly. However, from the ring currents and the hydrogen peroxide collection, the KB-tpy-Fe produced significantly more

hydrogen peroxide as it does not go through the "2+2" electron transfer pathway as observed for the V-tpy-Fe catalyst. This is the main electron transfer mechanism observed from our catalysts on Vulcan, where hydrogen peroxide is initially formed and then further reduces to water.

Comparing these results gathered from our heat-treated data we postulate that upon heat-treatment of the carbon support, some of the covalently attached tpy ligand breaks down into smaller fragments, as evidenced from the TGA of the tpy ligand (Figure S3.1). Currently, in literature the most prominent way to synthesize NPMCs is to heat-treat the precursors as it provides higher ORR activity in alkaline and acid due to the formation of active sites in the micropores of the carbon support. Literature suggests that through this process pyridinic nitrogen's can be formed on the edge planes of the carbons and coordinate with Fe, which is believed to be an ideal position for increased activity[52]. This suggests that upon heat treatment our catalyst surface is modified leading to the creation of more ideal sites on the support that can combine with the Fe to create a material that has higher activity[58]. This is consistent with the reports of more active Fe-N sites upon heat treatment (e.g. Fe-N_{2+2}/C) that lead to increased activity[59]. Both pyridinic N and graphitic N are shown to have higher performance, compared to other forms of nitrogens, such as pyrrolic N[51]. With our model catalyst design, we aim to only functionalize the surface with the most active nitrogenous groups (pyridinic). Other works show less specificity than our method due to the lack of control over the types of nitrogen that form after the high temperature heat-treatments[40-41, 51-52, 59-61]. Overall, these results show that the pore structure of the different carbon support have a large influence on the active sites that form in our model catalyst and on the catalytic activity.

3.4 Conclusion

In conclusion, we have shown that the choice in carbon support makes a significant difference on the ORR performance of our model N_3/C sites. The surface modification approach allows for creation of predefined sites on the carbon support without the need for heat treatment, which makes it advantageous for commercial and industrial applications. From this study, it is clear that, the choice of carbon support influences grafting efficiency and the accessibility of active sites that significantly influence the activity of the material towards ORR, especially in acidic media. We have shown here that employing a carbon

with a higher surface area, but microporous nature is not beneficial for our approach to create active ORR catalysts. Perhaps due to the location of the formed catalytically active sites, they are not located in the pores. Also, an important key factor of the catalyst design is to consider if the length and size of the molecular unit used to modify the surface, as larger molecules might not be able to graft into microporous supports while smaller units could still show effective grafting. Gaining further insight into the precise nature of the active sites through a surface modification approach and understanding the role each element plays could be critical to increasing activity and stability of catalytic platforms in the future.

3.5 Supporting Information
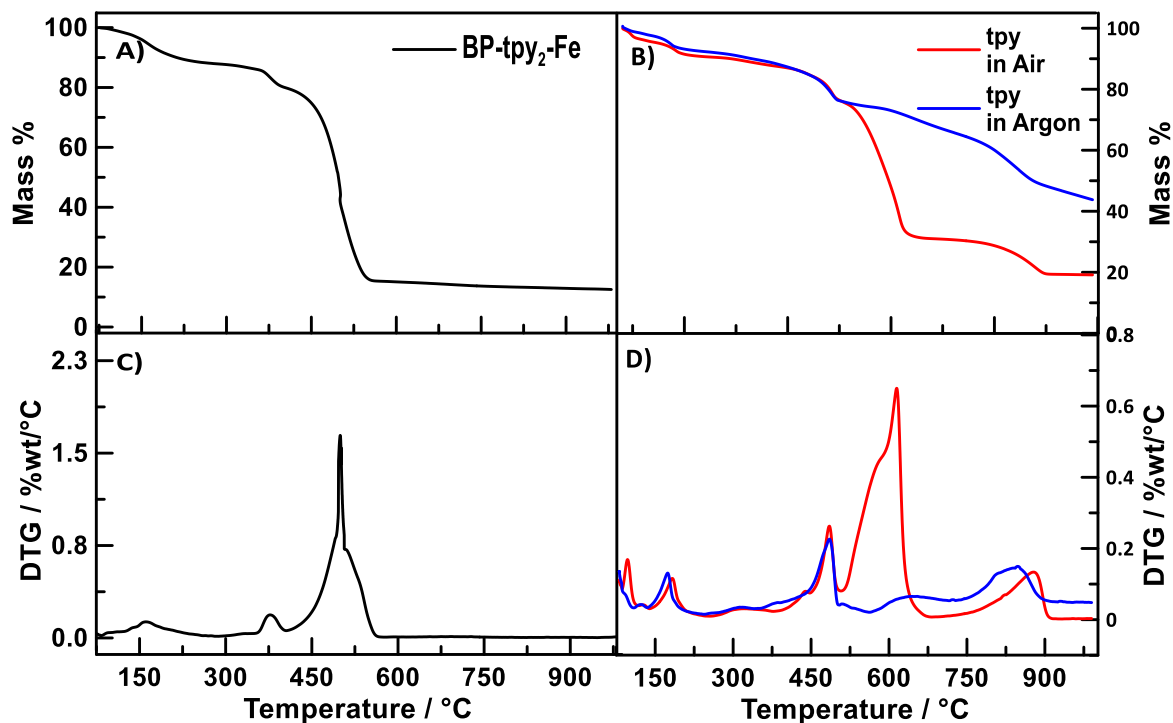
Supporting Information Figure S3.1) (A) TGA of BP-tpy$_2$-Fe at a scan rate of 10°C min^{-1} in an air atmosphere. (B) TGA of tpy ligand at a scan rate of 10°C min^{-1} in an air and argon atmosphere. (C) DTG of BP-tpy$_2$-Fe at a scan rate of 10°C min^{-1} in an air atmosphere. (D) DTG of tpy ligand at a scan rate of 10°C min^{-1} in an air and argon atmosphere.
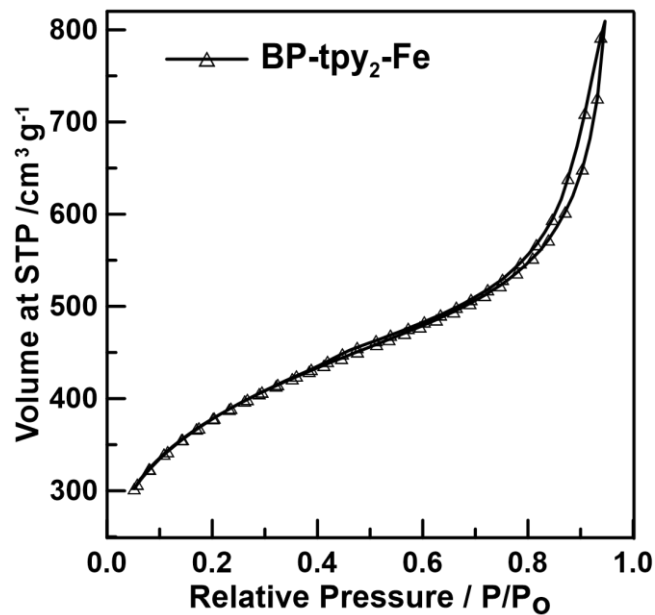
Supporting Information Figure S3.2) BET of BP-tpy$_2$-Fe using N$_2$ as an adsorbate.

For the BP-tpy$_2$-Fe sample, the surface area does not decrease significantly upon the addition of the tpy$_2$-Fe complex which indicates that there might not be a significant amount of the complex present on the surface of the material.
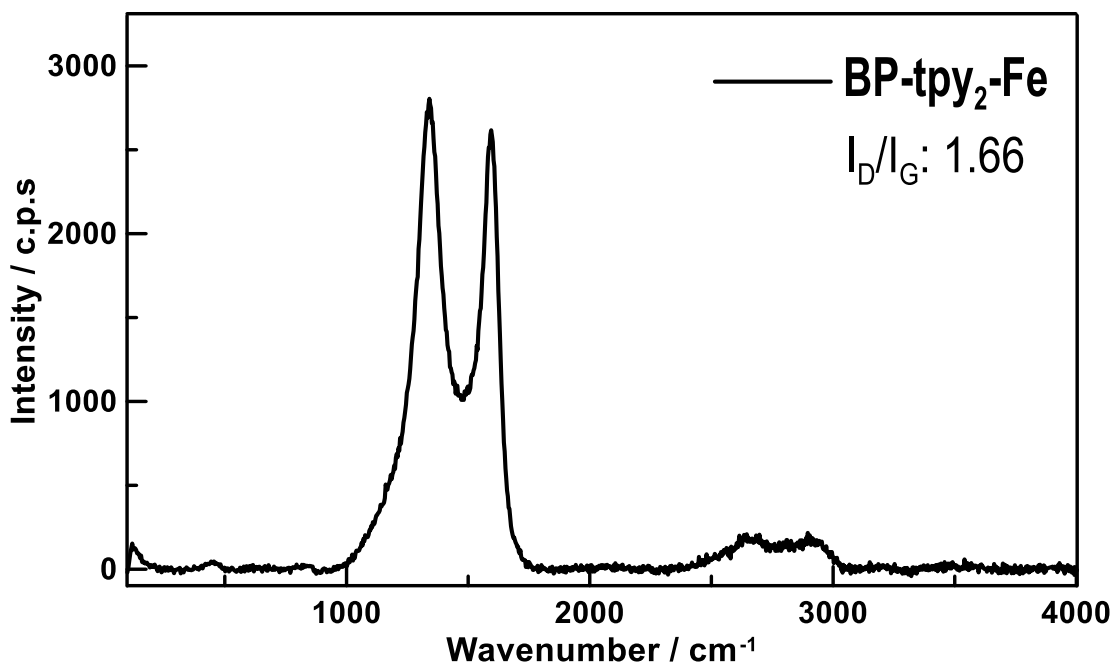
Supporting Information Figure S3.3) Raman spectra of the BP-tpy$_2$-Fe material.
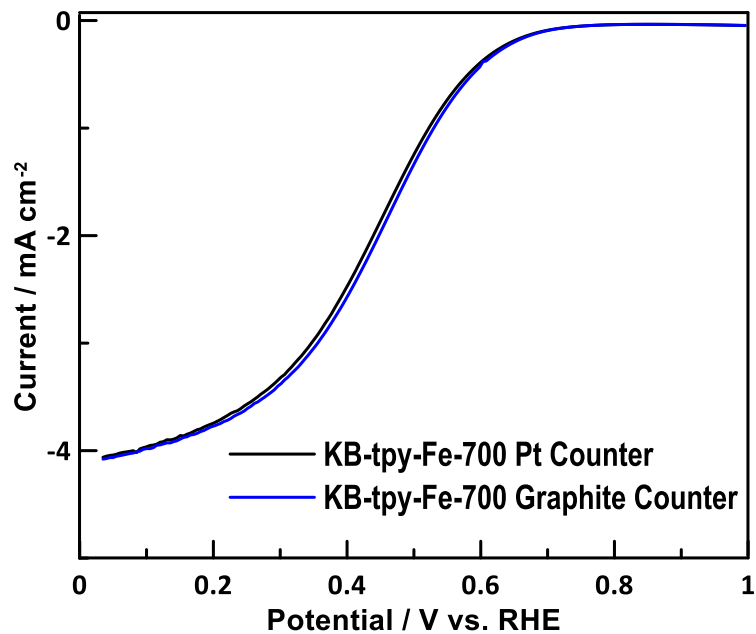
Supporting Information Figure S3.4) LSV of KB-tpy-Fe-700 material in O_2 saturated 0.1 M H_2SO_4 at 900 rpm with a sweep rate of 10 mV s^{-1} comparing the use of two different counter electrodes.
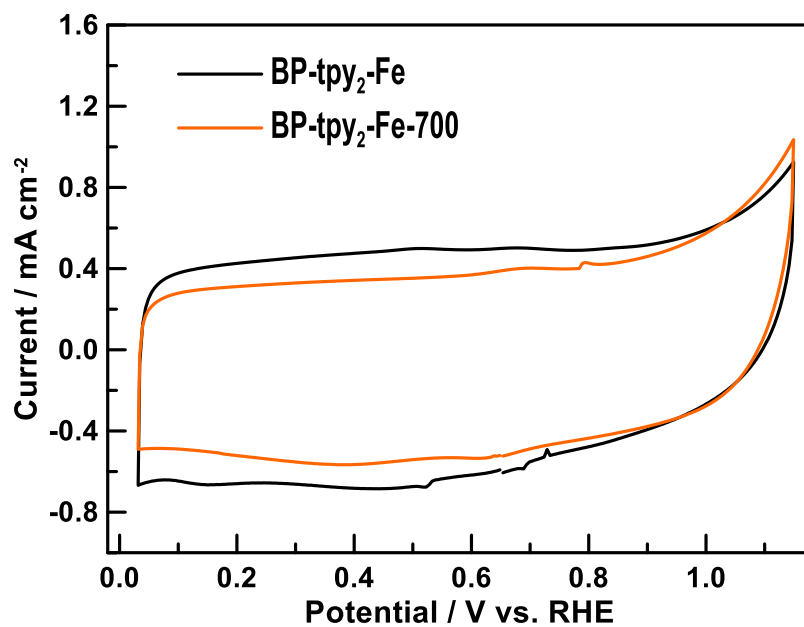
Supporting Information Figure S3.5) CV of BP-tpy$_2$-Fe and BP-tpy$_2$-Fe-700 in N_2 saturated 0.1 M H_2SO_4 at a sweep rate of 20 mV s^{-1}.
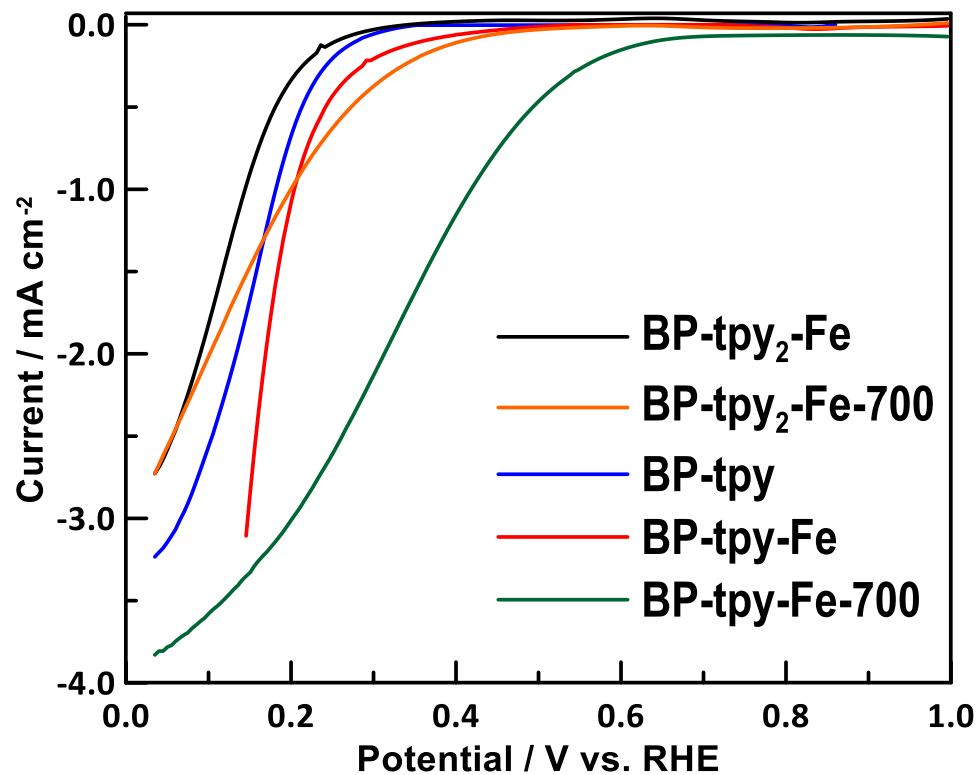
Supporting Information Figure S3.6) LSV of the BP-based catalyst materials in O_2 saturated 0.1 M H_2SO_4 at 900 rpm with a sweep rate of 10 mV s^{-1}.

Supporting Information Table S3.1) Onset potentials of all the catalysts in 0.1M H_2SO_4.

Catalyst	Onset Potential (V)	Half-Wave Potential (V)	Koutecky-Levich Analysis	
			Number of electrons transferred	i_k (mA cm^{-2})
BP-tpy$_2$-Fe	0.29	0.11	3.0	1.27
BP-tpy$_2$-Fe-700	0.44	0.14	3.6	4.20
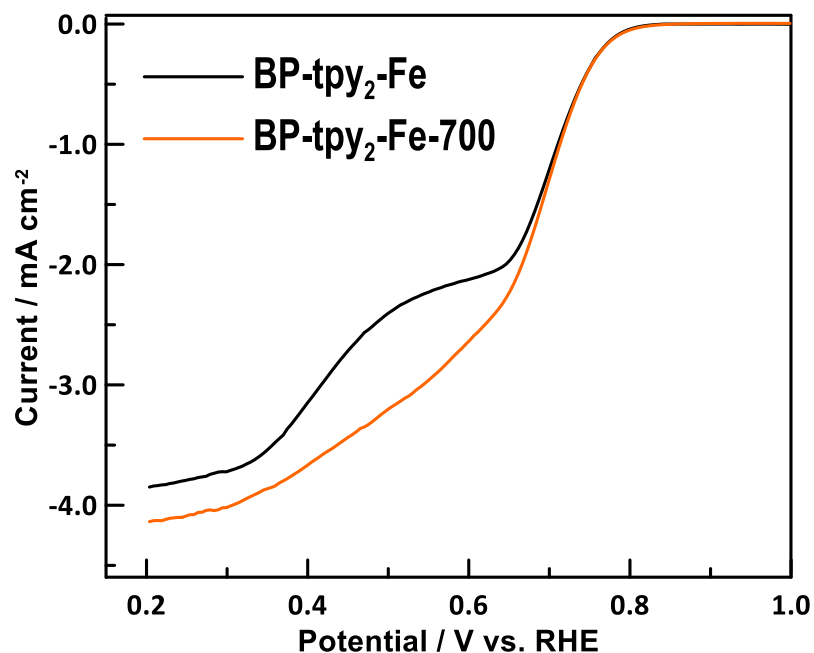
Supporting Information Figure S3.7) LSV of the BP-tpy$_2$-Fe materials in O$_2$ saturated 0.1 M KOH at 900 rpm with a sweep rate of 10 mV s^{-1}.

Supporting Information Table 3.2) Onset potentials of all the catalysts in 0.1 M KOH.

Catalyst	Onset Potential (V)	Half-Wave Potential (V)	Koutecky-Levich Analysis	
			Number of electrons transferred	i$_k$ (mA cm^{-2})
BP-tpy$_2$-Fe	0.81	0.71	3.3	56.36
BP-tpy$_2$-Fe-700	0.80	0.69	3.5	18.86
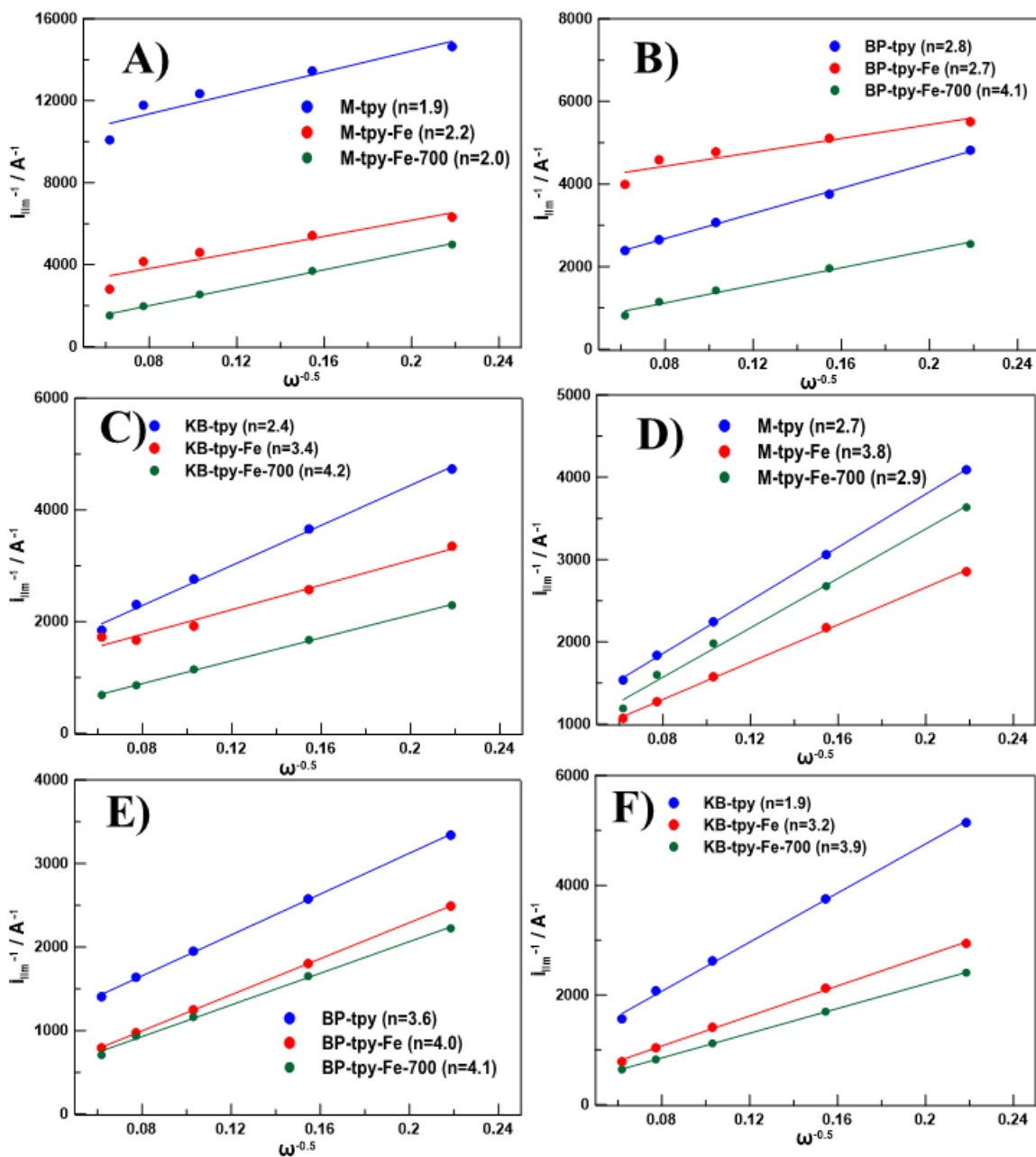
Supporting Information Figure S3.8) Kouteckey-Levich analysis of (A) MWCNT materials (B) BP materials and (C) KB materials in 0.1 M H_2SO_4. (D) MWCNT materials (E) Black pearls materials and (F) Ketjen Black materials in 0.1M KOH.
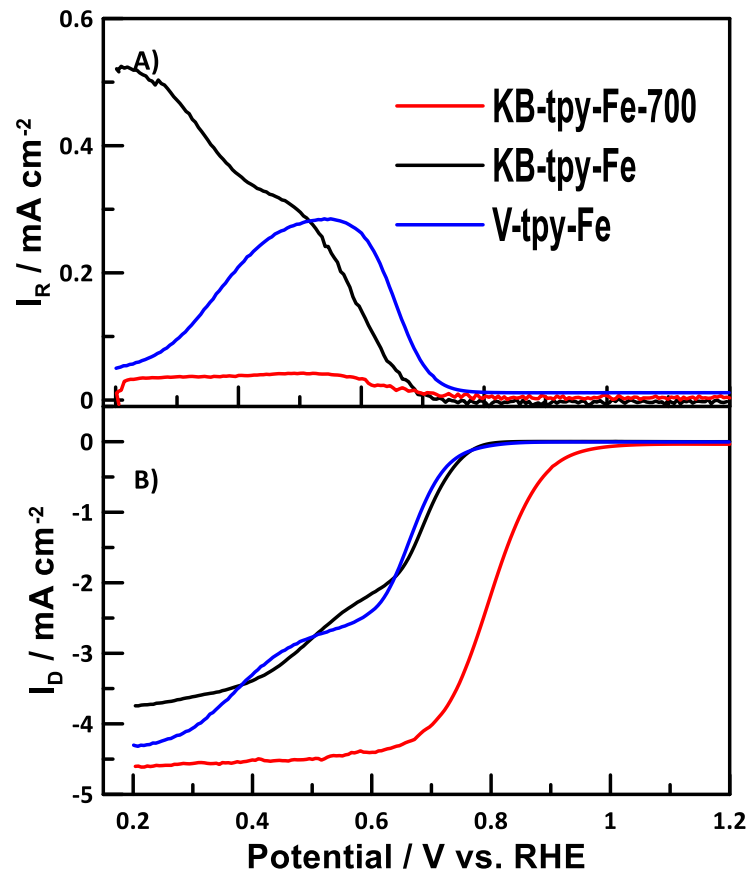
Supporting Information Figure S3.9) (A) Disk currents at 900rpm in O_2 saturated 0.1 M KOH (B) Ring currents at 900rpm in O_2 saturated 0.1 M KOH.
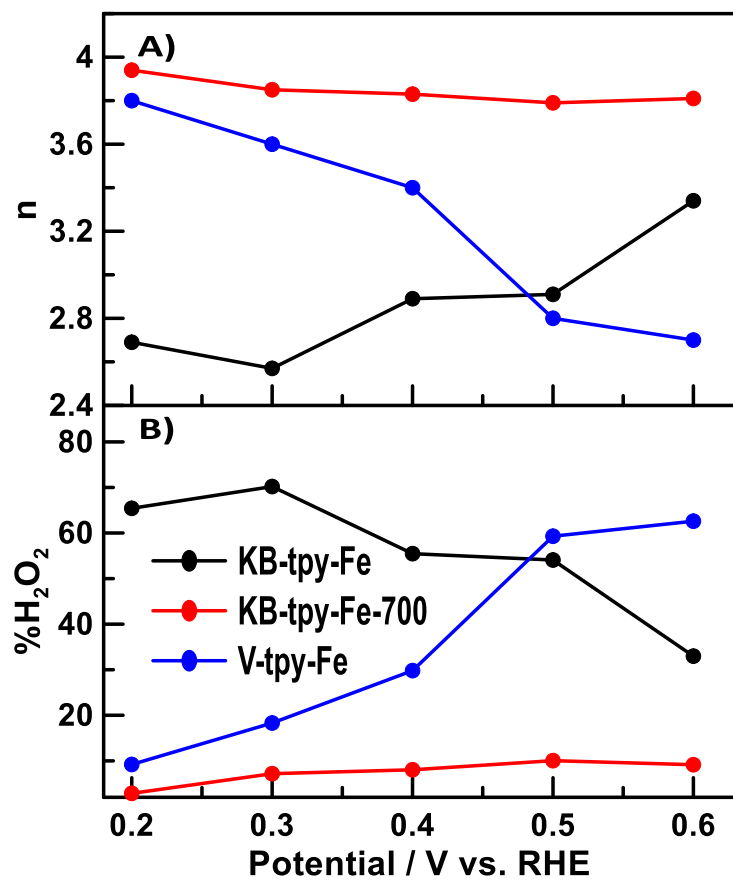
Supporting Information Figure S3.10) (A) Number of electrons transferred calculated from the peroxide collection experiment at 900rpm in O_2 saturated 0.1 M KOH (B) %H_2O_2 generated from the collection experiment at 900rpm in O_2 saturated 0.1 M KOH.
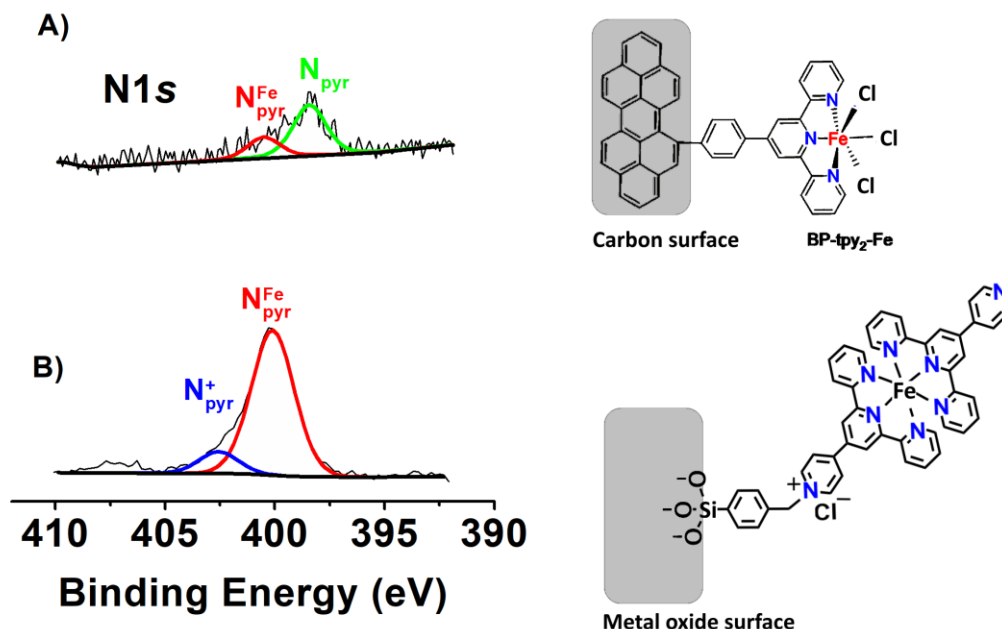
Supporting Information Figure S3.11) A comparison of N 1s region of (A) BP-tpy-Fe catalyst on carbon support and (B) an Fe(II) complex of similar nature deposited on ITO support. N 1s peaks of nitrogen atoms involved in the corresponding complex formation are located in a similar binding energy.

3.6 Acknowledgements

3.7 References

[1]   S. Rojas-Carbonell, K. Artyushkova, A. Serov, C. Santoro, I. Matanovic, P. Atanassov, *ACS Cat.* **2018**, *8*, 3041-3053.

[2]   Y. Mun, S. Lee, K. Kim, S. Kim, S. Lee, J. W. Han, J. Lee, *J. Am. Chem. Soc.* **2019**, *141*, 6254-6262.

[3]   J. H. Zagal, M. T. Koper, *Angew. Chem. Int. Ed. Engl.* **2016**, *55*, 14510-14521.

[4]   A. Kongkanand, M. F. Mathias, *J. Phys. Chem. Lett* **2016**, *7*, 1127-1137.

[5]   F. Jaouen, D. Jones, N. Coutard, V. Artero, P. Strasser, A. Kucernak, *Johnson Matthey Tech* **2018**, *62*, 231-255.

[6]   J. Herranz, F. Jaouen, M. Lefevre, U. I. Kramm, E. Proietti, J. P. Dodelet, P. Bogdanoff, S. Fiechter, I. Abs-Wurmbach, P. Bertrand, T. M. Arruda, S. Mukerjee, *J. Phys. Chem. C* **2011**, *115*.

[7]   A. Janßen, I. Martinaiou, S. Wagner, N. Weidler, A. Shahraei, U. I. Kramm, *Hyperfine Interact.* **2018**, *239*.

[8]   J. Tian, A. Morozan, M. T. Sougrati, M. Lefevre, R. Chenitz, J. P. Dodelet, D. Jones, F. Jaouen, *Angew. Chem. Int. Ed. Engl.* **2013**, *52*, 6867-6870.

[9]   H. Zhang, S. Hwang, M. Wang, Z. Feng, S. Karakalos, L. Luo, Z. Qiao, X. Xie, C. Wang, D. Su, Y. Shao, G. Wu, *J. Am. Chem. Soc.* **2017**, *139*, 14143-14149.

[10]   A. Serov, K. Artyushkova, P. Atanassov, *Adv. Ener. Mater.* **2014**, *4*, 1-7.

[11]   Q. Jia, N. Ramaswamy, H. Hafiz, U. Tylus, K. Strickland, G. Wu, B. Barbiellini, A. Bansil, E. F. Holby, P. Zelenay, *ACS Nano* **2015**, *9*, 12496-12505.

[12]   H. M. Barkholtz, D.-J. Liu, *Materials Horizons* **2017**, *4*, 20-37.

[13]   M. Lefèvre, J.-P. Dodelet, *Electrochim. Acta* **2008**, *53*, 8269-8276.

[14]   A. D. Pauric, A. W. Pedersen, T. Andrusiak, E. B. Easton, *J. Electrochem. Soc.* **2010**, *157*, B370-B375.

[15]   A. D. Pauric, B. J. MacLean, E. B. Easton, *J. Electrochem. Soc.* **2011**, *158*, B331-B336.

[16]   H. Schulenburg, S. Stankov, V. Schünemann, J. Radnik, I. Dorbandt, S. Fiechter, P. Bogdanoff, H. Tributsch, *J. Phys. Chem. B* **2003**, *107*, 9034-9041.

[17]   M. Rauf, Y.-D. Zhao, Y.-C. Wang, Y.-P. Zheng, C. Chen, X.-D. Yang, Z.-Y. Zhou, S.-G. Sun, *Electrochem. Commun.* **2016**, *73*, 71-74.

[18]   X. Li, G. Liu, B. N. Popov, *J. Power Sources* **2010**, *195*, 6373-6378.

[19]   H. Tan, Y. Li, X. Jiang, J. Tang, Z. Wang, H. Qian, P. Mei, V. Malgras, Y. Bando, Y. Yamauchi, *Nano. Ener.* **2017**, *36*, 286-294.

[20]   F. Jaouen, S. Marcotte, J. P. Dodelet, G. Lindbergh, *J Phys. Chem. B* **2003**, *107*, 1376-1386.

[21]   D. Banham, S. Ye, K. Pei, J.-i. Ozaki, T. Kishimoto, Y. Imashiro, *J. Power Sources* **2015**, *285*, 334-348.

[22]   F. Jaouen, F. Charreteur, J. Dodelet, *J. Electrochem. Soc.* **2006**, *153*, A689-A698.

[23]   A. H. M. Videla, L. Zhang, J. Kim, J. Zeng, C. Francia, J. Zhang, S. Specchia, *J. Appl. Electrochem.* **2013**, *43*, 159-169.

[24]   L. Osmieri, R. Escudero-Cid, M. Armandi, A. H. A. Monteverde Videla, J. L. García Fierro, P. Ocón, S. Specchia, *Appl. Catal. B. Eniv* **2017**, *205*, 637-653.

[25]   F. Charreteur, F. Jaouen, S. Ruggeri, J.-P. Dodelet, *Electrochim. Acta* **2008**, *53*, 2925-2938.

[26]   H. M. Fruehwald, I. I. Ebralidze, O. V. Zenkina, E. B. Easton, *ChemElectroChem* **2019**, *6*, 1350-1358.

[27]   G. Pognon, C. Cougnon, D. Mayilukila, D. Belanger, *ACS Appl. Mater. Interfaces* **2012**, *4*, 3788-3796.

[28]   G. Pognon, T. Brousse, D. Bélanger, *Carbon* **2011**, *49*, 1340-1348.

[29]   R. D. L. Smith, P. G. Pickup, *Electrochim. Acta* **2009**, *54*, 2305-2311.

[30]   M. Lefevre, E. Proietti, F. Jaouen, J. P. Dodelet, *Science* **2009**, *324*, 71-74.

[31]   F. J. Rawson, C. L. Yeung, S. K. Jackson, P. M. Mendes, *Nano Lett* **2013**, *13*, 1-8.

[32]   C. D. Wagner, L. E. Davis, M. V. Zeller, J. A. Taylor, R. H. Raymond, L. H. Gale, *Surf. Interface Anal.* **1981**, *3*, 211-225.

[33]   T.-C. Lin, G. Seshadri, J. A. Kelber, *Appl. Surf. Sci.* **1997**, *119*, 83-92.

[34]   U. Paulus, T. Schmidt, H. Gasteiger, R. Behm, *Journal of Electroanalytical Chemistry* **2001**, *495*, 134-145.

[35]   J.-Y. Choi, D. Higgins, Z. Chen, *J. Electrochem. Soc.* **2011**, *159*, B86-B89.

[36]   A. Zitolo, V. Goellner, V. Armel, M. T. Sougrati, T. Mineva, L. Stievano, E. Fonda, F. Jaouen, *Nat. Mater* **2015**, *14*, 937-942.

[37]   L. Wang, L. Zhang, J. Zhang, *Electrochim. Acta* **2011**, *56*, 5488-5492.

[38]   A. K. Farquhar, M. Supur, S. R. Smith, C. Dyck, R. L. McCreery, *Adv. Ener. Mater.* **2018**, *8*, 1-9.

[39]   B. D. Ossonon, D. Bélanger, *Carbon* **2017**, *111*, 83-93.

[40]   M. Sun, D. Davenport, H. Liu, J. Qu, M. Elimelech, J. Li, *J. Mat. Chem. A* **2018**, *6*, 2527-2539.

[41]   B. Liu, W. Dai, Z. Liang, J. Ye, L. Ouyang, *Int. J. Hydrog. Energy* **2017**, *42*, 5908-5915.

[42]   X. Zhang, Y. B. Mollamahale, D. Lyu, L. Liang, F. Yu, M. Qing, Y. Du, X. Zhang, Z. Q. Tian, P. K. Shen, *J. Catal.* **2019**, *372*, 245-257.

[43]   S. Y. Lee, J. Lyu, S. Kang, S. J. Lu, C. W. Bielawski, *J. Phys. Chem. C* **2018**, *122*, 11855-11861.

[44]   J. C. Lascovich, R. Giorgi, S. Scaglione, *Appl. Surf. Sci.* **1991**, *47*, 17-21.

[45]   A. Mezzi, S. Kaciulis, *Surf. Interface Anal.* **2010**, *42*, 1082-1084.

[46]   N. O. Laschuk, Ebralidze, II, J. Poisson, J. G. Egan, S. Quaranta, J. T. S. Allan, H. Cusden, F. Gaspari, F. Y. Naumkin, E. B. Easton, O. V. Zenkina, *ACS Appl. Mater. Interfaces* **2018**, *10*, 35334-35343.

[47]   Y. Zhu, X. Chen, J. Liu, J. Zhang, D. Xu, W. Peng, Y. Li, G. Zhang, F. Zhang, X. Fan, *ChemSusChem* **2018**, *11*, 2402-2409.

[48]   L. Yang, Y. Bai, H. Zhang, J. Geng, Z. Shao, B. Yi, *RSC Adv.* **2017**, *7*, 22610-22618.

[49]   A. Alsudairi, J. Li, N. Ramaswamy, S. Mukerjee, K. M. Abraham, Q. Jia, *J. Phys. Chem. Lett* **2017**, *8*, 2881-2886.

[50]   L. Osmieri, R. K. Ahluwalia, X. Wang, H. T. Chung, X. Yin, A. J. Kropf, J. Park, D. A. Cullen, K. L. More, P. Zelenay, *Appl. Catal. B. Eniv* **2019**, *257*, 117929.

[51]   S. K. Singh, K. Takeyasu, J. Nakamura, *Adv. Mater.* **2019**, *31*, e1804297.

[52]   G. Liu, X. Li, P. Ganesan, B. N. Popov, *Appl. Catal. B. Eniv* **2009**, *93*, 156-165.

[53]   S. Bhowmik, B. N. Ghosh, K. Rissanen, *Org. Biomol. Chem* **2014**, *12*, 8836-8839.

[54]   N. O. Laschuk, I. I. Ebralidze, D. Spasyuk, O. V. Zenkina, *Eur. J. Inorg. Chem.* **2016**, *2016*, 3530-3535.

[55]   G. Zhang, Q. Wei, X. Yang, A. C. Tavares, S. Sun, *Appl. Catal. B. Eniv* **2017**, *206*, 115-126.

[56]   N. Ramaswamy, S. Mukerjee, *Adv. Phys. Chem.* **2012**, *2012*.

[57]   N. Ramaswamy, S. Mukerjee, *J. Phys. Chem. C* **2011**, *115*, 18015-18026.

[58]   P. Matter, L. Zhang, U. Ozkan, *J. Catal.* **2006**, *239*, 83-96.

[59]   S. Wang, M. Zhu, X. Bao, J. Wang, C. Chen, H. Li, Y. Wang, *ChemCatChem* **2015**, *7*, 2937-2944.

[60]   M. Bron, S. Fiechter, P. Bogdanoff, H. Tributsch, *Fuel Cells* **2002**, *2*, 137-143.

[61]   L. Osmieri, R. Escudero-Cid, A. H. A. Monteverde Videla, P. Ocón, S. Specchia, *Renew. Energy* **2018**, *115*, 226-237.

Chapter 4. Effect of Transition Metals on the Oxygen Reduction Reaction Activity at Metal-N₃/C Active Sites

4.0 Preface

Part of the work described in this chapter has been published as: Fruehwald, H. M.; Ebralidze, I. I.; Melino, P. D.; Zenkina, O. V.; Easton, E. B., Effect of Transition Metals on the Oxygen Reduction Reaction Activity at Metal-N₃/C Active Sites. *ChemElectroChem.* **2021,** *8*, 53-61. doi: 10.1002/celc.202000954 with permission from Wiley-VCH GmbH.

In this chapter, we explore the role of the transition metal center on the activity of the M- N_3/C site (where M= transition and post transition metals: Co, Mn, Ni and Sn) for the oxygen reduction reaction. We continued to use the diazonium coupling chemistry to attach only the most active forms of pyridinic nitrogen to Vulcan carbon (N_3/C site, Chapter 2). Using this developed synthetic approach we altered the metal center used to observe the effect the transition metal has on the activity of the materials. We found that utilization of Fe resulted in the materials with the highest activity, followed by Co, Mn, and Ni. Most of the metals (Fe, Co, Mn, and Ni) were forming coordination adducts with N_3 units on the support that are believed to be catalytically active sites. On the contrary, incorporation of Sn in the material resulted in the significant deposition of Sn oxide agglomerates on the carbon surface as observed by SEM and TEM. This correlated to the lowest activity of the Sn-based system. The utility of different metal catalysts discussed here as oxygen evolution catalysts are explored in Chapter 9.

4.0 Abstract

The roles of various transition and post-transition metals in model non-precious-metal catalysts for the oxygen reduction reaction (ORR) are reported after being prepared via a molecularly defined terpyridine unit covalently attached to a carbon black support. We previously reported the use of a terpyridine-modified iron-based catalyst that allowed for the controlled deposition of highly active nitrogen functionalities on the carbon support, which adopts a $Fe-N_3/C$ active site formation. In this work, we expand on this idea by altering the metal center in the predefined active sites $M-N_3/C$ and compare the ORR reactivity of the isostructural set of catalysts, where M=Fe, Co, Ni, Mn, and Sn. The results show that the iron-based material was the most active catalyst in acid, whereas the cobalt-based catalyst was most active in base. In addition, nickel- and manganese-based materials showed promising activity for the ORR in both acidic and basic media. We demonstrate that, with a suitable templating bis-chelating nitrogenous ligand, the $M-N_3/C$ active site geometry is adopted with a wide range of non-precious-metal centers on a Vulcan carbon surface, and the resulting catalysts are ORR active in a range of conditions, further confirming the tunability and versatility of the N_3 site. As expected, post-transition metals, such as tin, do not coordinate to the N_3 nitrogenous ligand under synthetic conditions and deposits tin oxide(s). This study confirms the generality of the phenomenon of $M-N_3C$ as an ORR catalytic site.

4.1 Introduction

Proton Exchange Membrane Fuel Cells (PEMFC) are a promising clean energy system for portable and stationary applications in humanities battle against climate change[1-2]. PEMFCs take chemical energy in the form of hydrogen, or alcohols, and directly converts it to electrical energy[3]. To perform the reactions at the catalyst layers, Platinum coated carbon (Pt/C) is typically utilized at the anode and the cathode that range from 0.15-1.4 mg cm^{-2}. Due to the sluggish kinetics at the cathode, where oxygen is reduced to water, higher loadings of Pt, a rare and expensive metal, are often required to drive the reaction[4-7]. Thus, this results in costly ($50 kW^{-1}) fuel cell system costs[8]. As a result, the widespread implementation of PEMFC technology is hindered[9]. To combat these issues, investigations into the use of non-precious metal catalysts (NPMCs) have been explored as alternatives to the costly Pt-based analogs, especially for stationary systems[10].

91

NPMCs are typically compromised of a carbon source, nitrogen and transition metal. The classical way to synthesize these materials is through a heat treatment procedure to form what is believed to be the active sites of these catalysts[11-12]. Upon heat treatment there is a structural rearrangement that likely occurs to produce an Fe-N_{2+2}/C configuration that is widely believed to be the active sites for the oxygen reduction reaction (ORR)[13-16]. Of importance for these NPMCs are the types of nitrogen's present in the active sites, as certain types of nitrogen are more beneficial for improved activity. While, the importance of nitrogen in the active sites is commonly accepted, there is still discussion surrounding the choice of transition metal to be used in the active site[4, 17].

The most common metal that is employed in these NPMCs is iron. Based on some early work by Zagal, a volcano plot assessing metal porphyrins (N_4 or N_{2+2} active centers) for their catalytic performance showed that Fe was considered to be the most active metal whereas Co, Mn, and Ni exhibited some lesser activity[18-19]. Many other literature reports show that Fe is currently the highest performing metal when used in NPMCs[20-22]. In any case, numerous studies were investigating the influence of individual atomically dispersed metal centers, like Co or Mn alone to substitute iron completely, or in combination with Fe[4, 10, 17, 23-24]. While it is generally believed that the inclusion of Fe is responsible for higher activity, other transition metals could be utilized to create higher performing materials[6]. On the other hand, finding suitable replacements for Fe become necessary due to durability issues and degradation of these catalysts from the Fenton reaction[25-26].

Previously, we have investigated the effect of using a molecular-based receptor to graft a nitrogenous terpyridine-based receptor to graft a nitrogenous terpyridine-based ligand to selectively imprint the most active pyridinic nitrogen groups on the surface[27]. While it has been reported in the literature that a N_3 site might be a defect to the most widely accepted active site, we deliberately formed these sites specifically on the surface to assess the activity of sites that differ from the N_{2+2} type sites[2, 28-30]. A surface modification approach was adapted to functionalize the surface with the nitrogen and then iron was added to create coordination motifs on the surface[27, 31]. Next, we investigated the role that carbon supports played on our novel catalyst design and found that the least porous support (Vulcan XC-72 carbon) yielded the highest activity[32]. In this work we altered the nature of the transition metal of the N_3 site to study metal influence in our novel N_3 site for

its effectiveness for the ORR. Since some recent computational studies reported improved activity towards the ORR for tin-based materials[33-34], we also explored the effect of adding post transition metal Sn to the N_3-carbon surfaces.

4.2 Experimental

4.2.1 Materials

Sodium nitrate, methanol, sulfuric acid, potassium hydroxide, acetone, isopropyl alcohol, $SnCl_2 \cdot 2H_2O$, $CoCl_2 \cdot 6H_2O$, $MnCl_2 \cdot 2H_2O$, $NiCl_2 \cdot 6H_2O$, Nafion® perfluorinated solution were purchased from Sigma Aldrich. Vulcan XC-72 carbon was donated by Cabot.

4.2.2 Synthesis of the Catalysts

Commercial Vulcan XC-72 carbon was modified with 4'-(4-aminophenyl)-2,2':6'2"-terpyridine (tpy) according to previously published procedures[27, 35-38]. In brief, a 10 mL 10 mM solution of tpy in methanol was reacted with 10 mL 1 M $NaNO_2$ for 3 minutes before adding the solution to ca. 700 mg of commercial Vulcan XC-72 carbon black. The mixture was stirred overnight. The resulting mixture was gravity filtered and washed with methanol, acetone, and deionized water three times before drying in an oven to produce the V-tpy catalyst. V-tpy-M coordination motifs were synthesized by reacting an excess, of either 10 mM $SnCl_2$, 10 mM $NiCl_2$, 10 mM $CoCl_2$, or 10 mM $MnCl_2$, with respect to the stoichiometry of the ligand, with the V-tpy for 48 hours at room temperature while stirring. Materials were vacuum filtered and dried in the oven overnight to produce the V-tpy/Sn, V-tpy-Ni, V-tpy-Co, or V-tpy-Mn catalysts. A portion of the catalysts were subjected to a heat-treatment procedure using a Barnstead International type F21100 tube furnace at 700 ºC using a heating rate of 10 ºC min^{-1} and flowing N_2 at a flow rate of 60 mL min^{-1}. These samples are denoted as V-tpy/Sn, V-tpy-Ni-700, V-tpy-Co-700 and V-tpy-Mn-700. The catalysts were compared to our previously published V-tpy, V-tpy-Fe, andV-tpy-Fe-700 materials that were synthesized under similar conditions.

4.2.3 Physical Characterization

Catalysts were characterized via thermogravimetric analysis (TGA) using a TA instruments Q600 SDT thermal analyzer. The catalysts were heated using a heating rate of 5 ºC min^{-1} from room temperature to 1000 ºC while under an air atmosphere flowing at 20 mL min^{-1}. Pore size analysis was performed using a Quantachrome NOVAe 1200 pore analyzer using N_2 as an adsorbate. Scanning electron microscopy (SEM) measurements

were obtained using a HITACHI FlexSEM 1000. The energy of the beam was 5 kV with a working distance of 5 mm and a spot size of 20. TEM measurements were performed at the Canadian Centre for Electron Microscopy (CCEM) using a Zeiss Libra 2200MC transmission electron microscope system operating at 200 keV with a spot size of 1 nm. ImageJ software was utilized to analyze the images. X-ray photoelectron spectroscopy (XPS) was performed on a Thermo Scientific K-alpha Angle-Resolve that is equipped with a monochromated Al Kα (1486.7 eV) x-ray source and 180º double focusing hemispherical analyzer with effective charge compensation. A Shirley fit algorithm was used for background subtraction and Powell peak-fitting algorithm was used for data analysis.

4.2.4   Electrochemical Characterization

Oxygen reduction reaction activity was studied using a rotating ring disk electrode (RRDE) in O_2 sparged 0.1 M H_2SO_4 and 0.1 M KOH electrolyte solutions. Catalyst inks were prepared by sonicating 10 mg catalyst, 200 µL isopropyl alcohol, and 100 µL Nafion®, (to achieve a 95%-to-5% catalyst to Nafion® ratio), for 15 minutes followed by stirring overnight prior to use. 6 µL of catalyst ink was deposited on a 0.196 cm^2 glassy carbon electrode (302 µg cm^{-2} catalyst loading) and was rotated and dried under heat to produce the catalyst layer. The electrode was placed in an electrochemical cell containing either 0.1 M H_2SO_4 or 0.1 M KOH electrolyte with mercury/mercury sulphate reference electrode and a graphite rod counter electrode. N_2 sparged electrolyte was used to collect cyclic voltammograms at 20 mV s^{-1} prior to the ORR measurements. RRDE at 10 mV s^{-1} in N_2 sparged electrode was performed for background subtraction. RRDE curves were recorded in the presence of oxygen at 10 mV s^{-1}. The ring was held at 1.23 V vs RHE and the calibrated collection efficiency was 0.25. Before measurement the ring was calibrated with a ferro/ferricyanide redox couple. Measurements were made on a Pine Instruments model AFPC2 and Pine WaveDriver 20 with corresponding Aftermath software. Prior to electrochemical tests, glassware was cleaned with aqua regia. Durability studies were performed on the catalysts in N_2 sparged 0.1 M H_2SO_4 for 10,000 cycles at 50 mV s^{-1}. After every 5,000 cycles RRDE was performed on the material at 900 rpm in O_2 saturated 0.1 M H_2SO_4 at 10 mV s^{-1}.

4.3 Results and Discussion

A series of ORR catalysts abbreviated V-tpy-M (M=Fe, Co, Mn, Ni, Sn) were prepared on Vulcan carbon surfaces by initially embedding of the tpy moiety using previously reported procedure (V-tpy)[27] and following reaction of the resulting V-tpy-M surfaces with the corresponding solution of the metal salt, Scheme 4.1 (see section 4.2 for details). All catalysts were thoroughly characterized by TGA, XPS, BET, DTG, SEM, TEM, and, their activity for the ORR was explored in both acidic and basic conditions.
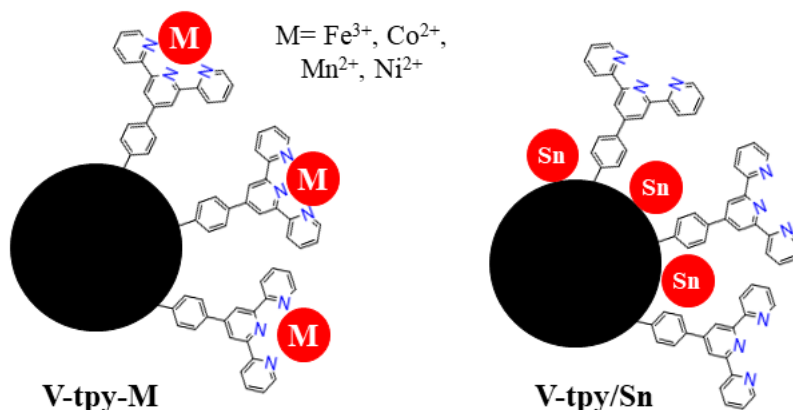
Scheme 4.1) Coordination of the transition metals and post transition metal to the V-tpy core.

4.3.1 Physical Characterization

Thermogravimetric analysis (TGA) was performed on the catalysts to estimate the metal loading and elucidated decomposition profiles of the catalysts (Figure 4.1). The various V-tpy-M catalysts were compared to the initial V-tpy surface. It is seen that the combustion temperature of the material decreases upon addition of each of the metals (Figure 4.1 inset), which was similarly seen from our previous works with Fe[27]. This was expected as the introduction of metals can act as a combustion catalyst under these conditions[27]. To further analyze the materials, the differential thermograms (DTG) were also recorded (Figure 4.1A). In each of the V-tpy-M catalysts there is a broad peak, or two peaks that appear in the spectra one at lower temperature ca. 500 ℃ and the other at higher temperatures ca. 600 ℃. The first peak is attributed to the combustion of the coordinated tpy ligand, while the second peak is attributed to the combustion of the carbon support itself[39]. The metal loading in each catalyst ranged from ca. 2-5% estimated by TGA using residual masses in Table 4.1. Observed metal loadings are very similar to the ca. 2%

reported by us for the V-tpy-Fe system, as well as consistent with other literature on related M-N-C catalysts[27, 40-45].
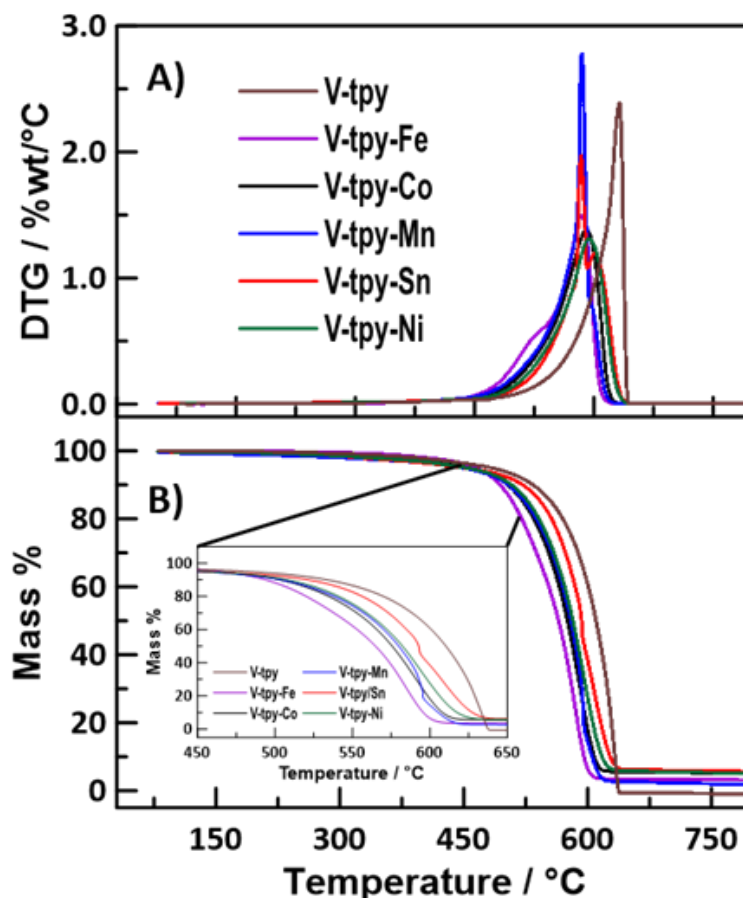
Figure 4.1) (A) Differential thermograms of the various V-tpy-M catalysts performed in an air atmosphere at a scan rate of 5 °C min^{-1} (B) Thermogavimetric analysis of the V-tpy-M catalysts performed in an air atmosphere at a scan rate of 5 °C min^{-1}.

Specific surface area and pore size distributions were determined from BET analysis for each catalyst and are presented in Figure S4.1 and Table 4.1. Upon functionalization of the tpy ligand to the carbon support, we had previously shown that the surface area decreases due to the tpy molecule blocking some of the pores[27, 39, 46]. This trend is observed for all of the V-tpy-M catalysts as well. The BET surface area decreases when the tpy and the metal are present on the carbon support. Upon heat-treatment of the material an increase in the surface area is observed, which is expected due to changes in the support caused by partial decomposition of the tpy molecule, as well as, the release of any physisorbed tpy molecules on the surface. This will allow for more access of the adsorbate into the pores of the carbon support[13, 32-33].

Table 4.1) Weight%, surface area, and XPS metal loadings for the V-tpy-M catalysts.

Material	TGA / Wt%	SSA$_{BET}$ / m^2 g^{-1}	XPS metal loading
V-tpy[27]	-	194	-
V-tpy-Fe[27]	2 %	206	-
V-tpy-Fe-700[27]	-	305	-
V-tpy-Co	4.7 %	127	-
V-tpy-Co-700	-	182	-
V-tpy-Mn	2.5 %	125	0.24 %
V-tpy-Mn-700	-	160	-
V-tpy-Ni	5.2 %	119	0.80 %
V-tpy-Ni-700	-	163	-
V-tpy/Sn	5.8 %	117	1.2 %
V-tpy/Sn-700	-	159	-

Scanning electron microscopy (SEM) was performed on all catalysts to determine the morphology of the modified carbon-based catalysts (Figure 4.2). All catalysts show morphology which is expected for a Vulcan-based carbon. Transmission electron microscopy (TEM) was also performed and correlated well with the SEM images. From the TEM there is little evidence of metal agglomerates on the surface for most of the V-tpy-M metal coordination motifs, which indicates that this modification approach yielded a monolayer of M-tpy on the carbon support for almost all the catalysts. However, for the V-tpy/Sn catalyst, TEM showed what appeared to be large agglomerates rich in Sn rather than coordinated to the tpy in the expected V-tpy-M coordination. From the EDS map (Figure 4.3) we see a large amount of Sn present in clusters on the surface which indicates that the Sn is not coordinating to the tpy and is instead forming agglomerates of tin oxides on the carbon surface. To further investigate this, XPS was performed on the catalysts.

97
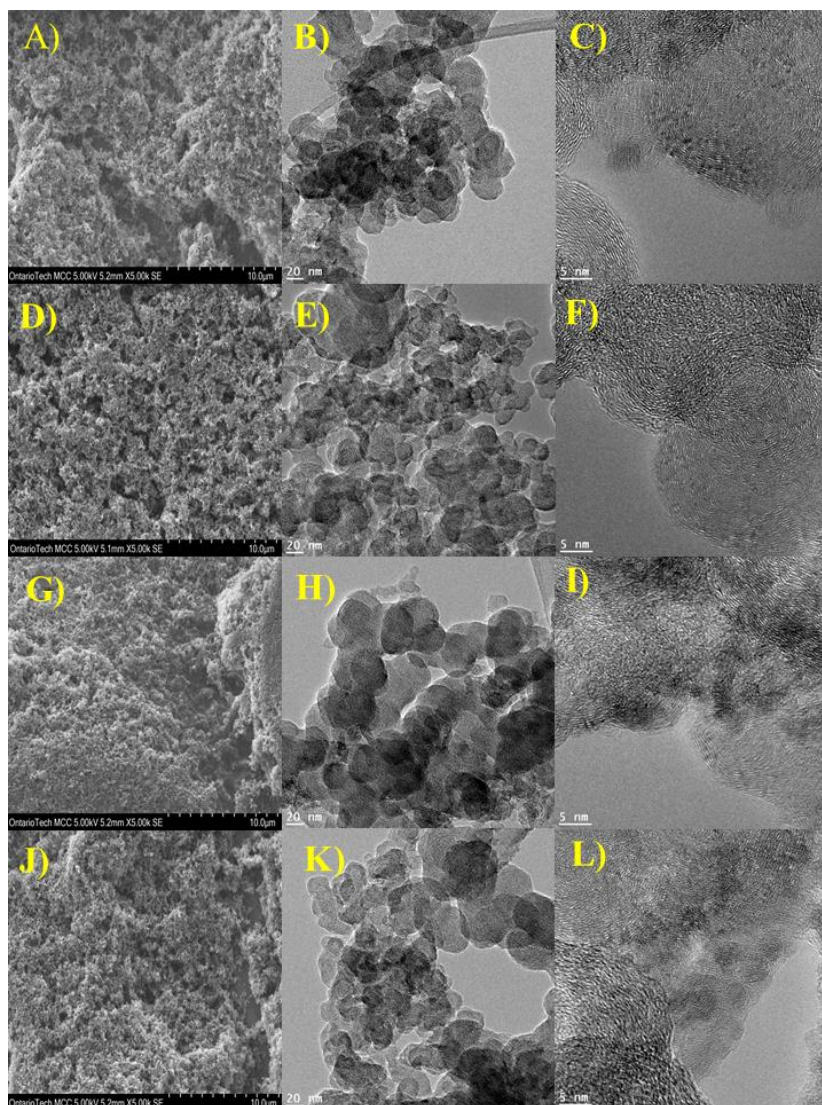
Figure 4.2) (A) SEM image of the V-tpy-Co catalyst, (B-C) TEM images of the V-tpy-Co catalyst at different magnifications (D) SEM image of the V-tpy-Mn catalyst. (E-F) TEM images of the V-tpy-Mn catalyst at different magnifications. (G) SEM image of the V-tpy/Sn catalyst. (H-I) TEM images of the V-tpy/Sn catalyst at different magnifications. (J) SEM image of the V-tpy-Ni catalyst (K-L) TEM images of the V-tpy-Ni catalyst at various magnifications.
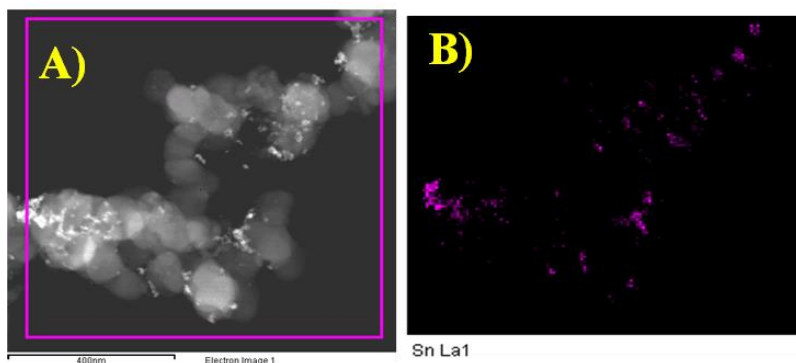
Figure 4.3) (A) STM image of the V-tpy/Sn catalyst and (B) EDA spectra of the Sn in the V-tpy/Sn catalyst.

XPS was performed on the catalysts to determine the surface composition (Figure S4.2-4.5). All catalysts were measured before and after the heat treatment protocol. The V-tpy-Co sample showed an N1s peak at 398.9 eV, which corresponds to the tpy pyridinic nitrogen[27, 47-48] (Figure S4.2B). However, there was only a trace amount of cobalt observed in the sample and the amount was unable to be accurately determined with XPS. Any signal observed from the Co $2p_{1/2}$ were hard to deconvolute from the background (Figure S4.2A). The presence of Co LMM Auger peaks that appear at 780 eV, Co $2p_{1/2}$ at 783 eV, and a shoulder at 785 eV that might be interpreted as the loss feature (typically for Co in any oxidation state) or as a satellite characteristic to Co(II) and Co(III), does not allow us to unambiguously claim the quantitative XPS loading for this element (Table 4.1)[49-50]. The heat-treated V-tpy-Co-700 data showed just Co traces on the surface that can be attributed to the partial decomposition of the tpy groups, which during decomposition carry out cobalt from the surface at those high temperatures[32].

V-tpy-Mn N1s spectrum (Figure S4.3B) displays a signal at 399.2 eV characteristic to the pyridinic nitrogen atoms in the metal-tpy mono-complexes[32, 47, 51]. Mn $2p_{1/2}$ and Mn $2p_{3/2}$ peaks were observed at 654.0 eV and 641.9 eV that is typical for Mn^{2+}[52]. The atmoic ratio of C:N:Mn is 95:0.79:0.24, this is close to the expected ratio of 3:1 of N:metal that would be expected for the mono-complex (1:1 metal-to-ligand stoichiometry). The V-tpy-Mn-700 sample after heat treatment again show negligible amounts of Mn due to partial decomposition of the M-tpy sites on the surface (Figure S4.3).

Similarly to the V-tpy-Co and V-tpy-Mn materials, V-tpy-Ni has the N 1s peak at 399.3 eV (Figure S4.4C) indicating the presence of nitrogen atoms on the surface as part

of tpy molecules. In the Ni 2p spectra (Figure S4.4A) we see peaks at 873.8 eV and 856.0 eV belonging to Ni^{2+}[53-54]. Deconvoluted peaks at 816.9 eV and 879.3 eV are satellite peaks of Ni in contact with oxygen[55-58]. The Ni_xO_y peaks could have originated from the initial starting salt, Ni can coordinate water molecules, or some Ni is free and interacting with oxygen moieties on the surface of the carbon. O1s spectrum (Figure S4.4B) shows a single peak with no shoulders, therefore the unambiguous deconvolution of a second peak is not possible, so it is more likely that the majority of Ni_xO_y peaks have come from the initial starting material. The N:Ni ratio is 0.8:0.08, suggesting that Ni are bonding to nitrogens from the tpy, and there is some excess of non-bounded tpy sites. After heat-treatment, the V-tpy-Ni-700 sample showed a significant decrease in the Ni 2p peaks as well (Figure S4.4A).

Finally, V-tpy/Sn XPS spectra were measured (Figure S4.5) and a clear peak in the N 1s spectra is observed at 398.5 eV, which indicates mostly free pyridinic nitrogens are present on the surface. From the Sn3d spectra, there are two peaks at 495 and 480 eV corresponding to Sn^{2+}[34, 59-60]. Interestingly, O1s spectra shows not only the presence of oxygen on the carbon surface but has a smaller peak (blue line) that is due to SnO on the surface. This data is in line with high-res TEM-EDS results supporting our idea that the Sn is not coordinating to the tpy centers, rather, it is in fact forming tin oxide species that agglomerate on the surface. Interestingly, after heat treatment the V-tpy/Sn-700 sample shows a drastic decrease in nitrogen, almost half of what it was before heat treatment. Further indicating that the metal acts to help retain nitrogen in the pyridinic state, without it the nitrogen functionalities do not survive well[31] (Figure S4.5). There is still a significant amount of tin in the sample, however, slightly less than the original V-tpy/Sn sample.

4.3.2 Electrochemical Characterization

Cyclic voltammetry (CV) in 0.1 M H_2SO_4 (Figure S4.6) was used to characterize and compare the catalysts to our previously published V-tpy and V-tpy-Fe materials. Upon addition of the tpy to the carbon support there is a small peak that forms at ca. 0.6 V in the CVs that we had previously attributed to some redox behavior corresponding to the tpy ligand on the surface[27, 32]. After addition of the metals, the capacitance of the materials increases, which can be attributed to the pseudocapactiance being imparted on the material

from the various metals. Upon heat treatment at 700 ℃ there is a slight depression of the peak observed, due to the partial decomposition of the active sites after heat treatments.

We assessed our materials for the ORR in O_2 saturated 0.1 M H_2SO_4 and the curves are presented in Figure 4.4. The catalysts were compared to V-tpy and V-tpy-Fe materials from our previous work[27]. The V-tpy material showed some activity for the ORR and the V-tpy-Fe had the highest onset potential (0.87 V). Upon addition of the other metals in the tpy site, we saw that the onset potentials after the addition of either Co, Mn, Ni, Sn are not as high as the V-tpy-Fe, but are quite similar. This is to be expected due to iron being the most highly performing non-precious metal for the ORR. The materials follow the trend of Fe>Co>Mn>Ni>Sn, which has been established in literature[18]. We were interested to test Sn for several reasons: first of all some literature stated promising activity of Sn alone, or in combination with Fe[33]; Second, we were interested to check the activity of post-transition metal and understand if there is a change of the mechanism/active centers when we move away from transition metals. Results show that the V-tpy/Sn system can be attributed to the different nature of the catalyst. We clearly see that addition of the tin to the N_3/C surface, instead of coordinating to nitrogenous chelating site to form Sn-N_3/C, tin forms significant amount of tin oxide agglomerates on the carbon surface. Computation studies of other groups indicated that this C-N-Sn active site could be favourable for the ORR[61-62], but for our experimental conditions N_3/C model system show no evidence of nitrogen-tin coordination, instead massive tin-oxide agglomeration is forming on the surface. In general, nitrogenous ligands have a much higher affinity to transition metals then to (post-transition metal). Experimentally it is quite difficult to produce the Sn-N coordination compounds that mimic the desired ORR active sites[63-64]. Thus, it will be challenging to produce a high density of Sn-N_3/C based active site. Even after heat-treatment, we observe the least activity from tin-based system compared to the other metals used in this study. Interestingly, our V-tpy-Co, V-tpy-Mn, V-tpy-Ni, and V-tpy/Sn catalysts reach a diffusion limited current, which we did not previously see with our V-tpy-Fe catalyst.
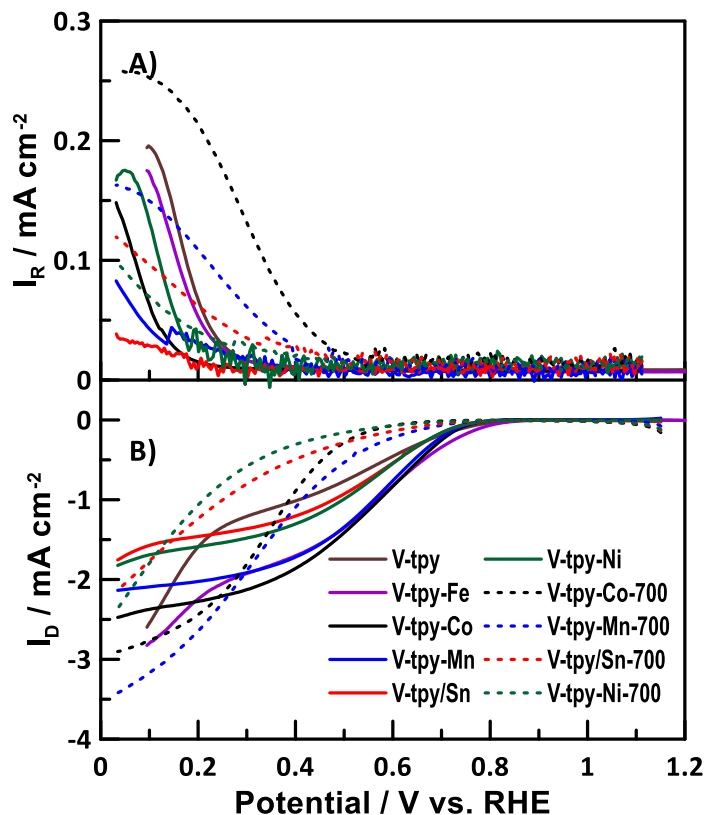
Figure 4.4) (A) Ring currents of the catalysts in O_2 saturated 0.1 M H_2SO_4 at 900 rpm at a scan rate of 10 mV s^{-1}. (B) Disk currents of the catalysts in O_2 saturated 0.1 M H_2SO_4 at 900 rpm at a scan rate of 10 mV s^{-1}.

After heat-treating all the materials at 700 °C, the activity of all the materials declined. This was expected from our synthetic approach of designing these catalysts. We have previously seen with the V-tpy-Fe catalyst that the activity declined after heat-treatment. We had attributed this to the formation of an undesirable N_{3+3} site forming on the surface. That site configuration had shown to almost completely inhibit the activity of the ORR as seen in further studies we had done[32]. This decline in activity upon heat-treatment is also observed for the other metals studied in this work. With heat-treatment, the catalysts have reduced onset potential and no longer reach diffusion-limited currents. Rather, it remains in a kinetically controlled region.

Using Koutecky-Levich analysis (Figure S4.7) we were able to determine electron transfer mechanisms and kinetic currents for all the catalysts (Table 4.2). Impressively, the number of electrons transferred for the V-tpy-Co and V-tpy-Mn was quite high for non-heat treated samples, since 4 electrons were transferred. This indicates that these materials are directly reducing O_2 into water. Both V-tpy-Co and V-tpy-Mn materials demonstrate

102

high kinetic currents for the ORR that were similar to V-tpy-Fe sample or higher in the V-tpy-Co catalyst. The V-tpy/Sn and V-tpy-Ni showed lower number of transferred electrons 3.5 and 3.6, respectively. This indicates that tin and nickel based materials are likely either producing hydrogen peroxide first, then further reducing to water, or different sites within the system are producing both water and hydrogen peroxide simultaneously. The kinetic currents for these metals are quite low owing to the lower activity from using Sn and Ni to produce active sites. After heat-treatment, the activity of the materials declined which is made evident by the decrease in the electron transfer numbers and the kinetic currents. For our two highest activity materials in this study, V-tpy-Co and V-tpy-Mn, the number of electrons transferred declined from 4 to 3 electron transfer processes. This indicates that upon heat-treatment more H_2O_2 is being produced which can be linked to the unfavourable structural rearrangements that occur during the heat treatment protocol. For the V-tpy-Ni-700 and V-tpy/Sn-700, significant reduction in activity occurs as the electron transfer process moves towards 2-electron process, indicating that H_2O_2 is the main product of the reaction for those catalysts.

Table 4.2) Onset potentials and Koutecky-Levich analysis of the catalysts in 0.1M H_2SO_4

Catalyst	Onset Potential at 0.1 mA cm^{-2} (V)	Half-Wave Potential (V)	i_k (mA cm^{-2})	Number of electrons transferred	
				KL (0.3 V vs RHE)	Peroxide
V-tpy-Co	0.78 ± 0.02	0.57	4.07 ± 0.36	4.06	3.5
V-tpy-Co-700	0.57 ± 0.03	-	4.13 ± 1.11	3.01	3.1
V-tpy-Mn	0.77 ± 0.01	0.57	3.26 ± 1.01	4.14	3.8
V-tpy-Mn-700	0.66 ± 0.03	-	4.81 ± 1.11	3.02	3.3
V-tpy-Ni	0.77 ± 0.03	0.57	2.35 ± 0.02	3.61	2.5
V-tpy-Ni-700	0.55 ± 0.05	-	0.80 ± 0.33	2.06	2.7
V-tpy/Sn	0.77 ± 0.01	0.56	2.06 ± 1.10	3.58	2.9
V-tpy/Sn-700	0.63 ± 0.04	-	1.19 ± 0.91	2.42	3.5
V-tpy[27]	0.85 ± 0.02	-	0.67 ± 0.03	3.80	3.7
V-tpy-Fe[27]	0.87 ± 0.04	-	3.34 ± 1.18	4.0	3.8

Rotating-ring disk (RRDE) measurements were performed on the catalysts to determine the amounts of peroxide produced, and a more accurate determination of the number of electrons transferred for the ORR from the catalysts (Figure 4.5)[65]. The number of electrons transferred (n) and the amount of hydrogen peroxide produced (%H_2O_2) were

calculated using the equations below, where I_D and I_R are the disk and ring currents, respectively, and N is the calibrated collection efficiency (Eq 4.1 and 4.2)[22]:

$$n = \frac{4I_D}{\left(I_R + \left(\frac{I_R}{N}\right)\right)} \qquad 4.1$$

$$\%H_2O_2 = \frac{200\left(\frac{I_R}{N}\right)}{\left(I_D + \left(\frac{I_R}{N}\right)\right)} \qquad 4.2$$

The number of electrons calculated for the catalysts showed that V-tpy-Co, and V-tpy-Mn are mainly undergoing 4-electron transfer processes to produce primarily water. For the ORR a 4-electron transfer process is ideal as it by-passes the 2-electron H_2O_2 intermediate which is a poison for NPMCs[2, 66]. The V-tpy-Ni and V-tpy/Sn catalysts show the lowest number of electrons transferred ca. 2.5 and 2.9, respectively at 0.3 V vs RHE. Most of the materials after the heat-treatment process have a lower number of electrons transferred. This could be due to the formation of undesirable active sites, or the loss of some active sites. Similar trends are seen in the production of hydrogen peroxide in the materials, where V-tpy-Ni produced the most H_2O_2 (ca. 75 %) followed by V-tpy/Sn (ca. 55%). Interestingly, there seemed to be less hydrogen peroxide produced for these catalysts after heat-treatment. This can be explained in the slight increase in the number of electrons transferred observed for the V-tpy/Sn and V-tpy-Ni catalysts after heat-treatment. For the rest of the materials after heat-treatment there is an increase in the amount of H_2O_2 produced. The best performing catalysts studied are the V-tpy-Co and V-tpy-Mn. However, the V-tpy-Co sample while having a low onset potential and relatively high number of electrons transferred, ca. 3.5, it is producing higher amounts of H_2O_2.
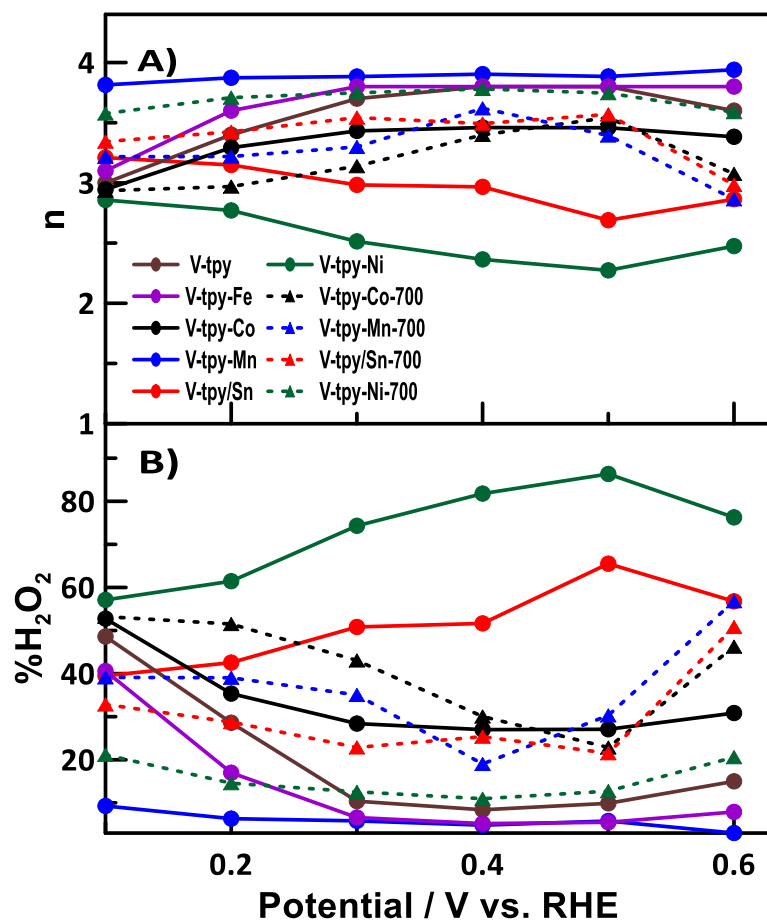
Figure 4.5) (A) Number of electrons transferred of the catalysts studied in O_2 saturated 0.1 M H_2SO_4 at 900 rpm at a scan rate of 10 mV s^{-1} (B) H_2O_2 production of the catalysts studied in O_2 saturated 0.1 M H_2SO_4 at 900 rpm at a scan rate of 10 mV s^{-1}.

Finally, we subjected the V-tpy-Co catalyst to a stability protocol suggested by the DOE for NPMCs to determine the durability of the active site. We performed 10,000 CV cycles and then assessed the ORR activity of the catalyst at 900 rpm in the fresh state, then after 1000, 5000, and 10,000 cycles (Figure S4.10-4.11). While the structural motif in this catalyst is unique, it is not immune to the degradation concerns observed for many of the NPMCs in literature. The loss of activity can be due to several issues such as the leaching of the transition metal in acidic media, protonation of the nitrogen groups, or prolonged H_2O_2 attack on the active sites during the ORR testing[10, 26, 67-71].

We also performed the ORR in 0.1 M KOH (Figure 4.6). The different metal catalysts were compared to the V-tpy-Fe and the results demonstrate that the onset potentials of the V-tpy-Co and the V-tpy-Mn showed the highest catalytic activity (Table 4.3). Notably, the onset potentials were even slightly lower than that of V-tpy-Fe. In the

LSV curves there are two apparent waves that appear for all the non-heat-treated metal catalysts. This indicates that the ORR mechanism is occurring either through two different catalytic sites or going through 2 different mechanistic pathways. After the heat-treatment process two waves in the disk current merge into one, while the onset potential of the V-tpy-Co-700 and the V-tpy-Mn-700 significantly increased compared to their non-heat-treated analogs. This may indicate merging two active sites into one as a result of heat-treatment.
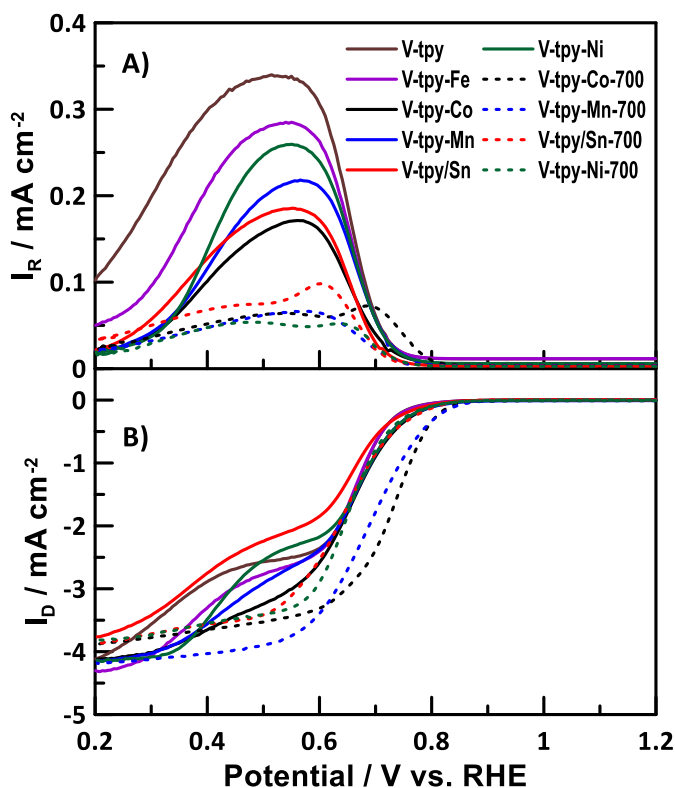
Figure 4.6) (A) Ring currents of the catalysts in O_2 saturated 0.1 M KOH at 900 rpm at a scan rate of 10 mV s^{-1} (B) Disk currents of the catalysts in O_2 saturated 0.1 M KOH at 900 rpm at a scan rate of 10 mV s^{-1}.

KL analysis was performed for all materials in 0.1 M KOH (Figure S4.9, Table 4.3). The V-tpy-Co and V-tpy-Mn materials had the highest number of electrons (4) transferred, which indicates that these catalysts are going through the favourable reaction pathway to reduce O_2 directly to water. Notably, V-tpy-Ni also transferred a high number of electrons (n) in basic media as well. We believe that the mechanism for direct conversion of O_2 to H_2O is more favored in base with the different metals. Not surprisingly, the V-tpy/Sn was the least active and transferred the lowest number of electrons (3.5) which still refers to the production of high amounts of H_2O_2 through a 2 step reaction[70]. After heat

treatment, the number of transferred electrons drastically lowers (to ca. 3) for most of the catalysts.

Table 4.3) Onset potentials and Koutecky-Levich analysis of all the catalysts in 0.1 M KOH.

Catalyst	Onset Potential at 0.1 mA cm^{-2} (V)	Half-Wave Potential (V)	i_k (mA cm^{-2})	Number of electrons transferred	
				KL (0.3 V vs RHE)	Peroxide
V-tpy-Co	0.80 ± 0.03	0.66	22.73 ± 4.10	3.9	3.8
V-tpy-Co-700	0.83 ± 0.01	0.74	33.12 ± 7.41	3.6	3.8
V-tpy-Mn	0.80 ± 0.04	0.67	43.74 ± 2.17	3.7	3.8
V-tpy-Mn-700	0.83 ± 0.01	0.70	58.10 ± 18.40	3.7	3.8
V-tpy-Ni	0.79 ± 0.03	0.68	30.83 ± 6.68	4.0	3.8
V-tpy-Ni-700	0.79 ± 0.02	0.65	24.71 ± 4.09	3.7	3.8
V-tpy/Sn	0.78 ± 0.02	0.67	18.73 ± 1.13	3.5	3.7
V-tpy/Sn-700	0.86 ± 0.01	0.65	33.95 ± 13.73	3.5	3.8
V-tpy[27]	0.79 ± 0.03	0.66	20.25 ± 3.28	3.2	3.2
V-tpy-Fe[27]	0.79 ± 0.02	0.66	24.81 ± 0.28	4.2	3.6

The number of electrons transferred and the H_2O_2 production were determined with RRDE (Figure 4.7). For all the catalysts studied there appears to be a 2-step reaction occurring, one where H_2O_2 is produced first and then converted to water[72]. This is seen in the ring currents (Figure 4.6A) where there is a sharp increase in the ring currents, then it starts to decrease. From the %H_2O_2 in Figure 4.7B this correlates well to high production of H_2O_2 at beginning of the reaction and as the reaction proceeds the amount decreases significantly. This is also evident from the lowering of the number of electrons transferred in the reaction, where at 0.3 V vs RHE the number of electrons is high for all the catalysts ca. 3.8.
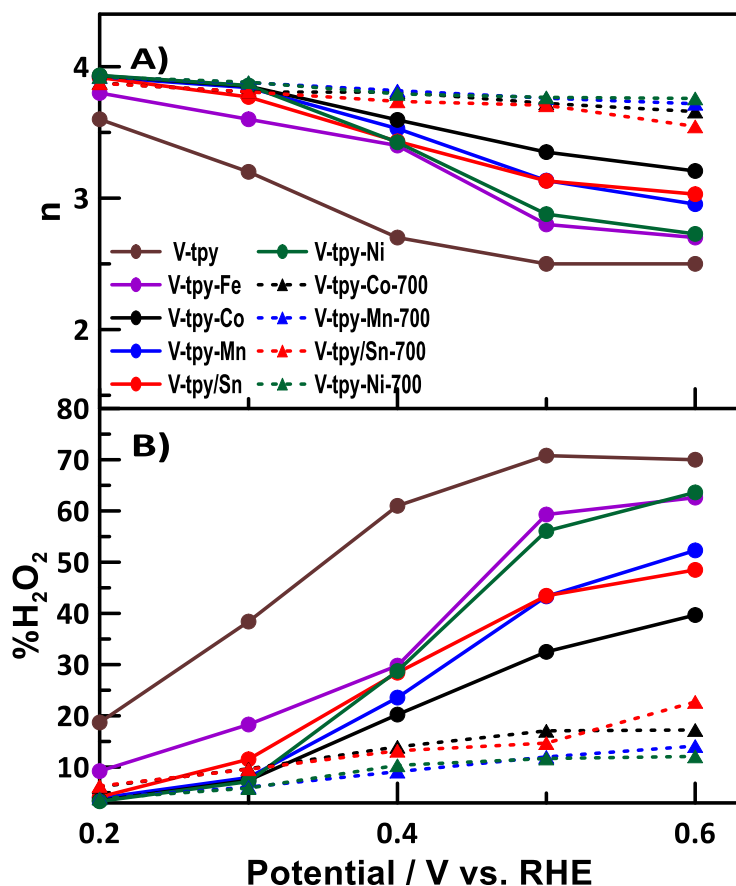
Figure 4.7) (A) Number of electrons transferred of the catalysts studied in O_2 saturated 0.1 M KOH at 900 rpm at a scan rate of 10 mV s^{-1} (B) H_2O_2 production of the catalysts studied in O_2 saturated 0.1 M KOH at 900 rpm at a scan rate of 10 mV s^{-1}.

Overall, the ORR results for all metal systems under investigation are very promising for low temperature NPMC design, showing that our surface modification approach can be used to prepare active catalysts using a wide range of abundant non-precious metals. Combining different ratios of the best performing metals with our novel N_3/C sites could result in catalyst material with enhanced activity due to synergistic effects of the different transition metals and post-transition metals in the catalyst design.

4.4 Conclusion

This work demonstrates the generality of our methodology to create molecularly defined catalysts using a terpyridine-based (tpy) templating unit. We report here on the preparation of a series of active non-precious metal catalysts by selective coordination of the corresponding transition metal center to well-defined nitrogenous chelating site covalently embedded into the carbon surface. By changing the nature of the transition metal

center we were able to alter the oxygen reduction reaction activity and tune the operation conditions (acid vs. base) of the material.

We have shown that upon introduction of Co, Mn, Ni, or Sn the activity remains relatively high for the ORR. As expected, the V-tpy-Co had the highest performance for the ORR and had a high onset potential while transferring mainly 4-electrons. After heat-treatment, the activity of the materials declined in acidic media, due to the unfavorable coordination motifs that could form on the surface under these conditions. Interestingly, introduction of the Sn to the V-tpy system showed no evidence of direct coordination of tin to nitrogenous site, instead massive agglomeration of Sn oxide species were present on the surface. However, the V-tpy/Sn system still showed some catalytic activity that confirm an idea that ORR could be supported by different active sites through wide variety of mechanistic pathways and more work is needed to elucidate exact mechanism of ORR with tin-based system. All catalysts performed well in alkaline solution.

Results of this study show wide range non-precious metals show beneficial activity for ORR when coordinated with distinct N_3/C geometry. This knowledge could be used in future generations of NPMCs.

4.5 Supporting Information
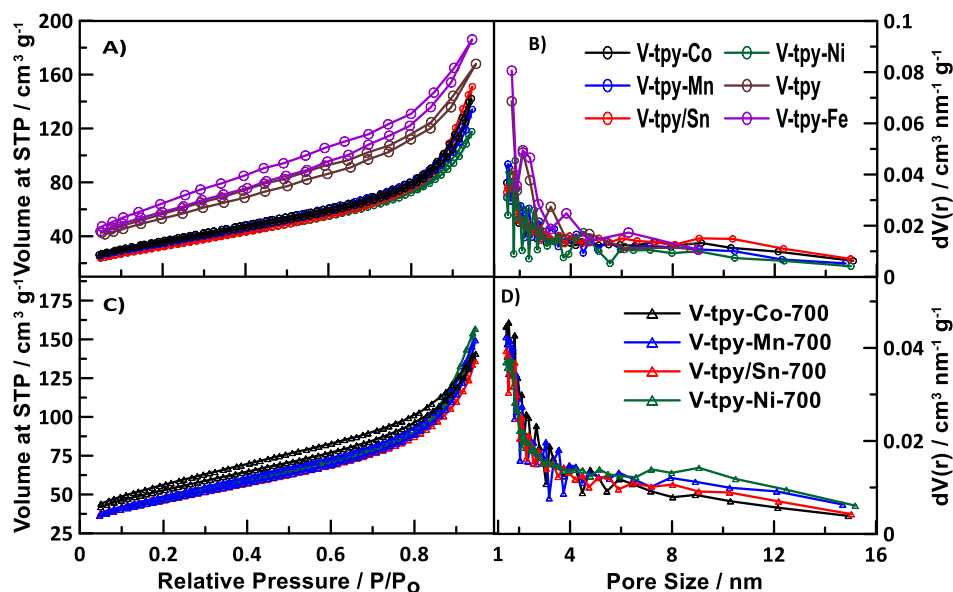
Supporting Information Figure S4.1) (A) Adsorption and desorption isotherms of the V-tpy-M catalysts using N_2 as the adsorbate (B) Pore size distribution of the V-tpy-M catalysts using N_2 as the adsorbate (C) Adsorption and desorption isotherms of the V-tpy-M-700 catalysts using N_2 as the adsorbate (D) Pore size distributions of the V-tpy-M-700 catalysts using N_2 as the adsorbate.
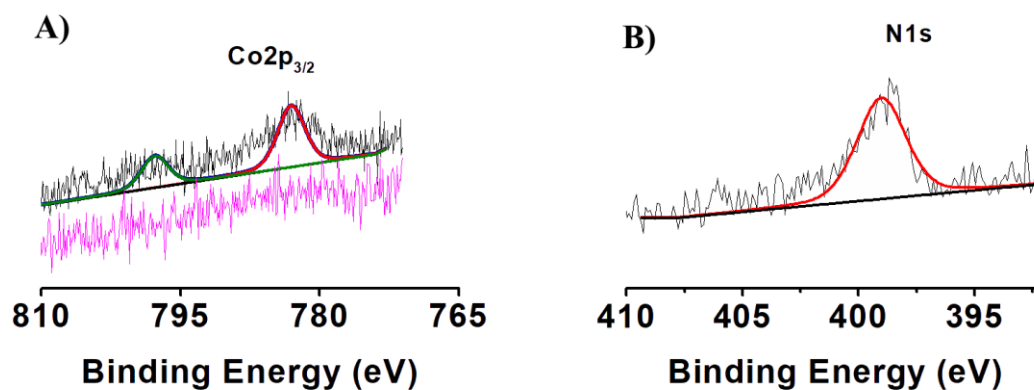
Supporting Information Figure S4.2) Representative XPS spectra of the V-tpy-Co: (A) experimental results of Co 2p area of as synthesized catalyst (black line), simultaneous 2p3/2 and 2p1/2 deconvolution (red and olive lines), and Co 2p area after heat treatment at 700°C (magenta). (B) N1s area.
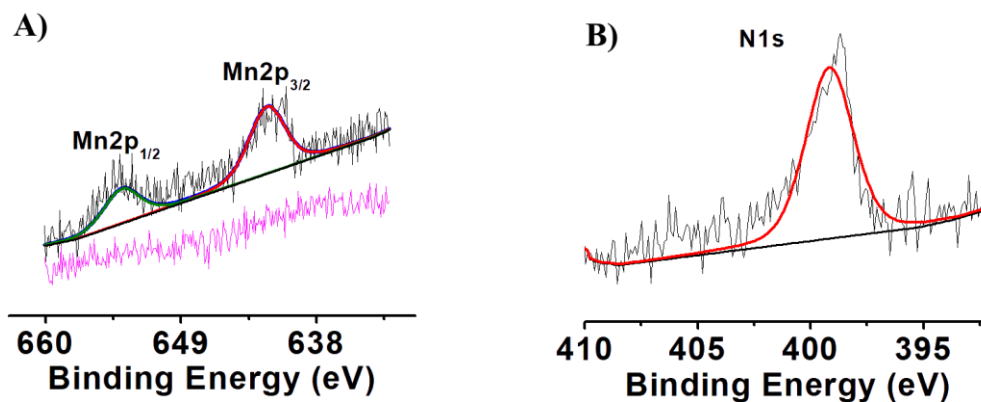
Supporting Information Figure S4.3) Representative XPS spectra of the V-tpy-Mn: (A) experimental results of Mn 2p area of as synthesized catalyst (black line), simultaneous 2p3/2 and 2p1/2 deconvolution (red and olive lines), and Mn 2p area after heat treatment at 700 °C (magenta). (B) N1s area.
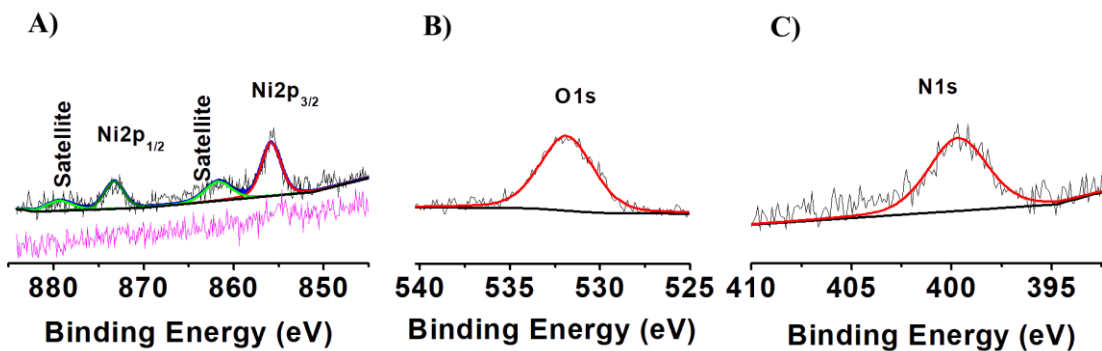
Supporting Information Figure S4.4) Representative XPS spectra of the V-tpy-Ni: (A) experimental results of Ni 2p area of as synthesized catalyst (black line), peak deconvolution allows resolving 2p3/2 and 2p1/2 peaks (red and olive lines), and satellite peaks (green lines). Ni 2p area after heat treatment at 700 °C are shown in magenta; (B) O1s area; (C) N1s area.
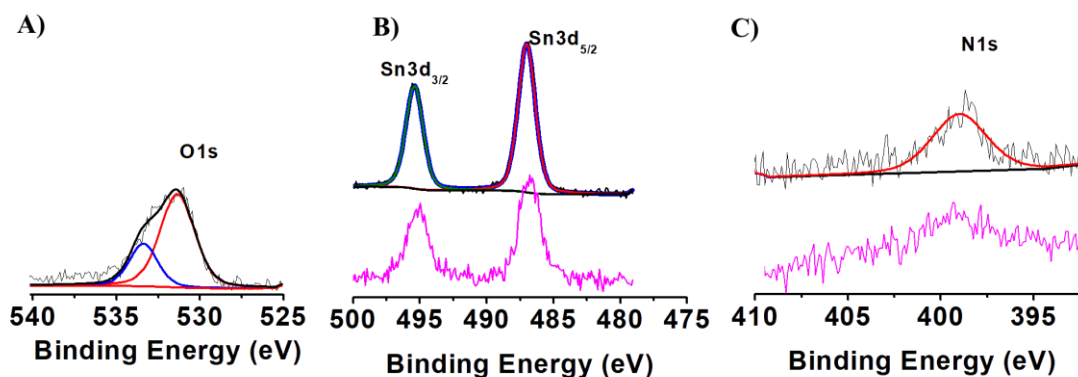
Supporting Information Figure S4.5) Representative XPS spectra of the V-tpy-Sn: (A) experimental results of O1s area of as synthesized catalyst (black line), peak deconvolution allows resolving two oxygen species (red and blue lines) of oxidized support and tin oxide, respectively. (B) Sn 3d area of as synthesized catalyst (black line), peak deconvolution allows resolving $3d_{5/2}$ and $3d_{3/2}$ peaks (red and olive lines). Sn 3d area after heat treatment (700°C) are shown in magenta. (C) experimental data for N1s area before heat treatment (black line), peak fitting (red line), and experimental data for N1s area after heat treatment (700 °C) are shown in magenta.
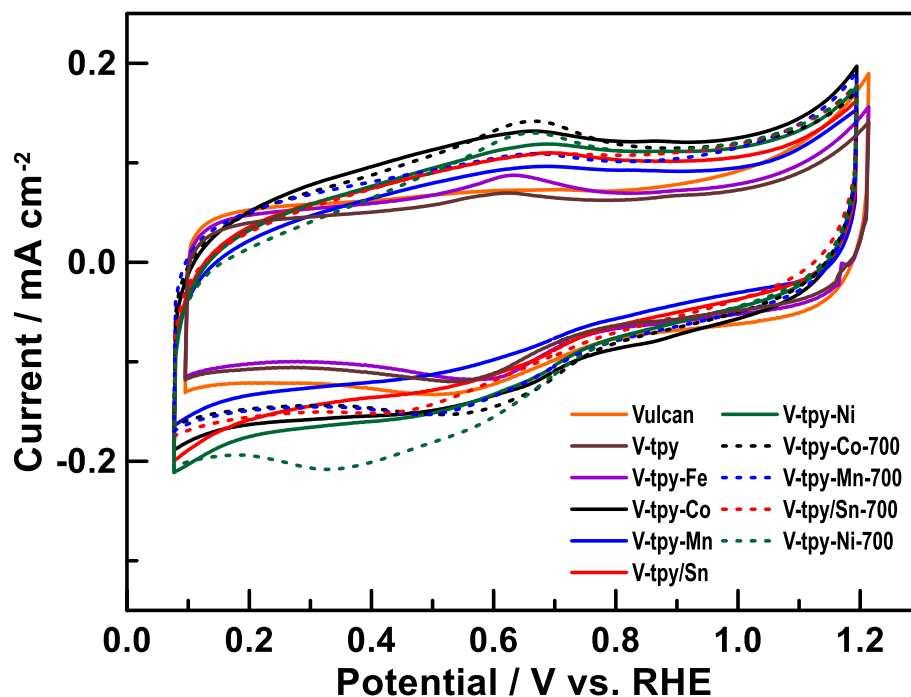
Supporting Information Figure S4.6) Cyclic voltammetry of the catalysts in N_2 purged 0.1 M H_2SO_4 at a scan rate of 20 mV s^{-1}.
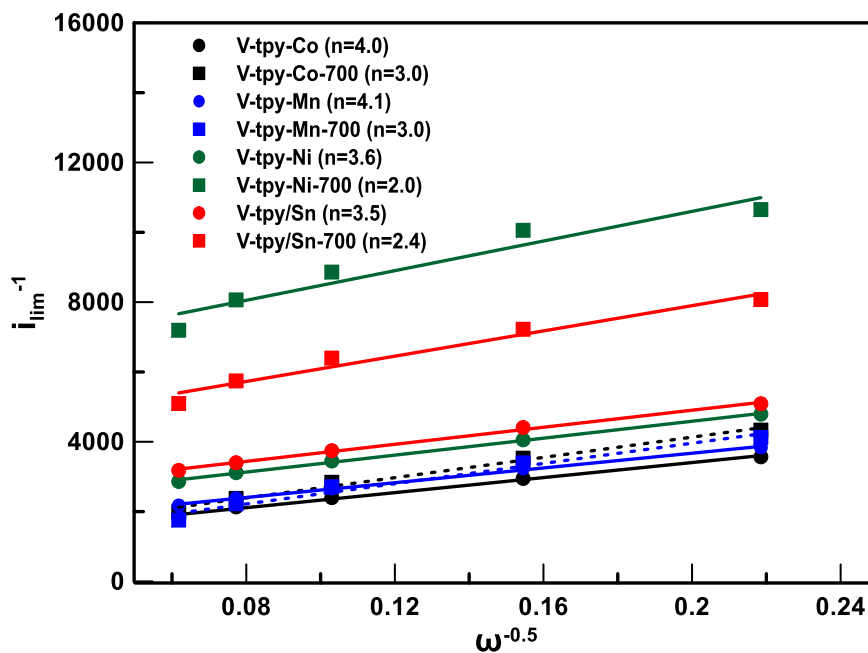
Supporting Information Figure S4.7) Koutecky-Levich analysis of the materials in 0.1 M H_2SO_4 at 0.3 V vs RHE.
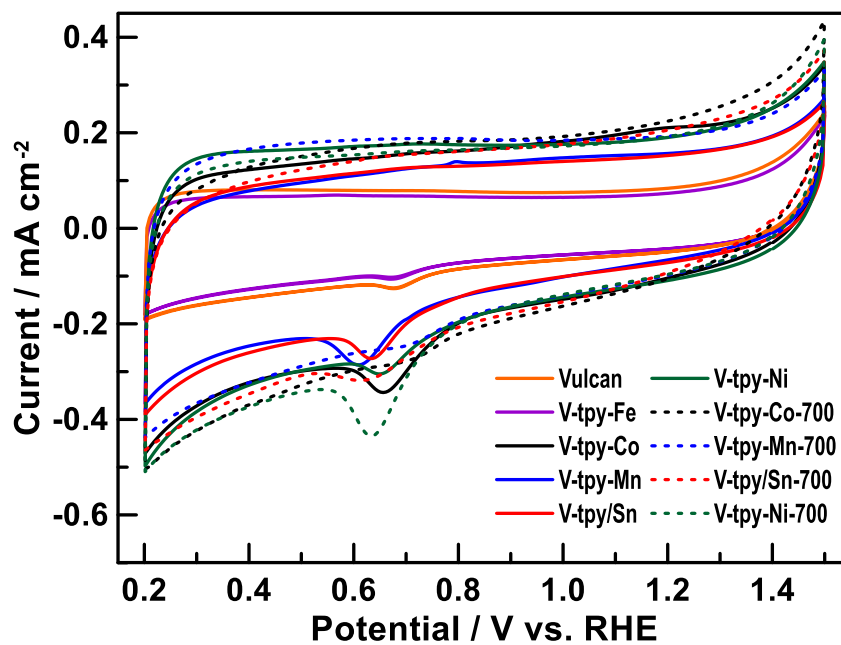
Supporting Information Figure S4.8) Cyclic Voltammetry at 20 mV s^{-1} in N$_2$ saturated 0.1 M KOH of the various catalysts.
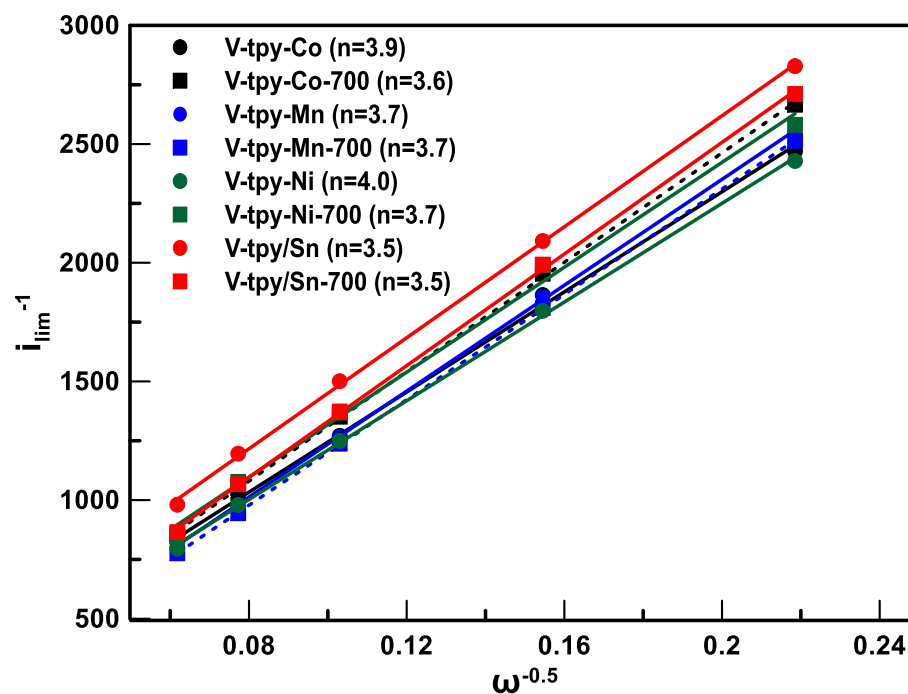
Supporting Information Figure S4.9) Koutecky-Levich analysis of the catalysts in 0.1 M KOH at 0.3 V vs RHE.
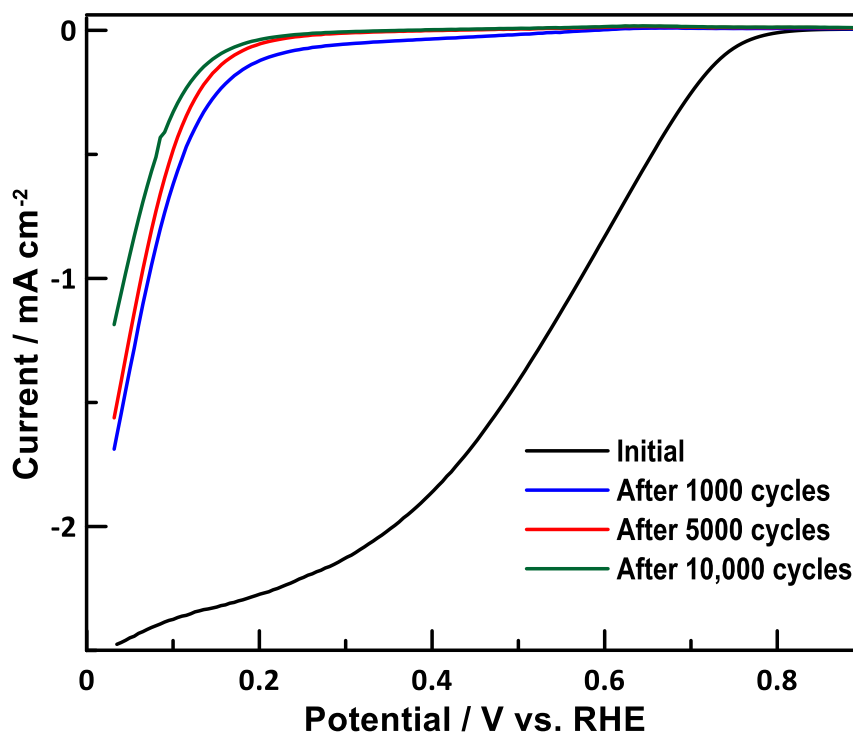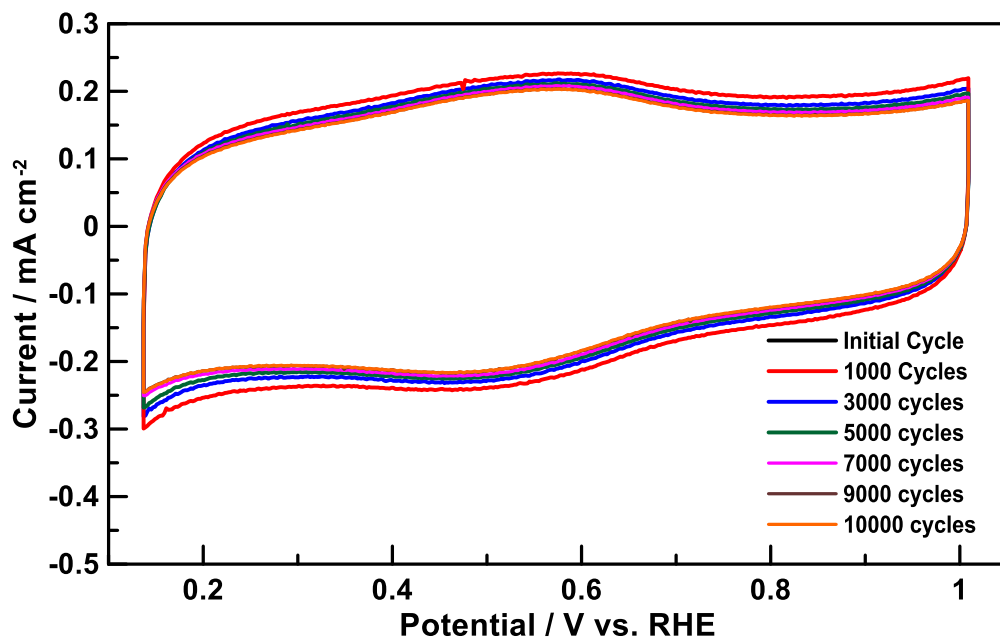
Supporting Information Figure S4.10) Cyclic voltammograms of the V-tpy-Co catalyst at 50 mV s^{-1} in N$_2$ saturated 0.1 M H$_2$SO$_4$.

Supporting Information Figure S4.11) ORR of the V-tpy-Co catalyst at 900 rpm in O$_2$ saturated 0.1 M H$_2$SO$_4$ at 10 mV s^{-1}.

4.6 Acknowledgements

4.7 References

[1]   C. Liu, F. Dong, Y. Wang, J. Guo, Y. Yang, Q. Gong, J. Qiao, *Int. J. Hydrog. Energy* **2019**.

[2]   C. W. B. Bezerra, L. Zhang, K. Lee, H. Liu, J. Zhang, Z. Shi, A. L. B. Marques, E. P. Marques, S. Wu, J. Zhang, *Electrochim. Acta* **2008**, *53*, 7703-7710.

[3]   Z. Chen, D. Higgins, A. Yu, L. Zhang, J. Zhang, *Energy Environ. Sci.* **2011**, *4*, 3167-3192.

[4]   A. Zitolo, N. Ranjbar-Sahraie, T. Mineva, J. Li, Q. Jia, S. Stamatin, G. F. Harrington, S. M. Lyth, P. Krtil, S. Mukerjee, E. Fonda, F. Jaouen, *Nat. Commun* **2017**, *8*, 957.

[5]   J. H. Zagal, M. T. Koper, *Angew. Chem. Int. Ed. Engl.* **2016**, *55*, 14510-14521.

[6]   Z. Zhang, D. Zhou, X. Bao, Z. Zhang, B. Huang, *Ionics* **2019**, *25*, 1953-1958.

[7]   L. Zhang, J. Zhang, D. P. Wilkinson, H. Wang, *J. Power Sources* **2006**, *156*, 171-182.

[8]   A. Wilson, G. Kleen, D. Papageorgopoulos, US Department of Energy, **2017**, p. 12.

[9]   L. Zhang, D. P. Wilkinson, Y. Liu, J. Zhang, *Electrochim. Acta* **2018**, *262*, 326-336.

[10]   X. Li, G. Liu, B. N. Popov, *J. Power Sources* **2010**, *195*, 6373-6378.

[11]   A. Serov, K. Artyushkova, P. Atanassov, *Adv. Ener. Mater.* **2014**, *4*, 1-7.

[12]   Q. Jia, N. Ramaswamy, H. Hafiz, U. Tylus, K. Strickland, G. Wu, B. Barbiellini, A. Bansil, E. F. Holby, P. Zelenay, *ACS Nano* **2015**, *9*, 12496-12505.

[13]   F. Charreteur, F. Jaouen, S. Ruggeri, J.-P. Dodelet, *Electrochim. Acta* **2008**, *53*, 2925-2938.

[14]   F. Jaouen, F. Charreteur, J. Dodelet, *J. Electrochem. Soc.* **2006**, *153*, A689-A698.

[15]   F. Jaouen, S. Marcotte, J. P. Dodelet, G. Lindbergh, *J. Phys. Chem. B.* **2003**, *107*, 1376-1386.

[16]   M. Lefevre, E. Proietti, F. Jaouen, J. P. Dodelet, *Science* **2009**, *324*, 71-74.

[17]   A. Sarapuu, L. Samolberg, K. Kreek, M. Koel, L. Matisen, K. Tammeveski, *J. Electroanal. Chem.* **2015**, *746*, 9-17.

[18]   J. H. Zagal, *Coord. Chem. Rev.* **1992**, *119*, 89-136.

[19]   C. Domínguez, F. J. Pérez-Alonso, M. Abdel Salam, J. L. Gómez de la Fuente, S. A. Al-Thabaiti, S. N. Basahel, M. A. Peña, J. L. G. Fierro, S. Rojas, *Int. J. Hydrog. Energy* **2014**, *39*, 5309-5318.

[20]   M. P. Karthikayini, T. Thirupathi, G. Wang, V. K. Ramani, R. K. Raman, *J. Electrochem. Soc.* **2016**, *163*, F539-F547.

[21]   J. Li, S. Ghoshal, W. Liang, M.-T. Sougrati, F. Jaouen, B. Halevi, S. McKinney, G. McCool, C. Ma, X. Yuan, Z.-F. Ma, S. Mukerjee, Q. Jia, *Energy Environ. Sci.* **2016**, *9*, 2418-2432.

[22]   M. Sun, D. Davenport, H. Liu, J. Qu, M. Elimelech, J. Li, *J. Mat. Chem. A* **2018**, *6*, 2527-2539.

[23]   J. Li, M. Chen, D. A. Cullen, S. Hwang, M. Wang, B. Li, K. Liu, S. Karakalos, M. Lucero, H. Zhang, *Nat. Catal.* **2018**, *1*, 935-945.

[24]   I. Roche, E. Chaînet, M. Chatenet, J. Vondrák, *J. Phys. Chem. C* **2007**, *111*, 1434-1443.

[25]   D. Banham, T. Kishimoto, T. Sato, Y. Kobayashi, K. Narizuka, J.-i. Ozaki, Y. Zhou, E. Marquez, K. Bai, S. Ye, *J. Power Sources* **2017**, *344*, 39-45.

[26]   D. Banham, S. Ye, K. Pei, J.-i. Ozaki, T. Kishimoto, Y. Imashiro, *J. Power Sources* **2015**, *285*, 334-348.

[27]   H. M. Fruehwald, I. I. Ebralidze, O. V. Zenkina, E. B. Easton, *ChemElectroChem* **2019**, *6*, 1350-1358.

[28]   C. E. Szakacs, M. Lefevre, U. I. Kramm, J. P. Dodelet, F. Vidal, *Phys. Chem. Chem. Phys.* **2014**, *16*, 13654-13661.

[29]   S. Wang, M. Zhu, X. Bao, J. Wang, C. Chen, H. Li, Y. Wang, *ChemCatChem* **2015**, *7*, 2937-2944.

116

[30]   K. Artyushkova, M. J. Workman, I. Matanovic, M. J. Dzara, C. Ngo, S. Pylypenko, A. Serov, P. Atanassov, *ACS Appl. Energy Mater.* **2017**, *1*, 68-77.

[31]   A. D. Pauric, B. J. MacLean, E. B. Easton, *J. Electrochem. Soc.* **2011**, *158*, B331-B336.

[32]   H. M. Fruehwald, I. I. Ebralidze, P. D. Melino, O. V. Zenkina, E. B. Easton, *J. Electrochem. Soc.* **2020**, *167*, 084520.

[33]   X. Zhang, J. Liu, Y. Qiao, A. Kong, R. Li, Y. Shan, *Electrochim. Acta* **2019**, *320*, 134593.

[34]   X. Zhao, T. Wen, J. Zhang, J. Ye, Z. Ma, H. Yuan, X. Ye, Y. Wang, *RSC Adv.* **2017**, *7*, 21678-21685.

[35]   F. J. Rawson, C. L. Yeung, S. K. Jackson, P. M. Mendes, *Nano Lett* **2013**, *13*, 1-8.

[36]   G. Pognon, C. Cougnon, D. Mayilukila, D. Belanger, *ACS Appl. Mater. Interfaces* **2012**, *4*, 3788-3796.

[37]   G. Pognon, T. Brousse, D. Bélanger, *Carbon* **2011**, *49*, 1340-1348.

[38]   B. D. Ossonon, D. Bélanger, *Carbon* **2017**, *111*, 83-93.

[39]   H. M. Fruehwald, O. V. Zenkina, E. B. Easton, *ECS Transactions* **2019**, *92*, 523-532.

[40]   J. Tian, A. Morozan, M. T. Sougrati, M. Lefevre, R. Chenitz, J. P. Dodelet, D. Jones, F. Jaouen, *Angew. Chem. Int. Ed. Engl.* **2013**, *52*, 6867-6870.

[41]   A. D. Pauric, A. W. Pedersen, T. Andrusiak, E. B. Easton, *J. Electrochem. Soc.* **2010**, *157*, B370-B375.

[42]   H. Schulenburg, S. Stankov, V. Schünemann, J. Radnik, I. Dorbandt, S. Fiechter, P. Bogdanoff, H. Tributsch, *J. Phys. Chem. B* **2003**, *107*, 9034-9041.

[43]   J.-Y. Choi, D. Higgins, Z. Chen, *J. Electrochem. Soc.* **2011**, *159*, B86-B89.

[44]   A. Zitolo, V. Goellner, V. Armel, M. T. Sougrati, T. Mineva, L. Stievano, E. Fonda, F. Jaouen, *Nat. Mater* **2015**, *14*, 937-942.

[45]   L. Wang, L. Zhang, J. Zhang, *Electrochim. Acta* **2011**, *56*, 5488-5492.

[46]   A. K. Farquhar, M. Supur, S. R. Smith, C. Dyck, R. L. McCreery, *Adv. Ener. Mater.* **2018**, *8*, 1-9.

[47]   N. O. Laschuk, Ebralidze, II, J. Poisson, J. G. Egan, S. Quaranta, J. T. S. Allan, H. Cusden, F. Gaspari, F. Y. Naumkin, E. B. Easton, O. V. Zenkina, *ACS Appl. Mater. Interfaces* **2018**, *10*, 35334-35343.

[48]   X. Li, H. Lei, J. Liu, X. Zhao, S. Ding, Z. Zhang, X. Tao, W. Zhang, W. Wang, X. Zheng, R. Cao, *Angew. Chem. Int. Ed. Engl.* **2018**, *57*, 15070-15075.

[49]   H. Li, X. Li, H. Lei, G. Zhou, W. Zhang, R. Cao, *ChemSusChem* **2019**, *12*, 801-806.

[50]   J. Meng, H. Lei, X. Li, J. Qi, W. Zhang, R. Cao, *ACS Catal.* **2019**, *9*, 4551-4560.

[51]   J. Poisson, H. L. Geoffrey, I. I. Ebralidze, N. O. Laschuk, J. T. S. Allan, A. Deckert, E. B. Easton, O. V. Zenkina, *J. Phys. Chem. C* **2018**, *122*, 3419-3427.

[52]   E. S. Ilton, J. E. Post, P. J. Heaney, F. T. Ling, S. N. Kerisit, *Appl. Surf. Sci.* **2016**, *366*, 475-485.

[53]   D. S. Hall, C. Bock, B. R. MacDougall, *J. Electrochem. Soc.* **2013**, *160*, F235-F243.

[54]   L. Trotochaud, J. K. Ranney, K. N. Williams, S. W. Boettcher, *J. Am. Chem. Soc.* **2012**, *134*, 17253-17261.

[55]   M. Ramadoss, Y. Chen, Y. Hu, W. Li, B. Wang, X. Zhang, X. Wang, B. Yu, *J. Power Sources* **2020**, *451*, 227753.

[56]   X. Meng, J. Han, L. Lu, G. Qiu, Z. L. Wang, C. Sun, *Small* **2019**, *15*, 1-10.

[57]   J. Juodkazytė, B. Šebeka, I. Savickaja, M. Petrulevičienė, S. Butkutė, V. Jasulaitienė, A. Selskis, R. Ramanauskas, *Int. J. Hydrog. Energy* **2019**, *44*, 5929-5939.

[58]   J. Liu, C. Wang, F. Rong, S. Wu, K. Tian, M. Wang, L. He, Z. Zhang, M. Du, *Electrochim. Acta* **2020**, 1-14.

[59]   H. Zhu, D. C. Rosenfeld, M. Harb, D. H. Anjum, M. N. Hedhili, S. Ould-Chikh, J.-M. Basset, *ACS Catal.* **2016**, *6*, 2852-2866.

[60]   S. S. Pan, S. Wang, Y. X. Zhang, Y. Y. Luo, F. Y. Kong, S. C. Xu, J. M. Xu, G. H. Li, *Appl. Phys. A* **2012**, *109*, 267-271.

[61]   A. S. Varela, W. Ju, A. Bagger, P. Franco, J. Rossmeisl, P. Strasser, *ACS Catal.* **2019**, *9*, 7270-7284.

[62]   P. Strasser, Abstract Electrolysis and Fuel Cell Discussions, **2019**, p. Abstract.

[63]   D. V. Naik, W. R. Scheidt, *Inorg. Chem.* **1973**, *12*, 272-276.

[64]   B. Z. Momeni, V. Noroozi, *Monatshefte für Chemie-Chemical Monthly* **2017**, *148*, 893-900.

[65]   P. Matter, L. Zhang, U. Ozkan, *J. Catal.* **2006**, *239*, 83-96.

[66]   C. W. B. Bezerra, L. Zhang, K. Lee, H. Liu, A. L. B. Marques, E. P. Marques, H. Wang, J. Zhang, *Electrochim. Acta* **2008**, *53*, 4937-4951.

[67]   G. Zhang, R. Chenitz, M. Lefèvre, S. Sun, J.-P. Dodelet, *Nano Energy.* **2016**, *29*, 111-125.

[68]   C. H. Choi, C. Baldizzone, J. P. Grote, A. K. Schuppert, F. Jaouen, K. J. Mayrhofer, *Angew. Chem. Int. Ed. Engl.* **2015**, *54*, 12753-12757.

[69]   G. Liu, X. Li, P. Ganesan, B. N. Popov, *Electrochim. Acta* **2010**, *55*, 2853-2858.

[70]   A. Ohma, K. Shinohara, A. Iiyama, T. Yoshida, A. Daimaru, *ECS Transactions* **2011**, *41*, 775.

[71]   L. Osmieri, C. Zafferoni, L. Wang, A. Videla, A. Lavacchi, S. Specchia, *ChemElectroChem* **2018**, *5*, 1954-1965.

[72]   G. Zhang, Q. Wei, X. Yang, A. C. Tavares, S. Sun, *Appl. Catal. B. Eniv* **2017**, *206*, 115-126.

Chapter 5. Hybrid Supercapacitor Electrode Materials via Molecular Imprinting of Nitrogenous Ligands and Iron Complexes into Carbon Support

5.0 Preface

In this chapter, we explore the role of the surface modification via diazonium coupling of nitrogenous ligands to a Vulcan carbon support from Chapter 2 for applications as a supercapacitor electrode. We continued to use the diazonium coupling chemistry to attach only the most active forms of pyridinic nitrogen to Vulcan carbon. In this chapter, various tpy-based nitrogenous ligands were used along with phenanthroline and the performance of the resulting materials with and without added iron were tested. The capacitance per molecule was calculated and used to observe significant increases of the capacitance for the systems enriched by nitrogen and iron. The changes to the capacitance were varied in degree based on the molecule used to modify the carbon. Interestingly, after long-term stability testing, the sample increased in capacitance indicating that a polymerization reaction was occurring. This polymerization is a beneficial process to reach the highest values of the capacitance for the systems under investigation.

5.0 Abstract

Novel hybrid supercapacitor materials were made by the covalent immobilization of nitrogenous ligands onto the surface of commercial carbon support (Vulcan XC-72), then coordinated to iron. The covalent attachment of the nitrogenous ligands allows for the controlled deposition of nitrogen functionalities on the surface of the carbon. The supercapacitor tests in acidic media showed significant growth of the capacitance as a result of the nitrogenous ligands on the support. Notably, the increase of the capacitance values directly correlates with the molecular loading on the surface. Following coordination of iron to the ligands on the surface further elevated the capacitance via Faradic reaction of the metal center. Remarkably, the overall capacitance of materials significantly increased after the course of long-term cycling tests (ca. 110% or higher). At the beginning of durability studies, a small decline in capacitance was observed, due to some extent of molecular decomposition on the surface of the electrode. However, the intense cycling further propagates a steady growth of the overall capacitance of the materials. This could be attributed to the process of polymerization of physisorbed molecules/radicals that result in the formation of a 3D network structure that eventually boosts the overall capacitance and the charge storage of the electrode.

5.1 Introduction

Our dependence on fossil fuels has led us into a global crisis with elevating effects of climate change. The evolution of greenhouse gases into the atmosphere result in global warming and severe changes in the precipitation patterns, which facilitates the occurrence of natural disasters like hurricanes, severe flooding, erosion of the marine coastline and severe heat waves. To mitigate the damage done by fossil burning, the development of alternative renewable eco-friendly fuels and materials for energy storage has become increasingly important[1-3]. The wide implementation of clean electrochemical technologies requires significant developments of fuel cells (to generate energy), and charge storage devices (to store and release energy).

Electric double-layer capacitors (EDLCs) are capable of storing large amounts of energy quickly, by forming an electric double layer at the electrode/electrolyte interface. Their low cost and generally longer cycle life compared to batteries[4] make them feasible,

effective, and environmentally friendly charge storage materials, that could be widely applied in different areas, including support of portable electronics[5-7] and electric vehicles.

EDLCs are classically made from carbon-based materials due to it's abundance, mechanical stability, surface area, and high electric conductivity[8-9]. The only limitation of the carbon-based EDLCs is their relatively low energy and power density[2, 10]. However, hybrid materials, combining the electrostatic interactions from the carbon electrodes and Pseudofaradaic or Faradaic (redox) processes from the suitable dopant(s), so-called supercapacitors (SCs), could resolve this limitation and offer increased charge storing capability and energy density[6, 11-12]. Rare earth transition metal-oxides (Ruthenium (Ru) oxide etc) are often used as dopants due to the ability of the metal center to adopt multiple valence states and support multiple redox processes that are elevating charge transfer and energy storage properties of the materials, however high cost of the dopant is hindering large scale application of the materials[1, 13-15]. Doping of carbon materials with heteroatoms (i.e. nitrogen, phosphorous, sulfur, boron) is an affordable alternative strategy that allows significant boosting of the EDLCs performance due to the additional electronic effects induced by dopant(s) that enhance charge storage of the materials[10]. Most commonly nitrogen functionalities are embedded in the carbon backbone via high-temperature pyrolysis of carbons with suitable nitrogen sources (N-containing molecule). High temperature treatment is very energy demanding and the procedure is very difficult to scale up which hampers wide applications of the resulting materials. In addition, pyrolysis results in the formation of different heteroatom-containing moieties non-homogeneously distributed on the surface of the carbon that results in the different properties across the material.

The procedure to synthesize these materials is lacking reproducibility and scalability and it is difficult to tune the performance of the materials due to the uncertainty with the functional groups caused by the heat treatment. Better control on what nitrogen groups form on the surface by using a molecularly defined method might open up more information about how to better build these materials for the future of supercapacitor electrodes to get the most energy and power out of the materials. Another method to add nitrogen functionalities is through the addition of electroactive molecules. Using nitrogenous ligands, attached to the surface, aids in the fast transfer of one or more

122

electron(s)[5]. The chemical attachment of molecules (especially covalent bonding to carbon) can enhance electronic effects as well as improve the amount and homogeneity of nitrogen functionalities on the surface, assist in ion adsorption, and aid in wettability[8, 16]. Polymers (such as polyaniline (PANI)) have also been used for supercapacitor design, however, they are not useful in aqueous capacitors due to oxidative degradation upon testing in prolonged exposure in the aqueous electrolyte[17].

Our group has previously published work on the design and synthetic methodology of the model system for a non-precious metal catalyst for the oxygen reduction reaction using a covalent method of attaching terpyridine and phenanthroline groups on the surface of a commercial Vulcan carbon support[18-19]. We were able to show that through a covalent bond of the terpyridine (tpy) group to the surface we could have some control over which nitrogen functional groups on the surface and were able to attach these on the carbon in a monolayer coverage[20]. Using a similar approach, we report here on the covalent attachment of various tpy- and phen- derivatives onto a commercial Vulcan carbon support. After attaching these nitrogen ligands to the surface, the effect of doping with the various nitrogen ligands on the performance of the systems can be observed and calculated though the specific capacitance of the materials. We calculated the amount of capacitance per tpy- and phen-molecule added to the carbon support and correlated that to the increase in specific capacitance of the material. We further reacted the material with the solution of iron(III) precursor (10 mM $FeCl_3$ in methanol) to achieve iron coordination to the molecular receptors on the surface (N-ligands) with a high affinity to iron. This is expected to further increase the energy and power density of the material due to Faradaic reaction of the nitrogen groups on the surface and separate Faradaic contribution from the incorporated iron. Using the combined charge storage capabilities of the iron as it changes oxidation state, with the heteroatom doped carbon may result in a new hybrid material with novel properties for applications in SC technology. We show that our model system can be used to characterize the amount of capacitance per molecule to help in the implementation of the next generation of SC materials for energy applications of the future.

5.2 Experimental

5.2.1 Materials

Commercial Vulcan XC-72 was purchased from Cabot Corporation. Isopropyl alcohol, 30% polytetrafluoroethylene in water, ferric chloride, methanol, acetone, and sulfuric acid were purchased from Sigma-Aldrich. TPG-H-090 Toray paper 30% Wet Proofing Carbon fibre paper was purchased from Fuel Cell Earth LLC. Nafion 115 membrane was purchased from Ion Power.

5.2.2 Synthesis of the modified carbons

Synthesis of the modified materials were followed via our previously published synthesis[18]. Briefly, 4'-(4-aminophenyl)-2,2':6'2'-terpyridine (tpyL), 1-aminophenanthroline (phen), or [2,2':6',2'-terpyidin]-4'-amine (tpyS) were attached to the commercial Vulcan carbon surface through a diazonium coupling reaction while stirring for 24 h. Equal volumes of a 10 mM solution of the desired ligand in methanol and 1 M $NaNO_2$ in methanol were added together and allowed to react for 3 min before being added to the carbon support. This reaction mixture was stirred for 24 h. The resulting material was vacuum filtered and washed with deionized water, acetone, and methanol 3 times. These materials are denoted V-phen, V-tpyL, and V-tpyS. An excess 10 mM solution of Fe^{3+} in methanol was added to the nitrogenous ligand modified materials in a 2:1 molar ratio to produce the nitrogen and iron-doped materials. This was allowed to react under room temperature conditions and stirring for 48 h. The resulting material was vacuum filtered and washed 3 times with deionized water, acetone, and methanol. These materials are denoted V-tpyL-Fe, V-phen-Fe, and V-tpyS-Fe. The synthesis of the $tpyL_2$ was performed using the same synthetic procedure, except a 2:1 stoichiometric ratio of ligand-to-metal complex was made by reacting the ligand and metal prior to the diazonium coupling step. Scheme 5.1 displays the structures of the various ligands used in this study. A portion of some of the materials were heat treated in a Thermo Lindberg/Blue M tube furnace at 700 ºC under N_2 atmosphere at a heating rate of 10 ºC min^{-1} and a flow rate of 80 mL min^{-1}.

5.2.3 Physical Characterization

Thermogravimetric analysis (TGA) was performed on the materials using a TA instruments SDT Q600 thermal analyzer. Samples were run at 5 ºC min^{-1} at a flow rate of

20 mL min^{-1} under both air and argon atmospheres. Pore size analysis was performed on a Quantachrome NOVAe 200 pore size analyzer. Samples were degassed for 6 h at 210 ºC prior to the analysis. Raman spectra were obtained using a Renishaw inVia confocal Raman microscope with a 2400 l mm^{-1} visible grating. Spectra were obtained using an exposure time of 30 s per scan at a 1 % laser power and the excitation wavelength of 50 mW 532 nm Nd:YAG laser. Scanning electron microscopy (SEM) was performed on the materials using a Hitachi FlexSEM 1000. The beam was set at a 5 kV with a working distance of 5 mm. the SEM was equipped with the energy dispersive spectroscopy (EDS) probe used for elemental analysis of surfaces.

5.2.4   Electrochemical Characterization

Supercapacitor materials were tested in a 3-electrode cell configuration were studied by using cyclic voltammetry (CV) and galvanostatic charge-discharge curves (GCD) in 0.5 M H_2SO_4. The ink containing 19 mg of material was dispersed in 1 mg of 10% polytetrafluoroethylene (PTFE) and 700 µL isopropyl alcohol which was sonicated for 15 min then stirred overnight. The resulting mixture was painted on a 1 cm^2 area of the carbon fibre paper electrode that resulted in a final mass on the electrode of ca. 2 mg cm^{-2}. The electrode was placed in a cell containing 0.5 M H_2SO_4 that was purged with N_2 gas for ca. 20 min prior to measurement. An Ag/AgCl double junction reference electrode was used along with a graphite rod counter electrode. The electrochemical measurements were performed using a Solartron Analytical 1470E potentiostat connected to a Solartron SI 1260 impedance/gain phase analyzer with corresponding CView and Zplot software. Data were obtained at 200, 100, 50, 20, 10 mV s^{-1} for the CV measurements. GCD curves were performed at 0.5, 1, 2, 5, 10 A g^{-1}. Capacity retention and coulombic efficiency measurements were performed using GCD curves at 2 A g^{-1} for 6000 cycles.

2-cell symmetric device testing was performed by using the electrodes described above. The coated carbon fibre paper electrodes with ca. 2 mg cm^{-2} were cut into 1 cm^2 disk electrodes. The two electrodes were hot pressed (80 ºC at 150 kg cm^{-2} for 90 s) between a Nafion 115 membrane separator. The electrodes were placed into a sandwich cell and tested electrochemically through CV as described above.

Specific capacitance was calculated using Eq. 5.1 where C_g is the gravimetric capacitance (F g^{-1}), I is the discharge current (A), Δt is the discharge time (seconds), m is the mass of active material (g) and ΔV is the voltage window (V)[16]

$$C_g = \frac{I\Delta t}{m\Delta V}$$ 5.1

5.3 Results and Discussion

A series of nitrogen-enriched carbon materials, V-tpyS, V-tpyS-Fe, V-tpyL, V-tpyL-Fe, V-tpyL$_2$-Fe, V-phen, and V-phen-Fe, were prepared using a commercial Vulcan carbon support (Scheme 5.1). The nitrogenous ligands were covalently attached to the carbon support using our previously reported procedures[18, 21]. Following the attachment of the nitrogenous ligand, the resulting materials were further functionalized with Fe^{3+} (Scheme 5.1A). All materials were characterized by thermogravimetric analysis (TGA), differential scanning calorimetry (DTG), Brunauer-Emmett-Teller analysis (BET), SEM, Raman, and their charge storage abilities were explored electrochemically in a 3-electrode cell under acidic conditions.
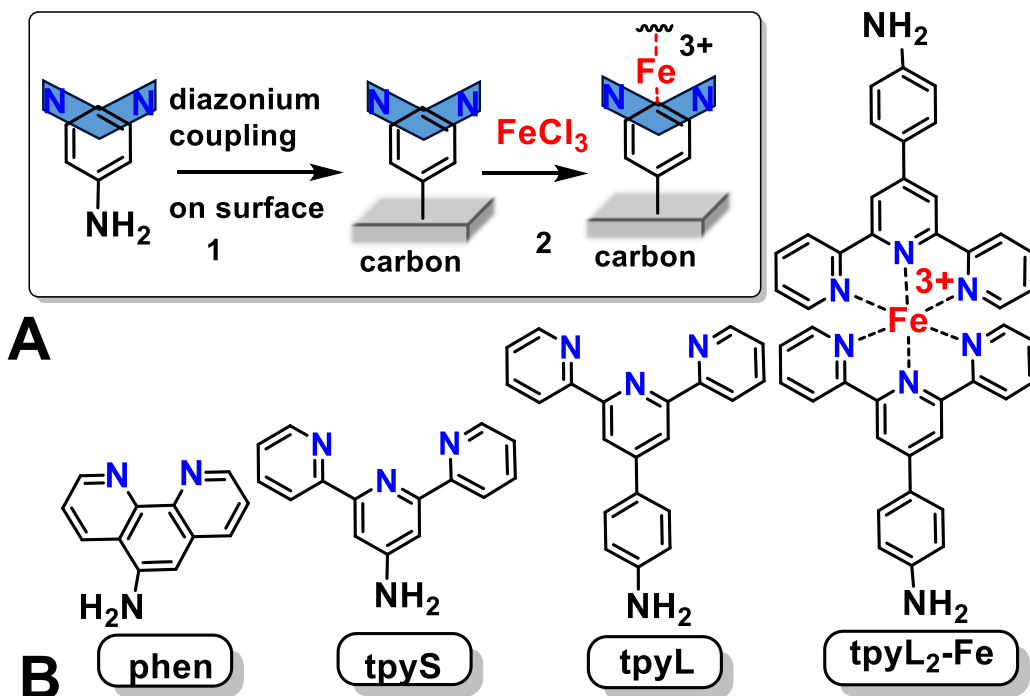
Scheme 5.1) (A) General scheme of carbon surface functionalization to prepare hybrid supercapacitor materials. (B) Nitrogenous ligands/metal complexes used in the materials' design.

5.3.1 Physical Characterization

TGA was performed on all the materials before and after the addition of iron to determine any morphology changes in the carbon structure upon immobilization of the nitrogenous ligands (N-ligands) to the carbon support and following coordination with iron. Modification of carbon support by N-ligands resulted in the lowering of the combustion temperature for all resulting hybrid materials (Figures S5.1A and C). this indicates significant changes in the carbon structure as a result of the immobilization of the N-ligand to the surface of the support[19, 21]. This is consistent with DTG results that demonstrate two well-defined peaks for combustion of the N-ligands at the lower temperatures (ca. 400 ℃- 500 ℃) and combustion at higher temperatures (ca. 600 ℃). the Fe content (weight percent, % of Fe) in the samples was calculated by taking into account the ash content remaining in the sample from the carbon support, and the results are presented in Table 5.1. The majority of the materials had Fe loadings of ca. 2% or less which is similar to other literature systems in the design of non-precious metal materials and with our previous work[18-19, 21-27]. In general, after the addition of iron we see further lowering of the combustion temperatures for all material under investigation, that is an expected outcome since iron could act as a combustion catalyst under the conditions of analysis[21].

To further analyze how the modification of carbon support by N-ligands affects surface properties and combustion temperatures we performed the TGA and DTG under inert argon atmosphere (Figure S5.1B and D). Under argon, modification of the supports with the N-ligands resulted in the lowering of the combustion temperatures, which was further decreased after modification with iron. However, no significant mass losses were detected for most of the samples until the temperature reached ca. 600 ℃ or above.

Table 5.1) TGA weight %, specific surface areas, EDS wt% and $I_D I_G$ ratios.

Material	TGA wt%	BET Specific Surface Area / $m^2\ g^{-1}$	EDS Fe wt%	I_D/I_G
Vulcan	-	220	-	1.43 ± 0.09
V-tpyL	-	197	-	1.34 ± 0.18
V-tpyL-Fe[18]	2%	206	-	1.52 ± 0.49
V-tpy-L-Fe-700	-	350	0.32	1.24 ± 0.40
V-tpyL$_2$-Fe	5.6%	177	-	1.39 ± 0.08
V-tpyS	-	179	-	1.57 ± 0.23
V-tpyS-Fe	0.4%	169	0.26	1.50 ± 0.17
V-phen	-	151	-	1.42 ± 0.04
V-phen-Fe	2.5%	162	1.24	1.63 ± 0.47

Pore size analysis was performed on the materials to determine how the specific surface area of the Vulcan carbon support changes upon modification with the N-ligands, and iron (Table 5.1). The nitrogen isotherms and the results of pore size distribution analysis are presented in Figure S5.2. Notably, we see the detectable decline of the surface area for all materials after functionalization by N-ligands. This could be attributed to the bulky N-ligands hindering some access to the pores, which results in the overall decrease in the active surface area[21, 28]. Nonetheless, the materials remain quite porous with high surface areas. This is important as the higher surface area is crucial for energy storage materials to ensure the efficient movement of the electrolyte through the pores to benefit the electrochemical charge storage properties[3, 10, 29].

Raman analysis was performed on the materials (Figure 5.1) to observe changes in the carbon support upon N-modification and indicate the level of disorder in the materials[30]. The I_D/I_G ratios calculated for each material from the D-band (1350 cm^{-1}) and G-band (1500 cm^{-1}) are presented in Table 5.1. N-enriched Vulcan supports demonstrate a clear decrease in the I_G/I_D ratio, this indicates the increase of the graphitization in the material upon modification[19, 31-33]. While this is a general trend, only V-tpyL sample showed a significant decrease in the I_D/I_G ratio while the V-tpyL$_2$-Fe and V-phen

demonstrated smaller changes. As a result of Fe coordination, most of the materials demonstrate the increase of the I_D/I_G ratio, that is indicative of the presence of some disturbances or defects in the lattice of the carbon[32, 34-37]. The addition of the Fe into the materials reduces the level of the graphitization by making a more amorphous material as a result of additional defects in the pristine graphitic structure. This can be done by disrupting the graphitic structure through the change in coordination environment and through Fe/C interaction that occurs prior to electrochemical cleaning protocols[32].
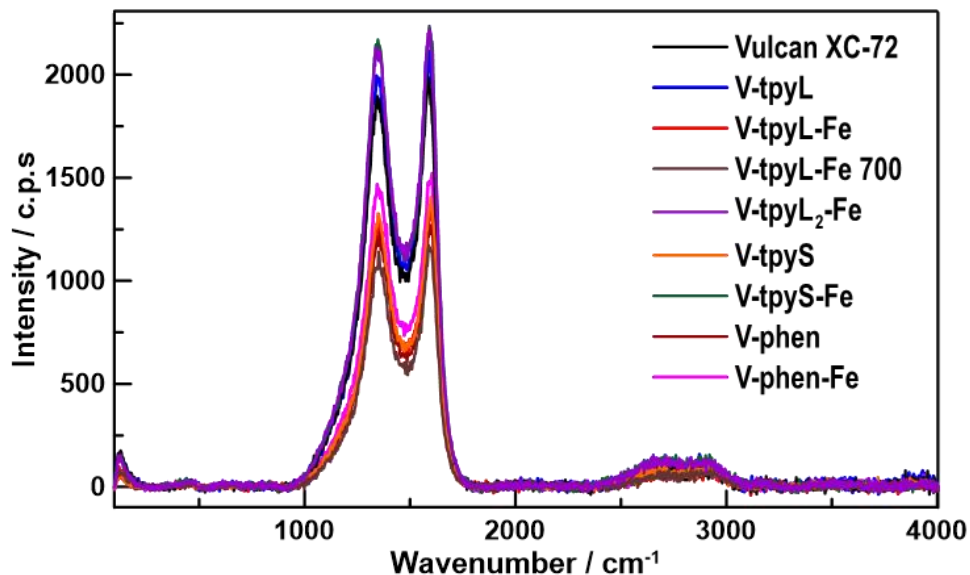
Figure 5.1) Raman Spectra of the initial carbon support and synthesized N-enriched hybrid materials.

No detectable changes in the morphologies of the materials were observed by SEM before and after modification (Figure S5.3). The surface features are consistent with surface morphology expected for Vulcan carbon, indicating that the surface modification yielded a monolayer of N-ligand on the surface. In general, all materials show a 3D porous structure of carbon which is beneficial for the efficient movement of the electrolyte ions within the material required for effective charge storage.

5.3.2 Electrochemical Characterization

Cyclic voltammetry (CVs) were performed in the 3-electrode SC testing set up in 0.5 M H_2SO_4 (Figure 5.2). Upon immobilization of the N-ligand to the support, new small peaks appeared in the CV due to redox activity from the nitrogenous groups[38]. After iron coordination, a pronounced redox peak appears at ca. 0.7 V which is characteristic of the $Fe^{2+/3+}$ redox couple. For all materials under investigation, CVs were recorded at various

scan rates (500, 200, 100, 50, 20, 10 mV s^{-1}) (Figure S5.4). For the modified materials, as the scan rate is increased the redox peaks are shifted to higher potentials. This is due to the slower kinetics of electrochemical electron transfer reaction as the scan rate increases. Using CVs at different scan rates, the surface coverage of the molecules could be estimated. To do this we plotted the peak current density versus the sweep rate to obtain a linear response. Using the slope of the line we were able to calculate the surface coverage per molecule using the following equation where m is the slope of the line, R is the gas constant (J K^{-1} mol^{-1}), T is temperature (K), n is the number of electrons, and F is Faraday's constant (C mol^{-1})[39] (Table 5.2).

$$\Gamma = m \frac{4RT}{n^2 F^2} \qquad\qquad 5.2$$
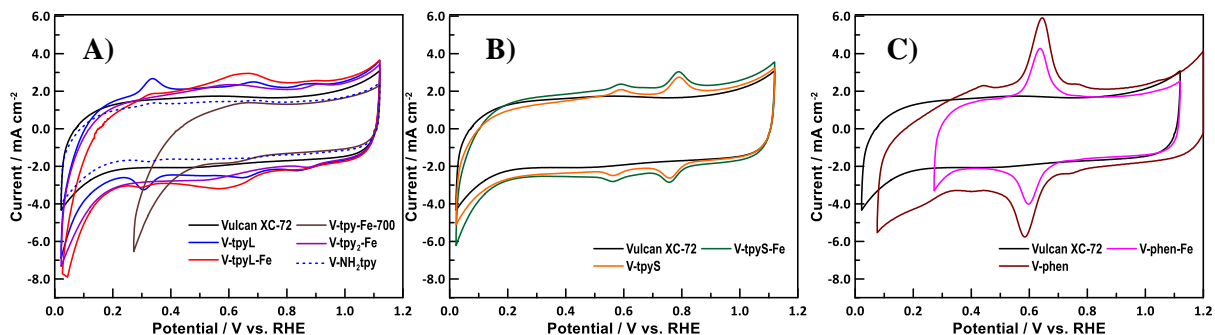
Figure 5.2) CVs of the materials at 50 mV s^{-1} in N$_2$ purged 0.5 M H$_2$SO$_4$ electrolyte.

Galvanostatic charge and discharge (GCD) analysis was performed to determine the specific capacitance of all tested materials (Figure 5.3). The GCD curves were measured at 0.5, 1, 2, 5, 10 A g^{-1} of active material on the electrode. Along with the overall capacitance, the capacitance increase per N-ligand molecule was determined from the surface coverage (Table 5.2). We were interested to determine the increase in capacitance of the system per each nitrogenous ligand/ iron complex that was added to the support. For the V-tpyL-Fe system, it is observed that the capacitance per molecule has increased when the iron is added to the system, from 1.336 x 10^{-9} µF molecule^{-1} to . We have attributed this capacitance increase to the Faradaic processes imparted by iron. While we see relatively small levels of iron uptake by materials, this is expected for the coordination of Fe to molecularly defined nitrogenous sites already covalently embedded into the surface of the carbon and forming a monolayer type of coverage. Thus, the surface coverage is not

130

expected to increase based on the same ligand (V-tpyL) of the mono-complex, $[Fe(tpyL)]^{3+}$ on-surface of the carbon, (V-tpyL-Fe) but the specific capacitance was higher for the bis-system (39 F g^{-1} for the V-tpyL, 31 F g^{-1} for the V-tpyL-Fe, and 51 F g^{-1} for V-tpyL$_2$-Fe) when compared to materials with no iron content. We attribute this to the increased nitrogen content as well as aromaticity from the second ligand present in this system[40]. The V-tpyS and V-tpyS-Fe samples showed the lowest surface coverages and specific capacitances. This shows that an extra ring in the ligand results in a significant impact on the carbon surface coverage. Moderate ligand elongation is reducing steric hinderance for diazonium coupling on the surface and thus affects the specific capacitance of the material. Finally, the V-phen and V-phen-Fe systems demonstrate the highest surface coverages of all the ligands studied. The amount of capacitance per molecule remained relatively similar for both V-phen and V-phen-Fe. The specific capacitance of the V-phen was 52.4 F g^{-1} and V-phen-Fe was 44.2 F g^{-1}, which is of the highest specific capacitances observed in this work. We attribute this great increase to the extended conjugated system of this ligand (that is planar and restricted to the rotation) compared to the tpy ligands that allow more efficient movement of the electrons and induce enhanced charge storage properties into the material.

Table 5.2) Surface coverage, capacitance per molecule, and specific capacitance of the systems studied.

Material	Surface coverage / molecules nm^{-2}	Capacitance per molecule / μF molecule^{-1}	Specific capacitance / F g^{-1}
Vulcan	-	-	34.2 ± 6.3
V-tpyL	0.218	1.336×10^{-9}	39.8 ± 10.9
V-tpyL-Fe	0.227	1.359×10^{-9}	31.0 ± 9.1
V-tpy-L-Fe-700	0.100	2.514×10^{-9}	33.7 ± 1.8
V-tpyL$_2$-Fe	0.282	1.506×10^{-9}	51.5 ± 15.8
V-tpyS	0.173	1.437×10^{-9}	28.1 ± 6.9
V-tpyS-Fe	0.170	1.044×10^{-9}	26.0 ± 11.8
V-phen	0.403	1.308×10^{-9}	54.2 ± 11.3
V-phen-Fe	0.348	1.479×10^{-9}	44.2 ± 8.8
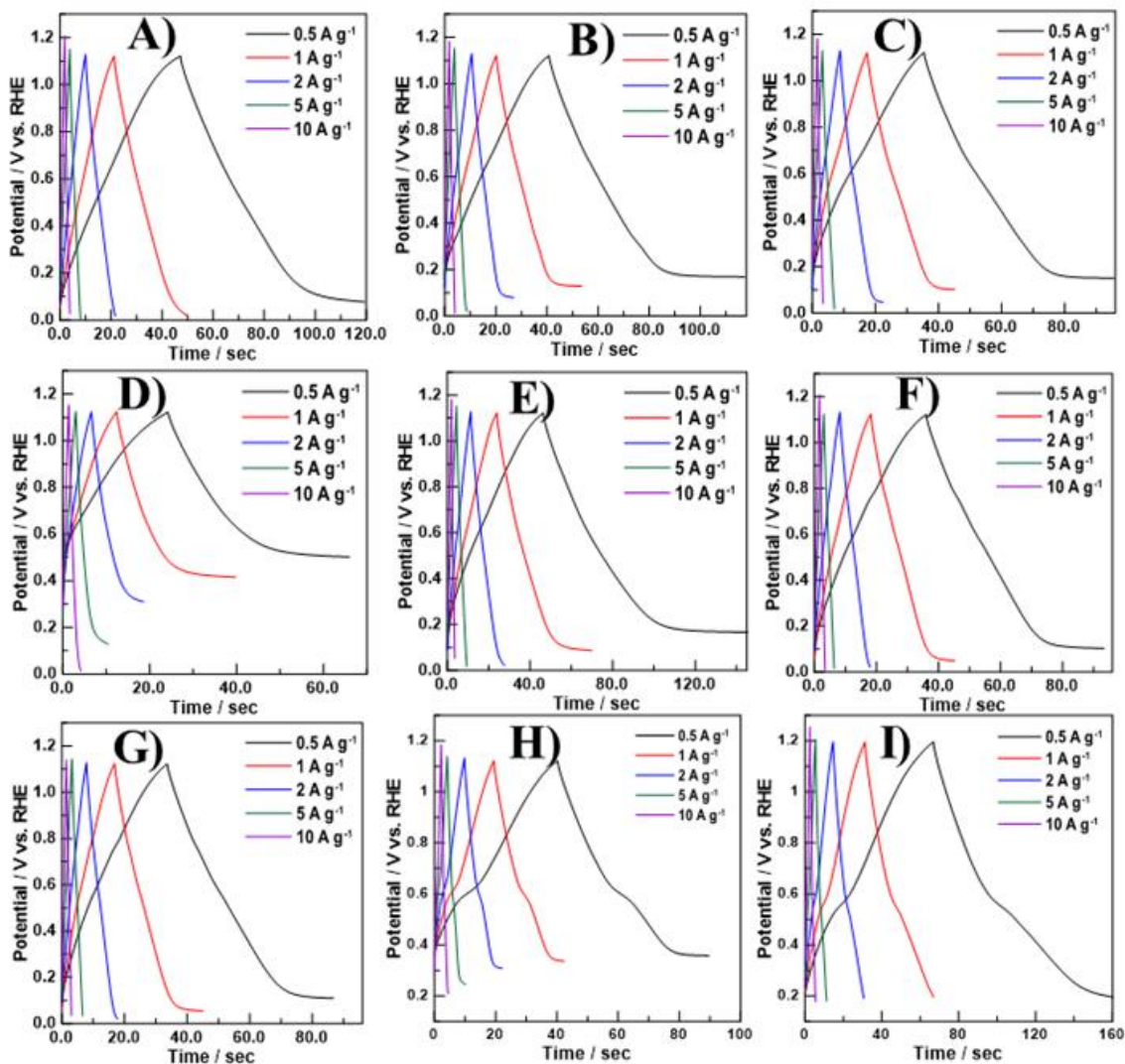
Figure 5.3) GCD curves in N_2 purged 0.5 M H_2SO_4 (A) Vulcan XC-72 (B) V-tpyL (C) V-tpyL-Fe (D) V-tpyL-Fe-700 (E) V-tpyL$_2$-Fe (F) V-tpyS (G) V-tpyS-Fe (H) V-phen (I) V-phen-Fe.

All of the systems were subjected to a long-term durability testing protocol (Figure 5.4). This involved 6000 GCD cycles at 2 A g^{-1} in 0.5 M H_2SO_4. For all the samples we observed a gradual increase in the specific capacitance over cycling, which was not expected as we anticipated some losses over cycling time. The blank Vulcan sample demonstrates a relatively small change in the capacitance over 6000 cycles and had a 5% loss of its original specific capacitance (after 6000 cycles). For the V-tpyL, V-tpyL-Fe, and V-tpyL$_2$-Fe there was an initial decline in the specific capacitance and ca. 30% of their original capacitance. However, after about 2000 cycles the capacitance starts to increase

132

again reaching in some cases gaining above 100% of the initial capacitance value. We have attributed this to some electropolymerization that may occur in the samples during long-term cycling. The initial capacitance decrease could be attributed to loss of iron or ligand in the acidic solution; however, the abovementioned acidic conditions provide an ideal environment for electropolymerization of any residual physisorbed ligands still bearing NH_2 group needed for polymerization[38, 41]. Through the vigorous cycling from the durability testing these linkages could detach from the surface and electropolymerize. In addition, and remaining radicals from the uncompleted diazonium coupling within the material will significantly facilitate this process, as weakly attached ligands using this method are not uncommon and can be responsible for the increase in the charge storage[42-43]. The growth of a polymer results in the growth of the additional porous 3D network on top of the carbon that allows for more effective charge storage within the hybrid material. With the heat-treated sample (V-tpyL-Fe-700) we still see the effective growth which could be due in part to the increase from a growing polymer, or from the growth of quinone/hydroquinone reaction that occurs in acidic media[29]. We believe it is attributed to both, as the increase in capacity retention reaches over 300%. Further evidence of polymer growth is seen in the CVs. CVs were collected after every 1000 cycles during the durability test (Figure S5.6). In all instances, there is peak growth, and the capacitance of the CV increases substantially throughout the durability testing, further evidence of the electropolymerization process. The same increases are seen with the V-tpyS, V-tpyS-Fe, and V-phen systems which we attributed as well to the growth of the polymetric network in the material. Lastly, the V-phen-Fe exhibited a sharp increase in the capacitance over stability tests until ca. 2000 cycles, then the capacitance stabilized for the remaining cycles with much less capacitance increase than the rest of the materials tested.
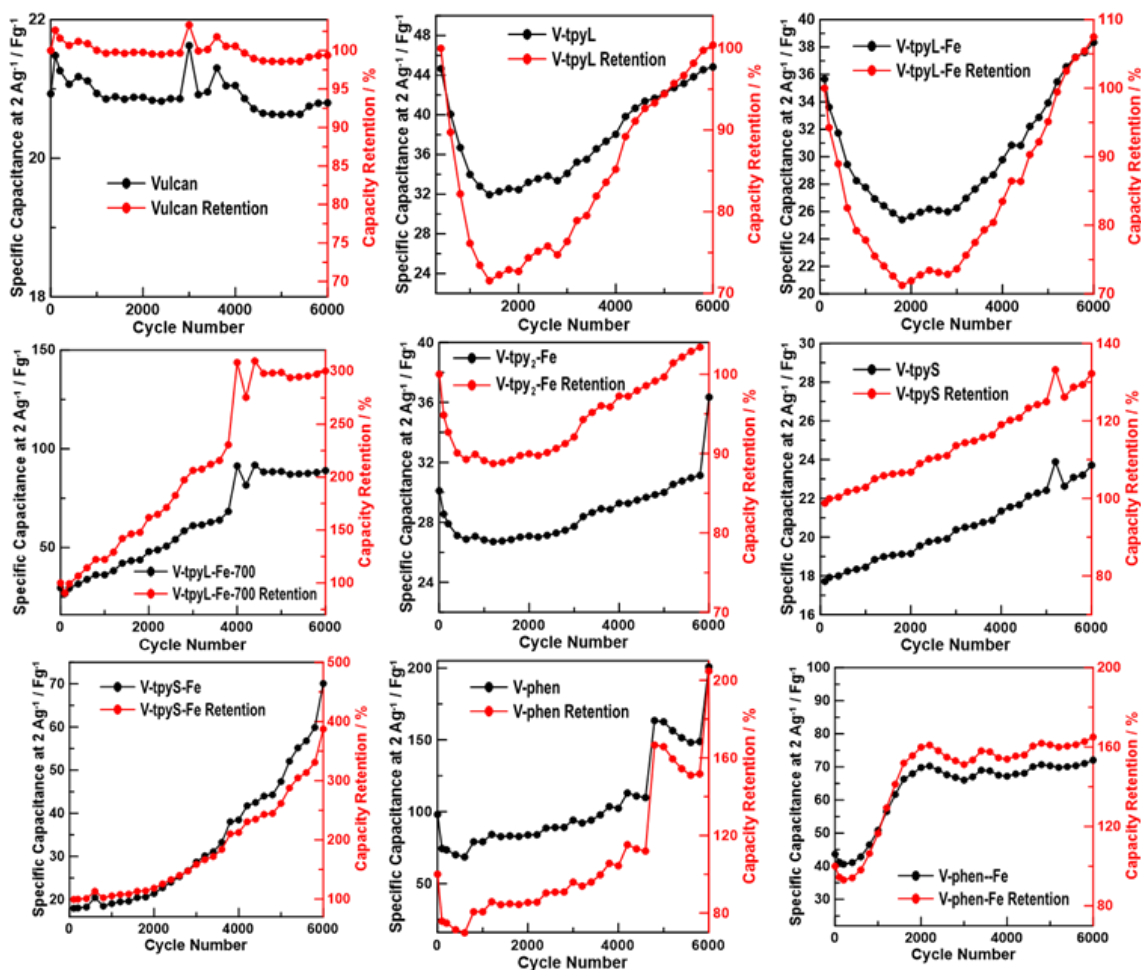
Figure 5.4) Capacity retention of the different systems used in this study.

To further test our theory regarding the polymer growth due to unreacted radical from the diazonium coupling, we physisorbed the tpyL ligand onto the Vulcan carbon and measured the SC tests and durability cycling (Figure S5.7). Notably, there was some non-significant growth observed in the V-NH$_2$tpy sample over the durability cycling, which is attributed to quinone/hydroquinone processes as this growth is drastically smaller in comparison to the growth observed for covalently modified systems, as well as, after 3000 cycles the growth from the CV stabilizes. The specific capacitance of material with physisorbed ligands was much lower than the capacitance of systems with chemisorbed ligands measured in this work. We believe that the conditions to grow a polymer network on carbon through durability cycling are much more enhanced when the diazonium coupling was performed /attempted, as it may generate free radicals, that in combination with the suitable conditions could initiate and facilitate the polymer growth on the surface.

However, some polymerization can be observed but it is significantly less pronounced compared to the other samples were diazonium coupling was performed.

Finally, we took our best material with the highest specific capacitance in the 3-cell set up, V-phen, and assembled it into a symmetrical full cell to assess the performance (Table 5.3). We also compared the V-phen to a bare Vulcan support in the same configuration. The resulting CVs are presented in the SI Figures S5.8-5.9. The bare Vulcan support had a specific capacitance of 17.8 F g^{-1}, with the phen addition the V-phen sample increased in capacitance to 42.8 F g^{-1}, showing the overwhelming positive role that the nitrogen groups have on the charge storage capabilities. The charge storage capabilities are slightly lower within the full-cell configuration which is expected due to the slower movement of electrolyte in and out of the porous supports, which lowers the specific capacitance values observed. However, the values remain similar to the 3-cell testing. Overall, this study shows the promising benefits of using this surface modification approach to functionalize material with nitrogen to design the next generation of SC electrode materials.

Table 5.3) Specific capacitance of the materials studied in the full cell configuration.

Material	Specific Capacitance / F g^{-1}
Vulcan	17.8
V-phen	42.8

5.4 Conclusion

Here we used our molecularly defined modification technique to selectively graft specific functional groups to the carbon surface for use in energy storage applications. The molecular imprinting of various nitrogenous-based ligands into the Vulcan carbon support yielded hybrid systems enriched by pyridinic nitrogens that are able to support the fast movement of ions within the systems for enhanced charge storage. The effect that the ligand structure and the conditions of surface functionalization have on the energy storage properties of the systems was investigated. We monitored the changes in capacitance of the materials per molecule of N-ligand/Fe complex through the various stages of material design and preparation. The materials showed increased charge storage capabilities as a result of immobilization of the N-ligand to the carbon support, where the phen- ligand

showed the highest increase in the charge storage capabilities due to the effect of the planar conjugated fuse-ring system which granted the efficient charge transfer within the molecule.

The long-term durability cycling of the materials resulted in the significant growth of the specific capacitances (up to 300% gain of the capacitance or 300% of the capacitance retention for all materials after 6000 cycles). We attributed this to the influence of the electropolymerization that resulted in the 3D polymeric network on the carbon support that further increased the specific capacitance of the hybrid material.

Overall, this work shows a systematic methodological approach to prepare a new generation of SC materials that focus on the controlled building of the specific functionalities on the surface to grant desired pre-determined properties to the materials. This work shows that covalent grafting of nitrogenous molecules into carbon support is a promising approach to create effective low-cost SC electrodes for future energy storage systems.

5.5 Supporting Information
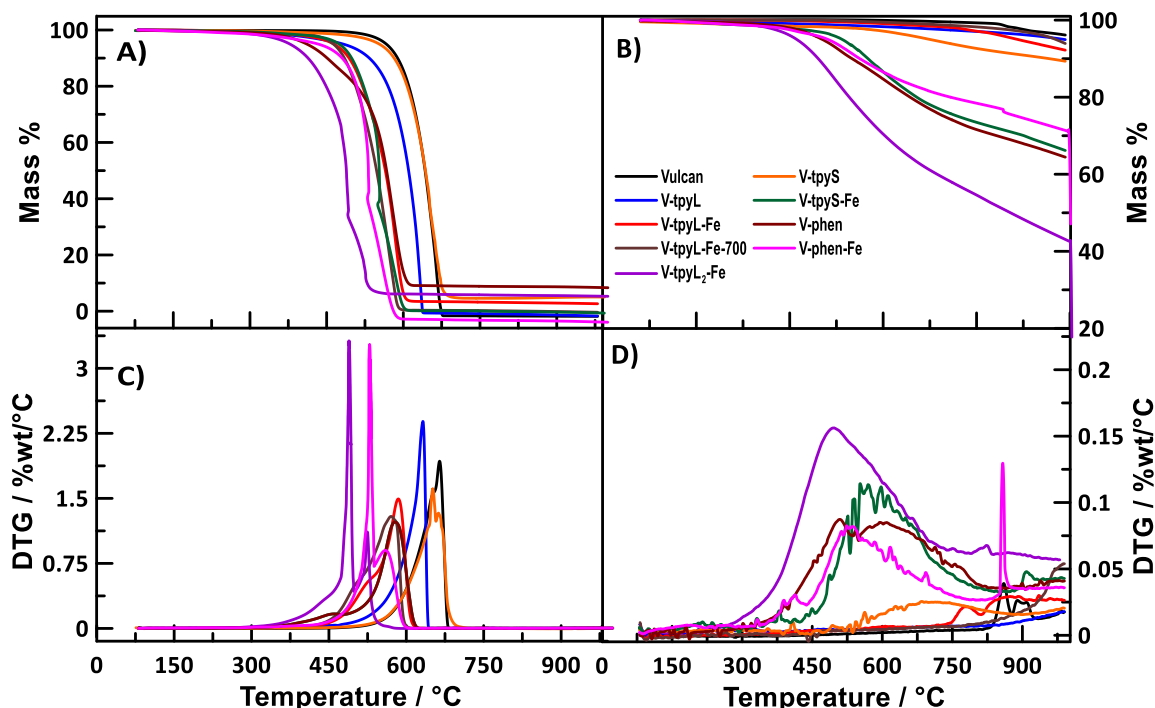
Supporting Information Figure S5.1) (A) TGA of the materials in air atmosphere at a scan rate of 5 °C min^{-1} (B) TGA of the materials in an argon atmosphere at a scan rate of 5 °C min^{-1} (C) DTG of the materials in an air atmosphere at a scan rate of 5 °C min^{-1} (D) DTG of the materials in an argon atmosphere at a scan rate of 5 °C min^{-1}.
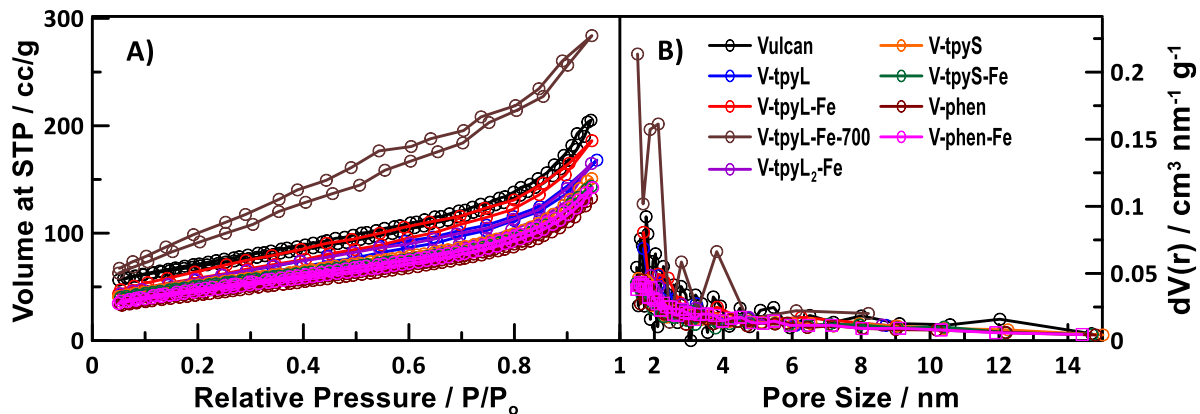
Supporting Information Figure S5.2) (A) Adsorption and desorption isotherms of the various materials studied (B) BJH pore size analysis of the various materials studied.
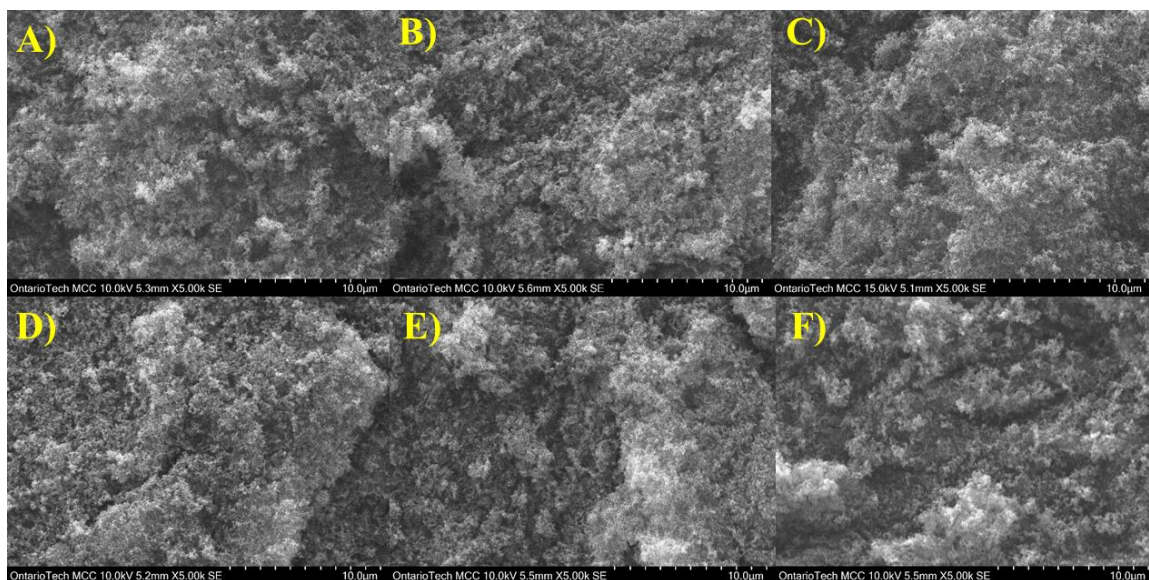
Supporting Information Figure S5.3) SEM images of (A) V-phen (B) V-phen-Fe (C) V-tpyS (D) V-tpyS-Fe (E) V-tpyL$_2$-Fe (F) V-tpyL-Fe-700.
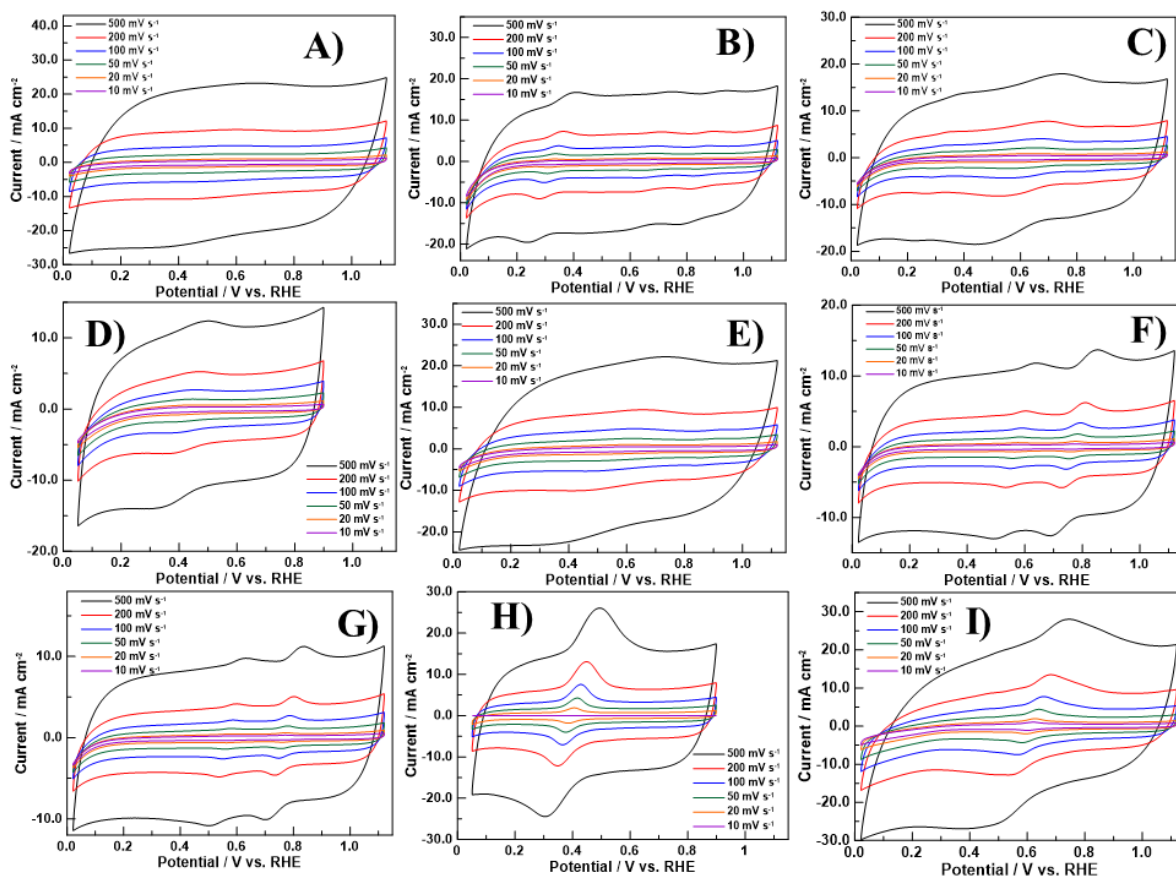
Supporting Information Figure S5.4) CVs in N$_2$ purged 0.5 M H$_2$SO$_4$ (A) Vulcan XC-72 (B) V-tpyL (C) V-tpyL-Fe (D) V-tpyL-Fe-700 (E) V-tpyL$_2$-Fe (F) V-tpyS (G) V-tpyS-Fe (H) V-phen (I) V-phen-Fe.
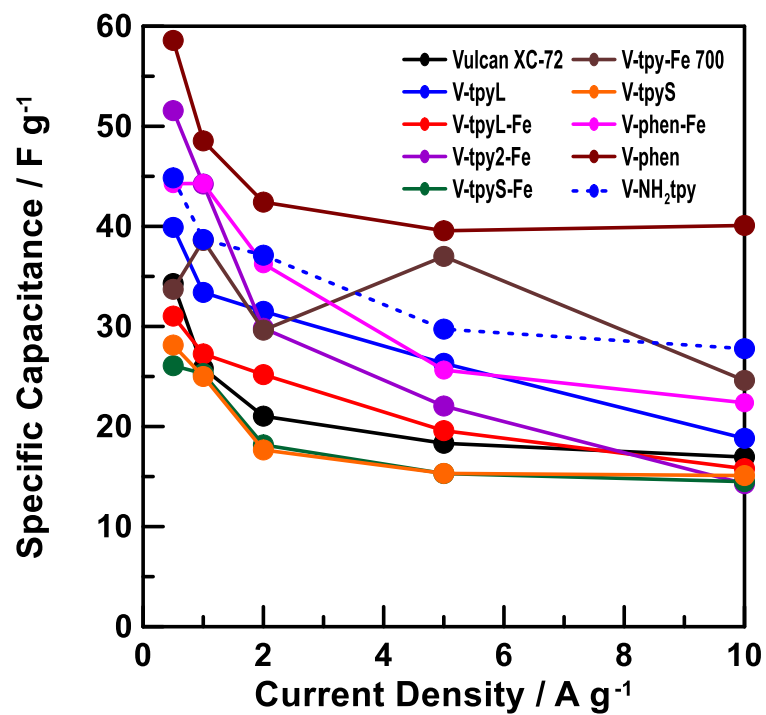
Supporting Information Figure S5.5) Rate capability plot of the measured systems.
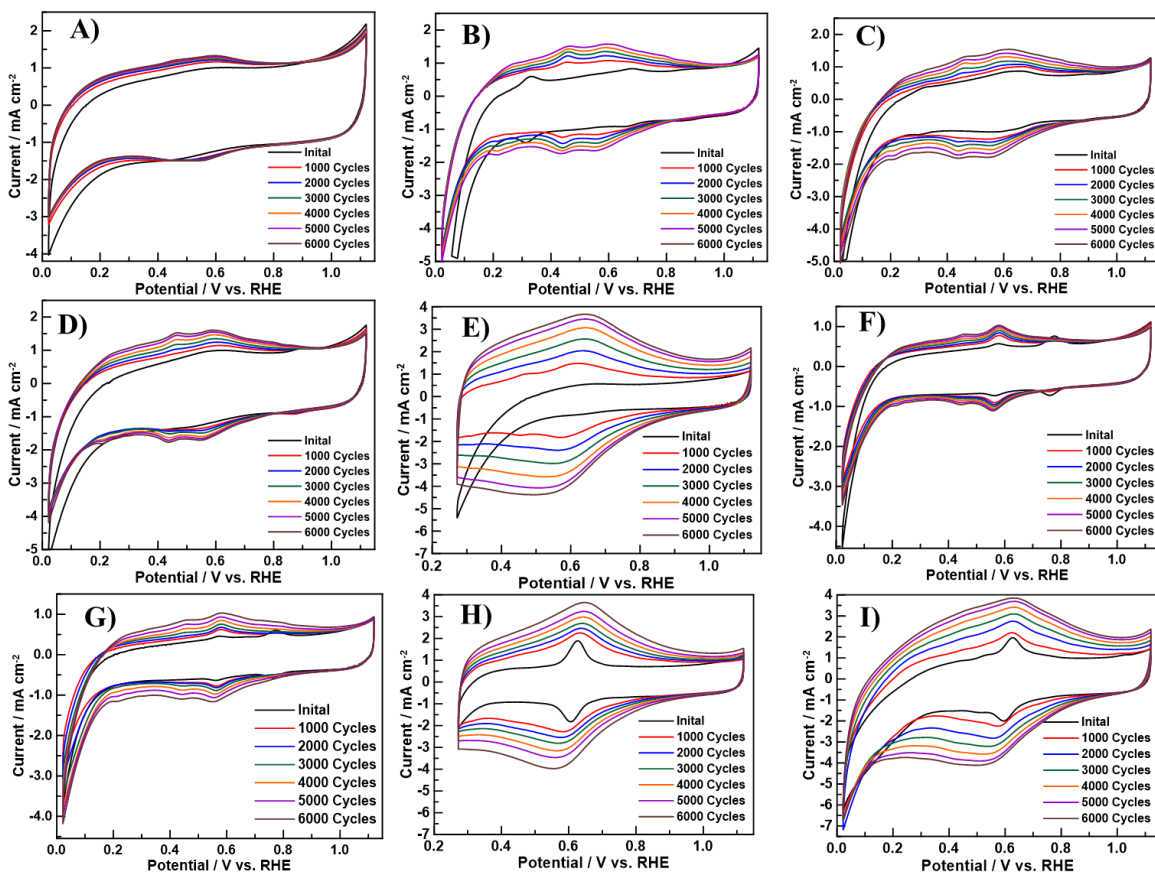
Supporting Information Figure S5.6) CVs in N$_2$ purged 0.5 M H$_2$SO$_4$ at 50 mV s^{-1} (A) Vulcan XC-72 (B) V-tpyL (C) V-tpyL-Fe (D) V-tpyL-Fe-700 (E) V-tpyL$_2$-Fe (F) V-tpyS (G) V-tpyS-Fe (H) V-phen (I) V-phen-Fe.
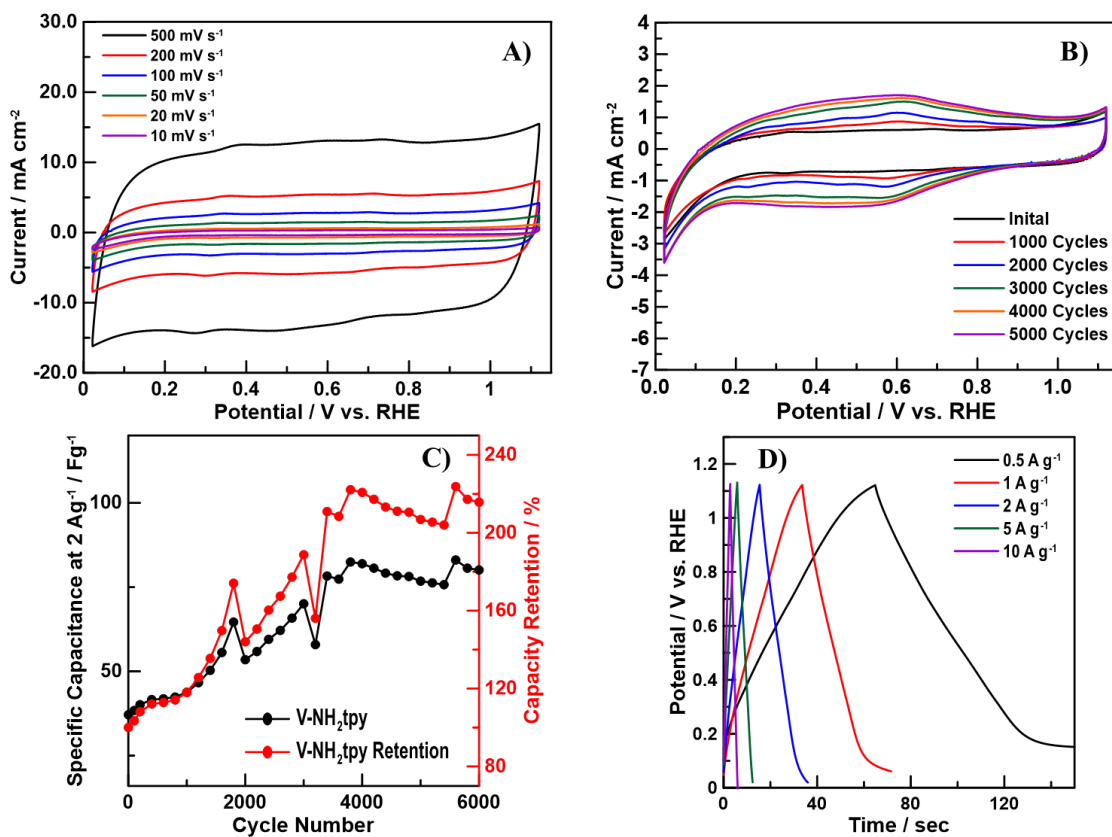
Supporting Information Figure S5.7) (A) CVs of the V-NH$_2$tpy in N$_2$ saturated 0.5 M H$_2$SO$_4$ (B) CVs of the V-NH$_2$tpy in N$_2$ saturated 0.5 M H$_2$SO$_4$ at a scan rate of 20 mV s^{-1} (C) Capacity retention of V-NH$_2$tpy in N$_2$ saturated 0.5 M H$_2$SO$_4$ at 2 A g^{-1} (D) GCD of the V-NH$_2$tpy in N$_2$ saturated 0.5 M H$_2$SO$_4$.
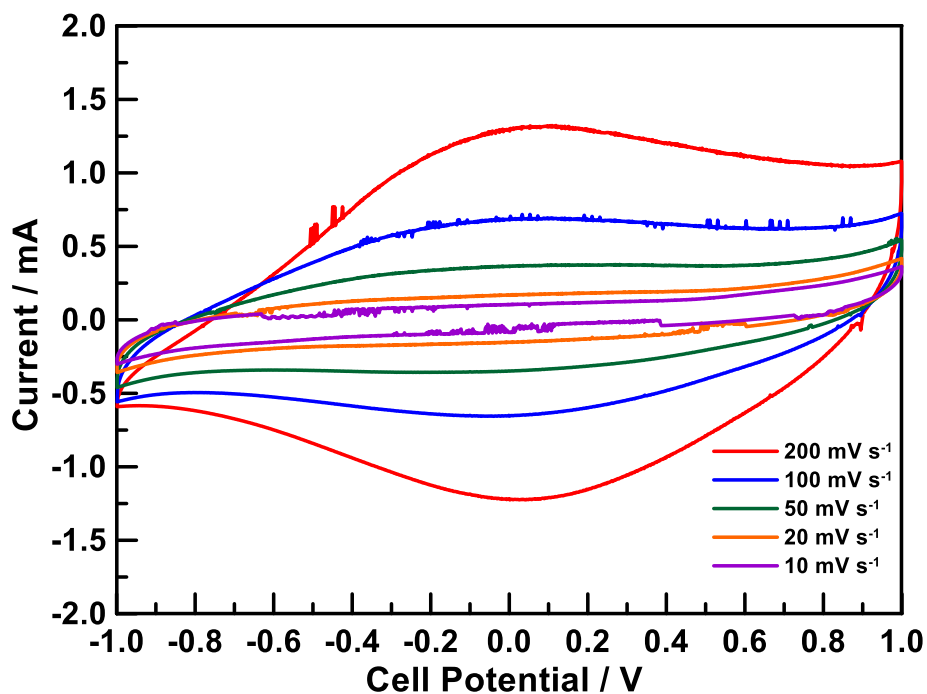
Supporting Information Figure S5.8) The Vulcan symmetric full-cell testing CVs at varying scan rates.

141
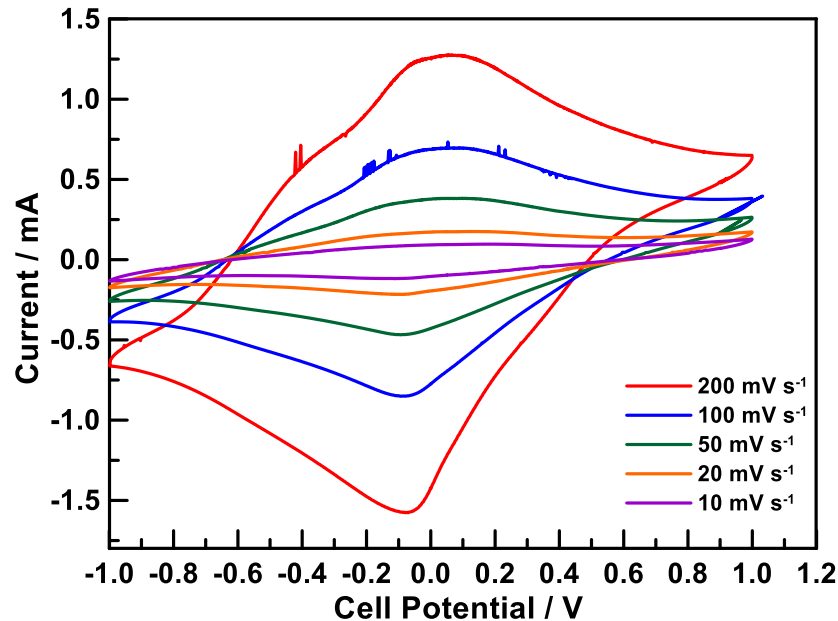
Supporting Information Figure S5.9) V-phen symmetric full-cell testing CVs at varying scan rates.

5.6 Acknowledgements

5.7 References

[1]   X. Liu, P. G. Pickup, *J. Power Sources* **2008**, *176*, 410-416.

[2]   S. Zhang, N. Pan, *Adv. Ener. Mater.* **2015**, *5*.

[3]   C. Xiong, Q. Yang, W. Dang, M. Li, B. Li, J. Su, Y. Liu, W. Zhao, C. Duan, L. Dai, *J. Power Sources* **2020**, *447*, 227387.

[4]   N. H. Basri, M. Deraman, R. Daik, M. T. M. Ayob, M. I. Sahri, N. S. M. Nor, B. N. M. Dolah, S. Soltaninejad, *Advanced Materials Research* **2015**, *1112*, 236-240.

[5]   G. Pognon, T. Brousse, D. Bélanger, *Carbon* **2011**, *49*, 1340-1348.

[6]   M. Toupin, D. Bélanger, I. R. Hill, D. Quinn, *J. Power Sources* **2005**, *140*, 203-210.

[7]   P. L. Taberna, P. Simon, J. F. Fauvarque, *J. Electrochem. Soc.* **2003**, *150*, A292-A300.

[8]   G. Pognon, C. Cougnon, D. Mayilukila, D. Belanger, *ACS Appl Mater Interfaces* **2012**, *4*, 3788-3796.

[9]   P. J. Hall, M. Mirzaeian, S. I. Fletcher, F. B. Sillars, A. J. R. Rennie, G. O. Shitta-Bey, G. Wilson, A. Cruden, R. Carter, *Energy Environ. Sci.* **2010**, *3*.

[10]   Z. Ji, N. Li, M. Xie, X. Shen, W. Dai, K. Liu, K. Xu, G. Zhu, *Electrochim. Acta* **2020**, *334*, 135632.

[11]   T. Brousse, D. Bélanger, J. W. Long, *J. Electrochem. Soc.* **2015**, *162*, A5185-A5189.

[12]   S. Mallakpour, A. Abdolmaleki, M. Mahmoudian, A. A. Ensafi, M. M. Abarghoui, *Journal of Materials Science* **2017**, *52*, 9683-9695.

[13]   X. Liu, T. A. Huber, M. C. Kopac, P. G. Pickup, *Electrochim. Acta* **2009**, *54*, 7141-7147.

[14]   X. Liu, P. G. Pickup, *J. Electrochem. Soc.* **2011**, *158*, A241-A249.

[15]   H. M. Fruehwald, R. B. Moghaddam, O. V. Zenkina, E. B. Easton, *Catal. Sci. Technol.* **2019**, *9*, 6547-6551.

[16]   J. Zhou, S. Xu, L. Ni, N. Chen, X. Li, C. Lu, X. Wang, L. Peng, X. Guo, W. Ding, *J. Power Sources* **2019**, *438*, 227047.

[17]   F. Fusalba, P. Gourec, D. Villers, D. Belanger, *J. Electrochem. Soc.* **2001**, *148*, A1-A6.

[18]   H. M. Fruehwald, I. I. Ebralidze, O. V. Zenkina, E. B. Easton, *ChemElectroChem* **2019**, *6*, 1350-1358.

[19]   H. M. Fruehwald, O. V. Zenkina, E. B. Easton, *ECS Transactions* **2019**, *92*, 523-532.

[20]   R. D. L. Smith, P. G. Pickup, *Electrochim. Acta* **2009**, *54*, 2305-2311.

[21]   H. M. Fruehwald, I. I. Ebralidze, P. D. Melino, O. V. Zenkina, E. B. Easton, *J. Electrochem. Soc.* **2020**, *167*, 084520.

[22]   J. Tian, A. Morozan, M. T. Sougrati, M. Lefevre, R. Chenitz, J. P. Dodelet, D. Jones, F. Jaouen, *Angew. Chem. Int. Ed. Engl.* **2013**, *52*, 6867-6870.

[23]   A. D. Pauric, A. W. Pedersen, T. Andrusiak, E. B. Easton, *J. Electrochem. Soc.* **2010**, *157*, B370-B375.

[24]   H. Schulenburg, S. Stankov, V. Schünemann, J. Radnik, I. Dorbandt, S. Fiechter, P. Bogdanoff, H. Tributsch, *J. Phys. Chem. B* **2003**, *107*, 9034-9041.

[25]   J.-Y. Choi, D. Higgins, Z. Chen, *J. Electrochem. Soc.* **2011**, *159*, B86-B89.

[26]   A. Zitolo, V. Goellner, V. Armel, M. T. Sougrati, T. Mineva, L. Stievano, E. Fonda, F. Jaouen, *Nat. Mater* **2015**, *14*, 937-942.

[27]   L. Wang, L. Zhang, J. Zhang, *Electrochim. Acta* **2011**, *56*, 5488-5492.

[28]   A. K. Farquhar, M. Supur, S. R. Smith, C. Dyck, R. L. McCreery, *Adv. Ener. Mater.* **2018**, *8*, 1-9.

[29]   Y. Dai, S. He, L. Yu, J. Liu, L. Gan, M. Long, *Journal of Physics and Chemistry of Solids* **2019**, *129*, 122-127.

[30]   N. Cai, J. Fu, H. Zeng, X. Luo, C. Han, F. Yu, *Journal of Alloys and Compounds* **2018**, *742*, 769-779.

[31]   B. D. Ossonon, D. Bélanger, *Carbon* **2017**, *111*, 83-93.

[32]   M. Sun, D. Davenport, H. Liu, J. Qu, M. Elimelech, J. Li, *J. Mat. Chem. A* **2018**, *6*, 2527-2539.

[33]   W. Wang, Y. Yang, X. Wang, Y. Zhou, X. Zhang, L. Qiang, Q. Wang, Z. Hu, *New J. Chem.* **2019**, *43*, 6380-6387.

[34]   B. Liu, W. Dai, Z. Liang, J. Ye, L. Ouyang, *Int. J. Hydrog. Energy* **2017**, *42*, 5908-5915.

[35]   X. Zhang, Y. B. Mollamahale, D. Lyu, L. Liang, F. Yu, M. Qing, Y. Du, X. Zhang, Z. Q. Tian, P. K. Shen, *J. Catal.* **2019**, *372*, 245-257.

[36]   L.-F. Chen, Z.-H. Huang, H.-W. Liang, W.-T. Yao, Z.-Y. Yu, S.-H. Yu, *Energy Environ. Sci.* **2013**, *6*.

[37]   G. Wang, X. Sun, J. Bai, L. Han, *Journal of Materials Science: Materials in Electronics* **2019**, *30*, 4665-4675.

[38]   A. D. Pauric, B. J. MacLean, E. B. Easton, *J. Electrochem. Soc.* **2011**, *158*, B331-B336.

[39]   A. L. Eckermann, D. J. Feld, J. A. Shaw, T. J. Meade, *Coord Chem Rev* **2010**, *254*, 1769-1802.

[40]   Y. Shu, J. Maruyama, S. Iwasaki, S. Maruyama, Y. Shen, H. Uyama, *J. Power Sources* **2017**, *364*, 374-382.

[41]   R. D. Smith, P. G. Pickup, *Electrochem. Commun.* **2009**, *11*, 10-13.

[42]   J. A. Cobos-Murcia, L. Galicia, A. Rojas-Hernández, M. T. Ramírez-Silva, R. Álvarez-Bustamante, M. Romero-Romo, G. Rosquete-Pina, M. Palomar-Pardavé, *Polymer* **2005**, *46*, 9053-9063.

[43]   X. Bao, Q. Zhao, H. Wang, K. Liu, D. Qiu, *Inorganic Chemistry Communications* **2013**, *38*, 88-91.

Chapter 6. Dual Role of the Carbon Materials Functionalized by Nitrogenous Ligands for Energy Storage and Production: Fuel cells and Supercapacitors.

6.0 Preface

In this chapter, the exploration of the use of the surface modification using diazonium coupling with a nitrogenous ligand (Chapter 2) to various commercial carbon supports for applications as a dual electrode material for fuel cell and supercapacitor applications. The diaonzium coupling chemistry was used to attach only the most active forms of pyridinic nitrogen using a phenazin ligand to various commercial carbon blacks that range in porosity (Vulcan XC-72, Black Pearls, Ketjen Black). The ORR activity was tested in both acidic and basic electrolytes and it was found that with the phenazin ligand, the heat treatment procedure provided the highest activity catalysts for the ORR. The charge storage application of these materials was tested and capacitance increases were seen when the nitrogen and iron were added. The heat-treatment provided a decrease in the activity due to the loss of nitrogen on the surface. The changes to the capacitance varied due to the porosity of the molecule used. Interestingly, after long-term stability testing, the sample increased in capacitance indicating that a polymerization reaction was occurring similar to the observations from Chapter 5.

6.0 Abstract

Dual-purpose fuel cell/supercapacitor materials were made by covalent embedding of phenazin-iron adducts into various commercial carbon supports (Vulcan XC-72, Black Pearls 2000, Ketjen Black 600). The diazonium coupling reaction allows controlled deposition of nitrogen functionalities to the carbon supports via the formation of the strong carbon-carbon bond between the nitrogenous ligand and carbon surface. Novel phenazin-functionalized carbon supports were prepared and fully characterized using thermogravimetric analysis, Raman spectroscopy, and BET pore size determination. Notably, the micro- and macrostructure and the porosity the carbon support drastically affected the catalytic activity of the system in oxygen reduction reaction (ORR). Interestingly, the heat treatment of the phenazin-based materials resulted in a significant increase in the ORR activity that is different from the trend we previously observed for terpyridine-based catalysts on Vulcan carbon that were demonstrating a significant decrease in the activity after heat treatment. Furthermore, the potential of the same materials to be used for energy storage was explored and their performance as supercapacitors was studied. The modification of the carbon surface by phenazin ligand shows significant improvement of the specific capacitance when examined in acidic media. Coordination of iron to the surface results in a further increase of the specific capacitance due to the additional Faradaic contributions. Interestingly, the heat treatment process was found to decrease the energy storage ability of the materials with a significant decrease of the specific capacitance. Thus, for phenazin-based materials, the heat treatment is a necessary step for the production of effective ORR catalysts but is undesirable for materials targeting mainly energy storage applications.

6.1 Introduction

The strong dependence of human society on fossil fuels resulted in a global crisis that initiated pronounced climate change. To mitigate the damage done by the burning of fossil fuels, the development of low-cost and efficient renewable energy systems has become important in today's society[1]. Some examples of efficient renewable energy technologies include developments in fuel cells, electric vehicles, and energy storage devices.

Fuel cells are ideal clean energy devices for stationary, portable, and transportation applications. Fuel cells utilize chemical energy in the form of hydrogen and oxygen and convert it to electrical energy[2]. To perform the reactions at the anode and the cathode, typically a platinum-coated carbon (Pt/C) catalyst is required. However, the oxygen reduction reaction (ORR) that occurs at the cathode, is often quite sluggish and thus requires high Pt loadings to reduce the overpotentials and make the device efficient[3-4]. Since platinum is a rare-earth, very expensive metal, to lower the cost while maintaining efficiency, alternative cathode materials are required[5-10].

Replacements for the Pt/C catalyst at the cathode currently rely on the use of non-precious metal catalysts (NPMCs). NPMCs are typically carbon-based catalysts, additionally enriched by nitrogen, and a transition metal(s)[3, 11-13]. It is commonly believed that nitrogenous centers, upon coordination with suitable middle or late transition metals, act as active sites to catalyze ORR. Research in this area rapidly expanded after a seminal report of Dodelet and coworkers that first defined a plausible active site of NPMCs that is responsible for the ORR. The active sites were created by pyrolysis of the carbon support, with a suitable iron precursor under nitrogen and/or ammonia atmosphere, to produce what is referred to as a Fe-N_{2+2}/C active site within the crystallites of the carbon support[12]. Thus, the major focus in the literature in the area has been placed on the development of high-performing catalysts prepared via high-temperature pyrolysis (above 900ºC), as the heating was believed to be an essential factor to form ORR active sites in the catalyst[7, 14-17]. However, this synthetic procedure has serious limitations. Indeed, high-temperature treatment results in a wide distribution of nitrogen-containing functional groups on the carbon support (pyridine, pyrrole, amide, and many other functionalities), where pyridinic nitrogens are widely believed to be the main contributor of higher activity[18-21] while pyrrolic nitrogens are believed to lower the activity of the catalyst. Thus, the abovementioned method yields little to no control over the type of nitrogen functionalities that form on the surface, some of which may be more beneficial to the ORR activity than others. That raises concerns of reproducibility and overall feasibility of this methodology for producing NPMCs and hampers their immediate application in industry for clean energy production.

For society to embrace the notions of clean energy production and consumption, feasible systems for energy conversion *and* energy storage need to be developed. Electric double-layer capacitors (EDLC) are an effective means of energy storage, as they are able to stockpile and rapidly release large amounts of energy in small timeframes, if necessary, which is essential for electric vehicles[22]. As well, EDLCs generally have longer cycle life cycles when compared to batteries[23]. EDLCs are typically made from carbon materials due to the abundance, mechanical stability, surface area, and favourable electronic properties that carbon-based materials possess[24]. However, the majority of reported systems demonstrate relatively low energy density[1, 25]. Doping of carbon materials with transition metals allows increasing charge storage and energy density capabilities of resulting EDLCs. The ability of the metals to store and deliver charge within a system (Faradaic activity) is based on the changes in the oxidation state(s) of the metals under respective redox potentials. Unfortunately, typically used dopants are rare earth expensive metals such as ruthenium (Ru) oxide[26-28]. While doping with Ru greatly aids in the ability of the materials to store charge, this is not a sustainable solution for energy storage[29].

To overcome these issues, a lot of research was done to explore the effect of doping the carbon materials with heteroatoms (i.e. nitrogen, boron, sulfur, phosphorous) to avoid usage of rare earth metals. The addition of heteroatoms has been shown to improve electronic properties (conductivity), aid in wettability, increase the cycling stability, and as a result, significantly increase the capacity of these materials[25, 30-32]. Using heteroatoms as dopants for carbon materials is a simple and effective way to impart additional pseudocapacitive behavior through Faradaic reactions between the heteroatoms and the electrolyte[33-34]. A vast majority of current literature has gone into the development of nitrogen-doped materials to further improve the energy and power density without the need for rare metals. Most of the research has adopted high-temperature thermal treatment methods to introduce nitrogen functional groups onto the surface of the carbon materials[35-38]. The high temperature regime required for the synthesis of these materials significantly elevates the cost of the materials and handicaps scale-up of the production for commercial applications. In addition, during heat treatment, non-homogenous distribution of heteroatoms on the surface of the carbon material is often observed. Inhomogeneity of the material may lead to different properties within different domains of the material which

may affect its suitability for device manufacturing. Domains with distinctly different properties (charge storage, electron transfer and diffusion properties) may lead to the formation of the localized areas/centers within the material that are prone to overheating and will result in a shortage and fast deterioration of the devices. It is important to be able to produce materials with homogenous distribution of the specific desired types of nitrogen functionalities (pyridine moieties) and to be able to fully control and tune the process, to get desired properties of the materials in the most reproducible way. The controlled, covalent deposition of molecularly defined nitrogenous moieties into carbon supports is a promising way to build novel materials for future generations of supercapacitor electrodes with high efficiency and extended durability. Interestingly, the additional incorporation of transition metals into these materials significantly imparts charge storage mechanisms of the device due to the Faradaic redox reactions occurring between the transition metal on the electrode surface and the electrolyte[23]. This is believed to further increase the capacity and the lifetime of the devices[1].

The combination of nitrogen-enriched carbon surfaces with non-precious metals is actively utilized to produce both effective fuel cells and supercapacitors, but rarely is the utility of such materials for both applications considered in the literature, even when synthetic methodologies are similar. Even the carbon types, such as high surface area carbon supports, are attractive and sought after in both applications. Notably, despite their similarities of N-functionalized carbons in materials design the two applications are rarely studied together using one common material. Here, we explore the potential of nitrogen and iron-doped materials for dual-purpose application: for both energy storage and generation (SC and FC, respectively).

Previously, we have explored ORR performance of the model active site created using the molecular imprinting of a terpyridine (tpy) moiety onto a commercial Vulcan carbon[39-42]. The diazonium coupling chemistry allows strong covalent embedding of the defined tpy functionality onto the carbon support via the formation of a strong carbon-carbon bond with the support. This deposition strategy allows to preserve the structure of the tpy unit and grants good exposure of the most active pyridinic nitrogens on the surface of the support. Following coordination of iron to the chelating nitrogenous tpy unit at ambient conditions creates the desired $Fe-N_3/C$ model active site for the ORR. The resulting

catalysts demonstrated high ORR activity without the need for high-temperature heat treatment procedures.

In this work, we are building on the fundamental surface modification approach targeted to attach only specific active catalytic sites onto carbon supports[42]. Here, the dipyrido[3,2-a:2',3'-c]phenazin-11-amine (phenazin) ligand (Scheme 6.1) via diazonium coupling was chemically embedded into different carbon supports and then the nitrogenous units on the surface were further reacted with the iron precursor to create active catalytic sites by the formation of metal-ligand coordination adducts. To evaluate the effect of the available surface area and type of porosity of the carbon supports, commercially available carbons with a wide range of surface areas (Vulcan XC-72, Black Pearls 2000, and Ketjen Black 600) were used and ORR activity of resulting materials was compared. The materials were tested for dual applications: as catalysts for the ORR and supercapacitor applications. We demonstrate a series of novel materials that show beneficial activity for both energy production (active catalyst for ORR in FC) and energy storage (SC).
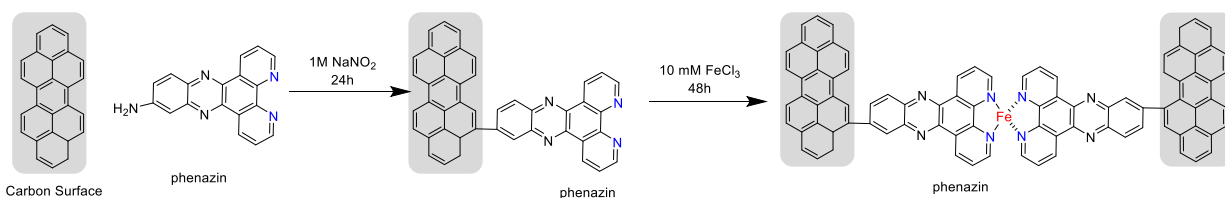
Scheme 6.1) Molecular structure of the phenazin ligand and diazonium coupling reaction scheme with the carbon supports.

6.2 Experimental

6.2.1 Materials

Sulfuric acid, potassium hydroxide, sodium nitrite, methanol, ferric chloride, Nafion® perfluorinated solution, isopropyl alcohol, 4-nitro-o-phenylenediamine, Pd/C (10%), hydrazine hydrate (50-60%), and 60% polyfluoroethylene in water perparation were purchased from Sigma-Aldrich. Phenanthroline-5,6-dione was synthesized according to the method reported by Bodige et al[43]. Vulcan XC-72 and Black Pearls 2000 was purchased from Cabot corporation. Ketjen Black 600 and TPG-H-090 Toray Paper 30% Wet Proofing Carbon Fibre paper was purchased from Fuel Cell Earth LLC.

6.2.2 Synthesis of dipyrido[3,2-a:2',3'-c]phenazin-11-amine (phenazin), 2

The amino-substituted phenazin, **2**, was synthesized through reduction of the nitro precursor, **1**, according to the following reaction scheme:
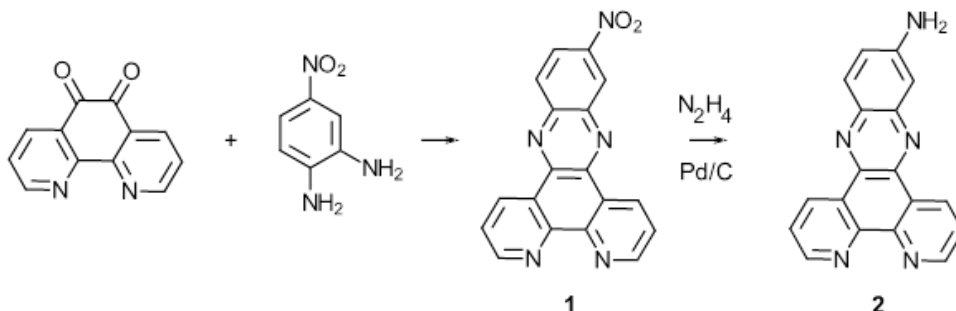
Scheme 6.2) Synthesis of phenazin molecule.

1: Phenanthroline-5,6-dione (1.00 g, 4.75 mmol) was dissolved in stirring ethanol (40 mL) with heating, under an argon atmosphere. Addition of 4-nitro-*o*-phenylenediamine (0.73 g, 4.77 mmol) to this solution caused an immediate color change from golden to deep red/violet. The solution was heated to reflux temperature for 3 hours, yielding a beige-colored suspension. After cooling the mixture in the freezer, overnight, the suspension was filtered and washed with a small quantity of ice-cold ethanol. The solid residue was then dried in an oven at 100 ºC for one hour before collecting: 1.39 g, 4.25 mmol, 89%. ^{1}H NMR (CDCl$_3$, 400 MHz): δ = 9.64 (m, 2H), 9.33 (m, 2H), 9.29 (d, J = 2.5 Hz, 1H), 8.68 (dd, J = 9.3, 2.5 Hz, 1H), 8.51 (d, 9.3 Hz, 1H), 7.85 (m, 2H) ppm.

2: Compound **1** (1.00 g, 3.06 mmol) and Pd/C (162 mg, 0.15 mmol, 5 mol% Pd) were stirred in ethanol (50 mL) under argon. Hydrazine hydrate (1.2 g, ~18 mmol) was added and the mixture was brought to reflux temperature for approximately 16 hours. It was then allowed to cool to room temperature before vacuum filtering over Celite. Washing with a copious amount of hot ethanol yielded an orange filtrate. Evaporation of the solvent afforded the product (0.89 g, 2.99 mmol, 98%). ^{1}H NMR (CDCl$_3$, 400 MHz): δ = 9.61 (dd, J = 8.2, 1.9 Hz, 1H), 9.57 (dd, J = 8.2, 1.9 Hz, 1H), 9.25 (dd, J = 4.5, 1.8 Hz, 1H), 9.22 (dd, J = 4.5, 1.8 Hz, 1H), 8.15 (m, 1H), 7.77 (m, 2H), 7.37 (m, 2H), 4.42 (s, 2H) ppm.

6.2.3 Modification of carbon surfaces

Commercial carbon blacks (Vulcan XC-72, Black Pearls 2000 and Ketjen Black 600) were modified with dipyrido[3,2-a:2',3'-c]phenazin-11-amine (phenazin) using

previously published procedures[41-42, 44]. Briefly, equal volumes of 10 mM solution of phenazin in methanol was reacted with a 1 M solution of $NaNO_2$ for 3 minutes before it was added to ca. 600 mg of either Vulcan XC-72, Black Pearls 2000, or Ketjen Black 600. The mixture was stirred overnight, then separated by gravity filtering. The solid fraction was washed with methanol and deionized water 3 times before drying in the oven. This produced either V-phenazin, BP-phenazin, or KB-phenazin materials, respectively. Iron was coordinated by reacting a 10-fold excess of $FeCl_3$ with respect to the ligand (20 mL of 10 mM $FeCl_3$) of the nitrogen modified carbon supports, for 48 hours, while stirring at room temperature. Materials were gravity filtered and washed 3 times with methanol and deionized water prior to drying in the oven (130 ºC, overnight) to produce V-phenazin-Fe, BP-phenazin-Fe, KB-phenazin-Fe. A portion of the Fe-coordinated materials were heat-treated in a tube furnace at 700ºC for 2 hours at a heating rate of 10ºC min^{-1} under a N_2 atmosphere flowing at 80 mL min^{-1}. These samples are denoted as V-phenazin-Fe-700, BP-phenazin-Fe-700, and KB-phenazin-Fe-700.

6.2.4   Physical Characterization

The materials were characterized using thermogravimetric analysis (TGA) via a TA instruments Q600 SDT thermal analyzer. The materials were run using a heating rate of 5ºC min^{-1} from room temperature to 1000ºC while flowing either air or argon atmosphere at 20 mL min^{-1}. Pore size determination was performed via a Quantachrome NOVAe 1200 pore analyzer using N_2 as the adsorbate. Raman spectra were collected using a Renishaw inVia confocal Raman microscope with a 2400 1 mm^{-1} (vis) grating. The excitation wavelength of the Nd:YAG laser (Renishaw) was 532 nm. Spectra were collected using an exposure time of 30 seconds per scan at a 1% laser power (50 mW) and a 50x objective. Scanning electron microscopy (SEM) images were collected using a HITACHI FlexSEM 1000. Beam energy was 5 kV using a working distance of 5 mm and a spot size of 20 nm. XPS analysis was performed using a Thermo Nexsa XPS with a monochromated Al Kα X-ray source (1486.7 eV). The data was analyzed using Advantage software and the spectra were baselined using the Smart algorithm. The elemental ratios were calculated by using Wagner sensitivity factors[45].

6.2.5 Electrochemical Characterization

The oxygen reduction reaction (ORR) was performed using a rotating ring-disk electrode (RRDE) in O_2-saturated 0.1 M H_2SO_4 or 0.1 M KOH electrolytes. Catalyst inks were prepared by adding together 10 mg of catalyst, 400 µL of 50:50 deionized water to isopropyl alcohol, and 100 µL Nafion® (to achieve a 95-to-5 catalyst to Nafion® ratio). The inks were ultra-sonicated for 15 minutes, then left to stir overnight prior to usage. For the deposition, 3 µL of catalyst ink was placed onto a 0.196 cm^2 glass carbon electrode, to obtain a 305 µg cm^{-2} catalyst loading, and the electrode was rotated and dried under heat to produce the homogeneously distributed catalyst layer. The electrode was placed in the electrochemical cell that contained either 0.1 M H_2SO_4 or 0.1 M KOH, a graphite counter electrode, and a mercury/mercury sulfate reference electrode. To collect cyclic voltammograms (CV), a N_2-saturated solution of the corresponding electrolyte was scanned at 20 mV s^{-1} prior to the ORR measurements, as well as a RRDE background scan at 10 mV s^{-1}, in order to subtract the background currents. RRDE measurements were performed in the presence of O_2 at a scan rate of 10 mV s^{-1} while the ring was held at 1.2 V vs RHE. The measurements were made on a Pine Instruments model AFPC2 and Pine WaveDriver 20 with the corresponding Aftermath software.

For performance testing the supercapacitor materials were studied in the 3-electrode configuration by using CV, electrochemical impedance spectroscopy (EIS) and galvanostatic charge-discharge measurements (GCD) in 0.5 M H_2SO_4. The inks for general measurements were made by dispersing 19 mg of active electrode material and 1 mg of 10% polytetrafluoroethylene (PTFE) into 700 mL of isopropanol. This mixture was sonicated for 15 minutes then stirred overnight before use. The inks were painted on 1 cm^2 carbon fiber paper (CFP) electrodes resulting in a active material loading of ca. 2 mg cm^{-2}. Each electrode was placed in a cell containing 0.5 M H_2SO_4 that was purged with N_2 gas for ca. 20 minutes. An Ag/AgCl double junction reference electrode was used along with a graphite counter electrode. The electrochemical measurements were performed using a Solartron Analytical 1470E potentiostat connected to a Solartron SI 1260 impedance/gainphase analyzer with corresponding CView and Zplot software. Data were obtained at 200, 100, 50, 20, 10 mV s^{-1} for the CV measurements. GCD curves were performed at 0.5, 1, 2, 5, 10 A g^{-1}. Capacity retention and coulombic efficiency

measurements were performed using GCD curves at 2 A g^{-1} for 6000 cycles. EIS was performed at ca. 0.4 V vs RHE to probe the double layer and at ca. 0.7 V vs RHE that targeted the faradaic contributions for the phenazin and Fe studied from 100,000 Hz to 0.1 Hz with an AC amplitude of 10 mV and 10 steps decade^{-1}.

6.3 Results and Discussion

A series of novel phenazin-based nitrogen-enriched iron-containing materials on carbon (V-phenazin-Fe, BP-phenazin-Fe, and KB-phenazin-Fe systems on Vulcan, Black Pearls, and Ketjen Black carbon supports, respectively) were prepared and their performance as materials for electrochemical energy storage and production was examined. The materials were characterized using TGA, BET, Raman, and SEM to determine the surface characteristics and the nitrogen and Fe loading and distribution with the surface of the catalyst before electrochemical testing. In addition, to understand the effect of the iron and the role of heat-treatment nitrogen-enriched surfaces before coordination of iron (V-phenazin, BP-phenazin, and KB-phenazin systems), or after coordination of iron but prior to heat-treatment (V-phenazin-Fe, BP-phenazin-Fe, and KB-phenazin-Fe systems) were isolated, fully characterized and their performance and potential for FC and SC applications were carefully studied.

6.3.1 Physical Characterization

Thermogravimetric analysis (TGA) was performed for all of the materials under air atmosphere (Figure 6.1). The combustion of the carbon supports occurred at ca. 500ºC for the Vulcan, Black Pearls, and Ketjen Black commercial carbon supports. Upon addition of the phenazin ligand the combustion temperature for all the carbon supports was lowered to ca. 350-450 ºC depending on the nature of carbon support. This occurs due to changes in the structure of carbon support upon modification with the ligand. After Fe coordination, the combustion temperature of all the materials was further lowered which could be contributed to the additional changes in the carbon support structure and/or the influence of iron that under these conditions could act as a combustion catalyst. We have previously observed a similar trend with a terpyridine-based ligand on the same type of carbon supports[39, 41-42]. In the differential thermogram (DTG) two peaks are present after the modification with the ligand which indicates the combustion of both the ligand and the carbon. The determination of Fe wt% via TGA is taking into account any ash content was

determined and presented in Table 6.1. The amounts of iron in the samples were ranging from ca. 2-5 wt% which are similar loadings to our previous materials.
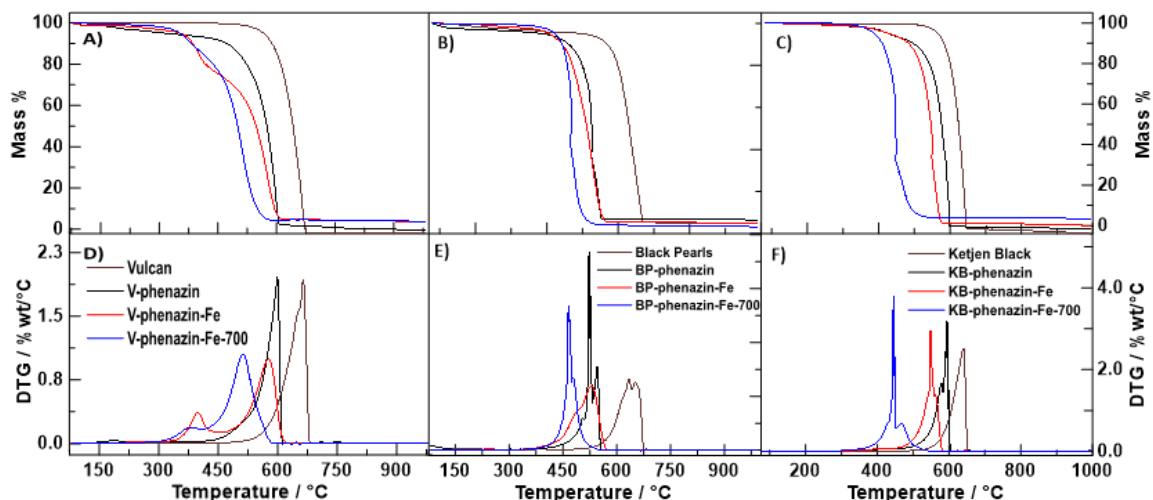
Figure 6.1) (A) TGA of Vulcan materials in air at a heating rate of 5 ℃ min[-1] (B) TGA of Black Pearls materials in air at a heating rate of 5 ℃ min[-1] (C) TGA of Ketjen black material in air at a heating rate of 5 ℃ min[-1] (D) DTG of Vulcan materials in air at a heating rate of 5 ℃ min[-1] (E) DTG of Black pearls in air at a heating rate of 5 ℃ min[-1] (F) DTG of Ketjen black material in air at a heating rate of 5 ℃ min[-1].

Pore size analysis was performed on the materials to determine how the specific surface area of the carbon supports changes upon modification with the phenazin and iron (Table 6.1). The nitrogen isotherms and the pore size distributions are presented in Figure S6.2. For all the materials, after the addition of the phenazin, the respective surface areas of each carbon support declined. We have attributed this to the bulkiness of the phenazin ligand that may hinder some access to the pores, which results in the overall decrease of the surface area[35, 42, 46]. After heat-treatment, the surface area increase, this is due to partial degradation of the phenazin structure on carbon surface after the heat-treatment which may reinstate the access the pores previously blocked by the ligand. Nonetheless, the materials remain quite porous with high surface areas. The pore volume of all the catalysts followed a similar trend as well, when the phenazin and Fe were added the measured pore volumes decreased due to blockage of some of the pores with the bulky phenazin molecule. Most of the pore volume was subsequently restored when the sample was heat treated. As well, changes in the pore sizes are observed, where the Black Pearls and Ketjen Black had smaller pore sizes compared to the Vulcan. This is expected as the Black Pearls and Ketjen

Black are more microporous than the Vulcan. This is important as the higher surface area may facilitate the formation of active sites on the surface and will accommodate the efficient movement of the electrolyte through the pores to ensure beneficial electrochemical charge storage properties[38, 47-48].

Detailed Raman spectroscopy analysis was performed on the materials (Figure S6.3) to observe changes in the carbon supports upon additions of the phenazin ligand. The I_D/I_G ratios were calculated for each materials D-band (1350 cm^{-1}) and G-band (1500 cm^{-1}) and are presented in Table 6.1. Upon modification of the carbon supports with phenazin ligand, there is a detectable decrease in the I_D/I_G ratio, which is characteristic of the increased graphitization of the material[32, 39, 49-50]. Upon Fe coordination, the I_D/I_G ratio was increasing for the majority of systems which may indicate some disturbances in the lattice of the carbon due to the addition of iron[31, 50-53]. After heat-treatment the I_D/I_G ratio further elevates due to a plausible increase in the graphitization and partial decomposition of the ligand on the carbon surface due to heat-treatment.

Table 6.1) Physical characterization data for the carbon modified materials.

Material	TGA / Fe wt%	BET Surface Area / m^2 g^{-1}	Pore Volume / cm^3 g^{-1}	Pore diameter / Å	I_D/I_G ratio
Vulcan XC-72	-	236	0.317	26.8	1.43
V-phenazin	-	62	0.105	33.9	1.33
V-phenazin-Fe	4.7%	55	0.107	38.9	1.44
V-phenazin-Fe-700	4.5%	98	0.118	24.0	1.45
Black Pearls	-	1431	1.224	17.1	1.63
BP-phenazin	-	1315	1.218	18.5	1.57
BP-phenazin-Fe	5.3%	1373	1.383	20.1	1.39
BP-phenazin-Fe-700	3.9%	1369	1.345	19.6	1.53
Ketjen Black	-	1658	2.071	24.9	2.35
KB-phenazin	-	416	0.578	27.7	2.12
KB-phenazin-Fe	1.7%	121	0.161	26.6	1.90
KB-phenazin-Fe-700	-	1122	1.411	25.1	2.17

The detailed morphologies of the materials studied using SEM (Figure 6.2) are consistent with what is expected for each of the carbon supports, indicating that the

modification with the phenazin and iron yielded homogenous coverage on the surface of each support. The samples demonstrated homogenous morphology with no significant grains or agglomerates of different nature observable by SEM. The higher surface area carbons (Black Pearls and Ketjen Black) show higher porosities in the SEM images which is expected and beneficial for SC applications since high electrode porosity is linked to high energy density output[54]. Notably, all materials show the extended 3D porous structure of the carbon which is ideal for applications for SC devices as porous networks ensure efficient facile movement of the ions in the electrolyte needed for effective charge storage performance of the materials.
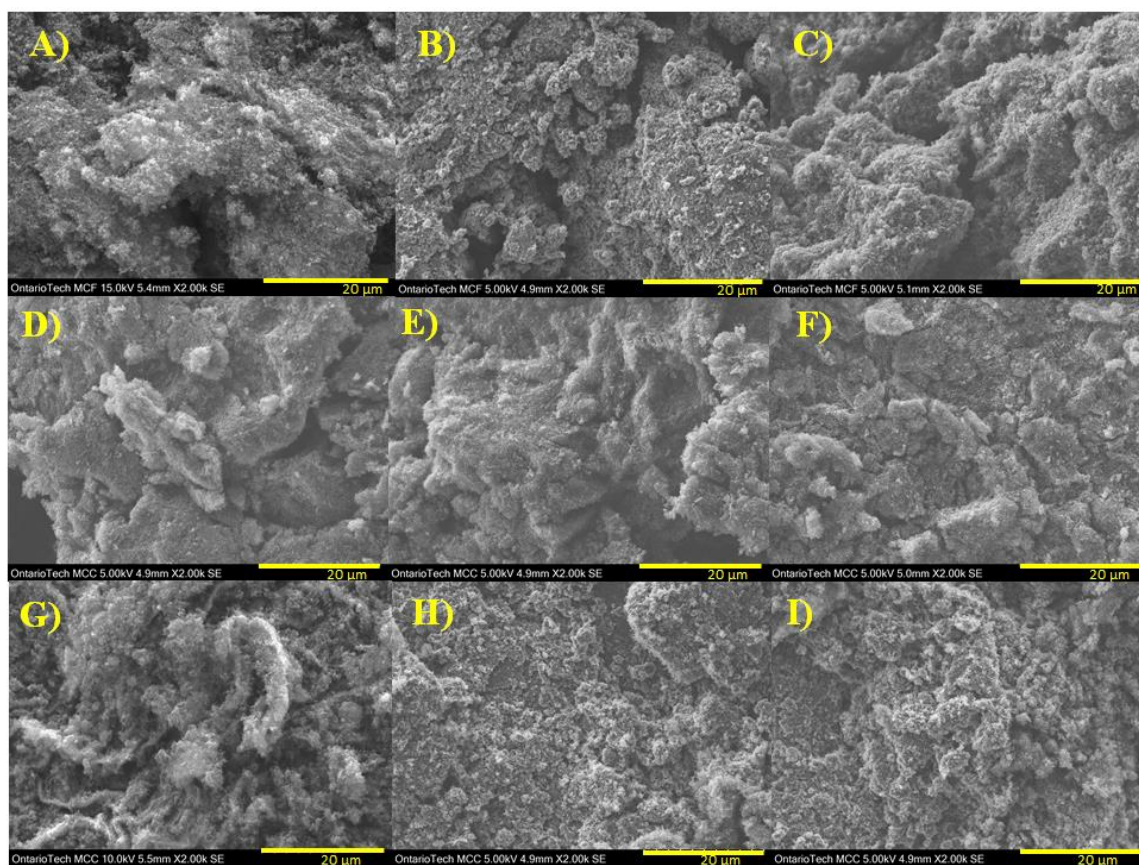
Figure 6.2) SEM image of (A) V-phenazin (B) V-phenazin-Fe (C) V-phenazin-Fe-700 (D) BP-phenazin (E) BP-phenazin-Fe (F) BP-phenazin-Fe-700 (G) KB-phenazin (H) KB-phenazin-Fe (I) KB-phenazin-Fe-700

XPS analysis was performed on all the catalysts and the results are presented in Table 6.2 and Figures S6.27-6.35. In all the samples the main components of the materials are carbon with greater than 90 At %. For all the samples they have a main C 1s peak that is centered at ca. 283.9 eV which correspond to mainly carbon. Two other small

deconvoluted peaks that appear in all samples are at 285.8 and 288.6 eV these correspond to C-N and C=O peaks in the material. These results indicate that for all the V, BP, and KB samples that the supports are predominantly carbon in nature.

The XPS spectra of the V-phenazin-Fe (Figure S6.28) confirms that there is the presence of both iron and nitrogen in the samples. The N 1s region shows the presence of 2 peaks at 399.4 and 401.6 eV that are characteristic of N_{pyr} and $N_{nitrate}$ atoms, respectively[55]. In the Fe 2p region there are two peaks present Fe $2p_{3/2}$ and Fe $2p_{1/2}$ at 712.0 and 725.1 eV, respectively. This peak is characteristic of Fe^{3+} ions in the material[41]. The ratios between the iron and nitrogen is Fe:N_{pyr}:$N_{nitrite}$ is 1.5:9.9:3.4. These results confirm there is an excess of some non-reacted pyridinic groups on the surface. Interestingly, after the heat-treatment procedure the ratios of Fe:N_{pyr} decrease to 0.3:6.3 indicating the loss of nitrogen and iron functionalities as seen through the BET and TGA results.

BP-phenazin-Fe also contained the iron and nitrogen atoms. The nitrogen XPS spectra (Figure S6.31) shows the same peaks as observed in the Vulcan samples. There is a N_{pyr} present at 399.1 eV and a $N_{nitrate}$ peak at 402.7 eV. Again, the two peaks that are related to Fe^{3+} are present in the Fe spectra: Fe $2p_{3/2}$ at 711.9 eV and Fe $2p_{1/2}$ at 724.69 eV. The ratio of the Fe:N_{pyr} in this sample is 0.07:0.5 which means there is a significant amount of free N_{pyr} on the surface of the materials. Interesting to note again that the heat treatment procedure lowered the ratios of the Fe:N_{pyr} to 0.03:0.5 which indicates a loss of Fe.

Finally, with the KB-phenazin-Fe sample the nitrogen and iron is seen on the carbon through the XPS results (Figure S6.34). Similar to the BP and V samples, there are peaks corresponding to N_{pyr} at 399.1 eV and $N_{nitrate}$ at 403.5 eV. Again, there are two peaks due to the Fe^{3+}: Fe $2p_{3/2}$ at 711.9 eV and Fe $2p_{1/2}$ 724.6 eV. The ratio of the Fe:N_{pyr} in the sample is 0.05:0.8 which is different from the V and BP materials which still had some free N_{pyr} in the materials. Again, after heat-treatment the N and Fe ratios decline to Fe:N_{pyr} 0.05:0.6, indicating a loss of nitrogen functionalities in the material.

Table 6.2) XPS atomic % for the carbon modified materials.

Material	XPS At% N	XPS At% Fe
Vulcan XC-72	-	-
V-phenazin	3.7	-
V-phenazin-Fe	2.0	6.71
V-phenazin-Fe-700	2.2	2.87
Black Pearls	-	-
BP-phenazin	2.7	-
BP-phenazin-Fe	2.5	1.1
BP-phenazin-Fe-700	3.3	0.1
Ketjen Black	-	-
KB-phenazin	2.4	-
KB-phenazin-Fe	2.4	0.8
KB-phenazin-Fe-700	1.5	0.7

6.3.2 Electrochemical Characterization

Cyclic voltammetry (CV) of all the carbon supports modified with the phenazin and Fe were performed in both acid and base electrolyte (Figure S6.4-5). For the Vulcan support, upon modification with the phenazin, 3 peaks appear in the CV. We have previously identified the peak at 0.6 V vs RHE to pyridinic nitrogens. This is due to the exposed pyridinic nitrogen from the phenazin ligand modified on the carbon support[40-42]. Two additional peaks attributed to being characteristic of the phenazin appear: one at high potentials (0.9 V) and one at low potentials (0.1 V). Upon addition of iron, the peak at 0.6 V becomes larger and broader due to the additional redox potential of the coordinated $Fe^{2+/3+}$ at 0.7 V. Interestingly, when the V-phenazin-Fe was heat-treated, the high and low potential peaks were no longer present and collapse to a single broad peak at ca. 0.6 V. This is likely due to the partial degradation of the ligand when the material is heat-treated. This same trend is similarly seen with the KB and BP supports, where the peaks at 0.1 V

and 0.6 V are still observed. However, the high potential peak at 0.9 V was not clearly detectable for the BP-phenazin and KB-phenazin samples due to the highly capacitive nature of the supports hindering the observation of this peak.

6.3.2.1 Oxygen Reduction Reaction Activity

Ideal catalyst for ORR should have high onset potentials (as close or higher than onset of Pt/C of 0.90 V vs RHE) and proceed via 4-electron pathway that results in the direct formation of the desired product, H_2O and majorly avoiding formation of high amounts of H_2O_2 that involve the transfer of only 2 electrons. The potential of the materials to catalyze oxygen reduction reaction (ORR) was studied in acidic media using a rotating ring-disk electrode (RRDE). The V-phenazin demonstrated quite low ORR activity. The system did not reach high currents or limiting currents, indicating that the process was largely diffusion limited. The onset potential of this material was quite poor at ca. 0.25 V (Figure 6.3A-B). Upon addition of iron, the V-phenazin-Fe sample reached higher currents and displayed a slightly improved value of the onset potential, from 0.25 V to 0.32 V (Table 6.3) that shows the benefits from the presence of the transition metal on the activity of the materials for ORR. Interestingly, upon heat-treatment the activity of the catalyst improved significantly reaching an onset potential of 0.63 V. Interestingly, this trend is different than what we have previously seen for the Vulcan support modified tpy ligand[41]. Previous work with the tpy ligand has shown that the heat-treatment has a significant, detrimental effect on the ORR activity of the resulting catalyst. This work highlights the influence of the coordinating ligand on the activity of the catalyst for the ORR. The percentage of generated H_2O_2 and number of transferred electrons were calculated (Figure S6.6A-B) using the following equations:

$$n = \frac{4I_D}{I_R + (\frac{I_R}{N})} \tag{6.1}$$

$$\%H_2O_2 = \frac{200(\frac{I_R}{N})}{I_D + (\frac{I_R}{N})} \tag{6.2}$$

The trend seen from the onset potentials matches the results that were observed for the percent H_2O_2 formation, and the number of transferred electrons calculated using Equations 6.1 and 6.2. With the V-phenazin and V-phenazin-Fe the percent H_2O_2 remains quite high at 20-50% while the number of electrons transferred is ca. 3. After heat-treatment

the percent H_2O_2 decreases to below 20% and the number of electrons transferred also increases to ca. 3.6 which is close to the ideal 4 electron transfer pathway.

The Black Pearls materials showed very similar trends to Vulcan materials. The BP-phenazin showed quite low activity and was only very slightly improved after the addition of the iron complex to the sample (Figure 6.3C-D). Similarly, the heat-treated BP-phenazin-Fe-700 was the highest performing material on the BP support. Although the utilization of this carbon support showed increased activity after heat treatment, overall, the activity was still lower than for the materials on the lower surface area Vulcan support. The Vulcan materials demonstrated similar values of percent H_2O_2 produced, and number of electrons transferred, however, they had higher onset potentials than those of the Black Pearls materials. The percent H_2O_2 and number of electrons transferred were calculated as the reaction was monitored (Figure S6.6C-D). BP-phenazin and BP-phenazin-Fe produced 40-50% H_2O_2 and underwent a 3-electron transfer process. After the heat-treatment, the activity of these materials improved. The percentage of H_2O_2 fell to below 19% and the number of electrons transferred increased to almost 4 electrons, all of which correspond to much better performance. In previous work with the tpy- ligand modification of the carbon supports, we had determined that lower surface areas showed better overall activity for the ORR[42]. A similar trend in activity is observed here for phenazin materials on the varying carbon supports utilized as catalysts for ORR. Even after heat treatment, the onset potentials of the materials on Vulcan are still higher when compared to the related material of Black Pearls support.

Finally, the Ketjen Black materials follow a similar trend to the Vulcan and Black Pearls supports. KB-phenazin and KB-phenazin-Fe showed very low activity, with only minor improvements in the activity upon addition of the iron (Figure 6.3E-F). Notably, after heat treatment the KB-phenazin-Fe-700 onset potential improved significantly, with onset potentials approaching the values that demonstrate V-phenazin-Fe-700 catalyst. Monitoring the reaction reveals that the percent H_2O_2 production remains high at ca. 32-41% and the number of electrons transferred is close to 3 (Figure S6.6E-F). After the heat treatment step, the percent H_2O_2 production as part of ORR decreased to 12% and the number of transferred electrons achieved the desired number of 4. With KB, a higher surface area carbon, we see that after heat treatment the activity of the materials

significantly increased, approaching the activity of the Vulcan-supported catalyst. As mentioned, the Vulcan carbon had previously been identified as our best performing support for modification by the nitrogenous ligands (by derivatives of terpyridine or phenanthroline), as we observed declining activity for ORR with an increase of the surface area. We see the same trend in this work using the phenazin ligand. This work confirms that the nature of the carbon support has a dramatic effect on the activity of the materials and often dictates some of the major properties of the material[42]. We had attributed this to the formation of various types of active sites and different accessibility of catalytic sites for higher surface area carbons.
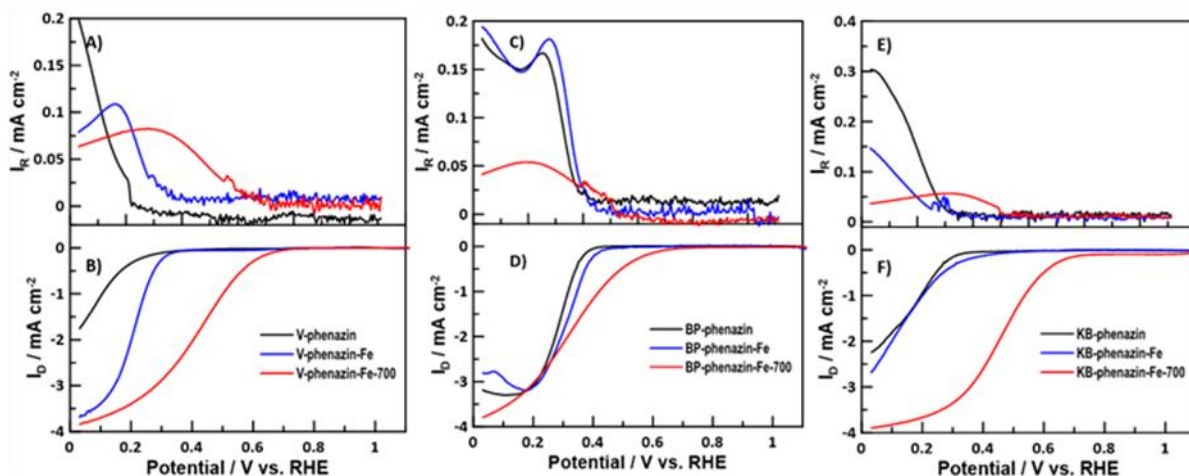
Figure 6.3) (A) Ring currents of the Vulcan materials in O_2 saturated 0.1 M H_2SO_4 at 900 rpm (B) disk currents of the Vulcan materials in O_2 saturated 0.1 M H_2SO_4 at 900 rpm (C) ring currents of the Black Pearls materials in O_2 saturated 0.1 M H_2SO_4 at 900 rpm (D) disk currents of the Black Pearls materials in O_2 saturated 0.1 M H_2SO_4 at 900 rpm (E) ring currents of the Ketjen Black materials in O_2 saturated 0.1 M H_2SO_4 at 900 rpm (F) disk currents of the Ketjen Black materials in O_2 saturated 0.1 M H_2SO_4 at 900 rpm.

Table 6.3) ORR activity of the materials in 0.1 M H_2SO_4.

Material	Onset Potential at 0.1 mA cm^{-2} / V	i_k / mA cm^{-2}	% H_2O_2 / at 0.3 V vs RHE	Number of electrons transferred / at 0.3 V vs RHE
V-phenazin	0.25 ± 0.05	0.94 ± 1.60	21.26 ± 3.59	3.57 ± 0.43
V-phenazin-Fe	0.32 ± 0.01	1.43 ± 0.67	50.54 ± 7.29	2.99 ± 0.51
V-phenazin-Fe-700	0.67 ± 0.03	11.43 ± 0.34	19.46 ± 1.61	3.61 ± 0.04
BP-phenazin	0.36 ± 0.01	2.04 ± 0.31	51.60 ± 7.33	2.97 ± 0.25
BP-phenazin-Fe	0.39 ± 0.01	2.68 ± 0.37	40.50 ± 7.71	3.19 ± 0.95
BP-phenazin-Fe-700	0.52 ± 0.02	6.15 ± 0.86	14.89 ± 3.66	3.70 ± 0.23
KB-phenazin	0.29 ± 0.01	0.13 ± 0.01	41.56 ± 9.87	3.17 ± 0.14
KB-phenazin-Fe	0.32 ± 0.01	0.37 ± 0.05	32.72 ± 6.71	3.35 ± 0.26
KB-phenazin-Fe-700	0.64 ± 0.02	13.67 ± 1.86	12.06 ± 0.65	3.76 ± 0.20

The materials were also tested for their ORR activity in basic 0.1 M KOH electrolyte (Figure 6.4). As expected, the activity of all the materials significantly improved in the basic media. This is a known phenomenon that the ORR activity increases in base since it prevents the protonation of the surface nitrogens that are easily protonated in acidic media[7, 56]. The onset potentials, number of electrons transferred, and percent H_2O_2 at 0.3 V vs RHE are presented in Table 6.4.
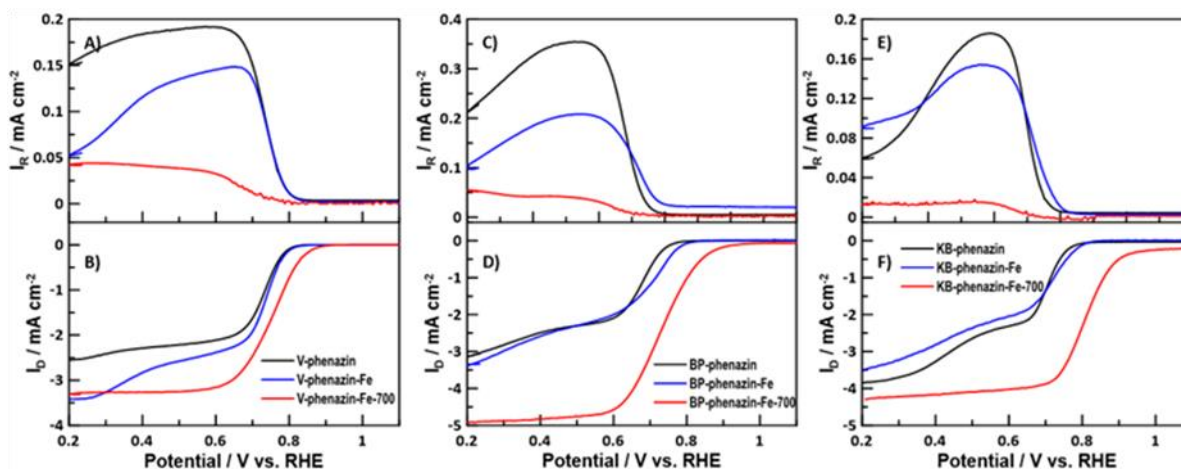
Figure 6.4) (A) Ring currents of the Vulcan materials in O_2 saturated 0.1 M KOH at 900 rpm (B) disk currents of the Vulcan materials in O_2 saturated 0.1 M KOH at 900 rpm (C) ring currents of the Black Pearls materials in O_2 saturated 0.1 M KOH at 900 rpm (D) disk currents of the Black Pearls materials in O_2 saturated 0.1 M KOH at 900 rpm (E) ring currents of the Ketjen Black materials in O_2 saturated 0.1 M KOH at 900 rpm (F) disk currents of the Ketjen Black materials in O_2 saturated 0.1 M KOH at 900 rpm.

For all types of materials (V, BP, KB) the addition of iron did not significantly affect the activity of the materials in ORR and the onset potentials were similar to the corresponding systems without iron. However, significant improvements in the ORR activity occurred after the heat-treatment procedure for all iron-containing materials. We had previously seen a similar effect with KB and BP systems using a terpyridine ligand. KB-phenazin-Fe-700 had the most dramatic increase in the onset potential after the heat-treatment procedure and the activity was the highest of all the catalysts studied. KB-phenazin-Fe-700 produced an onset potential similar to our best previous system, based on the terpyridine ligand on a KB support[42]. In the ring currents, we see the presence of a curve for all non-heat-treated materials. This correlates to the shouldering in the limiting disk currents. This is in line with "2+2" electron transfer process, where H_2O_2 is being produced first, then further converted to H_2O over the course of the reaction. In theory, this transformation could occur either on one active site or in two different types of catalytic sites on the surface of the material. Interestingly, after heat-treatment the second wave (near 0.4 V) in the disk currents disappears in both the disk and the ring currents, indicating that the active site(s) are only directly converting O_2 to H_2O. This could indicate that one of the active sites mainly responsible for the formation of by-products was effectively destroyed during the high-temperature treatment.

We used the ring and disk data to calculate the number of electrons transferred and the percent H_2O_2 over the potential range studied (Figure S6.7). For the Vulcan materials, the V-phenazin and V-phenazin-Fe samples catalyzed ORR with a transfer of ca. 3 electrons and produced higher amounts of H_2O_2 (over 20%). After heat-treatment, the ORR for the V-phenazin-Fe-700 sample behaved mainly as a 4-electron transfer process and produced below 10% H_2O_2 over the course of the reaction. We observe a similar trend in the BP systems where a 3-electron transfer process is occurring prior to heat treatment and a high amount of H_2O_2 (>20%) is being produced. After heat treatment the number of transferred electrons increases to 4 and the percent H_2O_2 remains below 10%. Finally, the KB samples follow the same trend. However, the heat-treated sample performs exceptionally well for the ORR with even lower ring currents (below 5%).

Table 6.4) ORR activity of the materials in 0.1 M KOH.

Material	Onset Potential at 0.1 mA cm^{-2} / V	i_k / mA cm^{-2}	% H_2O_2 / at 0.3 V vs RHE	Number of electrons transferred / at 0.3 V vs RHE
V-phenazin	0.77 ± 0.01	13.54 ± 0.68	42.43 ± 9.59	3.15 ± 0.24
V-phenazin-Fe	0.78 ± 0.01	18.07 ± 1.58	17.28 ± 5.18	3.65 ± 0.34
V-phenazin-Fe-700	0.85 ± 0.01	14.71 ± 2.00	9.44 ± 0.28	3.81 ± 0.01
BP-phenazin	0.73 ± 0.02	37.35 ± 4.87	53.78 ± 8.13	2.92 ± 0.13
BP-phenazin-Fe	0.77 ± 0.01	9.07 ± 1.27	25.02 ± 4.75	3.50 ± 0.36
BP-phenazin-Fe-700	0.83 ± 0.02	20.66 ± 2.82	6.58 ± 0.32	3.87 ± 0.17
KB-phenazin	0.73 ± 0.02	59.79 ± 10.26	15.03 ± 6.72	3.70 ± 0.13
KB-phenazin-Fe	0.75 ± 0.02	79.65 ± 17.28	19.83 ± 3.83	3.60 ± 0.28
KB-phenazin-Fe-700	0.86 ± 0.02	15.74 ± 2.18	2.33 ± 0.18	3.95 ± 0.79

6.3.2.2 Supercapacitor Applications

The materials were then tested in a supercapacitor setup, using 0.5 M H_2SO_4 in a 3-electrode cell. CV's at varying sweep rates from 500 mV s^{-1} to 10 mV s^{-1} were run to determine the surface coverage of the phenazin ligand on the carbon supports, to analyze the charge storing capabilities conferred to the carbon supports by the phenazine-containing ligand (Figure S6.8-10). The V-phenazin-Fe featured a surface coverage of 0.923 molecules nm^2 and upon heat treatment, the V-phenazin-Fe-700 coverage decreased to 0.859 molecules nm^2. We attribute the lowering of the surface coverage to the partial degradation of the phenazin molecule at elevated temperatures. The Black Pearls systems

showed a similar trend, where the surface coverage of materials, with and without iron, remained relatively similar at ca. 0.1 molecules nm^{-2}. Similar to the Vulcan materials, after heat-treatment, the surface coverage of the materials declined to 0.07 molecules nm^{-2}. We attribute this to the same partial degradation of the molecules on the surface after high-temperature treatments. For the BP case, the overall surface coverages were lower than for the Vulcan ones, due to the much higher surface area of the materials where perhaps a great concentration of the ligand could have been beneficial to further increase the surface coverage. Finally, for the KB materials, a similar trend is observed with the surface coverage. Initially, the functionalization of KB carbon with phenazin chelator results in the surface coverage of 0.539 molecules nm^{-2} and this increases to 0.891 molecules nm^{-2} with the addition of iron. After the heat treatment, the surface coverage of the phenazin molecule declines to 0.417 molecules nm^{-2}, which is lower than the original KB-phenazin material, indicating that the heat treatment is degrading and removing a significant amount of the ligand from the surface of this support.

The materials were studied by electrochemical impedance spectroscopy (EIS) to understand the pseudocapacitance of the materials, which would be attributed to the addition of the phenazin ligand (Figure S6.14-16). For the V-phenazin, the difference in capacitance values from the double layer (ca. 0.4 V) and the redox peak (ca. 0.7 V) was 48 mF cm^{-2}[57-58]. This indicates that the addition of the phenazin increases the capacitance of the material by an additional 48 mF cm^{-2}. A similar value was obtained for the V-phenazin-Fe sample with a pseudocapacitance of 43 mF cm^{-2}. The pseudo capacitance of the V-phenazin-Fe-700 could not be determined as the capacitance values from the double layer and Fe peak are quite similar, this is due to the growth in capacitance from the phenazine/dihydrophenazine over the course of testing in acidic media. For the BP system, a 12.1 mF cm^{-2} pseudocapacitance value was able to be calculated from the BP-phenazin showing the increase in charge storage after the addition of the nitrogen groups. In the BP-phenazin-Fe sample, the pseudocapacitance value increased to 19.1 mF cm^{-2} showing a further increase in the capacitance after the addition of the Faradaic contributions from the coordinated iron complex. After heat treatment, the BP-phenazin-Fe-700 remained constant at ca. 20 mF cm^{-2}. For the KB-phenazin sample a pseudocapactive value of 13.3 mF cm^{-2} was calculated, showing how the addition of the phenazin molecule benefits and

increases the capacitance of the original KB support. In the KB-phenazin-Fe an 8.6 mF cm^{-2} further increase was observed due to the Faradaic contributions of the Fe in the material. After heat-treatment the KB-phenazin-Fe-700 showed no significant difference in the double layer and the iron-based peak.
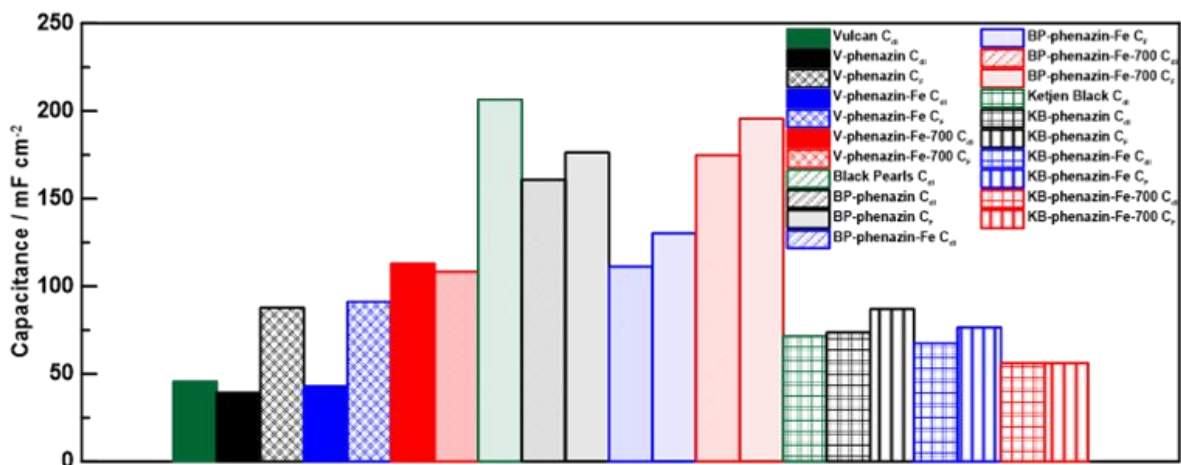
Figure 6.5) Bar graph comparing the C_{dl} values and the C_F values for each of the materials.

Galvanostatic charge-discharge (GCD) curves were performed at 0.5, 1, 2, 5, and 10 A g^{-1} on the materials to determine their specific capacitances and the charging/discharging rate capability (Figure 6.6, S6.11-13). The V-phenazin and V-phenazin-Fe samples exhibited specific capacitance values of 129.4 and 122.9 F g^{-1}, respectively. The addition of the iron centers into the material allowed Faradaic reactions on the surface involving the mechanism of changing of oxidation states in the Fe which led to higher specific capacitances being delivered. In Figure S6.11B and C the GCD curve resembles battery like behaviour. This is due to the redox properties of the phenazin and phenazin-Fe, respectively. At those potentials (0.1-0.4 V vs RHE) there are significant contributions from Faradaic processes occurring, which leads to the battery-like curves for the materials. The Vulcan XC-72 support only demonstrated a specific capacitance value of 34.2 F g^{-1} indicating that the addition of the phenazin and iron increased the capacitance of the support by $\Delta = 95.2$ F g^{-1}. Interestingly, the heat treatment procedure significantly lowered the specific capacitance of the material. This could be contributed to the decrease in the surface coverage of nitrogenous moieties, observed from the partial degradation of the ligand and leaching of it from the surface at high temperatures. More interestingly, we don't see similar losses in the activity during the ORR. On the contrary, the activity of the

material in the ORR increases, indicating that there must be a surface structural rearrangement that occurs which has benefits for the ORR but not for SC applications. From previous work we observe that the heat treatment results in detectable losses of nitrogen functionalities[40]. On the contrary, for the phenazin systems we still detect the presence of the pyridinic nitrogen groups on the surface after heat-treatment through the XPS results. In any case, for both SC and ORR applications this change in surface groups leads to drastic changes in the performance of these materials, where for ORR the activity increases, and for SC applications, the loss of surface-embedded nitrogen leads to a decrease in specific capacitance. These changes can be due to the ligand used. While in this work, we show that this bidentate ligand has higher activity for the ORR after heat treatment, this was not the case with our previous work using a tridentate ligand, terpyridine. In fact, with that work, we saw that the heat treatment actually decreased the activity of the catalyst[41]. The rate capability plot for the Vulcan systems showed the same trend for the specific capacitance values. The V-phenazin and V-phenazin-Fe samples show similar, lower current densities; however, the V-phenazin-Fe sample showed higher rate capability, due to lower voltage losses at higher currents. The V-phenazin-Fe-700 sample showed low rate capability due to the large voltage losses at high currents. For the BP materials, the specific capacitance of the BP-phenazin increased to 161.2 F g^1 when compared to the BP support of 142.9 F g^{-1}. The capacitance was further substantially increased to 287 F g^{-1} upon the addition of Fe to the system, unambiguously confirming the importance of both nitrogen's and iron's Faradaic contributions on the increased charge storage ability of the carbon materials. After heat treatment, the capacitance of BP-phenazin-Fe-700 decreased from the BP-phenazin-Fe value at 287 F g^{-1} to 220.4 F g^{-1}. In the KB materials, the KB-phenazin showed an increase of $\Delta = 57.7$ F g^{-1} from the KB support when the phenazin was added, showing the positive effect that the addition of the phenazin molecule has on the material. After the addition of iron, the capacitance value in the KB-phenazin-Fe increased slightly due to the Faradaic contributions of the Fe. However, similar to the BP and V systems, heat treatment of the material resulted in the specific capacitance decrease to $\Delta = 56.1$ F g^{-1} owing to the partial degradation and removal of the capacitive N-ligand and iron. For the GCD curves, it is noteworthy that the BP and KB systems do not attain their original voltages during testing (particularly at the lower

169

current densities). They instead finish at some open circuit potential. We believe that this could be due to self-discharge caused by both diffusion-controlled Faradaic processes on the surface (due to iron that could be dissolved in solution, which is oxidized and reduced in the potential window used, the result of which is a decline in potential) and through charge redistribution in the porous electrodes, where this results in a loss of voltage[59-62]. It is interesting to observe that for the ORR, the heat treatment, particularly on the higher surface area carbons, appears to increase the activity. However, this same trend is not observed when the material is used for supercapacitor applications. It is in fact producing lower charge storing capabilities when the materials are heat-treated.

To further analyze the surface chemistry reactions that contribute to the capacitances observed, we performed Dunn analysis in acidic media, which is presented in Table 6.6[24, 63]. Using the potential window of 1.2 V vs RHE and potential values ranging from 0.3-0.8 V vs RHE from CVs at various scan rates, a linear plot was made. The slope of the line gives the capacitive current and allows calculation of the percentage of current that came from capacitive or surface reactions. This analysis allows for the separation of the capacitive contributions from the diffusion-controlled processes which are due to surface-tethered groups. From Table 6.5, we can see that as the surface area of the carbon support increased (V<KB<BP), the capacitive current increased, due to the surface area of the carbon support. However, in each case, we can see that roughly half of the total capacitance is accounted to the capacitive contributions from the carbon supports. The pseudocapacitive surface functional groups (phenazin and iron) contribute to the other half of the capacitance observed. This further confirms that the surface functional groups greatly contribute the overall capacitance of the materials.
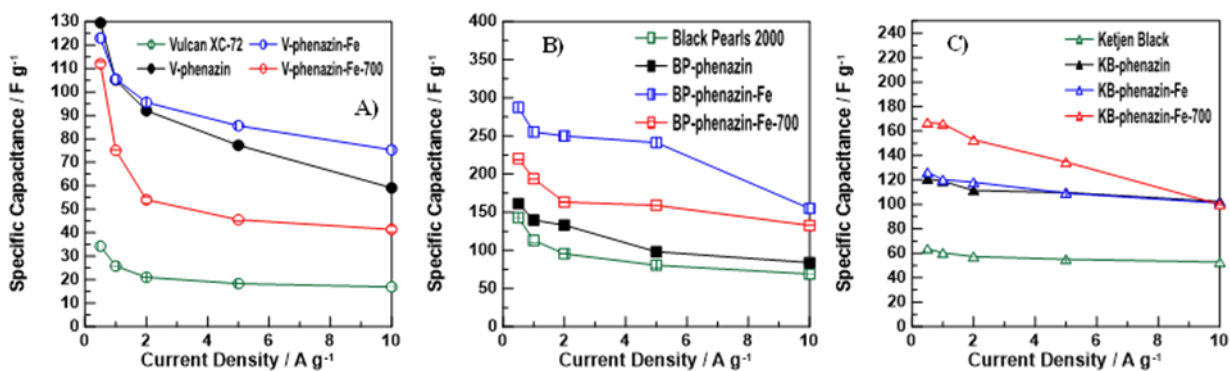
Figure 6.6) (A) Rate capability plot of the Vulcan system (B) Rate capability plot of the Black Pearls system (C) Rate capability plot of the Ketjen Black system.

We investigated the relationship between the surface area of the carbon support used and the specific capacitance that was calculated (Figure 6.7). Materials demonstrated an increase in their specific capacitance upon addition of the nitrogenous phenazin ligand and iron, and this in turn correlated to a lowering of the surface area, as determined by the BET measurements. Restoring some surface area after heat treatment was accompanied by a decrease of the specific capacitance, which was correlated with the partial decomposition of the phenazin ligand on the supports. We demonstrated that modification of the carbon by the phenazin ligand lowered the surface area due to partial blockage of the pores with the nitrogenous groups, but this significantly elevates the charge storage capability of the material due to the Faradaic contributions from the nitrogen and iron components. The Black Pearls systems showed less significant changes in surface area, but those materials initially demonstrated the greatest ability for charge storage. In comparison, the Ketjen Black samples, featuring significant changes in the surface area upon modification by phenazin, showed great improvements in the charge storage capabilities of those materials. The correlation between the surface area and charge storage are similar for all the materials studied; however, this work demonstrates that the (initially) high surface area carbon supports, such as BP, preserve their high charge storing capabilities after the addition of the bulky phenazin groups.
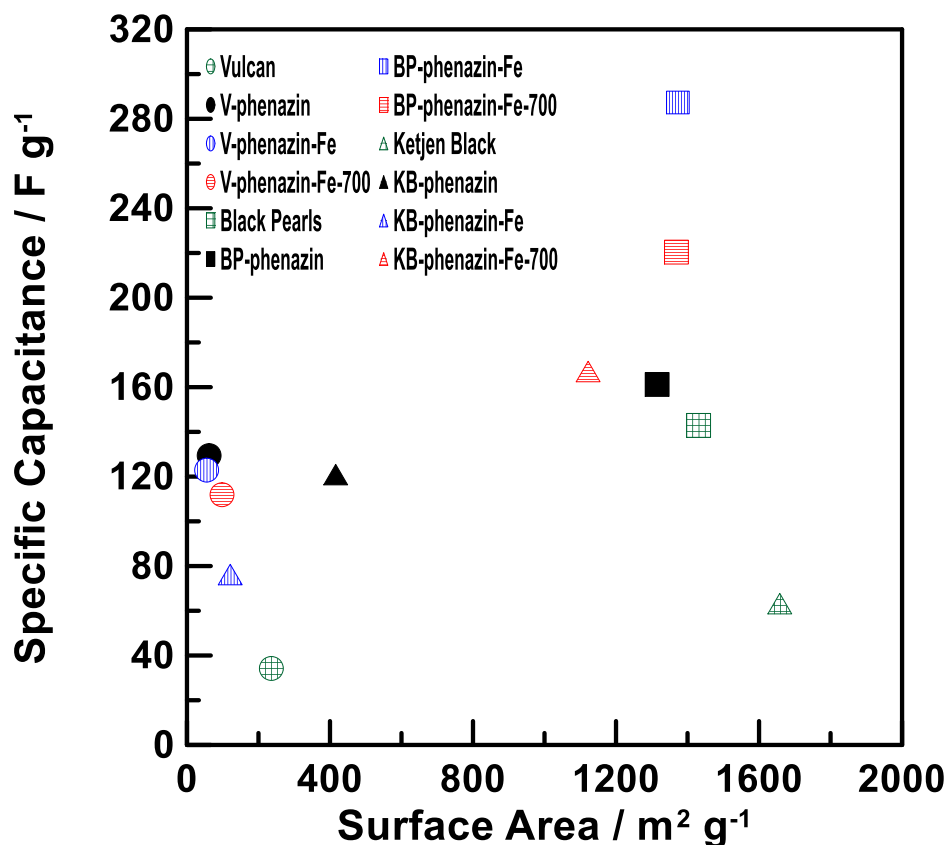
Figure 6.7) Relationship of all the materials between the surface area and the specific capacitance.

6.3.2.3 Stability

Since the KB-phenazin-Fe-700 performed exceptionally well for the ORR in both acidic and basic electrolyte we decided to further explore the stability of the material for the ORR using a DOE protocol over 10,000 cycles and measured the ORR activity after 1,000, 5,000, and 10,000 cycles (Figure 6.8). In acidic media, there is some increase in the capacitance in the CVs observed at ca. 0.40 V, which is due to the phenazine/dihydrophenazine process. The capacitance grows initially and then stabilizes by 3000 cycles. The ORR activity shows only a slight decay (ca. 3.2%) in the onset potential from the initial fresh catalyst whose onset potential was observed at 0.64 V. At 5000 cycles, the decay is more pronounced, and the catalyst loses 21.9% of its original activity. Finally, over the last 10,000 cycles, 41.9% of the original activity is lost. NPMCs are known to be less stable in acid due to leaching of the metal, and protonation of the nitrogen functionalities[19, 64-67]. Nonetheless, this catalyst is the most stable system that we have synthesized using our surface modification methodology in acidic media. In basic media, the growth in the CVs is not observed as in the acidic media, due to the quinone

172

peak not being formed in alkaline conditions (Figure S6.17). The capacitance decreases in this case after 3000 cycles. The ORR activity of the material in basic electrolyte decreases significantly by 1000 cycles, losing 12.8% of the material's original activity (difference between the onset potential of the initial and then after 1000 cycles). After 5000 cycles 16.3% of the activity is lost. Finally, after the full 10,000 cycles a total of 18.7% of the catalyst's activity is lost.

Table 6.5) Specific capacitances of the V, BP, and KB systems in 0.5 M H_2SO_4.

Material	Surface Coverage / molecules nm^{-2}	Gravimetric specific capacitance / F g^{-1}
Vulcan XC-72	-	34.2
V-phenazin	0.572	129.4
V-phenazin-Fe	0.923	122.9
V-phenazin-Fe-700	0.859	111.9
Black Pearls 2000	-	142.9
BP-phenazin	0.113	161.2
BP-phenazin-Fe	0.107	287.3
BP-phenazin-Fe-700	0.073	220.4
Ketjen Black	-	63.2
KB-phenazin	0.539	120.9
KB-phenazin-Fe	0.891	126.2
KB-phenazin-Fe-700	0.417	167.0

Table 6.6) The capacitive current contribution in the materials in 0.5 M H_2SO_4 within the potential window of 1.2 V vs RHE calculated using potentials between 0.3-0.8 V vs RHE

Material	Capacity Current Contribution / %
Vulcan XC-72	-
V-phenazin	35.3 ± 10.7
V-phenazin-Fe	56.1 ± 5.6
V-phenazin-Fe-700	52.0 ± 4.8
Black Pearls 2000	-
BP-phenazin	55.9 ± 5.8
BP-phenazin-Fe	63.5 ± 4.8
BP-phenazin-Fe-700	47.4 ± 13.4
Ketjen Black	-
KB-phenazin	75.1 ± 4.7
KB-phenazin-Fe	67.4 ± 7.0
KB-phenazin-Fe-700	56.0 ± 19.5
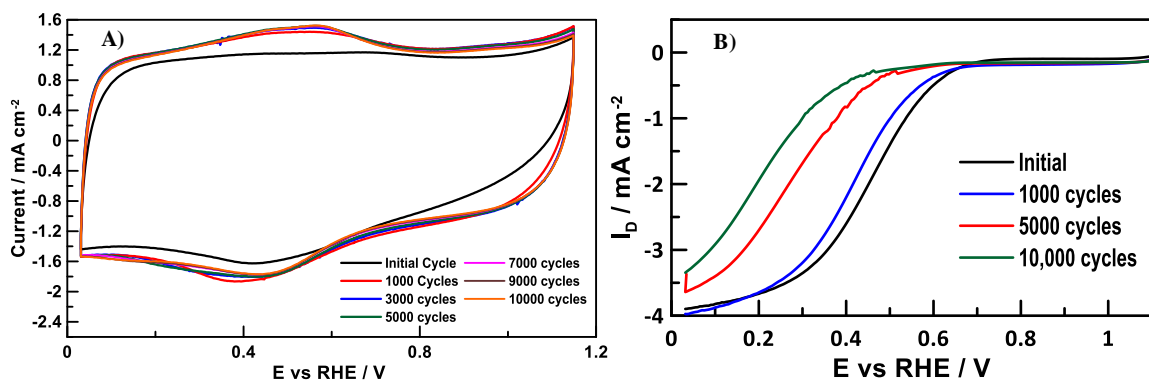
Figure 6.8) (A) CVs of the KB-phenazin-Fe-700 in N_2 saturated 0.1 M H_2SO_4 at a scan rate of 20 mV s^{-1} (B) ORR activity of the KB-phenazin-Fe-700 at 900 rpm in O_2 saturated 0.1 M H_2SO_4 at 10 mV s^{-1}.

All the materials (V, BP, KB) were tested for long-term stability during charge storage tests. The materials were subjected to a 6000 cycle GCD testing at 2 A g^{-1} to assess the capacitance changes in the materials over the course of the long-term stability tests. The CVs and the capacity retention plots are presented in Figures S6.18-23 and compiled results are presented in Figure S6.26. For all modified samples, the CVs show increases in

the capacitance over the course of cycling. This indicated that there was an increase of species contributing to the Faradaic reactions/Faradaic capacitance on the surface of the materials. For the carbon supports, this growth was less significant than when the phenazin and iron were present. Analyzing the specific capacitance and capacitance retention over the 6000 cycles shows that the modified materials produced increases in the specific capacitance to above ca. 110%. We attribute this increase to some electropolymerized effects on the surface due to any physisorbed or radical molecules that are getting polymerized on the surface during the long-term tests[68-69]. We hypothesize this is a combined effect from the presence of the nitrogenous ligand and iron since the bare carbon supports show no detectable changes in performance over the 6000 cycles. Any increases seen in the specific capacitance for bare carbons should be attributed to the growth in quinone/hydroquinone processes on the surface. The peaks seen in Figure S6.4A at 0 V are likely the reduction and oxidation of the phenazin ligand. There maybe incomplete removal of phenazin starting material from which would leave exposed NH_2 groups that would be willing to participant in the electropolymerzation reaction. As the increased cycling occurs, the capacitance increases due to the formation of a polymer, creating an ideal 3D network to aid in the increase of charge storage. This observation matches well with the rapid growth of the capacitance observed in the CVs.

6.4 Conclusion

Here, we used our novel surface modification approach to create a dual-function material that could be used for both energy storage and energy production applications. The surface modification by a phenazin-based structure allowed for the creation of the material, enriched by pyridinic units that are accessible on the surface for the enhanced ORR activity and for energy storage applications. The effect of altering the carbon support was investigated, as the surface area feature of the material is drastically important for both applications, but especially important for the supercapacitor applications, as it contributes to the formation of a porous 3D-polmyer network that allows for effective charge storage within the materials.

The materials showed improved activity for the ORR when subjected to a heat treatment protocol. The improvements in the activity are seen in both the acidic and basic media for the ORR. The KB-phenazin-Fe-700 sample showed incredibly high activity for

the ORR in both acidic and basic media, the highest that we have observed on any carbon support using this synthetic approach and comparable to, or higher than, other literature works. The stability of the KB-phenazin-Fe-700 material was tested, and it was found to be quite stable for up to 3,000 cycles for the ORR in acidic media. In basic media the catalyst was stable, only losing in totally 18% of its initial activity after 10,000 cycles.

Finally, the materials were tested for their activity as a supercapacitor electrode material, and it was observed that the performance of the materials has a significant dependence on the initial surface area of the carbon support used. When the phenazin ligand is attached, the surface area declines due to blocking of pores by the bulky molecule. This, however, increases the charge storing capabilities of the material significantly, due to the addition of the Faradaic contributions from the nitrogen functionalities. After heat treatment, the capacitance decreases due to the partial decomposition and removal of the nitrogen groups. During extensive stability testing over 6000 GCD cycles, the capacitance of the materials increased significantly due to electropolymerization reactions happening at the electrode any residual starting materials from the diazonium reaction.

Overall, this work shows that NPMCs that are currently used for the ORR could be also used as supercapacitor electrodes. For example, we showed that carbon modification by the N-ligand result in lowering of the surface area due to partial blockage of the pores with the nitrogenous groups, but this in turn significantly elevates the charge storage capability of the material due to the Faradaic contributions from the nitrogen and iron components. We observed the heat treatment step was beneficial for the ORR applications, but wasn't advantageous for the charge storage application, since they often produced lower specific capacitance values, compared to the non-heat-treated materials. So, the same material can be used for both energy storage and energy production. The overall design and requirements for both NPMCs are very similar, and the ability to use the materials for both FC and SC applications will be economically beneficial and resource-saving. Developing and utilizing a versatile material for both applications provides a unique method for creating the next generation of low-cost electrochemical energy materials.

6.5 Supporting Information
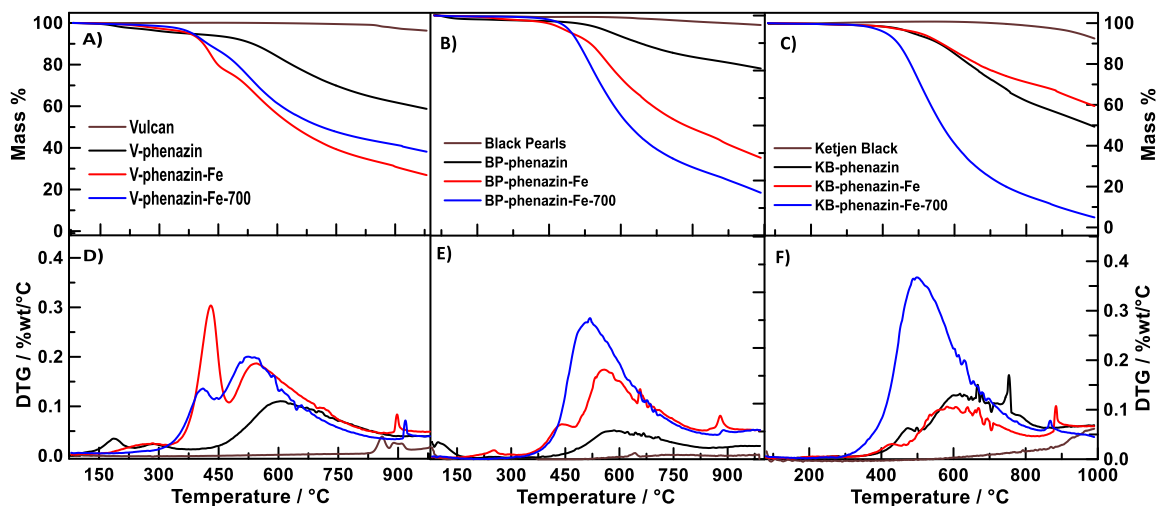
Supporting Information Figure S6.1) (A) TGA of Vulcan materials in argon atmosphere at a heating rate of 5ºC min^{-1} (B) TGA of Black pearls materials in argon atmosphere at a heating rate of 5ºC min^{-1} (C) TGA of Ketjen black materials in argon atmosphere at a heating rate of 5ºC min^{-1} (D) DTG of Vulcan materials in argon atmosphere at a heating rate of 5ºC min^{-1} (E) DTG of Black pearls materials in argon atmosphere at a heating rate of 5ºC min^{-1} (F) DTG of Ketjen black materials in argon atmosphere at a heating rate of 5ºC min^{-1}.
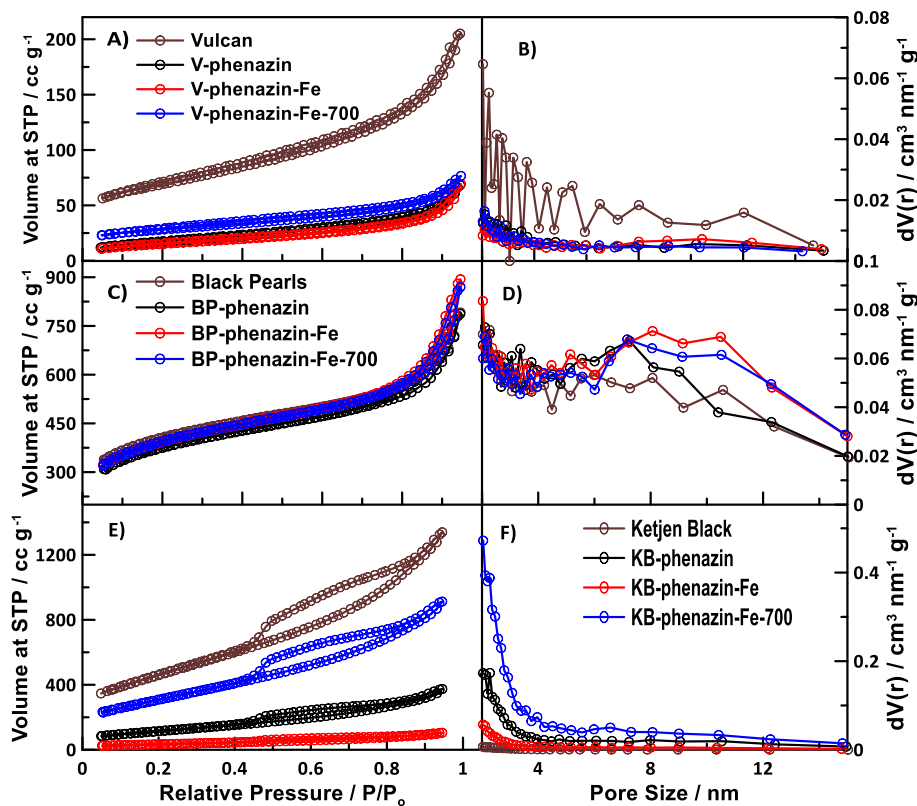
Supporting Information Figure S6.2) (A) N_2 isotherms of the Vulcan system (B) Pore size distribution of the Vulcan system (C) N_2 isotherms of the Black Pearls system (D) Pore size distribution of the Black Pearls system (E) N_2 isotherms of the Ketjen Black system (F) Pore size distribution of the Ketjen Black system.
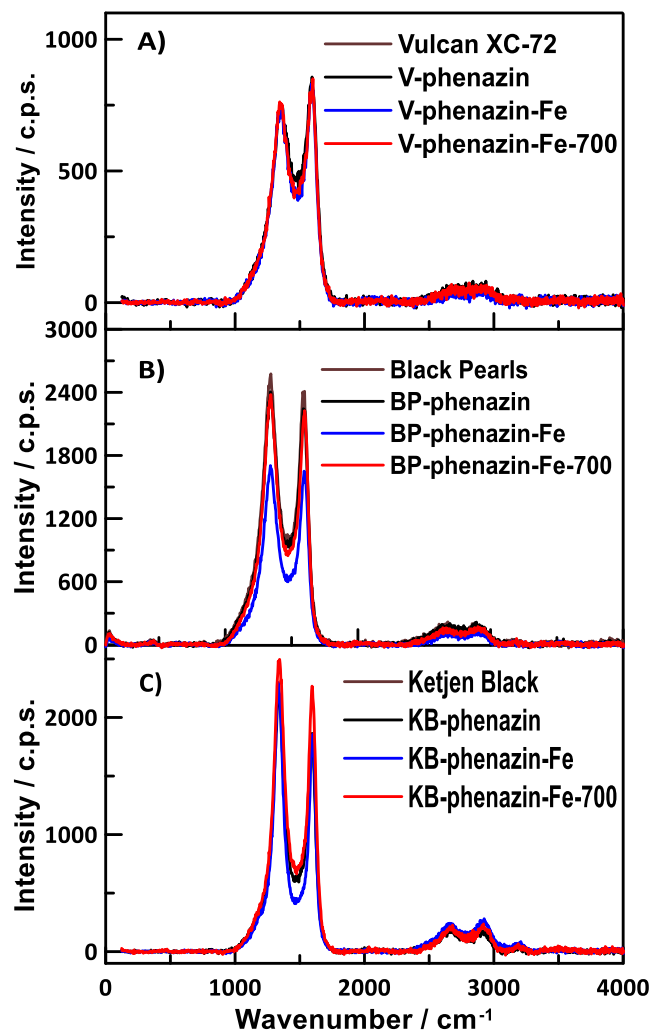
Supporting Information Figure S6.3) (A) Raman spectra of the Vulcan materials (B) Raman spectra of the Black Pearls materials (C) Raman spectra of the KB materials.
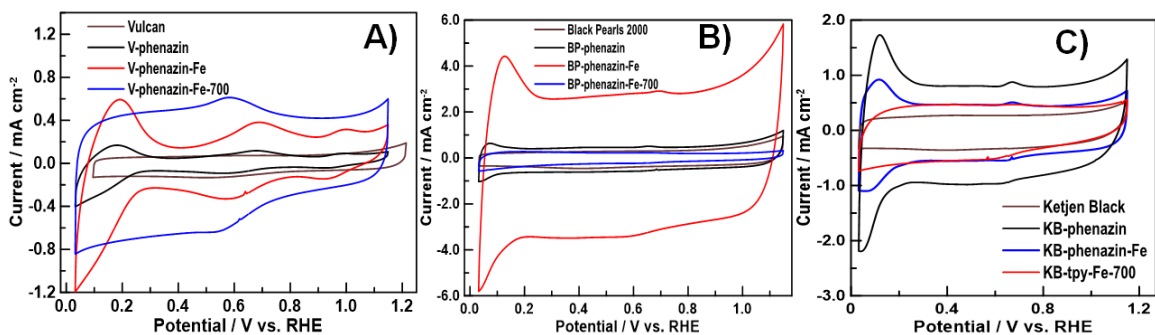
Supporting Information Figure S6.4) Cyclic voltammograms of (A) Vulcan systems in N_2 saturated 0.1 M H_2SO_4 at 50 mV s^{-1} (B) Black Pearls systems in N_2 saturated 0.1 M H_2SO_4 at 50 mV s^{-1} (C) Ketjen Black systems in N_2 saturated 0.1 M H_2SO_4 at 50 mV s^{-1}.
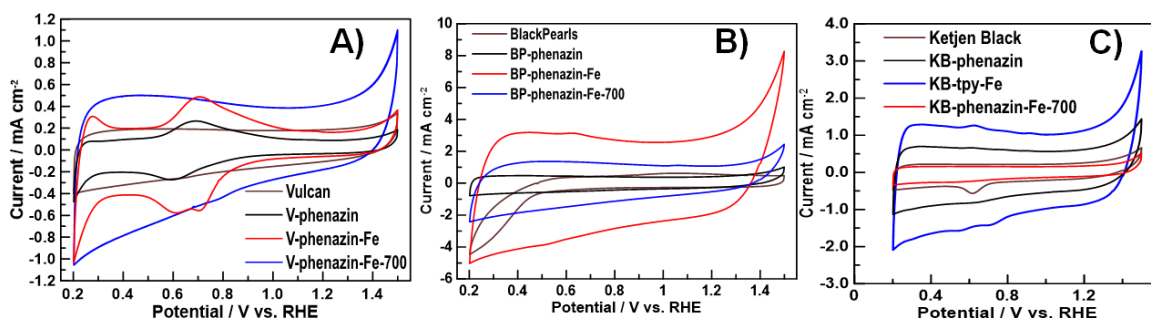
Supporting Information Figure S6.5) Cyclic voltammograms of (A) Vulcan systems in N_2 saturated 0.1 M KOH at 50 mV s^{-1} (B) Black Pearls systems in N_2 saturated 0.1 M KOH at 50 mV s^{-1} (C) Ketjen Black systems in N_2 saturated 0.1 M KOH at 50 mV s^{-1}.
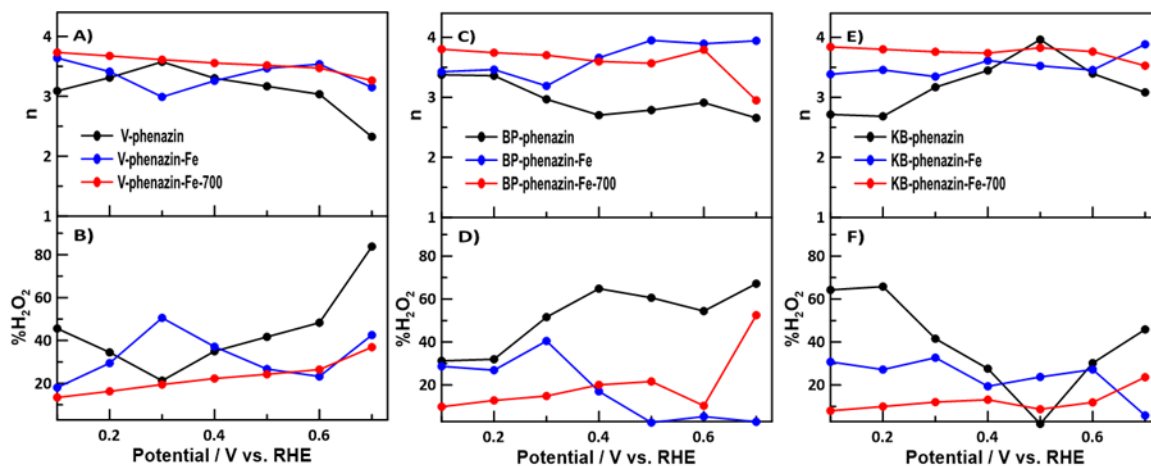
Supporting Information Figure S6.6) (A) number of electrons transferred for the Vulcan system at 900 rpm in O_2 saturated 0.1 H_2SO_4 (B) %H_2O_2 for the Vulcan system at 900 rpm in O_2 saturated 0.1 M H_2SO_4 (C) number of electrons transferred for the Black Pearls system at 900 rpm in O_2 saturated 0.1 M H_2SO_4 (D) %H_2O_2 for the Black Pearls system at 900 rpm in O_2 saturated 0.1 M H_2SO_4 (E) number of electrons transferred for the Ketjen Black systems at 900 rpm in O_2 saturated 0.1 M H_2SO_4 (F) %H_2O_2 for the Ketjen Black system at 900 rpm in O_2 saturated 0.1 M H_2SO_4.

179
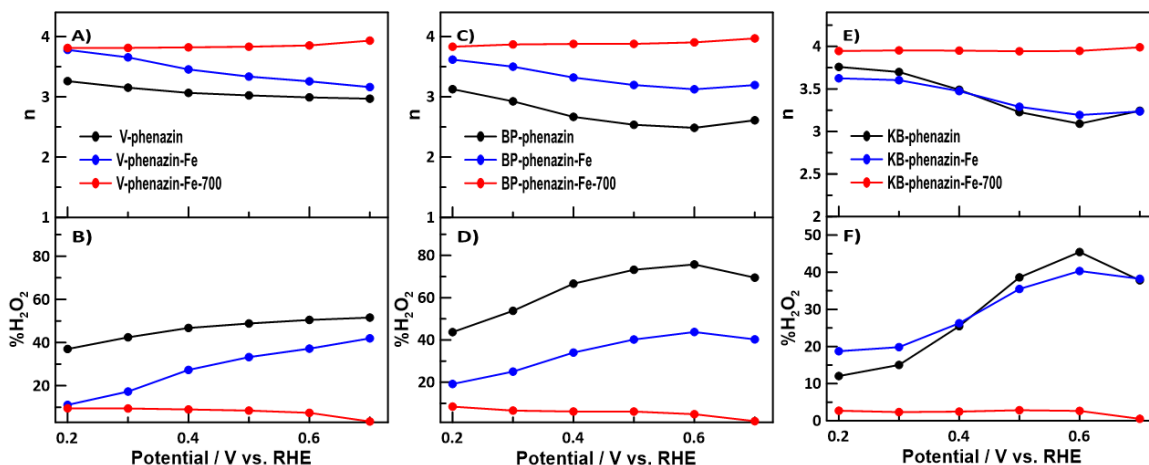
Supporting Information Figure S6.7) (A) number of electrons transferred for the Vulcan system at 900 rpm in O_2 saturated 0.1 KOH (B) %H_2O_2 for the Vulcan system at 900 rpm in O_2 saturated 0.1 M KOH (C) number of electrons transferred for the Black Pearls system at 900 rpm in O_2 saturated 0.1 M KOH (D) %H_2O_2 for the Black Pearls system at 900 rpm in O_2 saturated 0.1 M KOH (E) number of electrons transferred for the Ketjen Black systems at 900 rpm in O_2 saturated 0.1 M KOH (F) %H_2O_2 for the Ketjen Black system at 900 rpm in O_2 saturated 0.1 M KOH.
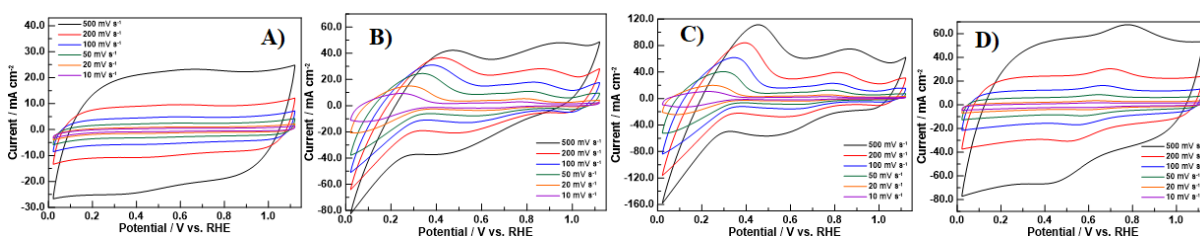
Supporting Information Figure S6.8) (A) CV's at varying sweep rates of Vulcan XC-72 support in N_2 saturated 0.5 M H_2SO_4 (B) CV's at varying sweep rates of V-phenazin in N_2 saturated 0.5 M H_2SO_4 (C) CV's at varying sweep rates of V-phenazin-Fe in N_2 saturated 0.5 M H_2SO_4 (D) CV's at varying sweep rates of V-phenazin-Fe-700 in N_2 saturated 0.5 M H_2SO_4.
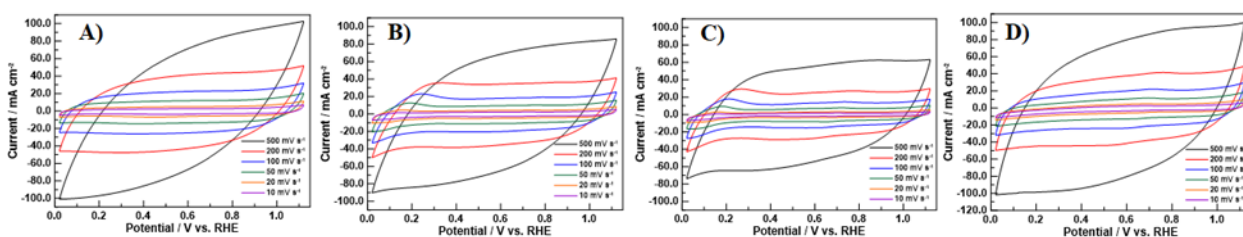
Supporting Information Figure S6.9) (A) CV's at varying sweep rates of Black Pearls 2000 support in N_2 saturated 0.5 M H_2SO_4 (B) CV's at varying sweep rates of BP-phenazin in N_2 saturated 0.5 M H_2SO_4 (C) CV's at varying sweep rates of BP-phenazin-Fe in N_2 saturated 0.5 M H_2SO_4 (D) CV's at varying sweep rates of BP-phenazin-Fe-700 in N_2 saturated 0.5 M H_2SO_4.
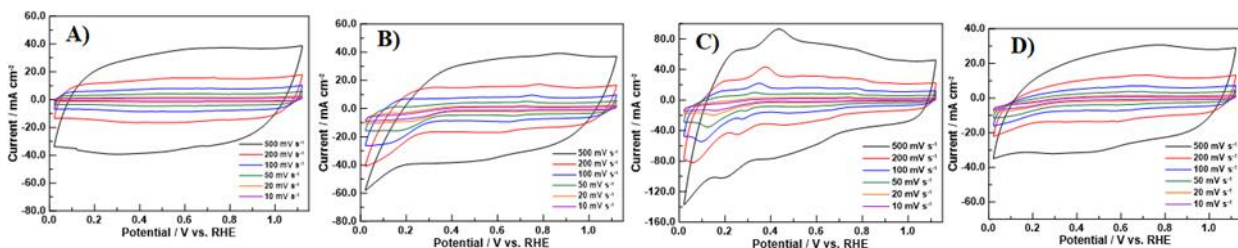
Supporting Information Figure S6.10) (A) CV's at varying sweep rates of Ketjen Black support in N_2 saturated 0.5 M H_2SO_4 (B) CV's at varying sweep rates of KB-phenazin in N_2 saturated 0.5 M H_2SO_4 (C) CV's at varying sweep rates of KB-phenazin-Fe in N_2 saturated 0.5 M H_2SO_4 (D) CV's at varying sweep rates of KB-phenazin-Fe-700 in N_2 saturated 0.5 M H_2SO_4.
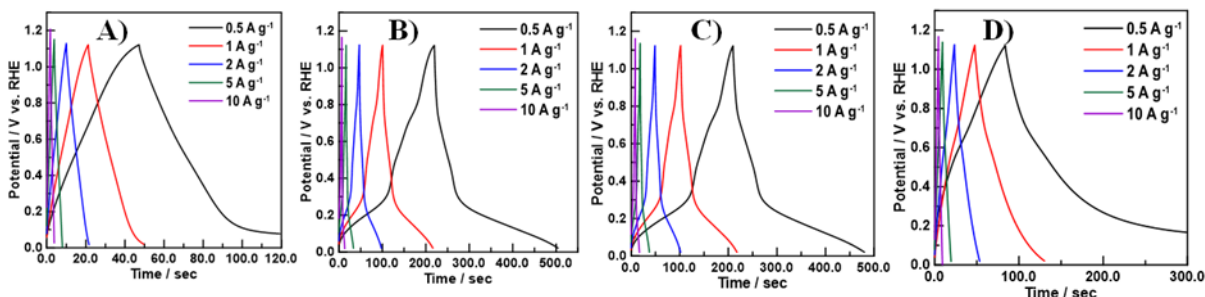
Supporting Information Figure S6.11) (A) GCD curves at varying current densities of Vulcan XC-72 support in N_2 saturated 0.5 M H_2SO_4 (B) GCD curves at varying current densities of V-phenazin in N_2 saturated 0.5 M H_2SO_4 (C) GCD curves at varying current densities of V-phenazin-Fe in N_2 saturated 0.5 M H_2SO_4 (D) GCD curves at varying current densities of V-phenazin-Fe-700 in N_2 saturated 0.5 M H_2SO_4.
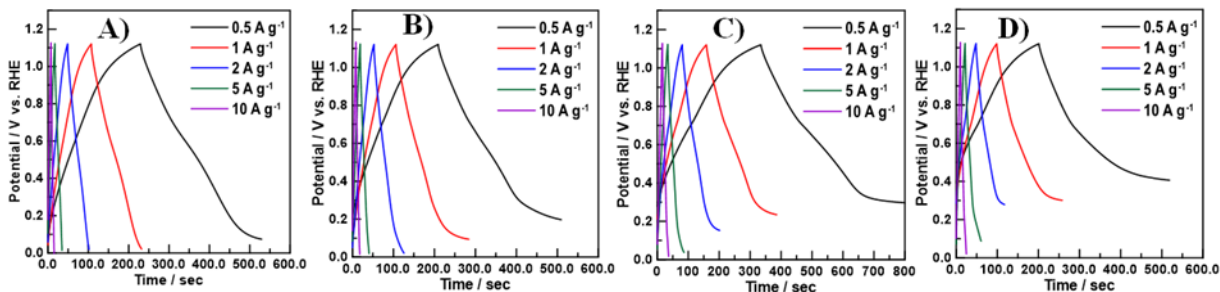
Supporting Information Figure S6.12) (A) GCD curves at varying current densities of Black Pearls 2000 support in N_2 saturated 0.5 M H_2SO_4 (B) GCD curves at varying current densities of BP-phenazin in N_2 saturated 0.5 M H_2SO_4 (C) GCD curves at varying current densities of BP-phenazin-Fe in N_2 saturated 0.5 M H_2SO_4 (D) GCD curves at varying current densities of BP-phenazin-Fe-700 in N_2 saturated 0.5 M H_2SO_4.
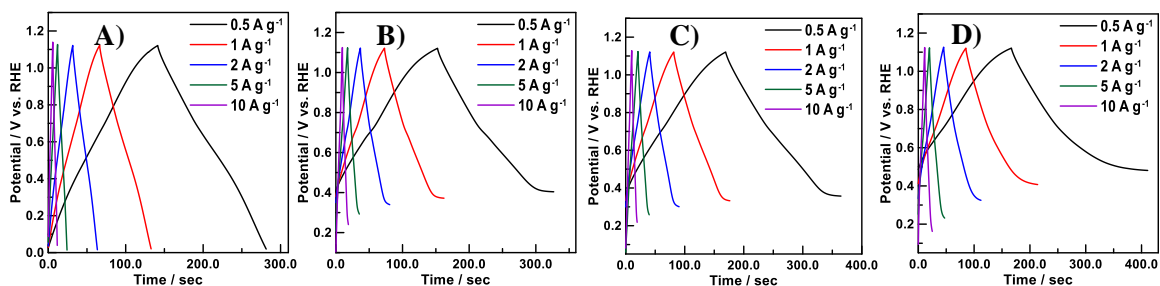
Supporting Information Figure S6.13) (A) GCD curves at varying current densities of Ketjen Black support in N_2 saturated 0.5 M H_2SO_4 (B) GCD curves at varying current densities of KB-phenazin in N_2 saturated 0.5 M H_2SO_4 (C) GCD curves at varying current densities of KB-phenazin-Fe in N_2 saturated 0.5 M H_2SO_4 (D) GCD curves at varying current densities of KB-phenazin-Fe-700 in N_2 saturated 0.5 M H_2SO_4.
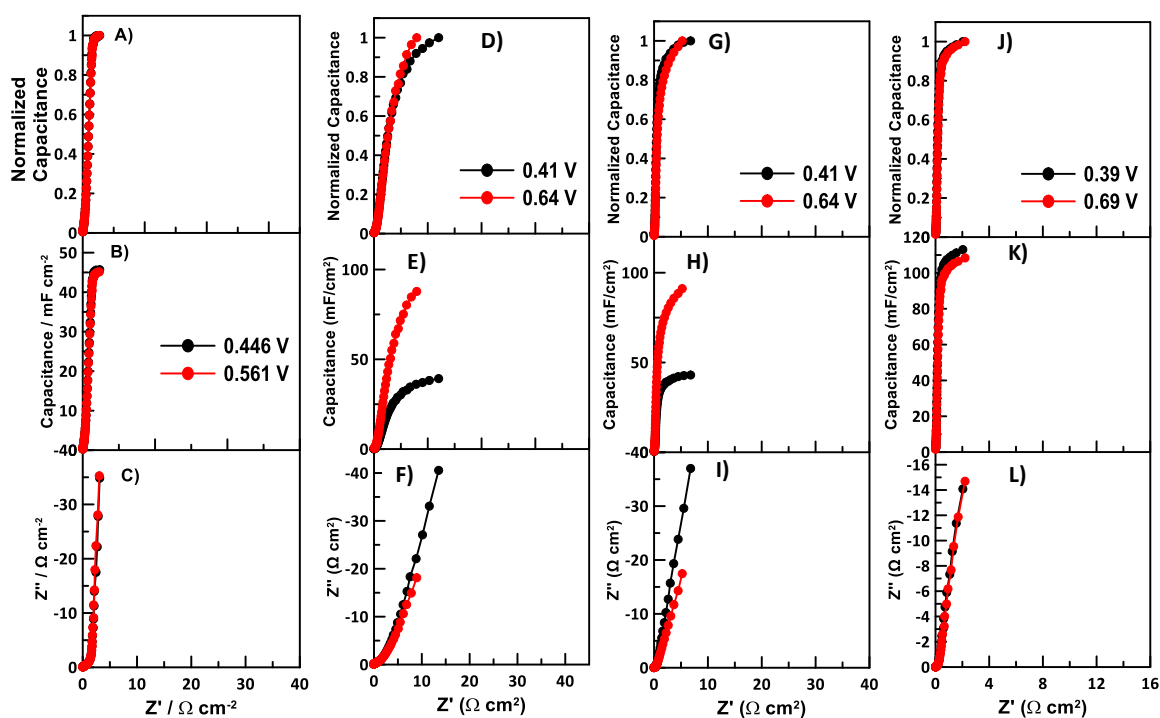
Supporting Information Figure S6.14) (A) Normalized capacitance plot of the Vulcan XC-72 support in N_2 saturated 0.5 M H_2SO_4 (B) Capacitance plot of the Vulcan XC-72 support in N_2 saturated 0.5 M H_2SO_4 (C) Nyquist plot of the Vulcan XC-72 support in N_2 saturated 0.5 M H_2SO_4 (D) Normalized capacitance plot of the V-phenazin in N_2 saturated 0.5 M H_2SO_4 (E) Capacitance plot of the V-phenazin in N_2 saturated 0.5 M H_2SO_4 (F) Nyquist plot of the V-phenazin in N_2 saturated 0.5 M H_2SO_4 (G) Normalized capacitance plot of the V-phenazin-Fe in N_2 saturated 0.5 M H_2SO_4 (H) Capacitance plot of the V-phenazin-Fe in N_2 saturated 0.5 M H_2SO_4 (I) Nyquist plot of the V-phenazin-Fe in N_2 saturated 0.5 M H_2SO_4 (J) Normalized capacitance plot of the V-phenazin-Fe-700 in N_2 saturated 0.5 M H_2SO_4 (K) Capacitance plot of the V-phenazin-Fe-700 in N_2 saturated 0.5 M H_2SO_4 (L) Nyquist plot of the V-phenazin-Fe-700 in N_2 saturated 0.5 M H_2SO_4.

Supporting Information Figure S6.15) (A) Normalized capacitance plot of the Black Pearls 2000 support in N_2 saturated 0.5 M H_2SO_4 (B) Capacitance plot of the Black Pearls 2000 support in N_2 saturated 0.5 M H_2SO_4 (C) Nyquist plot of the Black Pearls 2000 support in N_2 saturated 0.5 M H_2SO_4 (D) Normalized capacitance plot of the BP-phenazin in N_2 saturated 0.5 M H_2SO_4 (E) Capacitance plot of the BP-phenazin in N_2 saturated 0.5 M H_2SO_4 (F) Nyquist plot of the BP-phenazin in N_2 saturated 0.5 M H_2SO_4 (G) Normalized capacitance plot of the BP-phenazin-Fe in N_2 saturated 0.5 M H_2SO_4 (H) Capacitance plot of the BP-phenazin-Fe in N_2 saturated 0.5 M H_2SO_4 (I) Nyquist plot of the BP-phenazin-Fe in N_2 saturated 0.5 M H_2SO_4 (J) Normalized capacitance plot of the BP-phenazin-Fe-700 in N_2 saturated 0.5 M H_2SO_4 (K) Capacitance plot of the BP-phenazin-Fe-700 in N_2 saturated 0.5 M H_2SO_4 (L) Nyquist plot of the BP-phenazin-Fe-700 in N_2 saturated 0.5 M $H_2SO_4.$

Supporting Information Figure S6.16) (A) Normalized capacitance plot of the Ketjen Black support in N_2 saturated 0.5 M H_2SO_4 (B) Capacitance plot of the Ketjen Black support in N_2 saturated 0.5 M H_2SO_4 (C) Nyquist plot of the Ketjen Black support in N_2 saturated 0.5 M H_2SO_4 (D) Normalized capacitance plot of the KB-phenazin in N_2 saturated 0.5 M H_2SO_4 (E) Capacitance plot of the KB-phenazin in N_2 saturated 0.5 M H_2SO_4 (F) Nyquist plot of the KB-phenazin in N_2 saturated 0.5 M H_2SO_4 (G) Normalized capacitance plot of the KB-phenazin-Fe in N_2 saturated 0.5 M H_2SO_4 (H) Capacitance plot of the KB-phenazin-Fe in N_2 saturated 0.5 M H_2SO_4 (I) Nyquist plot of the KB-phenazin-Fe in N_2 saturated 0.5 M H_2SO_4 (J) Normalized capacitance plot of the KB-phenazin-Fe-700 in N_2 saturated 0.5 M H_2SO_4 (K) Capacitance plot of the KB-phenazin-Fe-700 in N_2 saturated 0.5 M H_2SO_4 (L) Nyquist plot of the KB-phenazin-Fe-700 in N_2 saturated 0.5 M H_2SO_4.

Supporting Information Figure S6.17) (A) CVs of the KB-phenazin-Fe-700 in N_2 saturated 0.1 M KOH at a scan rate of 20 mV s^{-1} (B) ORR activity of the KB-phenazin-Fe-700 at 900 rpm in O_2 saturated 0.1 M KOH at 10 mV s^{-1}.
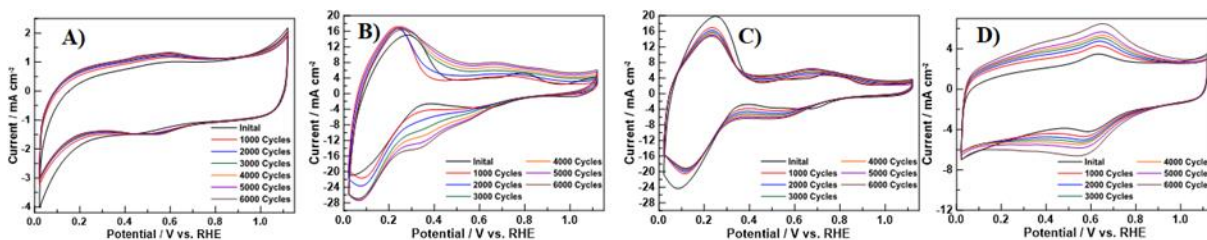
Supporting Information Figure S6.18) (A) Durability CV's of the Vulcan XC-72 support in N_2 saturated 0.5 M H_2SO_4 at 20 mV s^{-1} (B) Durability CV's of V-phenazin in N_2 saturated 0.5 M H_2SO_4 at 20 mV s^{-1} (C) Durability CV's of V-phenazin-Fe in N_2 saturated 0.5 M H_2SO_4 at 20 mV s^{-1} (D) Durability CV's of V-phenazin-Fe-700 in N_2 saturated 0.5 M H_2SO_4 at 20 mV s^{-1}.
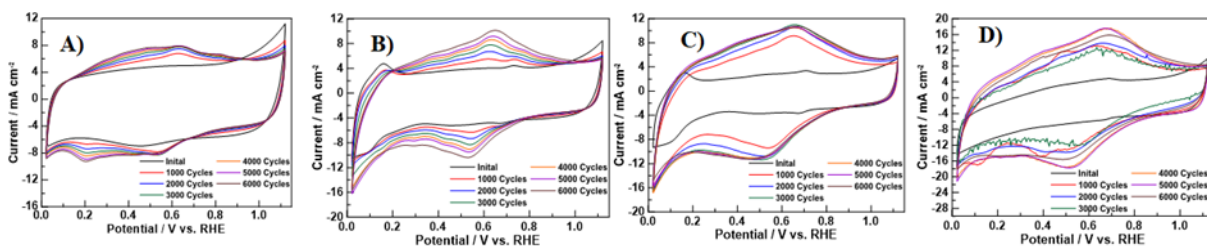
Supporting Information Figure S6.19) (A) Durability CV's of the Black Pearls support in N_2 saturated 0.5 M H_2SO_4 at 20 mV s^{-1} (B) Durability CV's of BP-phenazin in N_2 saturated 0.5 M H_2SO_4 at 20 mV s^{-1} (C) Durability CV's of BP-phenazin-Fe in N_2 saturated 0.5 M H_2SO_4 at 20 mV s^{-1} (D) Durability CV's of BP-phenazin-Fe-700 in N_2 saturated 0.5 M H_2SO_4 at 20 mV s^{-1}.
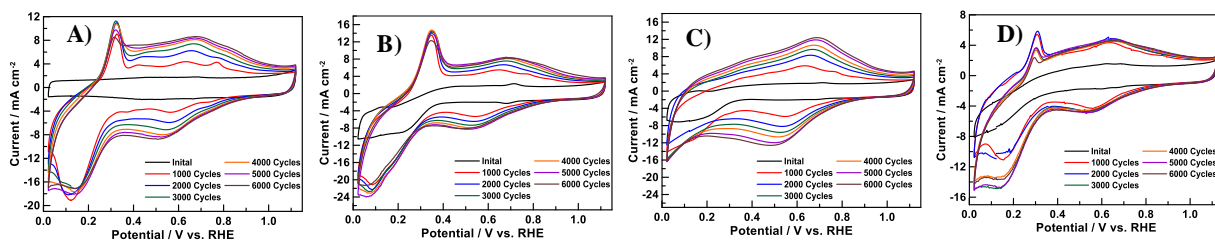
Supporting Information Figure S6.20) (A) Durability CV's of the Ketjen Black support in N_2 saturated 0.5 M H_2SO_4 at 20 mV s^{-1} (B) Durability CV's of KB-phenazin in N_2 saturated 0.5 M H_2SO_4 at 20 mV s^{-1} (C) Durability CV's of KB-phenazin-Fe in N_2 saturated 0.5 M H_2SO_4 at 20 mV s^{-1} (D) Durability CV's of KB-phenazin-Fe-700 in N_2 saturated 0.5 M H_2SO_4 at 20 mV s^{-1}.
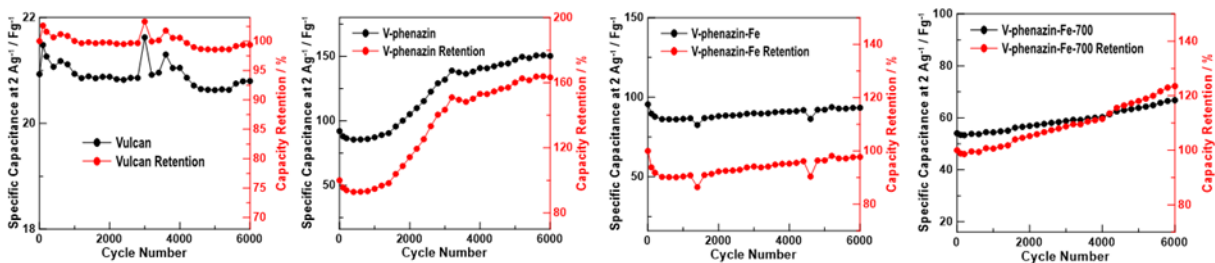
Supporting Information Figure S6.21) Capacity retention of the Vulcan systems in 0.5 M H_2SO_4 over the 6000 GCD cycles.
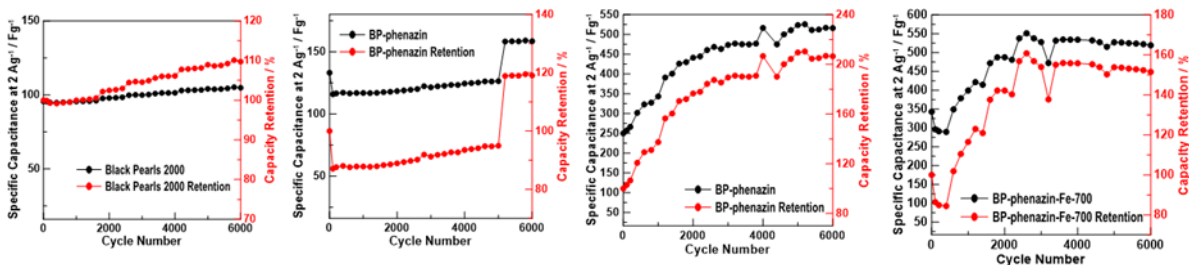
Supporting Information Figure S6.22) Capacity retention of the Black Pearls systems in 0.5 M H_2SO_4 over the 6000 GCD cycles.
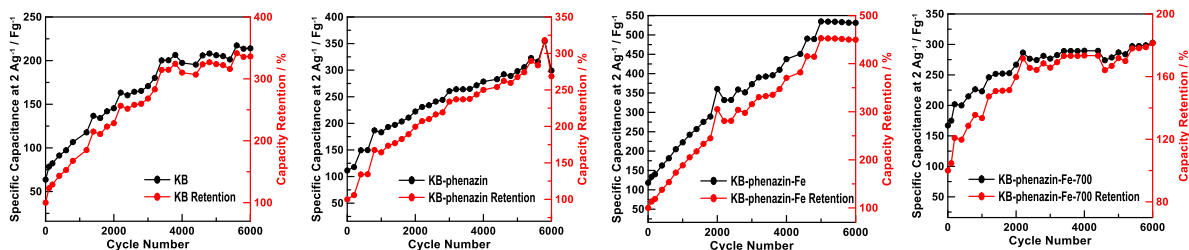
Supporting Information Figure S6.23) Capacity retention of the Ketjen Black systems in 0.5 M H_2SO_4 over the 6000 GCD cycles.
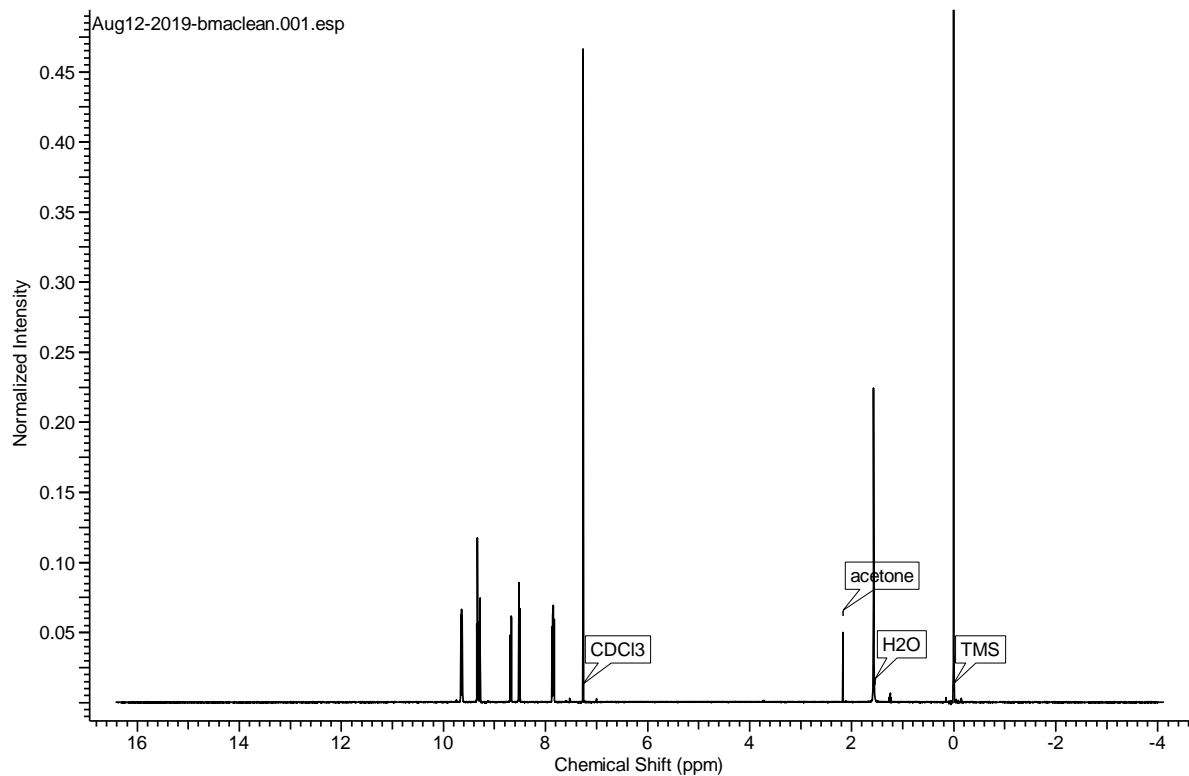
Supporting Information Figure S6.24) H^1-NMR spectra of compound **1** in $CDCl_3$, 400 MHz.
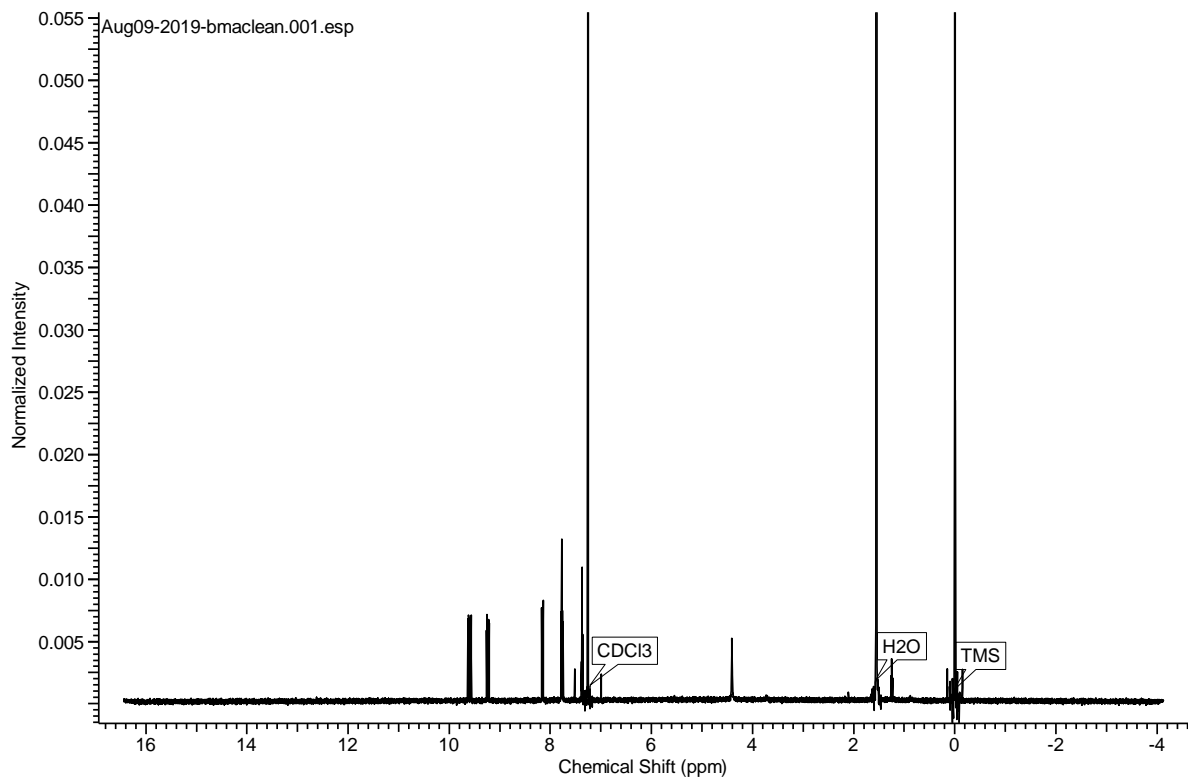
Supporting Information Figure S6.25) H[1]-NMR spectra of compound **2** in CDCl₃, 400 MHz.
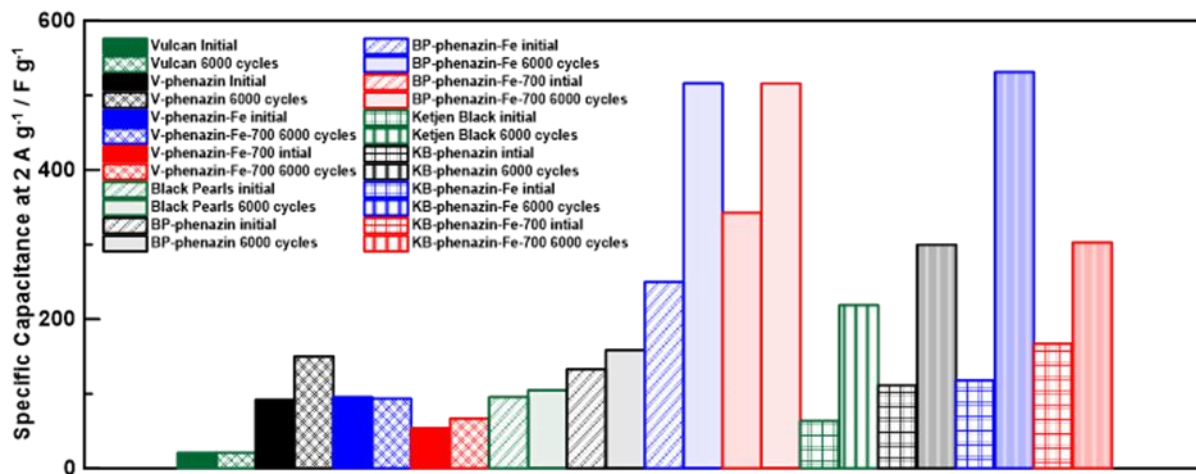
Supporting Information Figure S6.26) Bar graph comparing the specific capacitance values of the materials before and after subjected to long-term GCD stability testing.
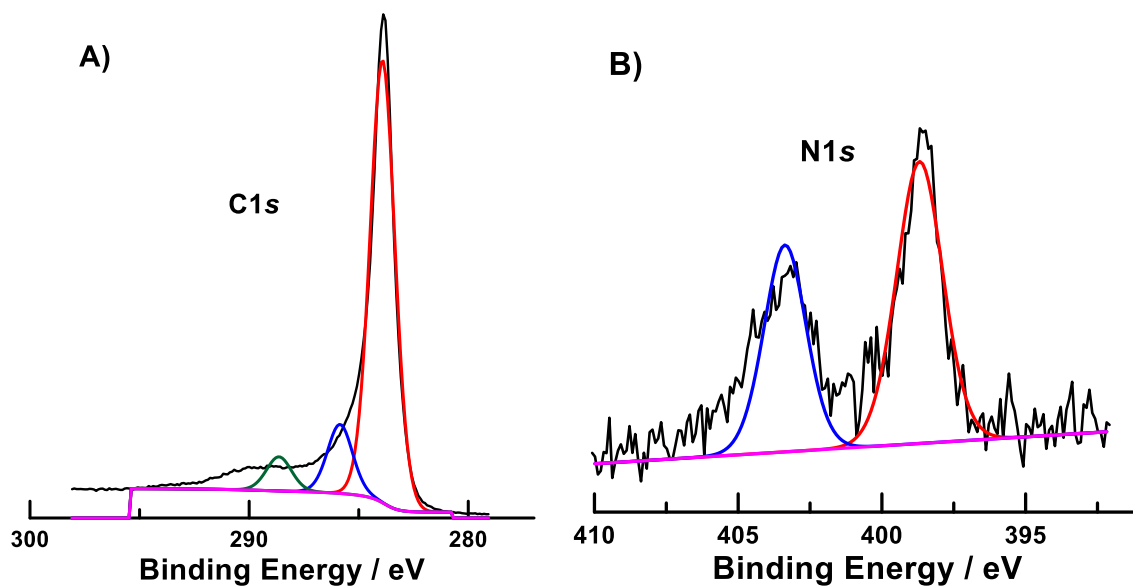
Supporting Information Figure S6.27) Representative XPS spectra of V-phenazin: (A) C 1s region, (B) N 1s region. Black lines show the experimental data, the red, blue, and green lines represent corresponding spectrum deconvolution and magenta line shows the background.
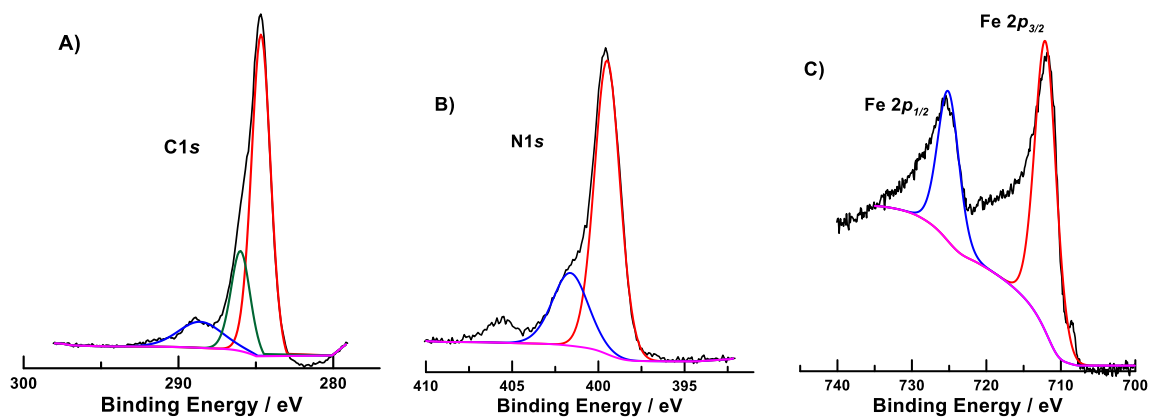
Supporting Information Figure S6.28) Representative XPS spectra of V-phenazin-Fe: (A) C 1s region, (B) N 1s region and (C) Fe 2p region. Black lines show the experimental data, the red, blue, and green lines represent corresponding spectrum deconvolution and magenta line shows the background.
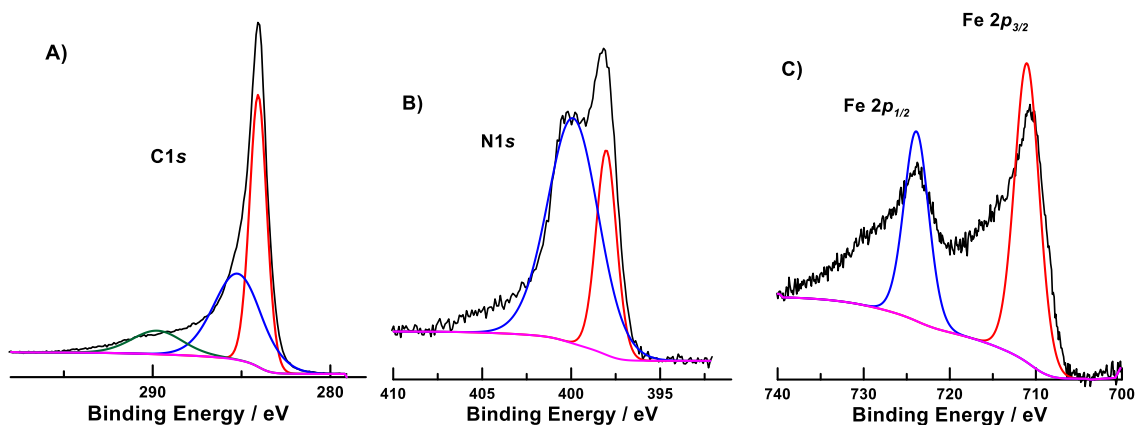
Supporting Information Figure S6.29) Representative XPS spectra of V-phenazin-Fe-700: (A) C 1s region, (B) N 1s region and (C) Fe 2p region. Black lines show the experimental data, the red, blue, and green lines represent corresponding spectrum deconvolution and magenta line shows the background.
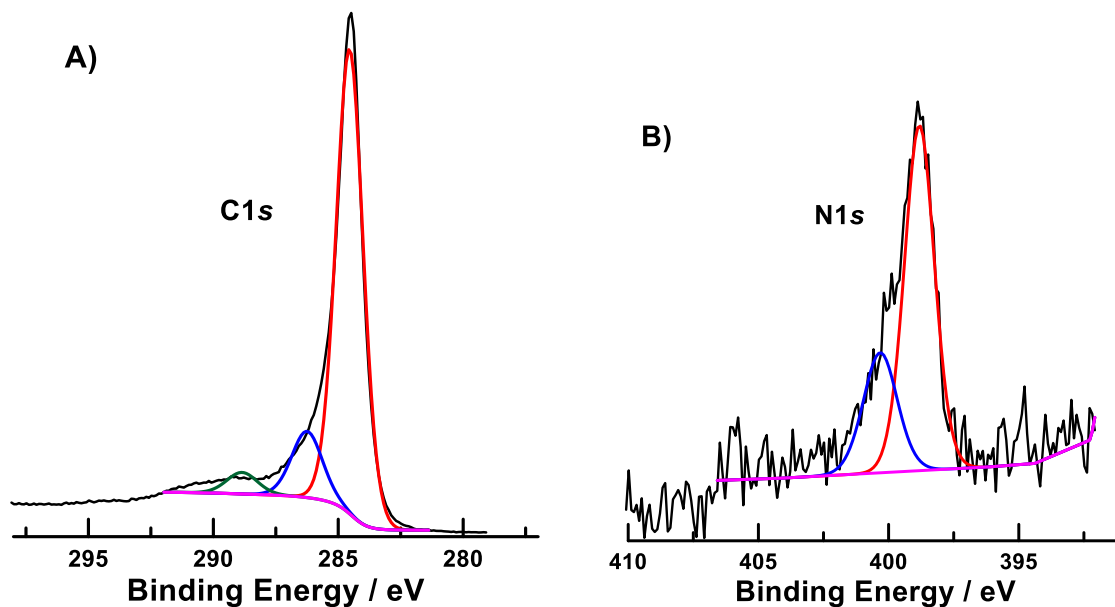
Supporting Information Figure S6.30) Representative XPS spectra of BP-phenazin: (A) C 1s region, (B) N 1s region. Black lines show the experimental data, the red, blue, and green lines represent corresponding spectrum deconvolution and magenta line shows the background.
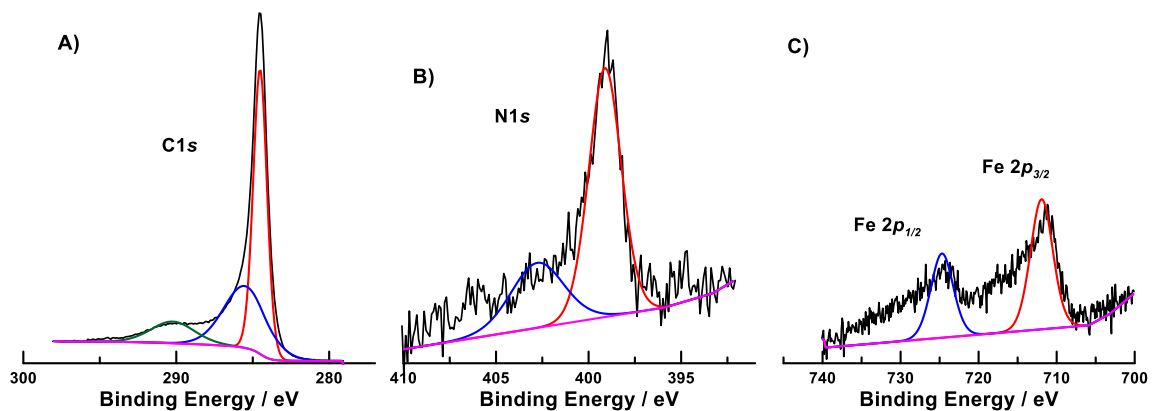
Supporting Information Figure S6.31) Representative XPS spectra of BP-phenazin-Fe: (A) C 1s region, (B) N 1s region and (C) Fe 2p region. Black lines show the experimental data, the red, blue, and green lines represent corresponding spectrum deconvolution and magenta line shows the background.
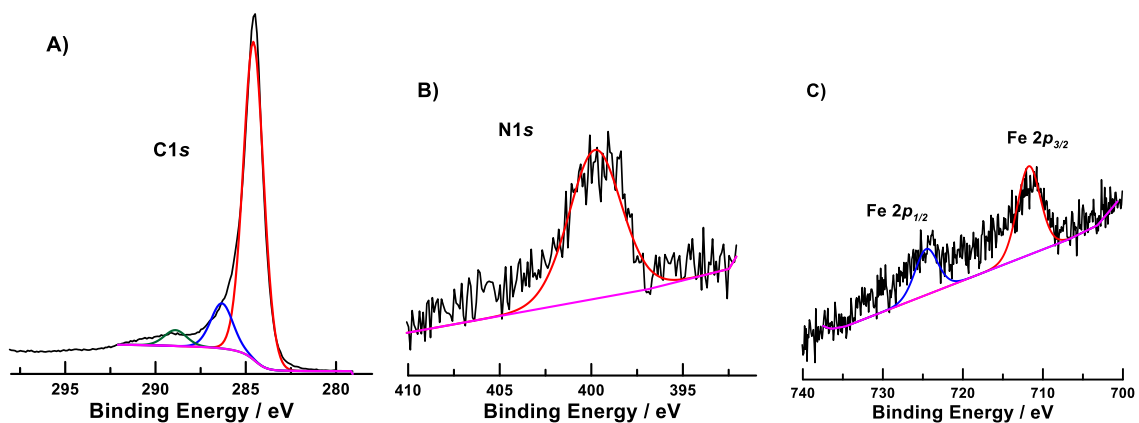
Supporting Information Figure S6.32) Representative XPS spectra of BP-phenazin-Fe-700: (A) C 1s region, (B) N 1s region and (C) Fe 2p region. Black lines show the experimental data, the red, blue, and green lines represent corresponding spectrum deconvolution and magenta line shows the background.
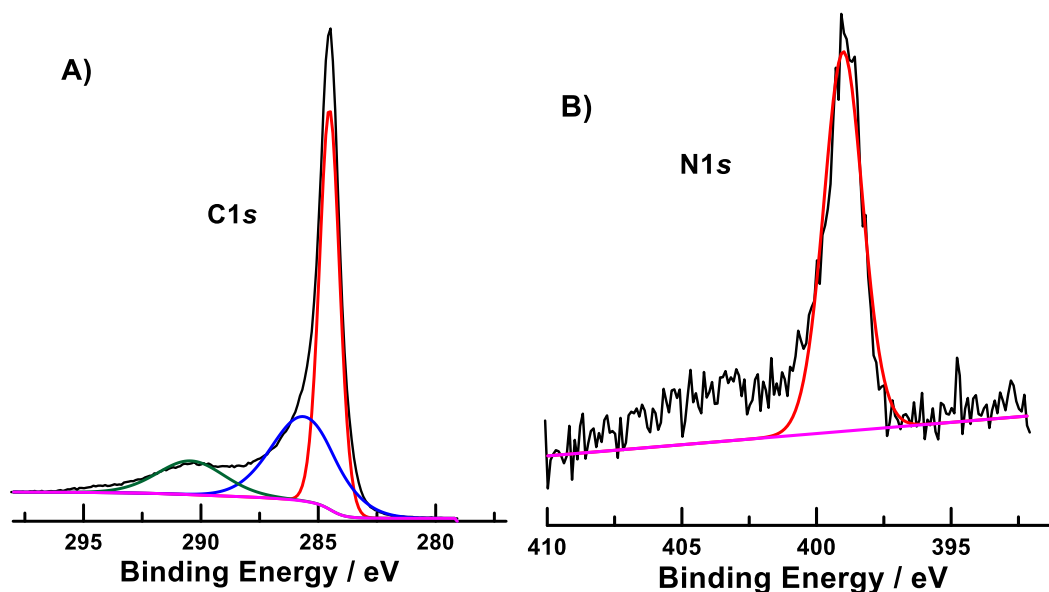
Supporting Information Figure S6.33) Representative XPS spectra of KB-phenazin: (A) C 1s region, (B) N 1s region. Black lines show the experimental data, the red, blue, and green lines represent corresponding spectrum deconvolution and magenta line shows the background.
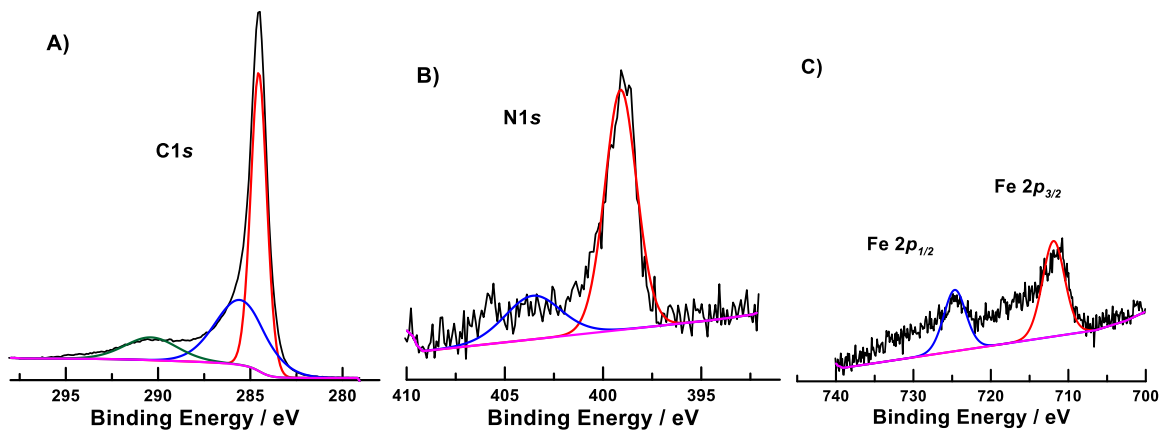
Supporting Information Figure S6.34) Representative XPS spectra of KB-phenazin-Fe: (A) C 1s region, (B) N 1s region and (C) Fe 2p region. Black lines show the experimental data, the red, blue, and green lines represent corresponding spectrum deconvolution and magenta line shows the background.

191
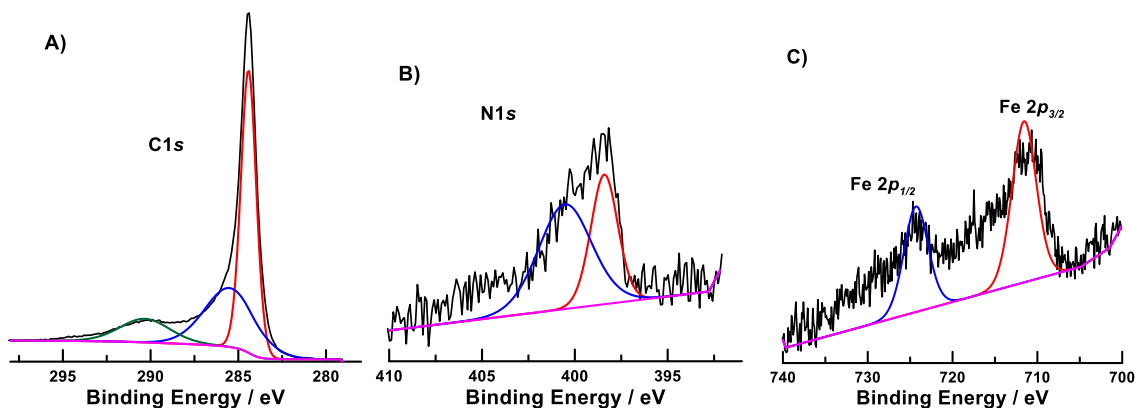
Supporting Information Figure S6.35) Representative XPS spectra of KB-phenazin-Fe-700: (A) C 1s region, (B) N 1s region and (C) Fe 2p region. Black lines show the experimental data, the red, blue, and green lines represent corresponding spectrum deconvolution and magenta line shows the background.

6.6 Acknowledgements

6.7 References

[1]   Z. Ji, K. Liu, N. Li, H. Zhang, W. Dai, X. Shen, G. Zhu, L. Kong, A. Yuan, *J. Colloid Interface Sci.* **2020**, *579*, 282-289.

[2]   S. Rojas-Carbonell, K. Artyushkova, A. Serov, C. Santoro, I. Matanovic, P. Atanassov, *ACS Cat.* **2018**, *8*, 3041-3053.

[3]   Y. Mun, S. Lee, K. Kim, S. Kim, S. Lee, J. W. Han, J. Lee, *J. Am. Chem. Soc.* **2019**, *141*, 6254-6262.

[4]   J. H. Zagal, M. T. Koper, *Angew. Chem. Int. Ed. Engl.* **2016**, *55*, 14510-14521.

[5]   A. Kongkanand, M. F. Mathias, *J. Phys. Chem. Lett* **2016**, *7*, 1127-1137.

[6]   F. Jaouen, D. Jones, N. Coutard, V. Artero, P. Strasser, A. Kucernak, *Johnson Matthey Tech* **2018**, *62*, 231-255.

[7]   J. Herranz, F. Jaouen, M. Lefevre, U. I. Kramm, E. Proietti, J. P. Dodelet, P. Bogdanoff, S. Fiechter, I. Abs-Wurmbach, P. Bertrand, T. M. Arruda, S. Mukerjee, *J. Phys. Chem. C* **2011**, *115*.

[8]   A. Janßen, I. Martinaiou, S. Wagner, N. Weidler, A. Shahraei, U. I. Kramm, *Hyperfine Interact.* **2018**, *239*.

[9]   J. Tian, A. Morozan, M. T. Sougrati, M. Lefevre, R. Chenitz, J. P. Dodelet, D. Jones, F. Jaouen, *Angew. Chem. Int. Ed. Engl.* **2013**, *52*, 6867-6870.

[10]   H. Zhang, S. Hwang, M. Wang, Z. Feng, S. Karakalos, L. Luo, Z. Qiao, X. Xie, C. Wang, D. Su, Y. Shao, G. Wu, *J. Am. Chem. Soc.* **2017**, *139*, 14143-14149.

[11]   A. Serov, K. Artyushkova, P. Atanassov, *Adv. Ener. Mater.* **2014**, *4*, 1-7.

[12]   Q. Jia, N. Ramaswamy, H. Hafiz, U. Tylus, K. Strickland, G. Wu, B. Barbiellini, A. Bansil, E. F. Holby, P. Zelenay, *ACS Nano* **2015**, *9*, 12496-12505.

[13]   H. M. Barkholtz, D.-J. Liu, *Materials Horizons* **2017**, *4*, 20-37.

[14]   M. Lefèvre, J.-P. Dodelet, *Electrochim. Acta* **2008**, *53*, 8269-8276.

[15]   A. D. Pauric, B. J. MacLean, E. B. Easton, *J. Electrochem. Soc.* **2011**, *158*, B331-B336.

[16]   A. D. Pauric, A. W. Pedersen, T. Andrusiak, E. B. Easton, *J. Electrochem. Soc.* **2010**, *157*, B370-B375.

[17]   H. Schulenburg, S. Stankov, V. Schulnemann, J. Radnik, I. Dorbandt, S. Fiechter, P. Bogdanoff, H. Tributsch, *J Phys Chem B* **2003**, *107*, 9034-9041.

[18]   M. Rauf, Y.-D. Zhao, Y.-C. Wang, Y.-P. Zheng, C. Chen, X.-D. Yang, Z.-Y. Zhou, S.-G. Sun, *Electrochem. Commun.* **2016**, *73*, 71-74.

[19]   X. Li, G. Liu, B. N. Popov, *J. Power Sources* **2010**, *195*, 6373-6378.

[20]   H. Tan, Y. Li, X. Jiang, J. Tang, Z. Wang, H. Qian, P. Mei, V. Malgras, Y. Bando, Y. Yamauchi, *Nano. Ener.* **2017**, *36*, 286-294.

[21]   F. Jaouen, S. Marcotte, J. P. Dodelet, G. Lindbergh, *J phys Chem B* **2003**, *107*, 1376-1386.

[22]   P. J. Hall, M. Mirzaeian, S. I. Fletcher, F. B. Sillars, A. J. R. Rennie, G. O. Shitta-Bey, G. Wilson, A. Cruden, R. Carter, *Energy Environ. Sci.* **2010**, *3*.

[23]   N. H. Basri, M. Deraman, R. Daik, M. T. M. Ayob, M. I. Sahri, N. S. M. Nor, B. N. M. Dolah, S. Soltaninejad, *Advanced Materials Research* **2015**, *1112*, 236-240.

[24] S. Breitenbach, N. Gavrilov, I. Pašti, C. Unterweger, J. Duchoslav, D. Stifter, A. W. Hassel, C. Fürst, *C* **2021**, *7*, 55.

[25] A. Gopalakrishnan, A. Yu, S. Badhulika, *Energy & Fuels* **2020**, *34*, 11508-11518.

[26] X. Liu, T. A. Huber, M. C. Kopac, P. G. Pickup, *Electrochim. Acta* **2009**, *54*, 7141-7147.

[27] X. Liu, P. G. Pickup, *J. Electrochem. Soc.* **2011**, *158*, A241-A249.

[28] X. Liu, P. G. Pickup, *J. Power Sources* **2008**, *176*, 410-416.

[29] Y. Wang, J. Wang, S. Morimoto, G. J. Hong Melvin, R. Zhao, Y. Hashimoto, M. Terrones, *Carbon* **2019**, *143*, 776-785.

[30] Y. Dai, S. He, L. Yu, J. Liu, L. Gan, M. Long, *Journal of Physics and Chemistry of Solids* **2019**, *129*, 122-127.

[31] G. Wang, X. Sun, J. Bai, L. Han, *Journal of Materials Science: Materials in Electronics* **2019**, *30*, 4665-4675.

[32] W. Wang, Y. Yang, X. Wang, Y. Zhou, X. Zhang, L. Qiang, Q. Wang, Z. Hu, *New J. Chem.* **2019**, *43*, 6380-6387.

[33] Y. Shu, J. Maruyama, S. Iwasaki, S. Maruyama, Y. Shen, H. Uyama, *J. Power Sources* **2017**, *364*, 374-382.

[34] N. Cai, J. Fu, H. Zeng, X. Luo, C. Han, F. Yu, *Journal of Alloys and Compounds* **2018**, *742*, 769-779.

[35] G. Pognon, T. Brousse, D. Bélanger, *Carbon* **2011**, *49*, 1340-1348.

[36] G. Pognon, C. Cougnon, D. Mayilukila, D. Belanger, *ACS Appl Mater Interfaces* **2012**, *4*, 3788-3796.

[37] X. Zhu, D. Hou, H. Tao, M. Li, *Journal of Alloys and Compounds* **2020**, *821*, 153580.

[38] C. Xiong, Q. Yang, W. Dang, M. Li, B. Li, J. Su, Y. Liu, W. Zhao, C. Duan, L. Dai, *J. Power Sources* **2020**, *447*, 227387.

[39] H. M. Fruehwald, O. V. Zenkina, E. B. Easton, *ECS Transactions* **2019**, *92*, 523-532.

[40] H. M. Fruehwald, I. I. Ebralidze, O. V. Zenkina, E. B. Easton, *ChemElectroChem* **2020**, *8*, 53-61.

[41]   H. M. Fruehwald, I. I. Ebralidze, O. V. Zenkina, E. B. Easton, *ChemElectroChem* **2019**, *6*, 1350-1358.

[42]   H. M. Fruehwald, I. I. Ebralidze, P. D. Melino, O. V. Zenkina, E. B. Easton, *J. Electrochem. Soc.* **2020**, *167*, 084520.

[43]   S. Bodige, F. M. MacDonnell, *Tetrahedron Lett.* **1997**, *38*, 8159-8160.

[44]   F. J. Rawson, C. L. Yeung, S. K. Jackson, P. M. Mendes, *Nano Lett* **2013**, *13*, 1-8.

[45]   C. D. Wagner, L. E. Davis, M. V. Zeller, J. A. Taylor, R. H. Raymond, L. H. Gale, *Surf. Interface Anal.* **1981**, *3*, 211-225.

[46]   A. K. Farquhar, M. Supur, S. R. Smith, C. Dyck, R. L. McCreery, *Adv. Ener. Mater.* **2018**, *8*, 1-9.

[47]   Z. Ji, N. Li, M. Xie, X. Shen, W. Dai, K. Liu, K. Xu, G. Zhu, *Electrochim. Acta* **2020**, *334*, 135632.

[48]   M. Toupin, D. Bélanger, I. R. Hill, D. Quinn, *J. Power Sources* **2005**, *140*, 203-210.

[49]   B. D. Ossonon, D. Bélanger, *Carbon* **2017**, *111*, 83-93.

[50]   M. Sun, D. Davenport, H. Liu, J. Qu, M. Elimelech, J. Li, *J. Mat. Chem. A* **2018**, *6*, 2527-2539.

[51]   B. Liu, W. Dai, Z. Liang, J. Ye, L. Ouyang, *Int. J. Hydrog. Energy* **2017**, *42*, 5908-5915.

[52]   X. Zhang, Y. B. Mollamahale, D. Lyu, L. Liang, F. Yu, M. Qing, Y. Du, X. Zhang, Z. Q. Tian, P. K. Shen, *J. Catal.* **2019**, *372*, 245-257.

[53]   L.-F. Chen, Z.-H. Huang, H.-W. Liang, W.-T. Yao, Z.-Y. Yu, S.-H. Yu, *Energy Environ. Sci.* **2013**, *6*.

[54]   F. Fusalba, P. Gourec, D. Villers, D. Belanger, *J. Electrochem. Soc.* **2001**, *148*, A1-A6.

[55]   N. O. Laschuk, Ebralidze, II, J. Poisson, J. G. Egan, S. Quaranta, J. T. S. Allan, H. Cusden, F. Gaspari, F. Y. Naumkin, E. B. Easton, O. V. Zenkina, *ACS Appl Mater Interfaces* **2018**, *10*, 35334-35343.

[56]   N. Ramaswamy, S. Mukerjee, *J. Phys. Chem. C* **2011**, *115*, 18015-18026.

[57]   O. R. Reid, F. S. Saleh, E. B. Easton, *Electrochim. Acta* **2013**, *114*, 278-284.

[58]   N. O. Laschuk, E. B. Easton, O. V. Zenkina, *RSC Adv.* **2021**, *11*, 27925-27936.

[59] J. Niu, B. E. Conway, W. G. Pell, *J. Power Sources* **2004**, *135*, 332-343.

[60] B. E. Conway, W. Pell, T. Liu, *J. Power Sources* **1997**, *65*, 53-59.

[61] S. Kazaryan, G. Kharisov, S. Litvinenko, V. Kogan, *J. Electrochem. Soc.* **2007**, *154*, A751.

[62] J. Black, H. A. Andreas, *Electrochim. Acta* **2009**, *54*, 3568-3574.

[63] J. Wang, J. Polleux, J. Lim, B. Dunn, *J. Phys. Chem. C* **2007**, *111*, 14925-14931.

[64] G. Zhang, R. Chenitz, M. Lefèvre, S. Sun, J.-P. Dodelet, *Nano. Ener.* **2016**, *29*, 111-125.

[65] D. Banham, S. Ye, K. Pei, J.-i. Ozaki, T. Kishimoto, Y. Imashiro, *J. Power Sources* **2015**, *285*, 334-348.

[66] C. H. Choi, C. Baldizzone, J. P. Grote, A. K. Schuppert, F. Jaouen, K. J. Mayrhofer, *Angew. Chem. Int. Ed. Engl.* **2015**, *54*, 12753-12757.

[67] G. Liu, X. Li, P. Ganesan, B. N. Popov, *Electrochim. Acta* **2010**, *55*, 2853-2858.

[68] J. Cobos-Murcia, L. Galicia, A. Rojas-Hernández, M. Ramírez-Silva, R. Álvarez-Bustamante, M. Romero-Romo, G. Rosquete-Pina, M. Palomar-Pardavé, *Polymer* **2005**, *46*, 9053-9063.

[69] X. Bao, Q. Zhao, H. Wang, K. Liu, D. Qiu, *Inorganic Chemistry Communications* **2013**, *38*, 88-91.

Chapter 7. High-performance water oxidation catalysts based on the spontaneous deposition of ruthenium on electrochemically exfoliated graphene oxide

7.0 Preface

Part of the work described in this chapter has been published as: Fruehwald, H. M.; Moghaddam, R. B.; Zenkina, O. V.; Easton, E. B., High-performance water oxidation catalysts based on the spontaneous deposition of ruthenium on electrochemically exfoliated graphene oxide. *Catal. Sci. Technol.* **2019,** *9*, 6547-6551. doi: 10.1039/c9cy02017a with permission from the Royal Society of Chemistry.

In this chapter, the exploration of the effect of using a simple and facile method to produce a high-performing water oxidation catalyst by preparing graphene oxide through electrochemical methods and subsequently doping it with various ruthenium salts. I explored the use of different ruthenium salts to study the effect of the Ru oxidation state on the activity and overall electrochemical long-term stability of the catalytic material. Notably, the ruthenium III salt showed the highest activity along with high stability of all the catalysts tested. The exfoliated graphene provided a high-performing, stable support that was low-cost and easy to produce. The resulting synthetic procedure showed a unique and simple way to produce novel high-performing materials. As a result, this synthetic methodology to dope metals onto the exfoliated graphene oxide was further explored for alkaline oxygen evolution using nickel in Chapter 8.

7.0 Abstract

Novel water oxidation reaction (WOR) catalysts prepared *via* spontaneously depositing Ru on electrochemical graphene oxide (EGO), Ru(III)@EGO and Ru(VII)@EGO, produced outstanding specific activities over 100 A g^{-1} (@ 1.8 V_{RHE}), WOR onset overpotentials of 0.2 V or less, and stable long term performances (1 mA cm^{-2}).

7.1 Introduction

Tremendous efforts have been recently directly towards replacing fossil fuels with renewable, greener, and more efficient energy storage/conversion systems, as the population and the resulting energy demand grow rapidly worldwide[1-5]. Such energy systems require sustainably active materials and readily available reactants (i.e. fuels) that do not contribute to pollution. One such renewable energy systems are fuel cells whose feeds are the product of the water oxidation reaction (WOR), which is the central anodic process in water electrolyzers to split water into its constituting compartments, i.e. H_2 and O_2[6]. This "cycle" is appealing in that the product of one system is the feed of another. While the fuel cell process is spontaneous and produces energy, the WOR is an endothermic reaction[7], meaning it requires energy to proceed. Electrochemical catalysis of WOR is a known subject of actively ongoing research, which involves the process to occur over a catalyst. Due to the sluggish kinetics associated with splitting water, electrochemical WOR at the most active iridium (Ir) and ruthenium (Ru)-based catalysts proceeds with significant overpotentials, which consequently decreases the efficiency of the reaction. There have been attempts to improve WOR performance of these catalyst materials by combining them with support materials, ligands, other transition metals, and tuning physical characteristics (e.g. crystallinity, particle size, morphology, etc.)[8-14].

Splitting water to yield O_2 and H_2 gases can be used in various renewable systems. H_2 can be stored (i.e. hydrogen storage) for future uses or can be transferred to H_2-fed devices (e.g. proton exchange membrane fuel cells, PEMFC) that oxidize hydrogen as part of their energy production process. O_2 is the cathodic reactant in PEMFC and also in Li-Air batteries, while it can also be used as a strong oxidizing agent[9, 15]. Nevertheless, to reduce the associated WOR overpotential and conduct the reaction at a reasonable pace the catalysts are mainly based on Ir, which is known as an extremely rare metal[10, 16-17]. Sustainable commercialization of the water electrolyzers depends upon abundancy of the

contributing materials. Either Ir should be replaced with less rare material and/or its activity per mass should be improved.

As a potential replacement for Ir, Ru is an interesting metal as it can exist in several oxidation states, which helps electron mobility that is part of any electrochemical reaction including WOR[8-9, 18]. Ru is reasonably active towards WOR, and is considerably less rare and expensive than Ir. However, Ru is prone to dissolution at high potentials in acid, which limits its application in PEM water electrolyzers. The knowledge of the Ru-based WOR catalysts is quite rudimentary, where there is hardly a systematic report of such materials outside the territory of transition metal complexes. This is primarily due to the inherent issues associated with Ru electrochemistry in acid where WOR is active[19-21]. As well, compared with Ir as the most active WOR catalyst, Ru-based materials still suffer from various issues such as more significant overpotentials, and slow kinetics[22]. Antimonene-supported Ru was shown to have great hydrogen evolution activity[23], taking advantage of the strong synergistic effect of the highly conductive support on the reaction. Furthermore, the homogeneous Ru ligand-based catalysts often seen in the literature typically require the addition of a strong oxidizing agent to promote the WOR, which can complicate the process[24]. Such increased complexity can lead to additional costs and uncontrolled products and side reactions. Taking into account that rationale, scaling up WOR materials require simple and cost-effective systems that are easily controlled (and tunable) while being sustainably active. 2D Graphene has various advantageous properties for renewable energy systems such as mechanical strength, fast electron transfer, high surface area, and it can be easily doped with metals[25-27]. Through electrochemical methods graphene oxide can be produced as a very low cost, and minimal environmental impact as opposed to other high-temperature methods[28]. We have hypothesized that by spontaneous deposition of the active RuO_x materials on the surface of the graphene oxide we can increase the number of active sites on the catalyst, thereby improving the activity and stability of the materials[10]. In a previous report, graphene was used to stabilize and enhance conductivity of the catalyst[29]. In this respect, the present work aims at using a facile method to deposit Ru oxide onto graphene oxide. Here we use a deposition protocol originally developed for spontaneous incorporation of RuO_x onto carbon materials[30]. We first synthesized graphene oxide *via* a one-pot electrochemical exfoliation of graphite. Then in an alkaline

solution containing various Ru salt the EGO spontaneously reacted with Ru ions to produce Ru@EGO composites. The result of such synthesis approach was a stable and active water oxidation catalysis.

7.2 Experimental

7.2.1 Materials

Sulfuric acid, oxalic acid, phosphoric acid, ruthenium (III) chloride monohydrate, isopropyl alcohol, and potassium hydroxide were purchased from Sigma Aldrich. Potassium perruthenate (VII) and graphite rods (6.3 mm diameter and 61 cm long) were purchased from Alfa Aesar. Nafion® was purchased from Ion Power Inc. TPG-H-090 Toray Paper 30% Wet Proofing Carbon fibre paper was purchased from Fuel Cell Earth LLC.

7.2.2 Catalyst Synthesis

Electrochemical graphene oxide was synthesized via a previously published procedure[31]. The synthesis of the modified EGO with ruthenium was adapted from literature procedures[32-33]. Briefly, electrochemically synthesized graphene oxide (EGO), and the desired ruthenium salt (Ru^{3+} or Ru^{7+}) were added to a reaction vessel in the presence of 1 M KOH. The amounts of material added afforded a targeted 5% metal loading on the EGO. The reaction was stirred under ambient conditions for 4 days. When the reaction was complete the Ru@EGO materials were centrifuged and washed with water, then aged in N_2 purged water for 1 week. After the aging procedure the samples were placed in an oven at ~ 70ºC to dry.

7.2.3 Physical Characterization

Catalysts were characterized by a HITACHI FlexSEM 1000 scanning electron microscope equipped with Energy dispersive spectroscopy (ED) analysis probe. EDS showed about 3% Ru deposited on EGO, which gives about 60% efficiency for the spontaneous reaction. TEM measurements were performed on a Zeiss Libra 200MC transmission microscope system operating at 200 keV using a slit width of 10 eV and a spot size of 1 nm. ImageJ software was used to calculate the particle size distribution. XPS measurements were performed on a Thermo Scientific K-Alpha Angle-Resolved X-ray photoelectron spectrometer with a monochromated Al Kα (1486.7 eV) X-ray source and 180º double focusing hemispherical analyzer with 128 channel detector with charge

compensation. A Shirley fit algorithm was used for the background subtraction and a Powell peak fitting algorithm was utilized for the data analysis. Pore size analysis was performed on a Quantachrome NOVAe 1200 analyzer. Thermogravimetric analysis was performed on a TA instruments Q600 SDT thermal analyzer. The samples were ran in an air atmosphere at 10 mL min^{-1} with a ramp rate of 5ºC min^{-1}. Raman Spectra were obtained using a Renishaw in Via confocal Raman Microscope with a Renishaw Centrus OMCN39 CCD detector. Exciation wavelength of the Nd:YAG laser (Renishaw) was 532 nm with a power output of 50 mW. Spectra were acquired by performing a scan from 100-4000 cm^{-1} with an exposure time of 30 seconds per scan, a laser power of 1% and at 50x objective. X-ray diffraction was measured using a Rigaku Ultima IV with Cu Kα radiation. Patterns were recorded over the 20-90º 2θ range with a step size of 0.02º. HRTEM Electron microscopy was performed at the Canadian Centre for Electron Microscopy (also supported by NSERC and other government agencies).

7.2.4 Electrochemical Characterization

The water oxidation reaction was studied using a carbon fibre paper electrode in 0.5 M H_2SO_4. Catalyst inks were made by sonicating 10 mg of catalyst, 200 µL deionized water, 200 µL isopropyl alcohol, and 100 µL Nafion®. 10 µL of the catalyst was dropped onto a piece of carbon fibre paper and dried with heat (200 µg cm^{-2} catalyst loading). A mercury/mercury sulfate reference electrode was used and a graphite rod was used as a counter electrode. The electrochemical measurements were performed using a Solartron Analytical 1470E potentiostat connected to a Solartron SI 1260 impedance/gain-phase analyze with corresponding Multistat and Zplot software.

7.3 Results and Discussion

Figure 7.1A and B shows the transmission electron micrographs (TEM) of the synthesized Ru(III)@EGO and Ru(VII)@EGO catalysts. From the TEM one can observe that the Ru(III)@EGO catalyst is rather amorphous, with some larger agglomerates of Ru on the EGO surface in comparison to Ru(VII)@EGO that appears to have less agglomeration and more evenly distributed Ru particles. We estimated the particle size distribution (inset Figure 7.1A and B) for the Ru(III)@EGO samples to be *ca.* 1.73 ± 0.78 nm in size, while particles were larger (2.7 ± 0.8 nm) for the Ru(VII)@EGO. The high

resolution TEM (HRTEM) images shown in the SI (Figure S7.11) also confirm the particle size measurement presented in Figure 7.1.
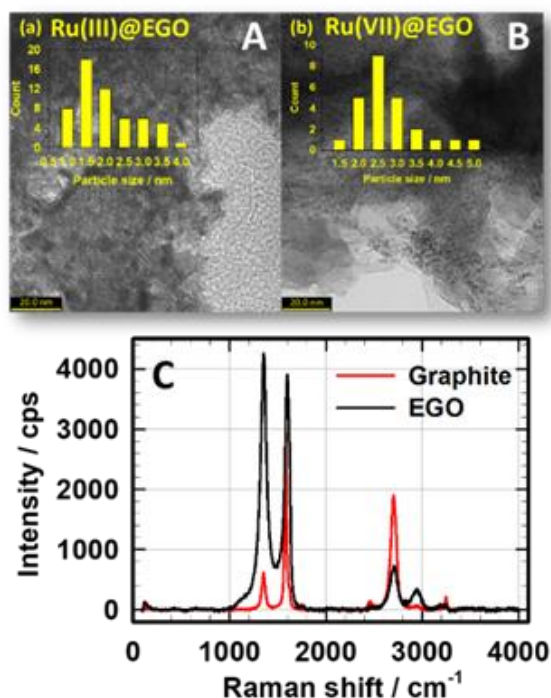
Figure 7.1) TEM images and particle size distributions of (A) Ru(III)@EGO and (B) Ru(VII)@EGO catalysts. (C) Raman spectrum of the graphite rod before and after electrochemical exfoliation to EGO.

Raman analysis was performed on the graphite rod before and after electrochemical exfoliation to characterize the EGO (Figure 7.1C) and distinguish it from the starting graphite. Characteristic peaks of graphite can be seen from samples before exfoliation. There is an intense peak at 1579 cm^{-1}, indicative of graphitic carbon in the form of sp^2 carbon vibrational mode, and a small D-band (or defect) peak at 1350 cm^{-1} due to some sp^3 carbons[27, 34]. After the electrochemical exfoliation an increase in the defect peak as observed, which indicates there are more defects in the carbon structure. Thus further shows to the addition of oxygen functional groups disrupting the sp^2 carbon lattice[35]. The 2D peak at 2701 cm^{-1} in the graphite spectrum red-shifted to 2704 cm^{-1} after exfoliation broadened, and its intensity decreased. These observations indicate that the multi-layered graphite has been converted to EGO, which ideally should be single-layered while we believe it still holds some layered structures[34-36]. Further confirmation of the successful exfoliation was inferred from BET analysis, which showed an expectedly low surface area of 10 m^2 g^{-1} for the EGO[37]. X-ray diffraction was also performed on the Ru@EGO

composites, in which characteristic peaks associated with Ru phases were not clearly observed (Figure S7.8), likely due to the amorphous nature of the catalysts. We performed extensive electron microscopy analysis on these samples, which consistently showed very small particles. The reader is referred to the supplementary information section (8.5) for detailed physical characterization of the materials.

Figure 7.2 displays potentiodynamic responses for the EGO (A) and Ru@EGO catalysts (B; corrected for the Ru mass) in 0.5 M H_2SO_4, at 20 mV s^{-1}. The mass corrected CVs for the Ru@EGO catalysts are plotted separately since a reasonable comparison was not possible with the EGO without metal. We also note that Ru is a pseudocapacitive metal[30], hence deconvoluted contribution of C and Ru to currents was not possible either. Nevertheless, the CV of EGO is dominated with broad reversible peaks centered at 0.65 (anodic, i.e. oxidation) and 0.50 V_{RHE} (cathodic i.e. reduction), superimposed on a quite large background current on both forward and reverse sweeps. The reversible peaks are known to represent oxygen containing functional groups on carbon (e.g. quinone-like structures)[38]. The charging current is characteristic of high surface area carbon materials. Once can estimate capacitance of the electrode by integrating the area with no faradaic feature (or subtracting the faradaic charges), which produced 166.1 F g^{-1} of carbon. Such a number represents a high specific capacitance for carbon[39-42].
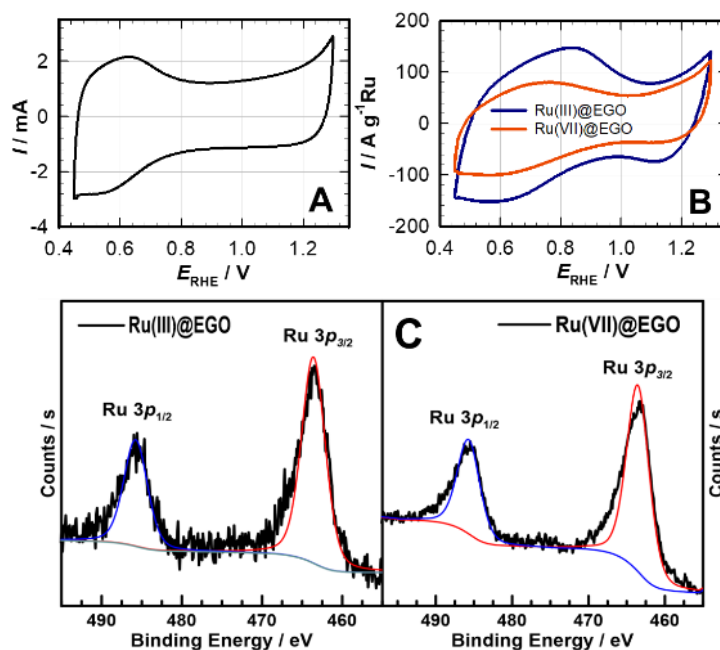
Figure 7.2) Cyclic voltammetry at 20 mV s^{-1} for (A) EGO and (B) Ru@EGO catalysts in 0.5 M H$_2$SO$_4$. (C) X-ray photoelectron spectroscopy profiles for Ru 3p of the Ru@EGO catalysts.

The CVs in Figure 7.2B, presenting voltammetry over the Ru@EGO catalysts, shows similar general electrochemical features. First, it is notable that the Ru(III)@EGO composite shows a greater charging and peak currents per mass of Ru. Second, peaks on both forward and reverse scans have shifted to more positive potentials, where they also show more potential separations than those over EGO. Such shift is more pronounced with the Ru(III)@EGO, with the anodic peak appearing at around 0.85 V$_{RHE}$ while its cathodic counterpart is centered at 0.55 V$_{RHE}$. These two peaks can also in part represent oxidation and reduction of RuO$_x$ species, which have been reported to occur around this potential region[32]. X-ray photoelectron analysis of the catalysts after thorough purification, Figure 7.2C, suggests domination of Ru(III) and possibly RuO$_2$, where one can detect Ru 3p peak at 463 (3/2) and 434 eV (1/2). Such observation can be due to unreacted Ru(III) that may have been strongly bound to the EGO surface (that multiple washing and mechanical shaking with water and alcohol could not dissolve it out). The supernatant of the synthesis batch was colorless after completion of the reaction, indicating no or minor remainder of the RuCl$_3$ salt (red). Therefore, Ru was likely deposited at EGO is either in the form of RuO$_x$ and/or in the form of Ru(III) composited with EGO.

Figure 7.3A shows linear sweep voltammetry (LSV) responses for the water oxidation reaction (WOR) over the Ru@EGO catalysts. For comparison and as a reference, a control experiment was also conducted on plain EGO. Theoretically, voltammetric WOR is expected to produce a sharp rising current profile at 1.23 V_{RHE} at the thermodynamic potential for water splitting, while in practice such a surge is only seen following a significant overpotential. From the Tafel plots in Figure 7.3B, one can extract onset for WOR to be around 1.35 and 1.38 V_{RHE} for Ru(III)@EGO and Ru(VII)@EGO, respectively, which indicates that Ru(III)@EGO is slightly better. Nevertheless, both catalysts produced remarkable mass specific performances, as obvious in Figure 7.3A, which shows mass corrected WOR activities for the Ru@EGO catalysts. This is an important parameter for a WOR catalyst to be of commercialization potential. However, there is no systematic protocol for such comparison, especially for Ru-based catalysts that are far less documented[43], as a consequence of their instability in acid. Using Ru(III)@EGO with an overpotential less than 0.5 V, a specific current of ca. 100 A g^{-1} of Ru can be sustained. As a representative measure of stability, Figure 7.3C shows that Ru(III)@EGO catalyst was reasonably stable, whose operation potential to maintain a constant current density of 1 mA cm^{-2} increased only slightly over the 24 h galvanostaic hold. Subsequent to the long term hold, voltammetric WOR was again conducted. The LSV profiles after the 24 h galvanostaic hold are also included in Figure 7.3A. They show significantly improved current values, more pronounced after 1.8 V_{RHE}. The effect is more significant over the Ru(VII)@EGO catalyst. The WOR onset potentials seem to have remained the same after the hold, suggesting unchanged reaction mechanisms. However, current after 1.75-1.80 V_{RHE} increased much sharper than before the hold. Zance *et al.*[44] suggested that such improvement is due to the increase in the surface functional groups. Since here EGO has also enhanced activity, we believe that a similar explanation can be extended to our catalysts.
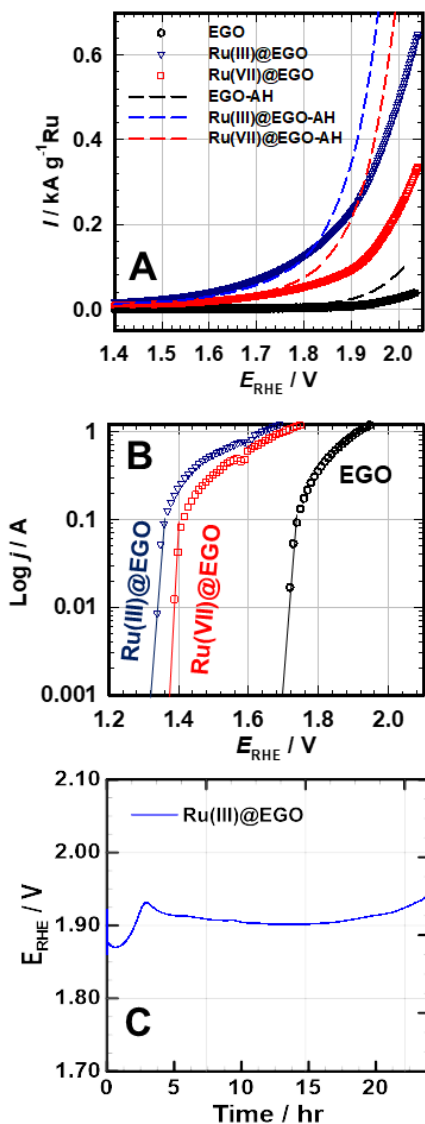
Figure 7.3) (A) Potentiodynamic water oxidation reaction (WOR) at EGO and Ru@EGO catalysts in 0.5 M H_2SO_4 at 10 mV s^{-1}, before and after 24 h hold at 1 mA cm^{-2}. (B) Tafel plots for the EGO and Ru@EGO catalysts. (C) 24 h galvanostatic hold at 1 mA cm^{-2} for the Ru(III)@EGO catalysts.

7.4 Conclusion

Spontaneous deposition of Ru onto electrochemically exfoliated graphene oxide (EGO) produced Ru@EGO composites with superbly high mass-specific activities and low overpotentials for water oxidation reaction (WOR) in acid. The EGO had the remarkably high specific capacitance (CV) of 166.1 F g^{-1}, which should result in providing greater electrochemically accessible reaction sites, accounting for the outstanding performances of the Ru@EGO catalysts. The Ru(III)@EGO was superior to the Ru(VII) counterpart, characterized with an earlier WOR onset and a larger mass corrected current density. The

Ru(III)@EGO composite showed sustainable long term galvanostatic polarization, with a slight increase in potential over a 24 h hold. This study is a spectacular pixel of a larger image, where Ru-based catalysts are being systematically developed for WOR in acid and in base. Introduction of the Ru@EGO catalysts is intended to challenge the dominance of the Ir-based catalysts that are known to be most active while containing rare Ir metal.

7.5 Supporting Information
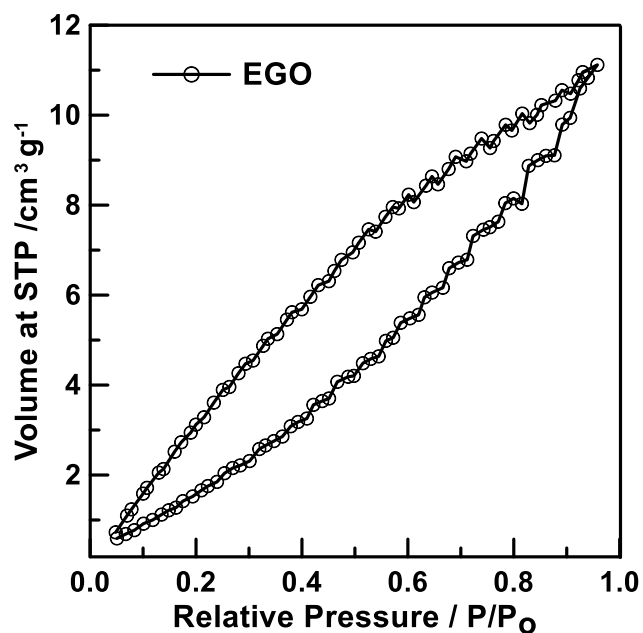
Supporting Information Figure S7.1) BET analysis of EGO with N_2 as the adsorbate.
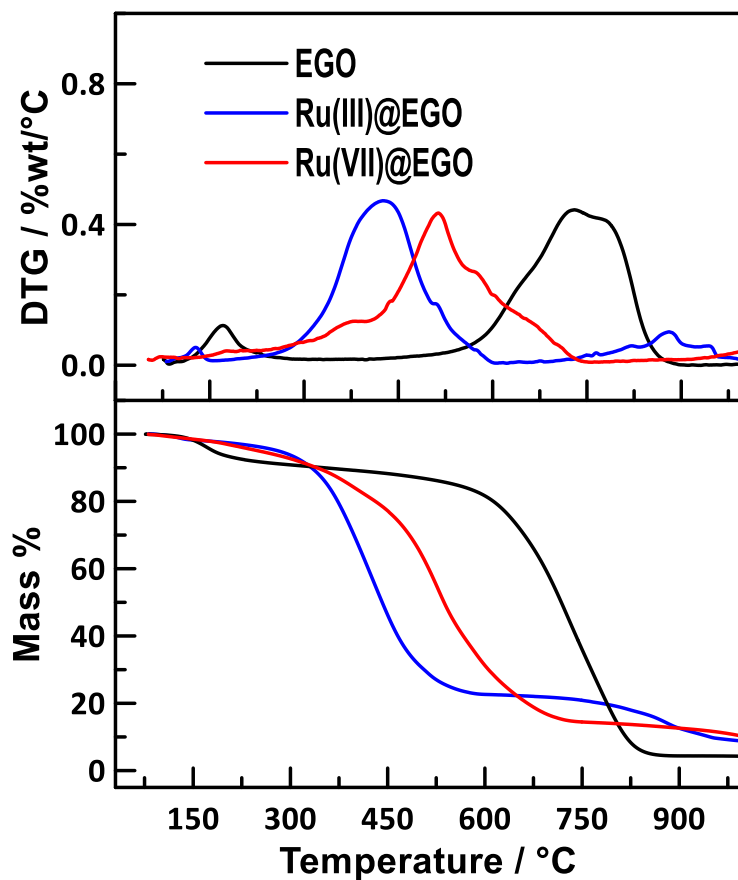
Supporting Information Figure S7.2) (A) Differential thermogram of the synthesized materials in an air atmosphere at 10ºC min^{-1}. (B) thermogravimetry of the materials in an air atmosphere at 10ºC min^{-1}.

TGA results show for the EGO sample a mass loss at 150ºC due to the removal of oxygen functional groups on the carbon. The combustion temperatures lower upon addition of the Ru metal. Metals in the presence of carbon can be combustion catalysts thus why the combustion temperature is lowered in the presence of Ru.
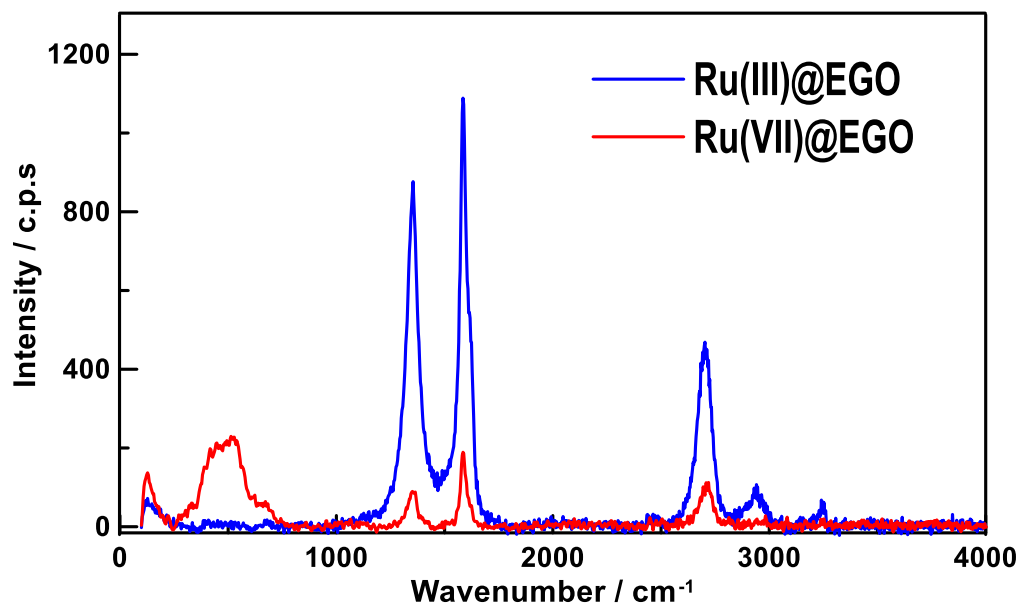
Supporting Information Figure S7.3) Raman spectra of the synthesized materials.

Raman peaks from the EGO are present in all cases (1500 cm^{-1}, 1300 cm^{-1}, and 2700 cm^{-1}). The broad peak present at 520 cm^{-1} is due to RuOx on the surface[45].
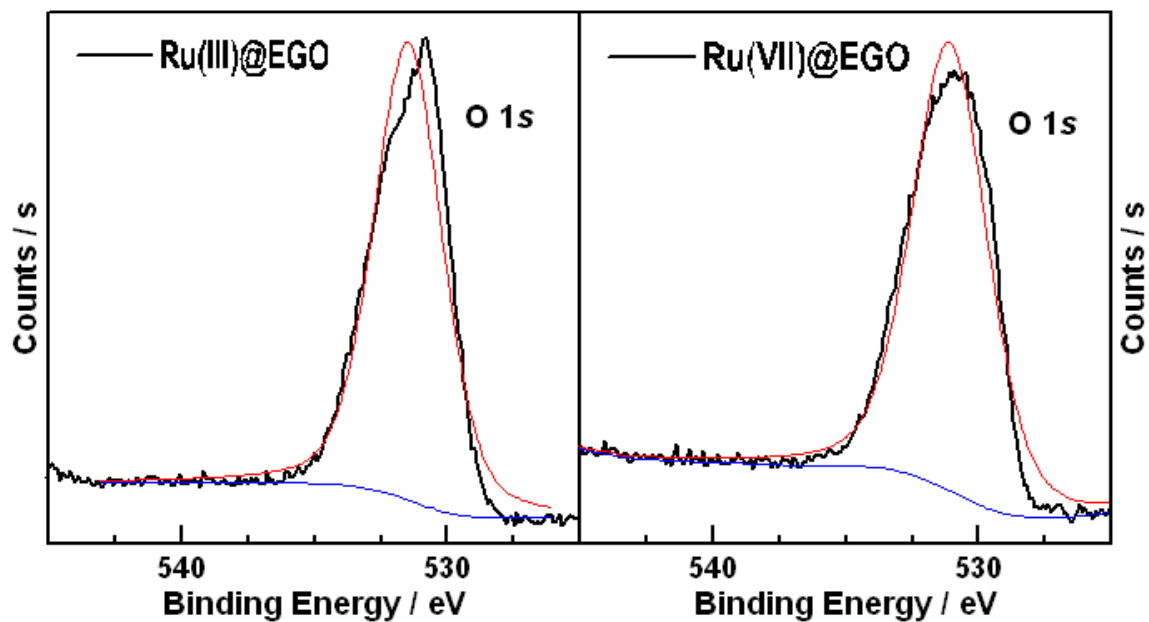
Supporting Information Figure S7.4) XPS O 1s spectra of the Ru(III)@EGO and Ru(VII)@EGO before testing. Red line corresponds to the O 1s.
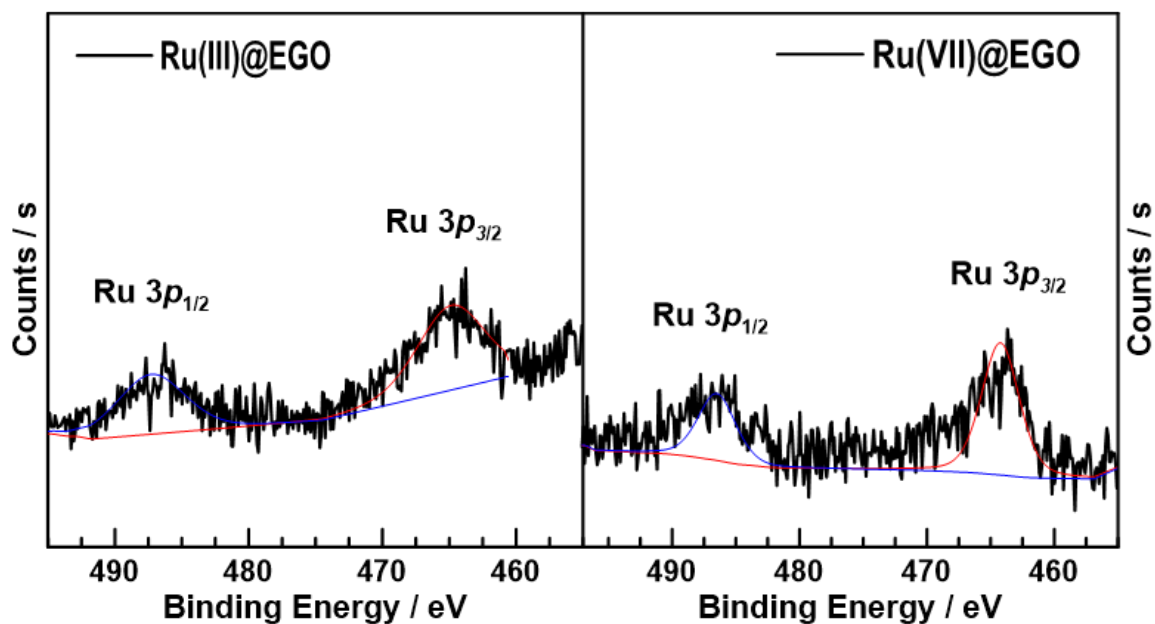
Supporting Information Figure S7.5) XPS spectra of the Ru 3p Ru(III)@EGO and Ru(VII)@EGO after WOR testing. Red line corresponds to the Ru 3p$_{3/2}$, blue line corresponds to Ru 3p$_{1/2}$.
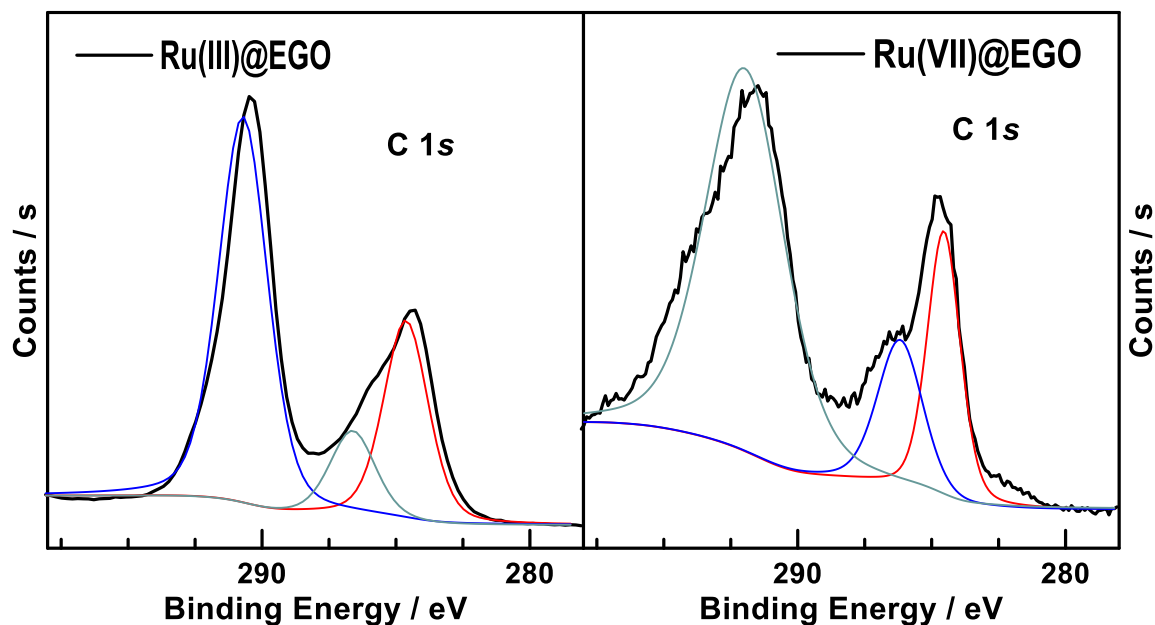
Supporting Information Figure S7.6) XPS spectra of the C 1s Ru(III)@EGO and Ru(VII)@EGO after WOR testing.
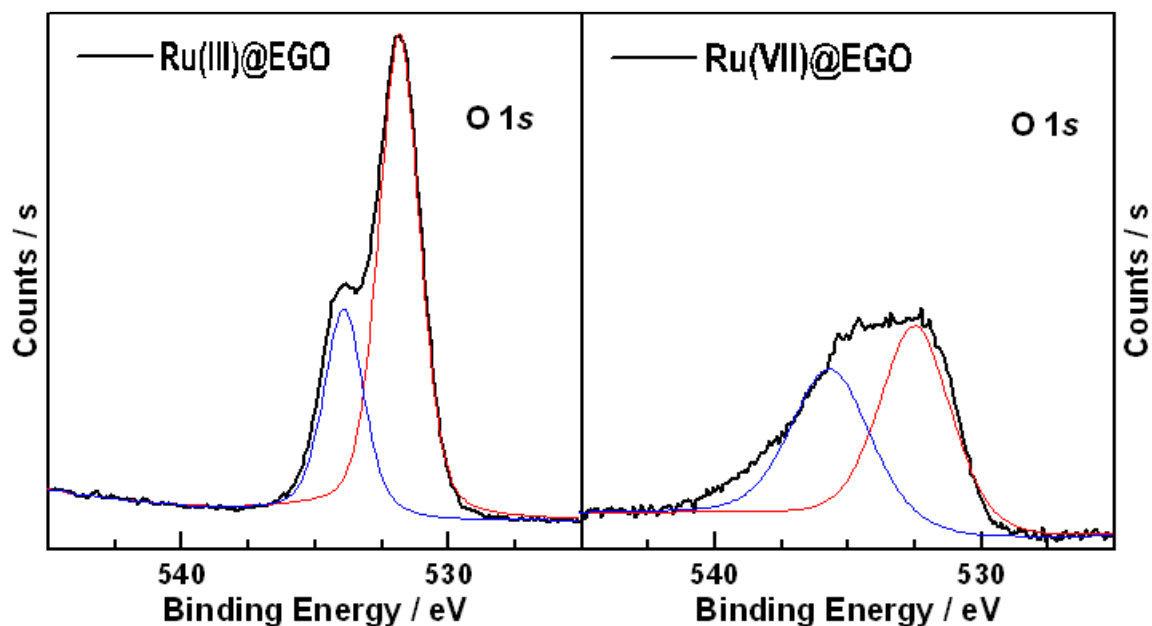
Supporting Information Figure S7.7) XPS O 1s spectra of the Ru(III)@EGO and Ru(VII)@EGO before testing. Red line corresponds to the O 1s.

Before WOR testing on the materials the Ru species present as indicated by XPS is RuO_2 at 529.3 eV, this is characteristic of RuO_2[46-47]. In the Ru $3p$ spectra the peak at 463.68 eV is also indicative of RuO_2 species present on the surface. After testing for over 24 hours, the C 1s for both Ru(III)@EGO and Ru(VII)@EGO show signs of the substrate oxidizing over the course of the constant testing. It is also clear from the Ru $3p$ spectra after the 24 hours of testing that some Ru is leaching from both samples, however from both this spectra and the O 1s after the fact that the dominate species present is still RuO_2. The peak at 535 eV in the O 1s spectra is due to oxygen groups in the Nafion® ionomer used in the test.
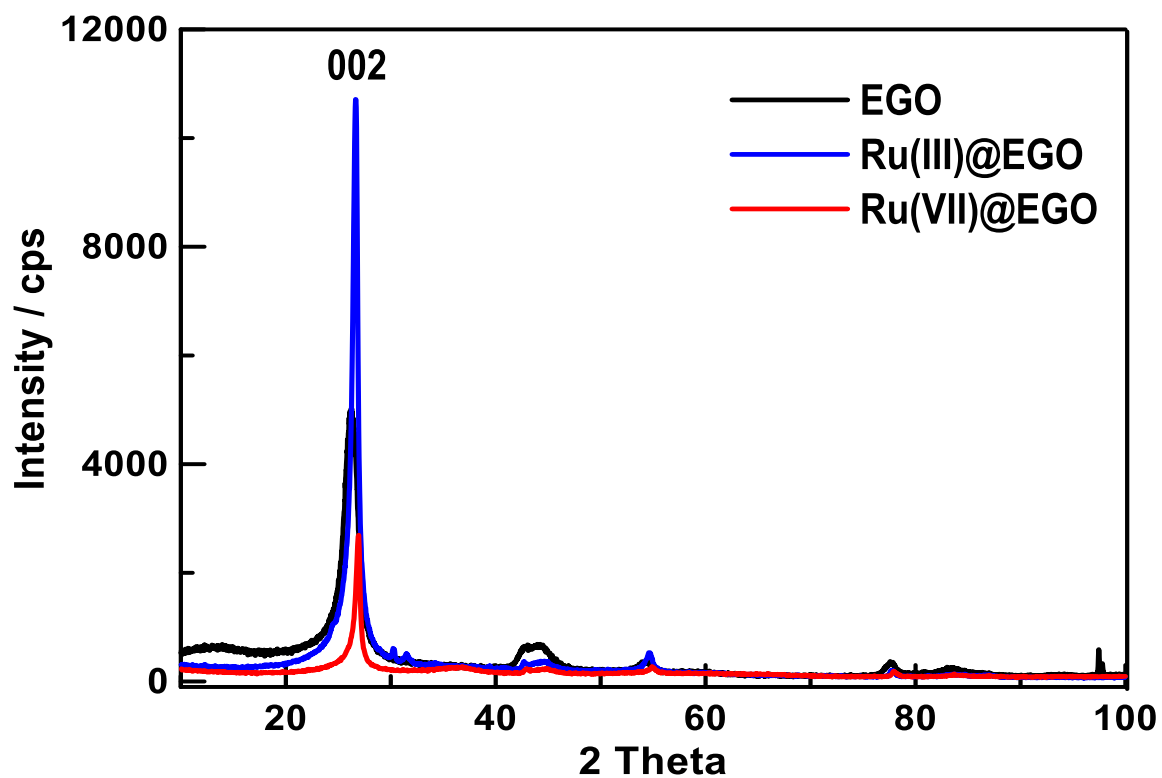
Supporting Information Figure S7.8) XRD spectra of the synthesized Ru(III)@EGO and Ru(VII)@EGO.

Based on the TEM analysis and particle size distributions of the Ru materials it is clear that the Ru is amorphous and thus makes characterization with XRD challenging. However, the peak at 26° for the Ru(VII)@EGO sample has greatly decreased which could be an indication that the Ru(VII)@EGO is more oxidized than the Ru(III)@EGO sample[48].
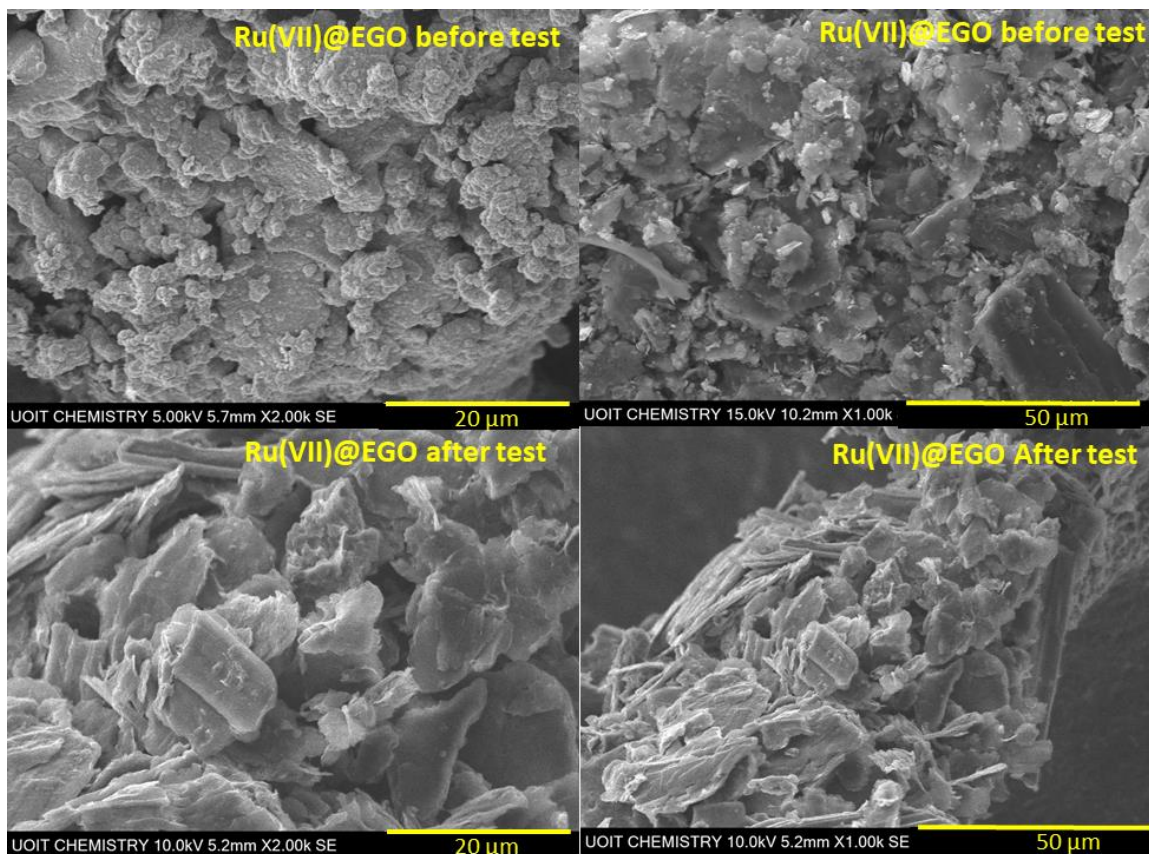
Supporting Information Figure S7.9) SEM images of (A-B) Ru(VII)@EGO sample before WOR testing and (C-D) after WOR testing.
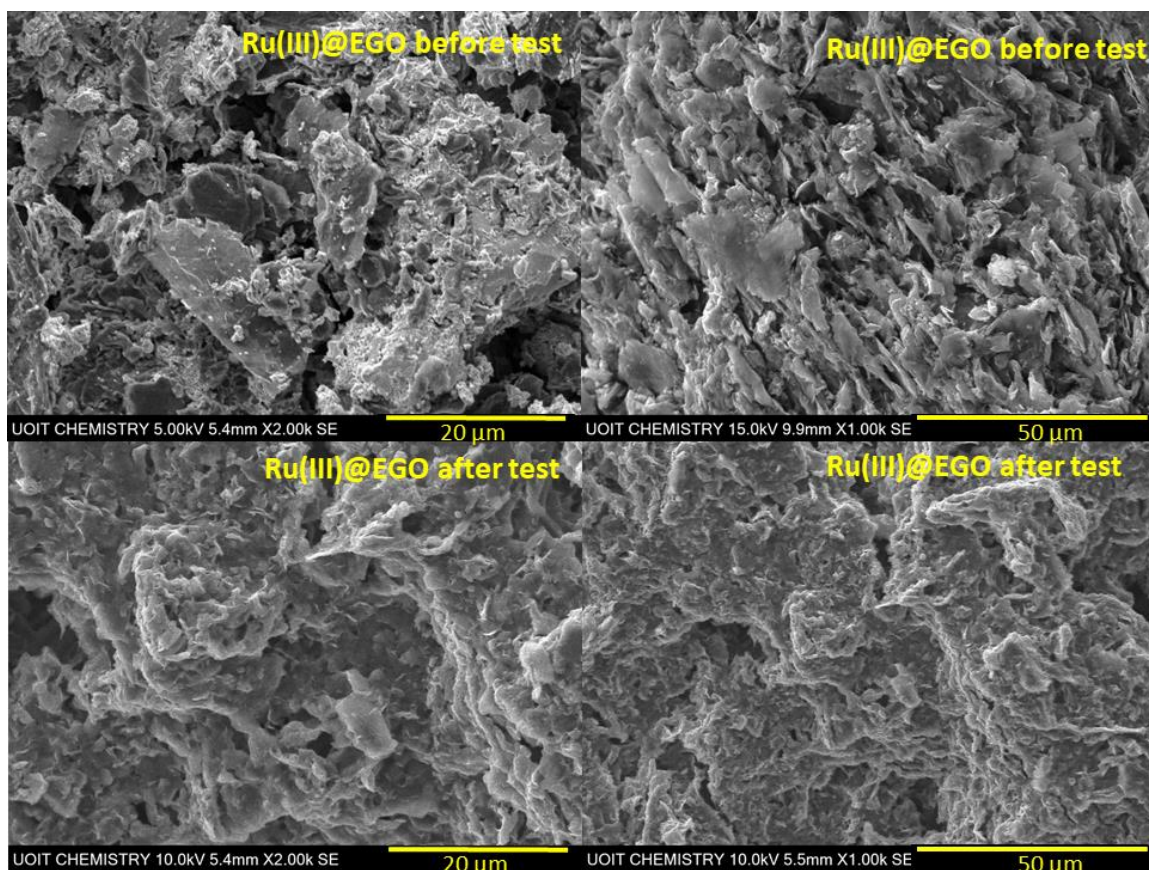
Supporting Information Figure S7.10) SEM images of (A-B) Ru(III)@EGO sample before WOR testing and (C-D) after WOR testing.
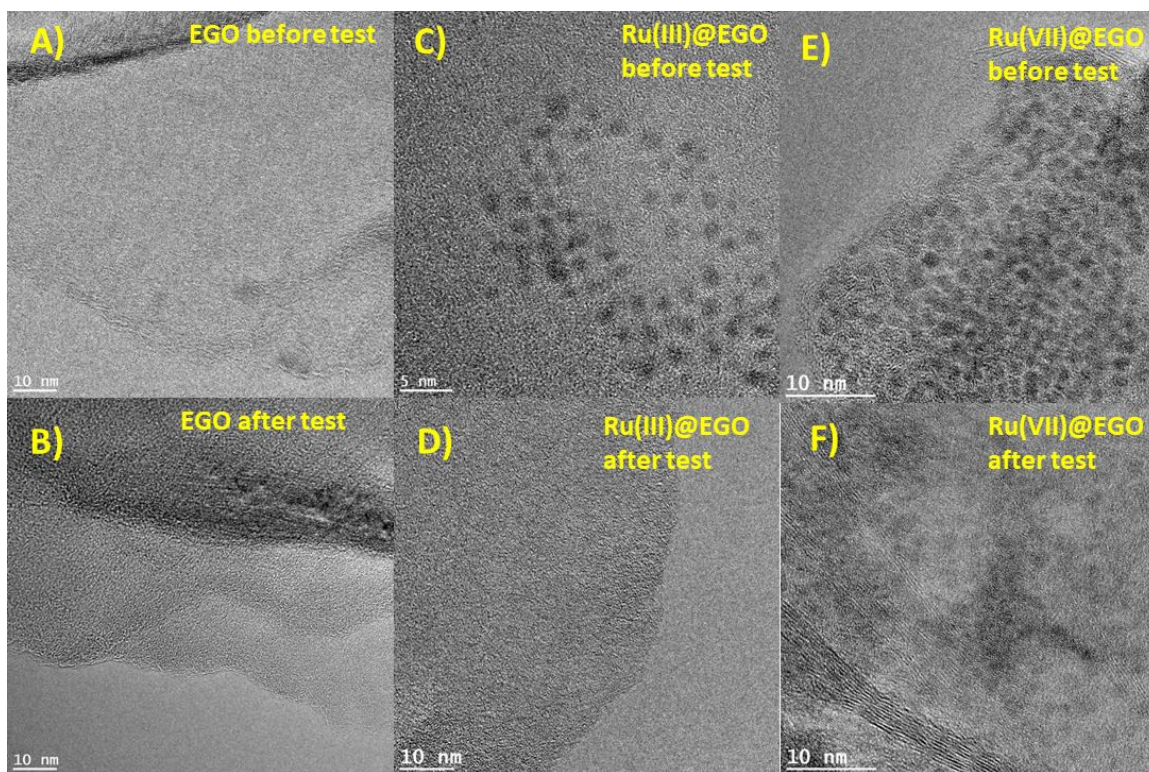
Supporting Information Figure S7.11) HRTEM images of (A) EGO before WOR testing (B) EGO after WOR testing (C) Ru(III)@EGO before WOR testing (D) Ru(III)@EGO after WOR testing € Ru(VII)@EGO before WOR testing (F) Ru(VII)@EGO after test.

7.6 Acknowledgements

7.7 References

[1]   U. Martinez, S. Komini Babu, E. F. Holby, P. Zelenay, *Curr. Opin. Electrochem.* **2018**, *9*, 224-232.

[2]   Q. Chen, J. Miao, L. Quan, D. Cai, H. Zhan, *Nanoscale* **2018**, *10*, 4051-4060.

[3]   B. Y. Guan, X. Y. Yu, H. B. Wu, X. W. D. Lou, *Adv. Mater.* **2017**, *29*, 1703614.

[4]   Z. J. Han, C. Huang, S. S. Meysami, D. Piche, D. H. Seo, S. Pineda, A. T. Murdock, P. S. Bruce, P. S. Grant, N. Grobert, *Carbon* **2018**, *126*, 305-312.

[5]   L. Ni, W. Tang, X. Liu, N. Zhang, J. Wang, S. Liang, R. Ma, G. Qiu, *Dalton Trans* **2018**, *47*, 3775-3784.

[6]   Y. Xu, B. Zhang, *ChemElectroChem* **2019**, *6*, 3214-3226.

[7]   A. Steinfeld, *Int. J. Hydrog. Energy* **1998**, *23*, 767-774.

[8]   M. Gil-Sepulcre, M. Bohler, M. Schilling, F. Bozoglian, C. Bachmann, D. Scherrer, T. Fox, B. Spingler, C. Gimbert-Surinach, R. Alberto, R. Bofill, X. Sala, S. Luber, C. J. Richmond, A. Llobet, *ChemSusChem* **2017**, *10*, 4517-4525.

[9]   J. M. Kamdar, D. B. Grotjahn, *Molecules* **2019**, *24*.

[10]   T. Qiu, Z. Liang, W. Guo, S. Gao, C. Qu, H. Tabassum, H. Zhang, B. Zhu, R. Zou, Y. Shao-Horn, *Nano. Ener.* **2019**, *58*, 1-10.

[11]   A. C. Sander, S. Maji, L. Francas, T. Bohnisch, S. Dechert, A. Llobet, F. Meyer, *ChemSusChem* **2015**, *8*, 1697-1702.

[12]   J. J. Concepcion, D. K. Zhong, D. J. Szalda, J. T. Muckerman, E. Fujita, *ChemComm* **2015**, *51*, 4105-4108.

[13]   F. Li, L. Li, L. Tong, Q. Daniel, M. Gothelid, L. Sun, *ChemComm* **2014**, *50*, 13948-13951.

[14]   L. Wang, L. Duan, Y. Wang, M. S. Ahlquist, L. Sun, *ChemComm* **2014**, *50*, 12947-12950.

[15]   N. Govindarajan, A. Tiwari, B. Ensing, E. J. Meijer, *Inorg. Chem.* **2018**, *57*, 13063-13066.

[16]   D. Lebedev, C. Copéret, *ACS Appl. Energy Mater.* **2018**, *2*, 196-200.

[17]   A. Macchioni, *Eur. J. Inorg. Chem.* **2019**, *2019*, 7-17.

[18]   R. Matheu, M. Z. Ertem, C. Gimbert-Surinach, X. Sala, A. Llobet, *Chem. Rev.* **2019**, *119*, 3453-3471.

[19]   S. Haschke, D. Pankin, V. Mikhailovskii, M. K. S. Barr, A. Both-Engel, A. Manshina, J. Bachmann, *Beilstein J. Nanotechnol* **2019**, *10*, 157-167.

[20]   R. Kötz, H. Lewerenz, S. Stucki, *J. Electrochem. Soc.* **1983**, *130*, 825.

[21]   L. Sévery, S. Siol, S. Tilley, *Inorganics* **2018**, *6*.

[22]   Y. Gao, Y. Wei, Z. Lu, X. Chen, D. Wang, *J. Energ. Chem.* **2019**, *35*, 49-54.

[23]   Y. Li, J. Chen, J. Huang, Y. Hou, L. Lei, W. Lin, Y. Lian, X. Zhonghua, H. H. Yang, Z. Wen, *ChemComm* **2019**, *55*, 10884-10887.

[24] S. W. Gersten, G. J. Samuels, T. J. Meyer, *J. Am. Chem. Soc.* **2002**, *104*, 4029-4030.

[25] M. B. Avinash, K. S. Subrahmanyam, Y. Sundarayya, T. Govindaraju, *Nanoscale* **2010**, *2*, 1762-1766.

[26] X. Li, H. Wang, J. T. Robinson, H. Sanchez, G. Diankov, H. Dai, *J. Am. Chem. Soc.* **2009**, *131*, 15939-15944.

[27] W. Tu, J. Lei, S. Zhang, H. Ju, *Chemistry* **2010**, *16*, 10771-10777.

[28] K. Kakaei, K. Hasanpour, *J. Mat. Chem. A* **2014**, *2*.

[29] H. Xu, S. Ci, Y. Ding, G. Wang, Z. Wen, *J. Mat. Chem. A* **2019**, *7*, 8006-8029.

[30] X. Liu, P. G. Pickup, *J. Power Sources* **2008**, *176*, 410-416.

[31] J. Liu, C. K. Poh, D. Zhan, L. Lai, S. H. Lim, L. Wang, X. Liu, N. Gopal Sahoo, C. Li, Z. Shen, J. Lin, *Nano. Ener.* **2013**, *2*, 377-386.

[32] X. Liu, P. G. Pickup, *J. Electrochem. Soc.* **2011**, *158*, A241-A249.

[33] R. B. Moghaddam, C. Wang, J. B. Sorge, M. J. Brett, S. H. Bergens, *Electrochem. Commun.* **2015**, *60*, 109-112.

[34] S. Niyogi, E. Bekyarova, M. E. Itkis, H. Zhang, K. Shepperd, J. Hicks, M. Sprinkle, C. Berger, C. N. Lau, W. A. deHeer, E. H. Conrad, R. C. Haddon, *Nano Lett* **2010**, *10*, 4061-4066.

[35] H. Lim, J. S. Lee, H. J. Shin, H. S. Shin, H. C. Choi, *Langmuir* **2010**, *26*, 12278-12284.

[36] R. Beams, L. Gustavo Cancado, L. Novotny, *J. Phys. Condens. Matter.* **2015**, *27*, 083002.

[37] D. Long, W. Li, L. Ling, J. Miyawaki, I. Mochida, S. H. Yoon, *Langmuir* **2010**, *26*, 16096-16102.

[38] D. M. Anjos, J. K. McDonough, E. Perre, G. M. Brown, S. H. Overbury, Y. Gogotsi, V. Presser, *Nano. Ener.* **2013**, *2*, 702-712.

[39] A. Garcıa-Gómez, G. Moreno-Fernández, B. Lobatob, T. A. Centeno, *Phys. Chem. Chem. Phys* **2015**, *17*, 15687-15690.

[40] H. Su, S. Lin, S. Deng, C. Lian, Y. Shang, H. Liu, *Nanoscale Adv.* **2019**, *1*, 2162-2166.

[41]   C. Tran, D. Lawrence, F. W. Richey, C. Dillard, Y. A. Elabd, V. Kalra, *ChemComm* **2015**, *51*, 13760-13763.

[42]   K. Urita, C. Urita, K. Fujita, K. Horio, M. Yoshida, I. Moriguchi, *Nanoscale* **2017**, *9*, 15643-15649.

[43]   M. Zhang, J. Chen, H. Li, P. Cai, Y. Li, Z. Wen, *Nano. Ener.* **2019**, *61*, 576-583.

[44]   S. S. Zance, S. Ravichandran, *Appl. Phys. A* **2019**, *125*, 456.

[45]   J.-J. Jhao, C.-H. Lin, T.-K. Yeh, H.-C. Wu, M.-C. Tsai, C.-K. Hsieh, *Surf. Coat. Technol.* **2017**, *320*, 263-269.

[46]   M. Ernst, W. Sloof, *Surface and Interface Analysis: An International Journal devoted to the development and application of techniques for the analysis of surfaces, interfaces and thin films* **2008**, *40*, 334-337.

[47]   D. J. Morgan, *Surf. Interface Anal.* **2015**, *47*, 1072-1079.

[48]   K. Krishnamoorthy, M. Veerapandian, K. Yun, S.-J. Kim, *Carbon* **2013**, *53*, 38-49.

Chapter 8. Ni on graphene oxide: a highly active and stable alkaline oxygen evolution catalyst

8.0 Preface

Part of the work described in this chapter has been published as: Fruehwald, H. M.; Moghaddam, R. B.; Melino, P. D.; Ebralidze, I. I.; Zenkina, O. V.; Easton, E. B., Ni on graphene oxide: a highly active and stable alkaline oxygen evolution catalyst. *Catal. Sci. Technol.* **2021,** *11*, 4026-4033. doi: 10.1039/d1cy00297j with permission from the Royal Society of Chemistry.

In this chapter, the exploration of the effect of using the simple and facile method reported in Chapter 7 to produce a nickel-doped graphene oxide as an inexpensive, high-performing, and highly stable oxygen evolution catalyst in alkaline media. I explored the stability of the material over harsh long term testing conditions over 28 hours of constant testing. The nickel catalyst showed improved activity after an activation galvanostatic hold. The resulting material provided a high-performing, and ultra-stable support that was low-cost and simple to produce a robust active catalytic material. The oxygen evolution reaction in alkaline media of other non-noble metals will be investigated in Chapter 9.

8.0 Abstract

A novel oxygen evolution (OER) catalyst was prepared by reacting $NiCl_2 \cdot 6H_2O$ (Ni precursor) with electrochemically exfoliated graphene oxide (EGO) at mild reaction conditions, where the formation of Ni oxide nanoparticles and their deposition onto EGO occurs simultaneously. The resulting Ni@EGO catalyst was tested for OER in base, where it produced high stability and superior performances. Electron microscopy indicated that Ni@EGO had a uniform morphology, which together with the excellent electronic conductivity of the EGO support, must have contributed to the outstanding OER performance of the catalyst. The Ni@EGO catalyst showed superior OER activity with very low overpotential of 250 mV, which gave rise to the substantial current density of 750 A g^{-1} at 1.6 V. Upon performing long term exhaustive galvanostatic stability tests at 10 mA cm^{-2}, the Ni@EGO was highly stable and it improved over the course of the polarization. During performance studies, significant morphological changes of the material occur within the material as judged by electron microscopy. We believe the notable enhancement of the catalytic activity observed for the system during durability testing could be attributed to electrochemical cleaning of the surface from catalytically inactive nickel aggregates and due to chemical modification of the EGO material by NiOOH species.

8.1 Introduction

Detrimental effects of the long-endeared fossil fuels on the environment, together with the inherently low efficiency of such energy sources, have led to the pleasantly fierce race of finding alternatives fuels[1-2]. In this respect, the development of renewable and efficient green technologies have been of great focus. One such promising area is the electrochemical splitting of water to produce hydrogen for use as fuel and to be stored, and is the main reaction of water electrolyzers[3-4]. Specifically, the clean production of hydrogen *via* electrochemical splitting of water is highly attractive for use as a fuel in devices such as fuel cells[5]. The oxygen evolution reaction (OER) takes place at the anode in electrolyzers and is quite sluggish. To reduce overpotentials the catalyst materials often rely on (noble) metals such as Pt, Ru, and Ir[6-7]. However, the high cost and limited abundance of those materials hinder their commercial application in electrolyzers[7]. Thus, for the next generation of oxygen evolution electrocatalysts, it becomes essential to find alternative catalyst materials that count on more abundant viable metals[1].

Cost-efficient alternative catalysts based on Fe, Ni, and Co have become promising alternatives to precious and rare metals[5, 7]. Nevertheless, catalytic systems based on non-noble metals are still far from commercialization, due to various issues such as sluggish kinetics, high overpotentials, aggregation of nanoparticles, and poor stability[3, 8]. The understanding of the active sites, structural changes, and mechanisms of action throughout the OER is rudimentary, while combining them with other metals of catalyst supports has shown promising improvements in activity[3, 9]. Ni-Based catalysts are some of the most reported non-noble alkaline OER catalysts due to the favourable nickel (Ni) centered redox properties and surface area of the metal which often leads to enhanced activity in alkaline water electrolysis[7, 10-12]. Such progress has made it possible to run alkaline oxygen evolution more efficiently, whereas the development of better catalysts is still an ongoing topic of research[9, 13]. Thus, the search for novel straightforward synthetic approaches that will allow for the facile development of OER materials targeting lower overpotentials and increased long-term stability, is an important research goal. One emerging approach in literature involves the incorporation of well-defined metal nanoparticles into carbon supports. Using carbon is beneficial since carbon materials are inexpensive, offer good electronic properties, and provide a suitable support for the uniform distribution of metal particles. This allows for a high density of active sites to be present on the material, along with the high conductivity of the carbon to enhance charge transfer resistances[5-7, 14]. The popularity of the graphene oxide as a promising catalyst support is rapidly growing. Graphene oxide is graphene with a significant amount of oxygen containing functional groups[15]. The classical way of making graphene and graphene derivatives involves the use of strong oxidizing agents such as in Hummer's method[16]. Alternatively, it has been shown that the conversion of graphite into graphene can be run *via* electrochemical exfoliation of a graphite rod in electrolyte solution[17]. Thus graphene oxide can be produced on relatively large scales much quicker, and more cost efficiently[18].

Previously, we had developed a one-pot method for depositing Ru nanoparticles on electrochemically synthesized graphene oxide as a novel OER catalyst in acidic media[8]. We targeted graphene oxide as our support due to its high electrical conductivity and surface area[19-20]. The deposition of either Ru(III) or Ru(VII) salts produced Ru(III)@EGO and Ru(VII)@EGO catalysts that were remarkably active for OER in acid.

221

Here we employ a similar synthetic methodology to prepare a nominal 5wt% Ni@EGO catalyst that shows supreme activity for the OER under alkaline conditions. We have targeted a metal content in the sample of 5% as previous studies with structurally similar Ru@EGO system showed that this was the optimal metal loading to grant the highest activity. Several reports showed improvements in the OER activity when carbon was employed as support for Ni-based catalysts[21]. When designing this catalyst, we hypothesized that the oxygen functional groups on the graphene should be beneficial sites for the effective distribution of the Ni nanoparticles within the surface of the support. The resulting novel Ni@EGO catalyst showed low OER overpotentials and ultra-high stability in alkaline media.

8.2 Experimental

8.2.1   Catalyst Synthesis

Electrochemical synthesized graphene oxide (EGO) and the one-pot synthesis of the NiO (nickel oxide) on the EGO were prepared *via* previously published procedures[8, 22-23]. The EGO was synthesized based on the electrochemical exfoliation of a high purity graphite rod following a literature procedure[23]. Briefly, a graphite rod was electrochemically exfoliated by applying 4 V to the rod in equal parts 1 M Oxalic acid, 1 M sulfuric acid, and 1 M phosphoric acid. The EGO flakes were sonicated for 1 hour then dried in the oven at 50ºC to produce the EGO support used in this work. Electrochemical exfoliation was used to minimize the incorporation of traces of metals during synthesis. The EGO and nickel chloride hexahydrate ($NiCl_2 \cdot 6H_2O$, Ni precursor) were combined in a round bottom flask with 35 mL of purified 1 M KOH. The reaction was allowed to stir for 4 days under ambient conditions. Upon completion, the reaction was centrifuged and washed with deionized water to remove any unreacted Ni and placed in the oven to dry (80ºC). Then 30 mL of deionized water was added to the resulting solid and this mixture was purged by N_2 for 45 minutes, then capped and left to age for a week[24]. Then the water was decanted and resulted material dried to afford the Ni@EGO catalyst (ca. 100 mg). A Ru(III)@EGO material was synthesized *via* a procedure previously published by us[8]. The solution of KOH (1 M) was purified to remove any Fe contaminants from the KOH following literature procedures[12, 25].

8.2.2 Physical Characterization

The Ni@EGO catalyst was characterized *via* thermogravimetric analysis (TGA) using a TA instruments Q600 SDT thermal analyzer. The catalyst was heated at a heating ramp of 10ºC min^{-1} from room temperature to 1000ºC while under an air and argon atmosphere flowing at 20 mL min^{-1}. Surface area and pore size analysis were preformed using a Quantachrome NOVAe 1200 pore analyzer using N_2 as an adsorbate. X-ray diffraction (XRD) measurements were obtained using a Rigaku Ultima IV with Cu Kα radiation. Diffraction patterns were recorded over the 20-100º 2θ range with a step size of 0.01º. Scanning electron microscopy (SEM) measurements were obtained using a HITACHI FlexSEM 1000. The beam was operated at 10 kV with a working distance of 10 mm and a spot size of 30 and was equipped with energy dispersive spectroscopy (EDS) analysis probe for the determination of elemental composition. TEM measurements were performed at the Canadian Centre for electron microscopy using a Zeiss Libra 200MC transmission electron microscope system operating at 200 keV with a spot size of 1 nm. ImageJ software was utilized to determine the particle size distributions using 569 particles. Inductively coupled plasma-optical emission spectroscopy (ICP-OES) was performed using a Varian Vista MPX CCD Simultaneous ICP-OES. The plasma flow was 15 L min^{-1}, nebulizer flow was 0.75 L min^{-1}, viewing height was 10 mm and the pump rate was 15 rpm. X-ray photoelectron spectroscopy (XPS) was performed using a Thermo Fisher K-alpha instrument equipped with Al Kα monochromated beam source (E=1486.7 eV).

8.2.3 Electrochemical Characterization

Carbon fibre papers coated with catalyst ink were used to study the OER in purified 1 M KOH. Catalyst inks were prepared by adding 10 mg of catalyst, 200 µL deionized water, 200 µL isopropyl alcohol, and 100 µL Nafion®. Inks were sonicated for 15 minutes and then 10 µL of the catalyst ink was drop coated onto a 1 cm^2 section of the carbon fibre paper electrode and dried under heat (200 µg cm^{-2} catalyst loading). A Hg/HgSO$_4$ electrode and a graphite rod formed reference and counter electrodes, respectively. The electrochemical measurements were performed using a Solartron Analytical 1470E potentiostat connected to a Solartron SI 1260 impedance/gain phase analyzer with corresponding Multistat and Zplot software (Scribner Associates, Inc.). Electrochemical impedance spectroscopy was performed on the material at a DC bias of 1.46 V from 100

000 Hz to 0.1 Hz with a AC amplitude of 10 mV and 10 steps per decade. 1.46 V was chosen so there was no interference from Ni and thus the true double layer, C_{dl} could be determined.

8.3 Results and Discussion

The Ni@EGO catalyst was characterized by thermogravimetric analysis (TGA) to assess changes to the carbon support after incorporation of nickel into the system and to estimate the metal loading in the sample[24, 26]. The combustion temperature of the Ni@EGO material decreased dramatically when compared to initial EGO support[8, 27]. Taking into account the ash content from the carbon support, the Ni content of the catalyst was found to be ca. 6.6 wt%. Several decomposition peaks are seen in the differential thermograms (DTG) (Figure 8.1C and D) due to the decomposition of the nickel oxide present on the surface occurring at ca. 300ºC along with the combustion of the carbon starting at 350ºC. When performing in an argon environment, the Ni@EGO DTG (Figure 8.1D) showed decomposition peaks related to the Ni oxides on the surface. At ca. 700ºC the EGO starts to decompose at those high temperatures, seen in both the Ni@EGO and EGO samples.
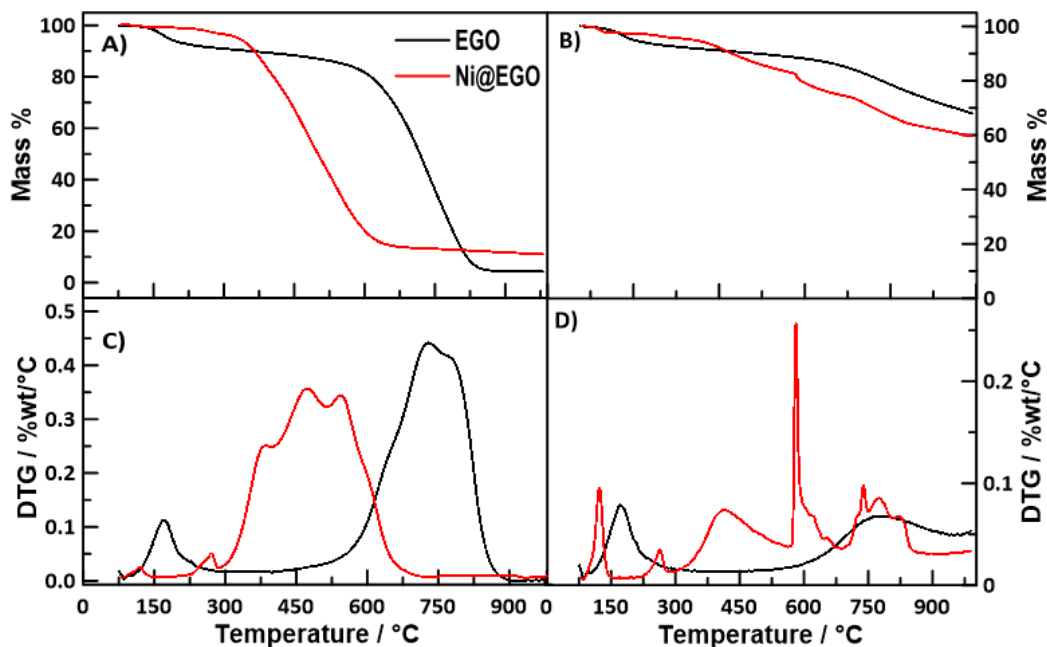
Figure 8.1) (A) TGA of the Ni@EGO at a scan rate of 10ºC min^{-1} in air atmosphere (B) TGA of the Ni@EGO at a scan rate of 10 ºC min^{-1} in an argon atmosphere (C) DTG of Ni@EGO at a scan rate of 10 ºC min^{-1} in air atmosphere (D) DTG of the Ni@EGO at a scan rate of 10 ºC min^{-1} in an argon atmosphere.

Surface area and pore size analysis was performed on the Ni@EGO and compared to the bare EGO support (Figure S8.1). Upon addition of the Ni to the EGO, the surface area slightly increased[28-29] (Table 8.1). We attribute this to the possible interaction of the Ni nanoparticles on the surface with adjacent EGO sheets which could slightly increase the surface area of the material. The BJH pore size distribution of the Ni@EGO showed signs of higher mesoporosity in comparison to the EGO, which could indicate that the graphene sheets are in stronger intercalation upon addition of the metal creating a mesoporous-like material[7, 30]. The addition of the relatively large nickel nanoparticles may result in the agitation of the intrinsic order in the EGO structure (for example disrupting weak non-covalent interactions, π- π stacking or/and hydrogen bonding, between two adjacent sheets) and as a result to create more porous structures. Nonetheless, the increase in the surface area is beneficial for the material as more active sites will be exposed on the surface, thus increasing activity[5].

Table 8.1) Weight % Ni, surface area, and particle size of the Ni@EGO catalyst.

Material	Metal wt%	SA_{BET} (m^2 g^{-1})	I_D/I_G ratio	Particle Size (nm)	
	ICP			XRD	TEM
EGO	-	10.26 ± 2.03	2.7	-	-
Ni@EGO	$2.7\% \pm 0.8\%$	13.53 ± 6.77	1.7	3.2	2.2 ± 1.3

Figure 8.2A shows the Raman spectra obtained for the bare EGO support and the Ni@EGO catalyst. Intense peaks appeared at 1354 cm^{-1} (D-band) and 1548 cm^{-1} (G-band) over both, which are assigned to vibrations from the carbon support[7]. I_D/I_G ratio can be used to determine the extent of graphitization in the material. The I_D/I_G ratios of 2.7 and 1.7 were found for the EGO and Ni@EGO respectively. This indicates that the Ni@EGO catalyst becomes more graphitic after the addition of the nickel species[31-32]. This argument is further amplified by the characteristic peak at 2711 cm^{-1}, which allow for the estimation of the number of graphitic layers. The 2711 cm^{-1} peak over Ni@EGO is remarkably stronger than that over EGO. It implies that the introduction of Nickel has increased the quantity of the graphitic layers, likely due to the interaction of the nickel species with adjacent sheets[33-35].
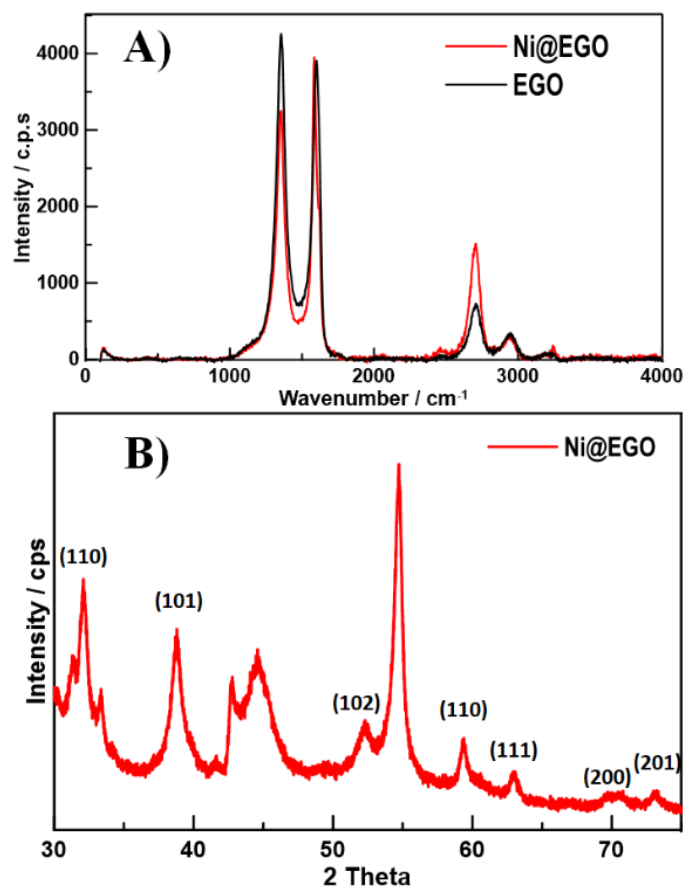
Figure 8.2) (A) Raman spectra of the Ni@EGO catalyst compared to the EGO support. (B) XRD pattern of the Ni@EGO catalyst.

To determine the crystallite, and particle size, XRD analysis was conducted over the Ni@EGO catalyst. The full spectrum is presented in Figure S8.2, where the expected (002) diffraction peak from the EGO is present in the spectra. A slower scan was recorded in the range of 40-90º 2θ to characterize the peaks and particle size of the Ni species (Figure 8.2B). The ICDD card number determined for the nickel species is: 01-089-3080, which correlates to NiO. Various peaks related to trace amounts of different crystallites of NiOOH are present on the surface of the EGO appearing at 32.0º, 38.7º, 52.4º, 59.4º, 63.1º, 70.4º, 73.3º, 2θ. These peaks are characteristic of the (110), (101), (102), (110), (111), (200), (201) diffraction lines of NiOOH, respectively[12, 21, 36-38]. Using the (110) peak at 52.4º 2θ the crystallite size was determined to be 32 Å, in close agreement with the TEM results.

The morphology of the Ni@EGO catalyst was characterized before and after stability test using SEM (Figure 8.3). The morphology of the Ni@EGO fresh sample shows plate-like features of the graphene carbon support (Figure 8.3A and C)[35]. To highlight

regions where Ni particles might be present, back-scattered electron (BSE) images were captured (Figure 8.3B). In the fresh sample, the uniform distribution of Ni particles is noticeable on the surface. After electrochemical stability tests, the carbon support has likely corroded due to the high potentials required for the OER, so there are fewer graphene-plate like structures (Figure 8.3D and F). After the stability test, more distinct Ni particles were seen in the BSE images, owing to the oxidative removal of the carbon support as part of the corrosion, leaving a higher relative (to carbon) quantity of the Ni particle present in the sample (Figure 8.3E). We performed ICP-OES to determine an accurate Ni loading on the EGO, which showed that there was 2.7 wt% Ni in the fresh sample. After stability testing there was 1.2 wt% Ni present in the sample due to some loss of Ni which is likely due to the carbon corrosion where some of the metal leached out along with the corrosion of the carbon.
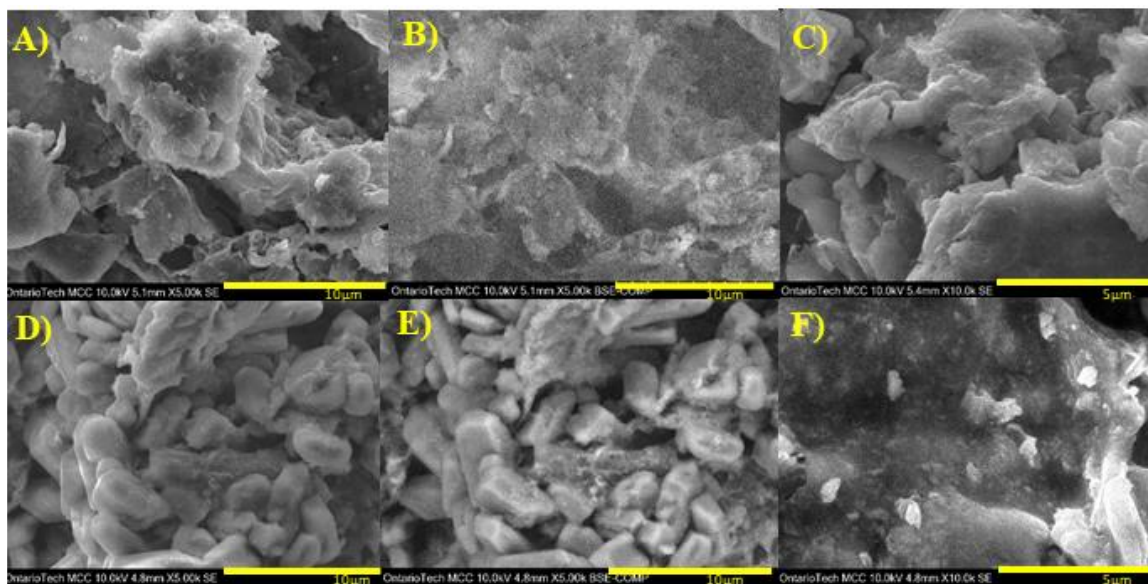
Figure 8.3) (A) SEM image of Ni@EGO-fresh (B) BSE image of Ni@EGO-fresh (C) SEM image of Ni@EGO-fresh (D) SEM image Ni@EGO-AT (E) BSE image of Ni@EGO-AT (F) SEM image of Ni@EGO-AT.

Particle sizes of the Ni@EGO fresh and AT (after stability test) were determined by TEM analysis (Figure 8.4). For the fresh Ni@EGO sample, the individual particle size distribution could not be determined. This was attributed to a thick and rapidly forming oxide layer, which blocked and limited the active Ni sites, thus making the observation of individual particles difficult[3, 5, 9, 30]. Scanning tunneling electron microscopy (STM) was performed on the fresh sample (Figure 8.4C) which clearly showed the regions rich in Ni

nanoparticles. The Ni@EGO-AT sample showed more distinct particles on the surface. We attribute this to the activation process, which cleans the surface, thus we were able to measure particle sizes in this sample. The average particle size was ca. 2.2 ± 1.3 nm, which indicates that the Ni particles were partially amorphous[39]. From the STM over the Ni@EGO-AT it is apparent that there is still similar distribution of Nickel nanoparticles on the surface of the EGO[6]. These results are consistent with the SEM measurements.
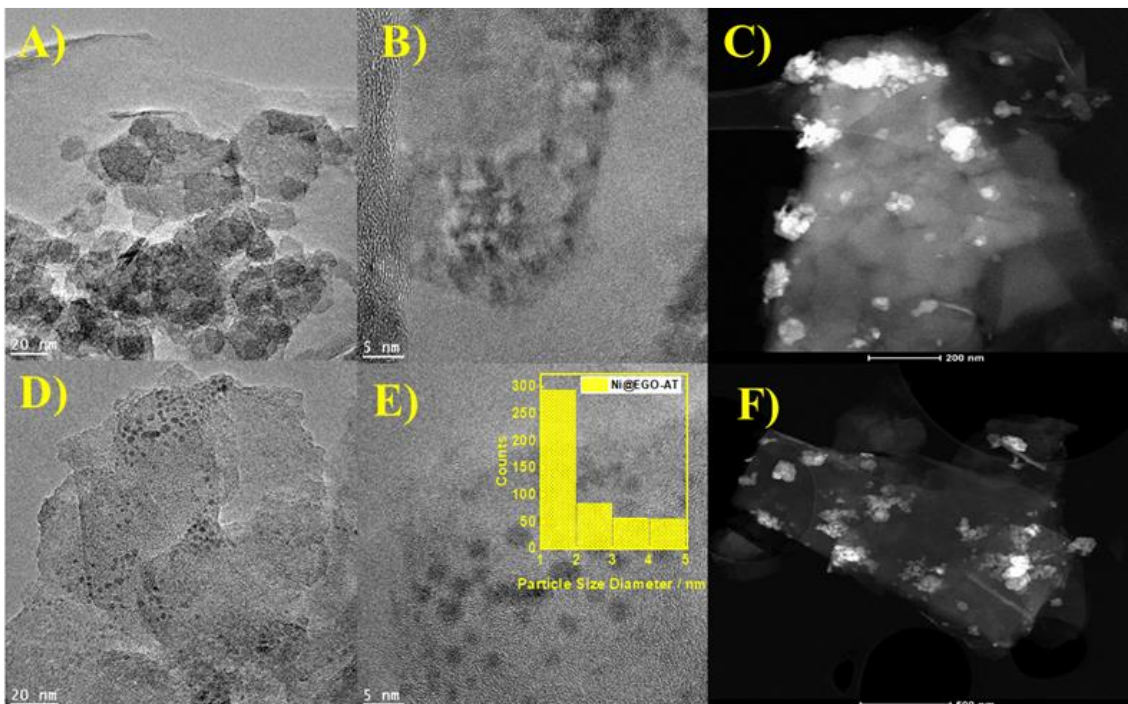
Figure 8.4) (A) and (B) TEM image of the fresh Ni@EGO-fresh (C) STM image of the fresh Ni@EGO (D) and (E) TEM image of Ni@EGO-AT (F) STM image of the Ni@EGO-AT Inset: particle size distribution of the Ni@EGO-AT.

XPS of Ni@EGO allows for determining of the chemical composition of the catalyst (Figure 8.5). Ni $2p_{3/2}$ peak is centred at 855.9 eV, which is typical for Ni(II)[40]. Peak deconvolution by applying a mixture of Gaussian and Lorentzian shapes on iterative Smart Background results in the $2p_{3/2}$ and $2p_{1/2}$ peaks with separation of 17.8 eV. The relatively small FWHM of the main lines of 2.56 eV and the absence of shoulders allow us to suggest that one type of Ni(II) is present in the material. Two large shake-up satellite peaks characteristic to Ni-O bonding are observed at 861.8 and 879.9 eV, respectively. Very similar characteristic XPS features were previously reported for nickel hydroxide[41]. Oxygen O1s signal can be deconvoluted into two peaks. The peak located at 531.3 eV is often assigned to contributions from C=O groups, while the peak at 533.1 eV is

characteristic to C-OH groups[42]. A minor O1s peak related to Ni-O bonding that was reported to appear at 530.6 eV[41] overlaps with the major peak and cannot be unambiguously resolved. The main peak at 284.5 eV of the carbon C1s area (Figure 8.5C) comes from C-C and C-H bonding. The peak at 258.8 eV is related to carbon atoms bonded to electron-withdrawing oxygen forming C-OH, C-O-C, and C=O species. Peak area normalization between C1s, O1s, and Ni2p using relative XPS sensitivity factors are determined by Wagner[43] gives C:O:Ni stoichiometric ratio as 57:27:3. Notably, no traces of Fe contamination was detected in the 700-740 eV range that is typical for the most prominent Fe 2p lines (Figure S8.15). To further confirm there were no traces of Fe in the fresh catalyst and after testing, atomic absorption spectroscopy (AAS) was performed on the materials. In both cases no traces of Fe were observed. The concentrations of the Ni@EGO and Ni@EGO-AT were below the limit of detection of the instrument (1 ppm).
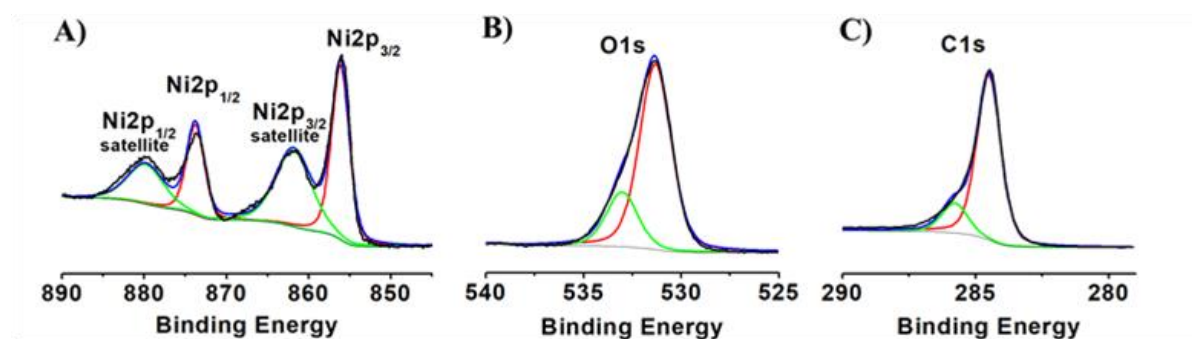
Figure 8.5) XPS spectra of Ni@EGO demonstrating (A) Ni2p (B) O1s and (C) C1s areas.

8.3.1 Electrochemical Characterization

Figure S8.4 shows potentiodynamic responses (20 mV s^{-1} of the bare EGO and Ni@EGO catalysts in purified 1 M KOH, before and after 1 h galvanostatic polarization at 1 mA cm^{-2}. For comparison, responses towards OER over our best in-acid Ru(III)@EGO catalyst are also overlaid[8]. The fresh Ni@EGO electrode shows a peak present at ca. 1.38 V, which can be assigned to the conversion of Ni(OH)$_2$ to β-NiOOH[9, 44-45]. The Ru(III)@EGO sample shows a broad oxidation peak at ca. 1.15 V followed by its reduction counterpart at 1 V on the reverse scan to demonstrate Ru oxide electrochemistry[46-50]. After the 1 h at 1 mA cm^{-2} hold, the EGO shows decreased capacitance, due to some carbon corrosion. For the Ni@EGO catalyst, the β-NiOOH peak grows substantially and moves towards more positive potential. Throughout this change, the surface of Ni(OH)$_2$ converts to β-NiOOH and subsequently γ-NiOOH. The later form of the NiOOH is known to be

catalytically more active, which together with more accessible active sites-evidenced by the larger signal, gave rise to the stronger electrochemistry[1-3, 12, 30, 38].

The catalysts were tested for the OER in 1 M KOH in their fresh state, after the 1 h stability test at 1 mA cm^{-2}, and after a 24 h stability test at 1 mA cm^{-2} (Figure 8.6). As expected, OER activity of the EGO sample was insignificant. The Ni@EGO catalyst showed the highest activity for the OER, followed by the Ru(III)@EGO catalyst. The onset potentials were determined and tabulated along with standard deviations in Table 9.2. Our Ru(III)@EGO catalyst performed similarly to reported Ru-based catalysts in literature, showing OER onset potentials of around 1.4-1.5 V vs RHE[51-52]. The Ni@EGO showed remarkable OER performance under substantially smaller OER overpotential that most other reports on OER using high loadings of Ni. To the extent of our knowledge, there were no literature examples reporting as low as 300 mV overpotential at 10 mA cm^{-2}, whereas the Ni@EGO has an even lower overpotential of ca. 290 mV at 10 mA cm^{-2}[1-2, 6-7, 14, 25, 28, 30, 53]. A comparative analysis of different literature catalysts is presented in Table 9.3. Notably, the Ru(III)@EGO catalyst showed some activity decay after the 24 h stability test, while the Ni@EGO electrode maintained performance over the 24 h stability measurement. Finally, the Tafel slope was determined to be 63.3 mV dec^{-1}, 66.8 mV dec^{-1}, 67 mV dec^{-1} for the Ni@EGO, Ru(III)@EGO, and EGO catalysts, respectively (Figure S8.4). The Ni@EGO showed the lowest slope, and thus had the faster kinetics for the OER. The slope is drastically smaller than the slope reported for other Ni/carbon systems (12 mV dec^{-1} larger slope or greater[6, 14, 54]).

Notably, there are some very interesting reports on Ni/graphene systems in the literature that are reporting good activity and low onset potentials. For example, in a study by Faisal *et al.* Ni on nitrogen-doped graphene was used to obtain an onset potential of 1.48 V and a Tafel slope of 98 mV dec^{-1}[55]. In another study by Chen *et al.* the authors synthesized a Ni nitrogen doped graphene support and was able to achieve an overpotential of 320 mV[56]. Finally, a study by Ai *et al*. produced a Ni@graphene catalyst with an overpotential of 370 mV[57]. Notably, in comparison to the above forementioned, the system reported here demonstrated significantly lower overpotentials (290 mV) and low Tafel slopes and thus faster OER kinetics. To determine the effect of carbon support on our materials we had synthesized a Ni@Vulcan catalyst using the same synthetic procedure

described, with a commercial carbon support. It was observed that the Ni@Vulcan catalyst had lower activity compared to the Ni@EGO catalyst, these results are shown in Section 8.5. Overall, our material showed that low loadings of Ni onto carbon supports provided a low overpotential and highly stable material for OER.

Table 8.2) Onset potentials of the catalysts tested

Catalyst	Onset potential fresh (V)	Onset potential after 1h hold (V)	Onset Potential after 24 h hold (V)
Ni@EGO	1.484 ± 0.008	1.480 ± 0.007	1.470 ± 0.011
Ru(III)@EGO	1.551 ± 0.008	1.567 ± 0.004	1.574 ± 0.010
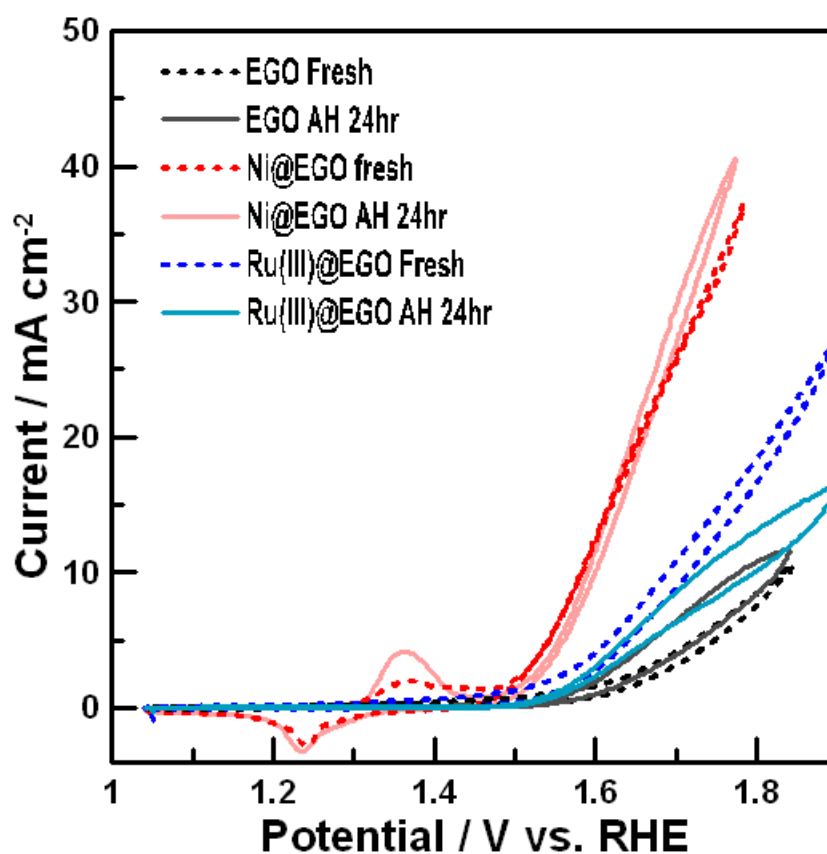
Figure 8.6) Cyclic voltammograms of Ni@EGO and Ru(III)@EGO in 1 M KOH at a scan rate of 5 mV s^{-1}.

Table 8.3) Comparison of onset potentials from literature compared to this work

Catalyst	Ni loading	Overpotential at 10 mA cm^{-2}	Surface area / m^2 g^{-1}	Catalyst loading / mg cm^{-2}	Ref.
Ni@EGO	2.7%	290 mV	13.53	0.06	This work
Ni$_{0.95}$Fe$_{0.05}$(OH)$_2$	75%	260 mV	-	-	[12]
Ni/Ni$_3$Fe/B-CNT	-	265 mV	166.45	0.279	[7]
NiFe(III)-LDH	-	270 mV	-	2	[1]
NiO@mC	99%	290 mV	-	-	[6]
a-LNF(t-d)	60%	300 mV	2.3	-	[53]
FTO/NiO	100%	300 mV	-	-	[2]
rGO/Ni$_2$P	80%	320 mV	112	0.1	[5]
Ni HO-np/CF	75%	330 mV	68.64	0.135	[25]
Ni/rGO-(light)	-	306 mV	-	-	[14]

Electrochemical impedance spectroscopy (EIS) was performed on the catalysts (Figure S8.5), The double layer capacitance (C$_{dl}$) was determined to be 25.4 mF cm^{-2}, 29.2 mF cm^{-2}, 7.6 mF cm^{-2}, for the Ni@EGO, Ru(III)@EGO, and EGO, respectively. C$_{dl}$ values for reported Ni/C systems are on average 10 mF cm^{-2} or lower[1, 6-7, 35, 58]. The high C$_{dl}$ from our Ni@EGO system is attributed to the capacitive behaviour imparted from the EGO carbon support along with the Faradaic contributions the metal imparts on the surface.

Galvanostatic polarization at a constant current of 1 mA cm^{-2} in 1 M KOH (Figure 8.7) was performed as a measure of catalytic stability of Ni@EGO. Figure S8.7 shows profiles after 1 h hold at 1 mA cm^{-2}. The Ni@EGO catalyst shows the lowest OER overpotential compared with Ru(III)@EGO and the EGO. The performances of all catalysts are relatively stable and these testing conditions. To make the conditions more exhaustive, we then extended the galvanostatic hold to 24 hours (Figure 8.7A). The Ni@EGO system reached the lowest overpotential, and note only was highly stable over the 24 hours of constant current polarization but showed somewhat decreased overpotential after stability tests, likely due to further activation of the catalyst[59]. A similar but slower

decrease in over potential was also seen from Ru(III)@EGO, which was also quite stable during the 24 h hold. Finally, we subjected the materials to a harsher stability test at a current density of 10 mA cm^{-2} for 1 hour (Figure 8.7B). Consistently, the Ni@EGO had the lowest overpotential and was the only electrode to have stable catalytic performance over this harsher measurement, where both EGO and Ru(III)@EGO systems dramatically decayed, showing much larger overpotentials to produce the requested current density.
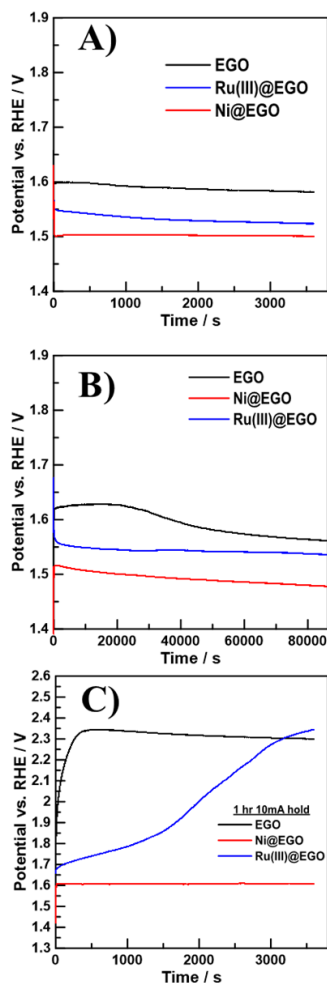
Figure 8.7) (A) 1 hour galvanostatic hold at 1 mA cm^{-2} (B) 24 hour galvanostatic hold at 1 mA cm^{-2} (C) 1 hour galvanostatic hold at 10 mA cm^{-2}.

8.4 Conclusion

The facile deposition of nickel nanoparticles on EGO led to the Ni@EGO catalyst that was exceptionally active towards the OER in base, with a desirable overpotential as low as 290 mV and stable over long term galvanostatic polarization at 10 mA cm^{-2}, much lower than majority of previously reported catalytic systems. The catalysts demonstrate activity in part to high-performing nickel-containing catalysts. Notably, current catalyst utilized

nickel as the only metallic component, while most known high-performing catalysts required the combination of iron and nickel to reach high activity. Our system offers a unique opportunity to explore solely nickel-based catalytic activity without interference or synergetic influence of other metal additives. Indeed, multi-metal catalytic systems could adopt very different mechanisms to catalyze OER but it is harder to understand and more difficult to control and re-produce the system performance. Our catalyst was made under very mild conditions using inexpensive materials and showed impressive durability over various harsh stability tests. This study demonstrates the potential of graphene-based non-precious metal catalysts as a promising and stable replacement of expensive iridium or ruthenium-based catalysts for the OER in alkaline media. The synergetic interaction between the Ni hydroxides and the conductivity of the graphene oxide in the material shows promise for the next generation of alkaline OER catalysts.

8.5 Supporting Information
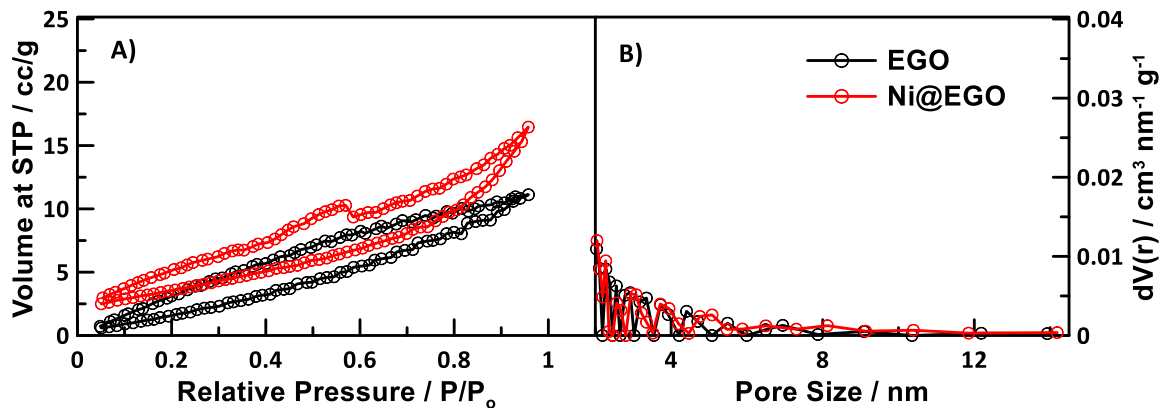
Supporting Information Figure S8.1) (A) Pore size isotherms using N_2 as an adsorbate (B) BJH pore size distributions obtained using N_2 as an adsorbate.
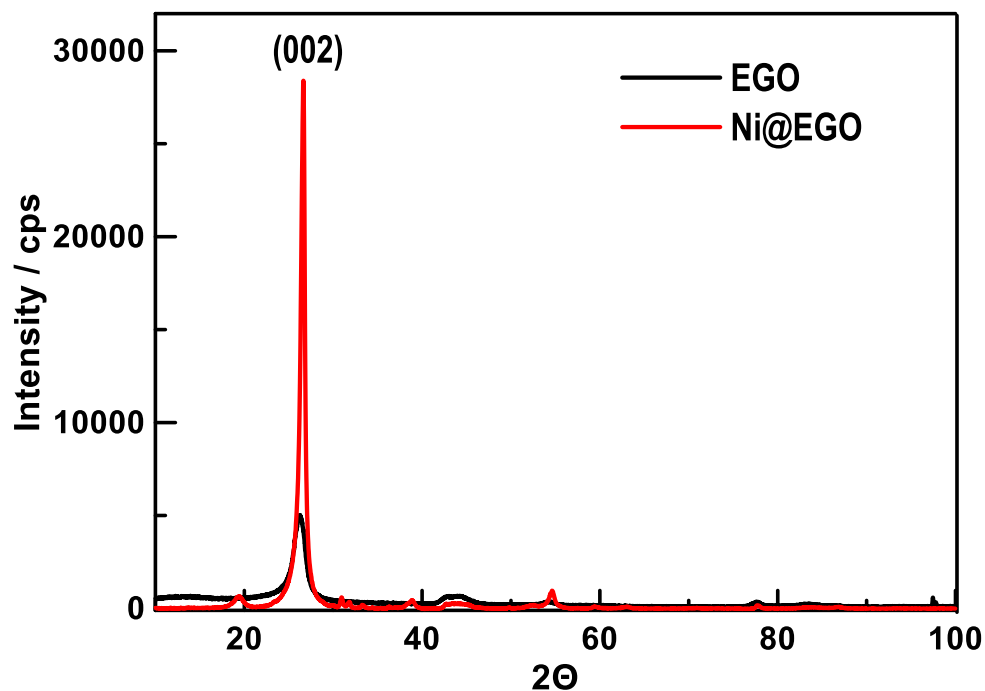
Supporting Information Figure S8.2) XRD spectra of the EGO compared to the Ni@EGO.

Equation	y = a + b*x
Plot	Intensity
Weight	No Weighting
Intercept	1.46425 ± 0.09343
Slope	19.77484 ± 0.0071
Residual Sum of Squar	0.04326
Pearson's r	1
R-Square (COD)	1
Adj. R-Square	1
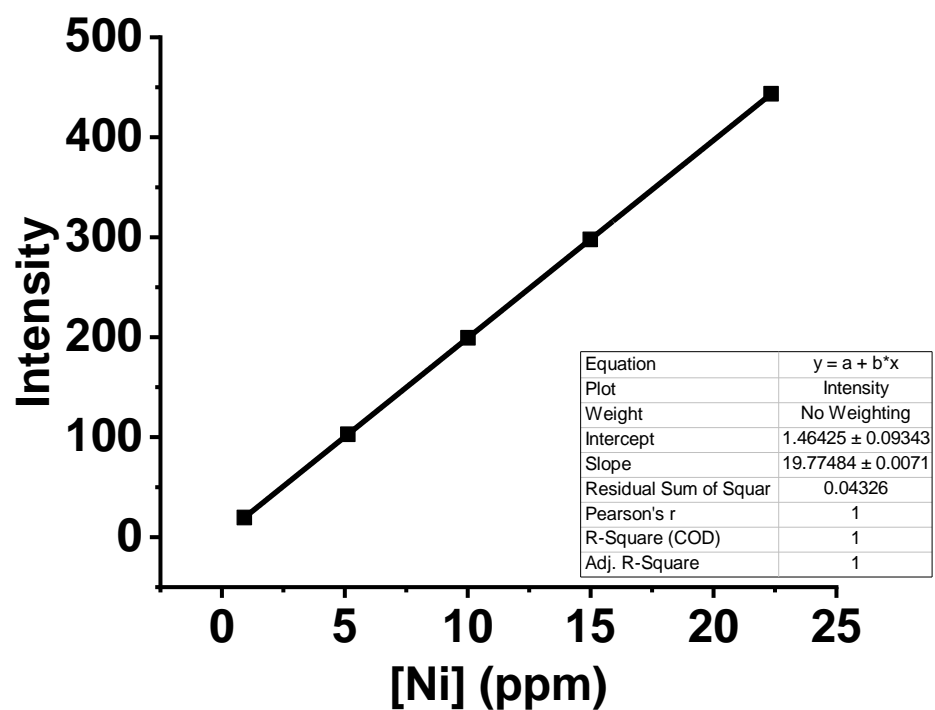
Supporting Information Figure S8.3) ICP-OES calibration curve for the determination of nickel content in the Ni@EGO samples.
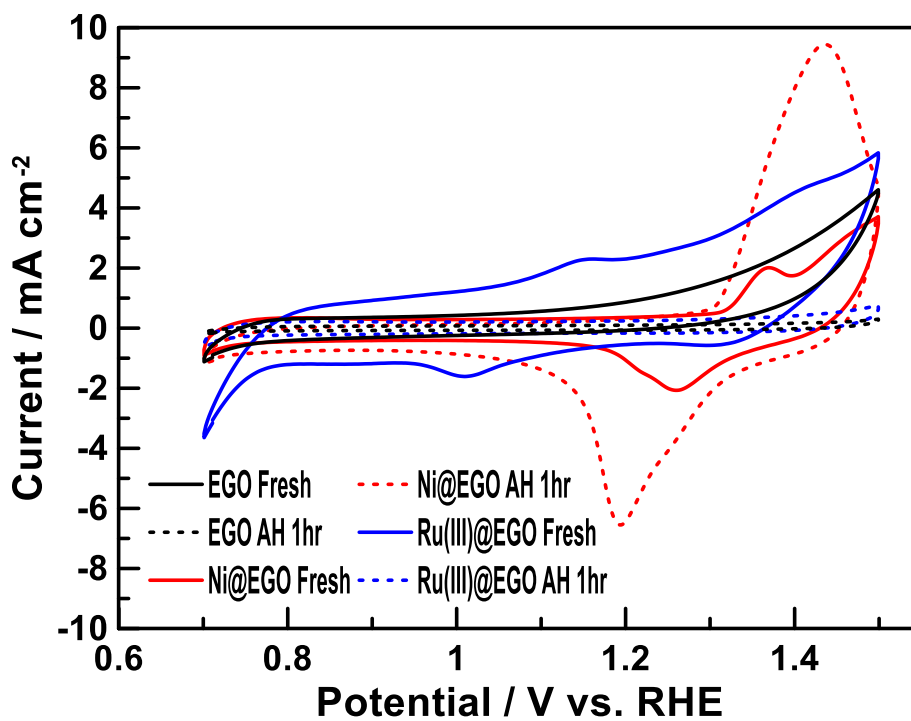
Supporting Information Figure S8.4) Cyclic voltammograms of Ni@EGO and Ru(III)@EGO in 1 M KOH at a scan rate of 20 mV s^{-1}.
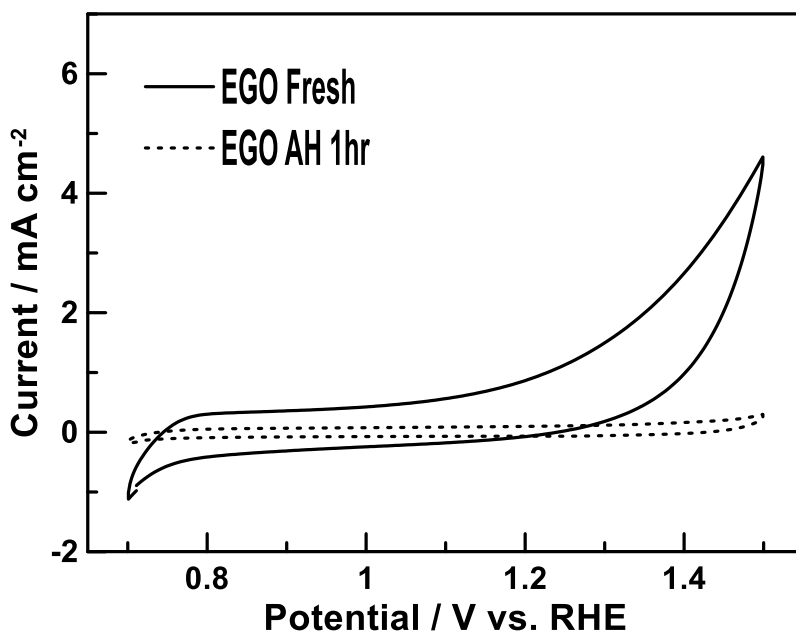
Supporting Information Figure S8.5) Cyclic voltammograms of EGO in 1 M KOH at a scan rate of 20 mV s^{-1}.
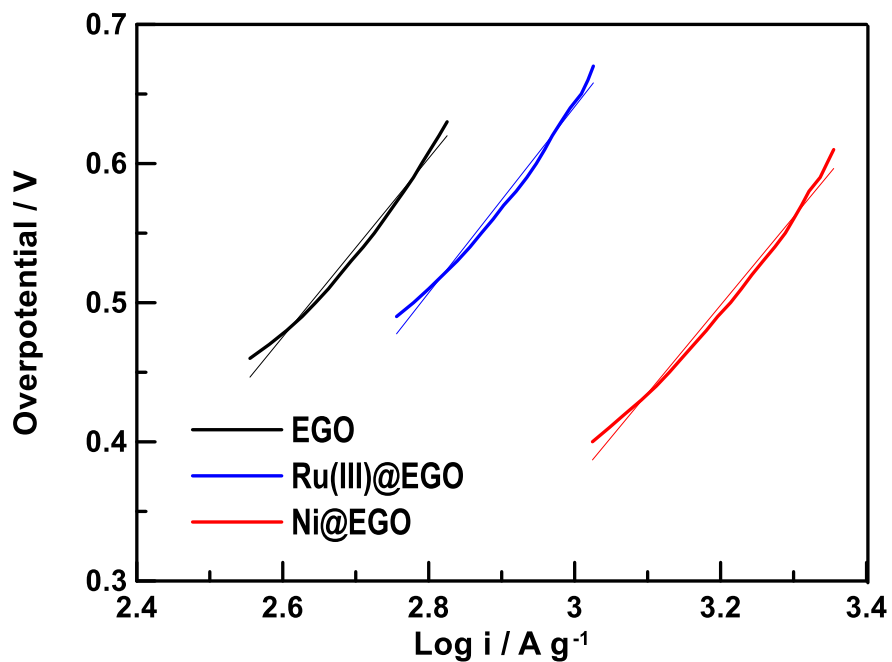
Supporting Information Figure S8.6) Tafel analysis of the catalysts studied in 1 M purified KOH.
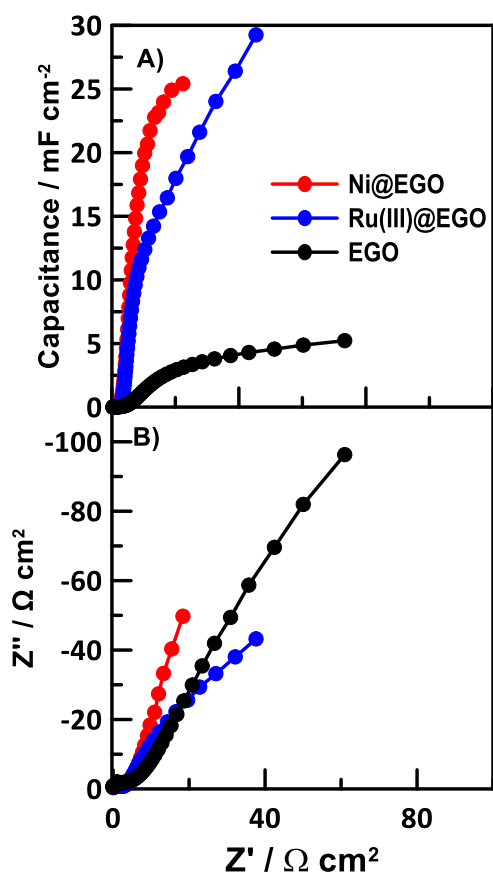
Supporting Information Figure S8.7) Electrochemical impedance spectroscopy of the catalysts at 1.46 V vs RHE (A) capacitance plot of the catalysts studied (B) Nyquist plots of the catalysts studied.
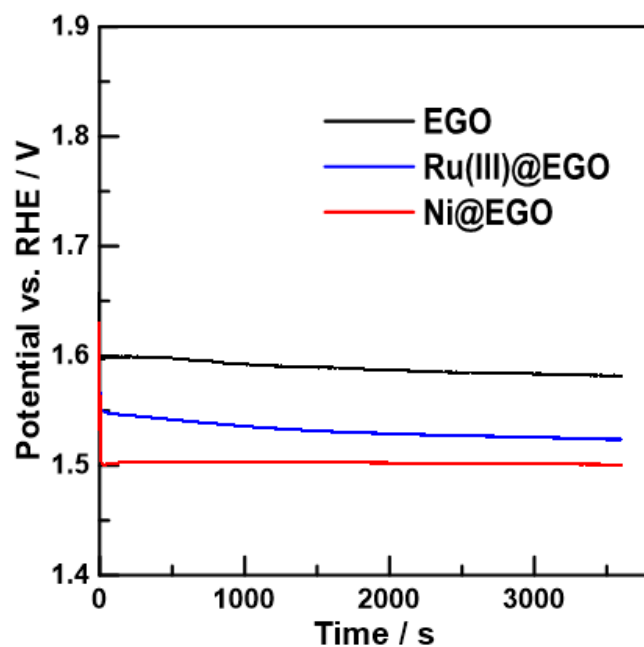
Supporting Information Figure S8.8) 1 hour galvanostatic hold at 1 mA cm^{-2} in 1 M KOH.
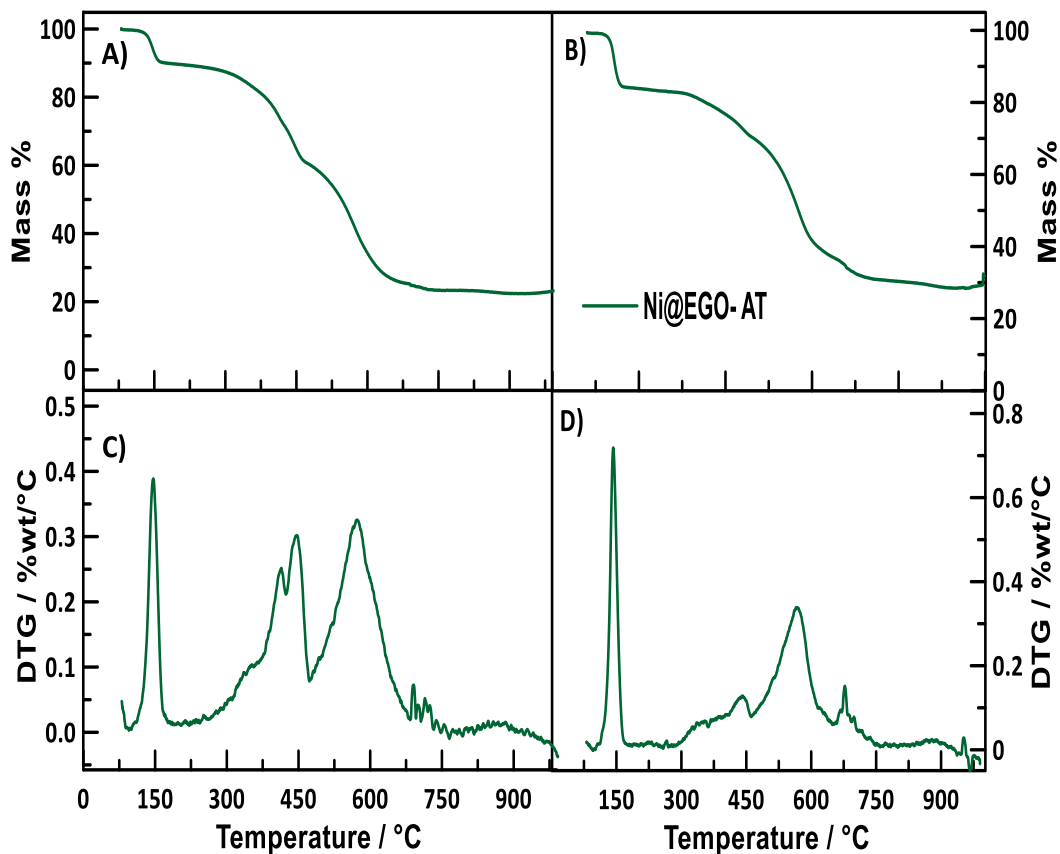
Supporting Information Figure S8.9) (A) TGA of the Ni@EGO-AT at a scan rate of 10°C min^{-1} in air atmosphere (B) TGA of the Ni@EGO-AT at a scan rate of 10°C min^{-1} in an argon atmosphere (C) DTG oof Ni@EGO-AT at a scan rate of 10°C min^{-1} in an air atmosphere (D) DTG of the Ni@EGO at a scan rate of 10°C min^{-1} in an argon atmosphere.
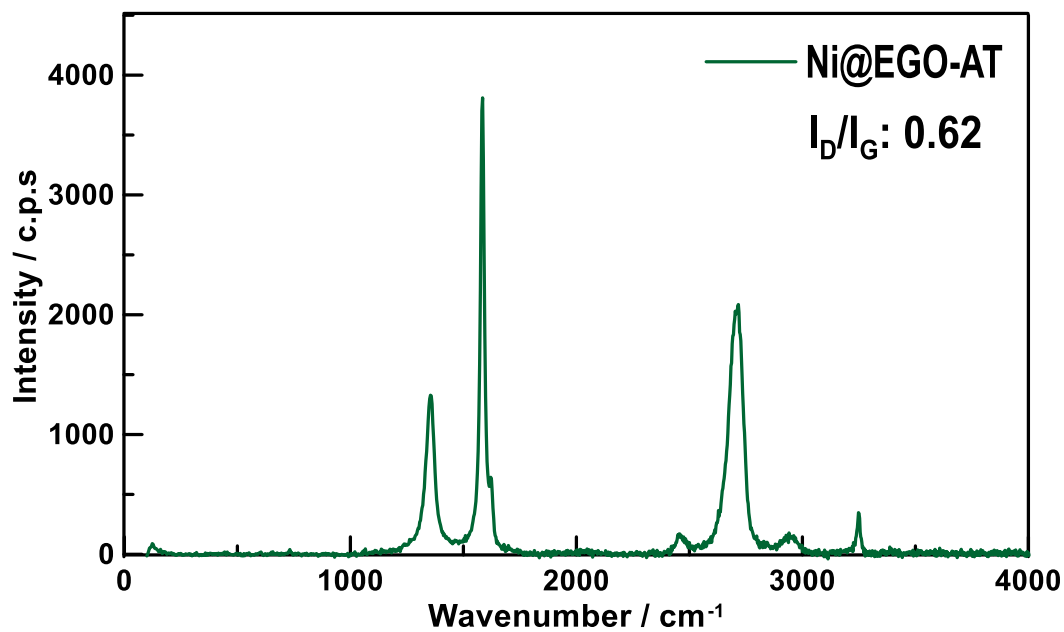
Supporting Information Figure S8.10) Raman spectra of the Ni@EGO-AT.
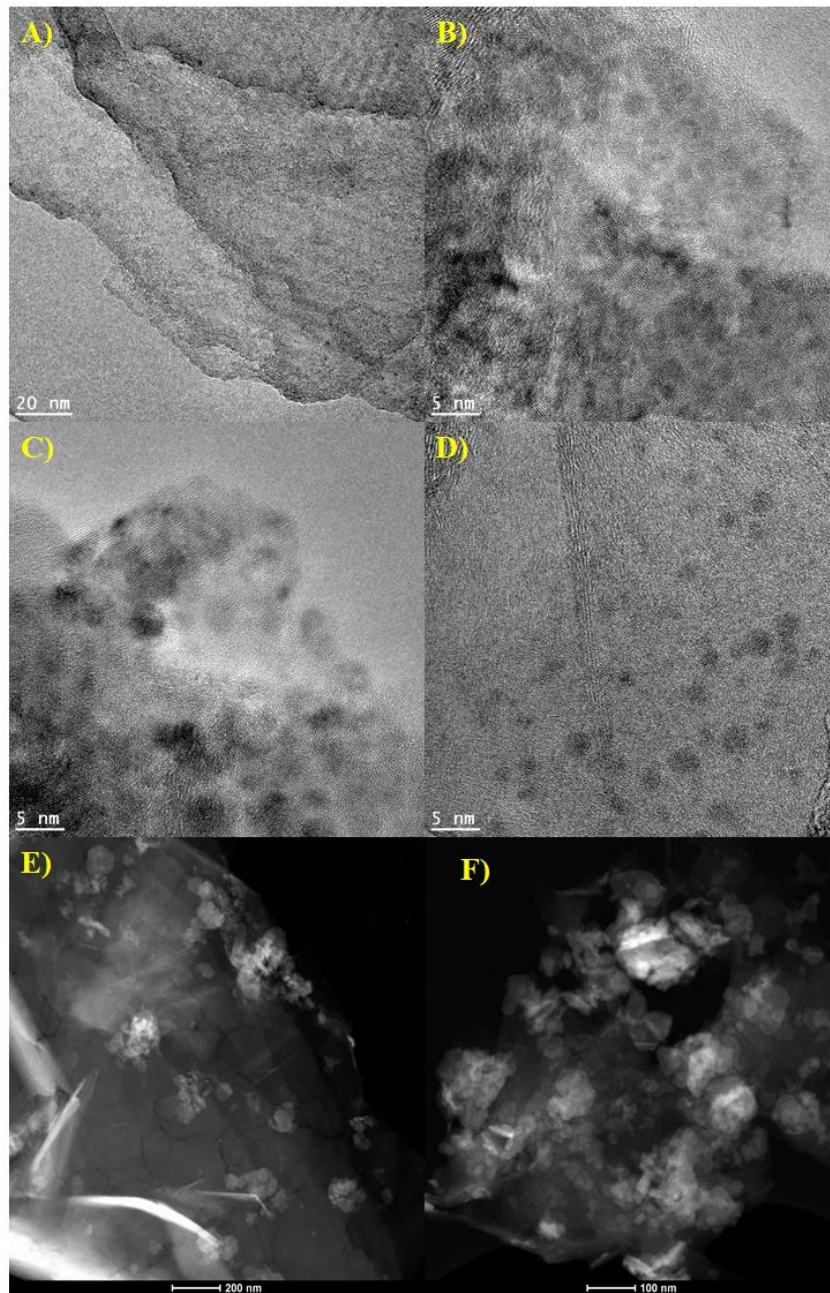
Supporting Information Figure S8.11) HRTEM images of (A-D) Ni@EGO-AT catalyst (E-F) STM images of the Ni@EGO-AT catalyst.
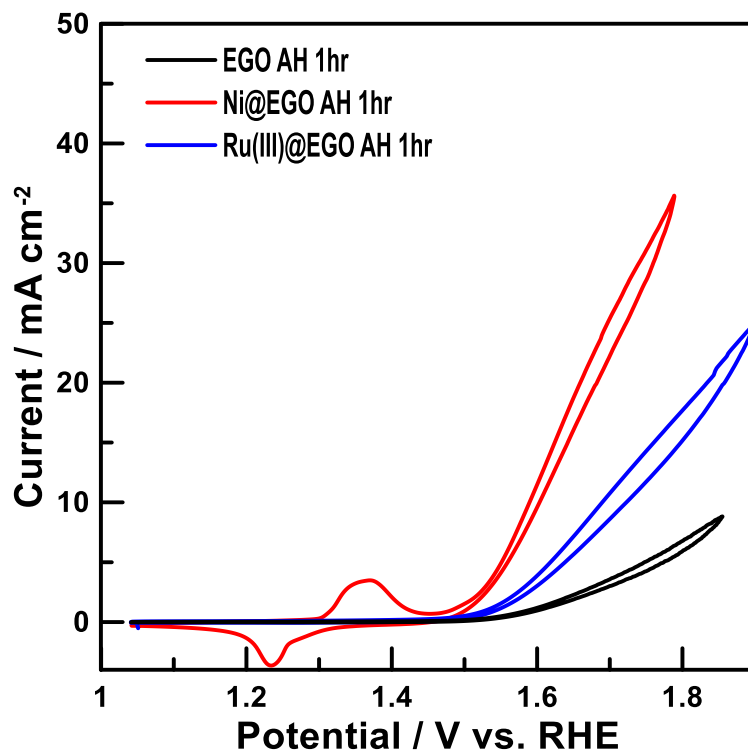
Supporting Information Figure S8.12) Cyclic voltammograms of Ni@EGO and Ru(III)@EGO in 1 M KOH at a scan rate of 5 mV s^{-1}.
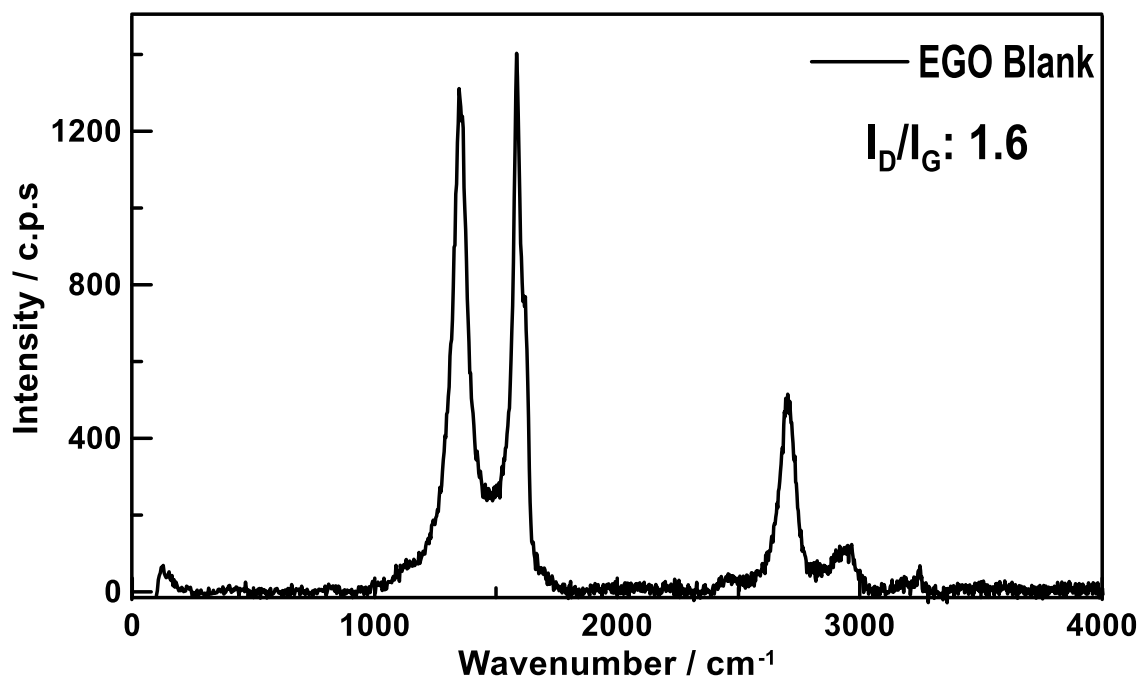
Supporting Information Figure S8.13) Raman spectra of the EGO synthesized in the same conditions without the addition of Ni.
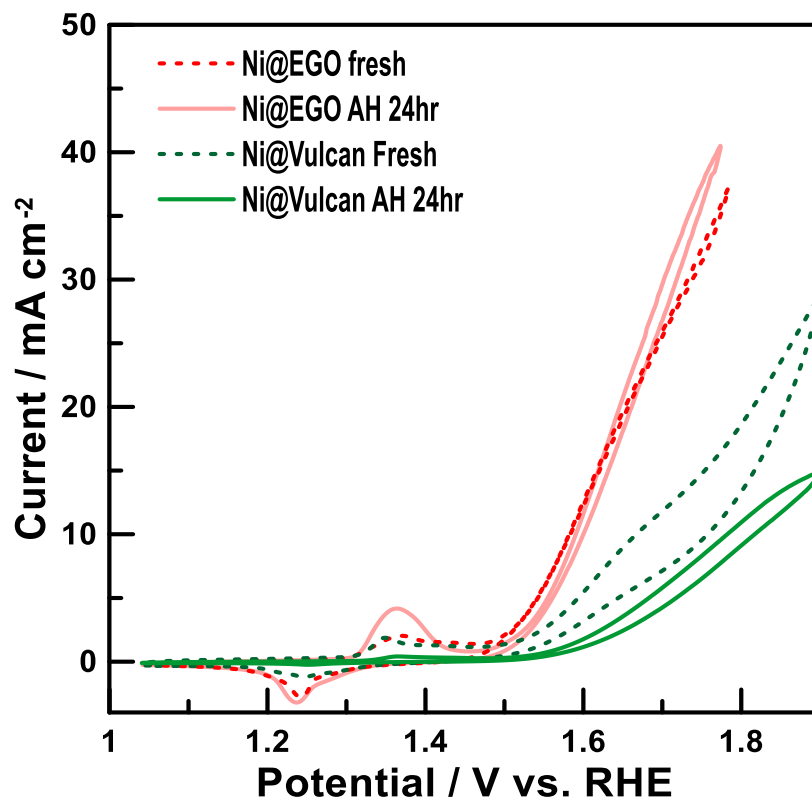
Supporting Information Figure S8.14) Cyclic voltammograms of Ni@EGO and Ni@Vulcan in 1 M KOH at a scan rate of 5 mV s^{-1}.
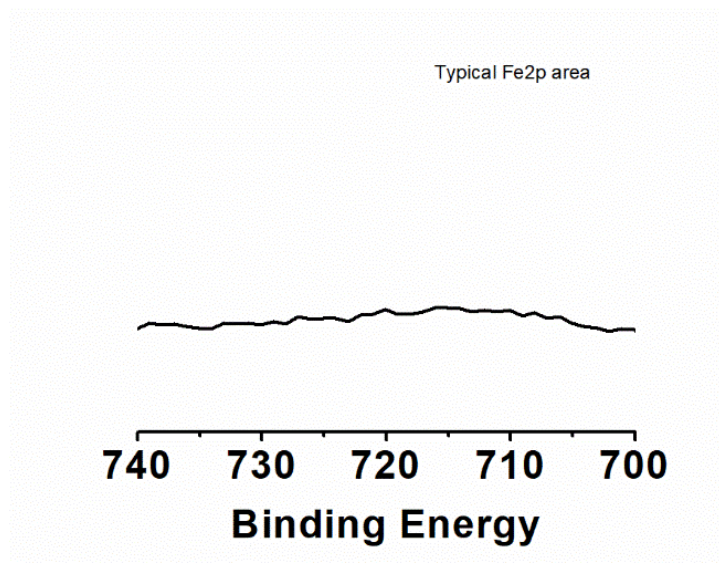
Supporting Information Figure S8.15) XPS spectra of the Fe 2p region of the Ni@EGO catalyst.

8.6 Acknowledgements

8.7 References

[1] X. Meng, J. Han, L. Lu, G. Qiu, Z. L. Wang, C. Sun, *Small* **2019**, *15*, 1-10.

[2] J. Juodkazytė, B. Šebeka, I. Savickaja, M. Petrulevičienė, S. Butkutė, V. Jasulaitienė, A. Selskis, R. Ramanauskas, *Int. J. Hydrog. Energy* **2019**, *44*, 5929-5939.

[3] L. Trotochaud, S. W. Boettcher, *Scripta Materialia* **2014**, *74*, 25-32.

[4] M. Hao, V. Charbonneau, N. Fomena, J. Gaudet, D. Bruce, S. Garbarino, D. A. Harrington, D. Guay, *ACS Appl. Energy Mater.* **2019**, *2*, 5734-5743.

[5] P. Li, R. Chen, S. Tian, Y. Xiong, *ACS Sustain. Chem. Eng.* **2019**, *7*, 9566-9573.

[6] J. Liu, C. Wang, F. Rong, S. Wu, K. Tian, M. Wang, L. He, Z. Zhang, M. Du, *Electrochim. Acta* **2020**, 1-14.

[7] M. Ramadoss, Y. Chen, Y. Hu, W. Li, B. Wang, X. Zhang, X. Wang, B. Yu, *J. Power Sources* **2020**, *451*, 227753.

[8] H. M. Fruehwald, R. B. Moghaddam, O. V. Zenkina, E. B. Easton, *Catal. Sci. Technol.* **2019**, *9*, 6547-6551.

[9] D. S. Hall, C. Bock, B. R. MacDougall, *J. Electrochem. Soc.* **2013**, *160*, F235-F243.

[10] W. Zhou, X.-J. Wu, X. Cao, X. Huang, C. Tan, J. Tian, H. Liu, J. Wang, H. Zhang, *Energy Environ. Sci.* **2013**, *6*, 2921-2924.

[11] M. Y. Gao, J. R. Zeng, Q. B. Zhang, C. Yang, X. T. Li, Y. X. Hua, C. Y. Xu, *J. Mat. Chem. A* **2018**, *6*, 1551-1560.

[12] L. Trotochaud, S. L. Young, J. K. Ranney, S. W. Boettcher, *J. Am. Chem. Soc.* **2014**, *136*, 6744-6753.

[13] M. Bodner, A. Hofer, V. Hacker, *Wiley Interdiscip. Rev. Energy Environ* **2015**, *4*, 365-381.

[14] L. Gu, C. Zhang, Y. Guo, J. Gao, Y. Yu, B. Zhang, *ACS Sustain. Chem. Eng.* **2019**, *7*, 3710-3714.

[15]   K. Krishnamoorthy, M. Veerapandian, K. Yun, S.-J. Kim, *Carbon* **2013**, *53*, 38-49.

[16]   J. Guerrero-Contreras, F. Caballero-Briones, *Mater. Chem. Phys.* **2015**, *153*, 209-220.

[17]   M. Coroş, F. Pogăcean, M.-C. Roşu, C. Socaci, G. Borodi, L. Mageruşan, A. R. Biriş, S. Pruneanu, *RSC Adv.* **2016**, *6*, 2651-2661.

[18]   P. Yu, S. E. Lowe, G. P. Simon, Y. L. Zhong, *Curr. Opin. Colloid Interface Sci.* **2015**, *20*, 329-338.

[19]   M. B. Avinash, K. S. Subrahmanyam, Y. Sundarayya, T. Govindaraju, *Nanoscale* **2010**, *2*, 1762-1766.

[20]   Y. Xu, Z. Liu, X. Zhang, Y. Wang, J. Tian, Y. Huang, Y. Ma, X. Zhang, Y. Chen, *Adv. Mater.* **2009**, *21*, 1275-1279.

[21]   E. Farjami, M. A. Rottmayer, L. J. Deiner, *J. Mat. Chem. A* **2013**, *1*, 15501-15508.

[22]   R. B. Moghaddam, C. Wang, J. B. Sorge, M. J. Brett, S. H. Bergens, *Electrochem. Commun.* **2015**, *60*, 109-112.

[23]   J. Liu, C. K. Poh, D. Zhan, L. Lai, S. H. Lim, L. Wang, X. Liu, N. Gopal Sahoo, C. Li, Z. Shen, J. Lin, *Nano. Ener.* **2013**, *2*, 377-386.

[24]   X. Liu, P. G. Pickup, *J. Electrochem. Soc.* **2011**, *158*, A241-A249.

[25]   C. Wang, R. B. Moghaddam, M. J. Brett, S. H. Bergens, *ACS Sustain. Chem. Eng.* **2016**, *5*, 1106-1112.

[26]   X. Liu, T. A. Huber, M. C. Kopac, P. G. Pickup, *Electrochim. Acta* **2009**, *54*, 7141-7147.

[27]   H. M. Fruehwald, I. I. Ebralidze, O. V. Zenkina, E. B. Easton, *ChemElectroChem* **2019**, *6*, 1350-1358.

[28]   F. B. Saiah, B. L. Su, N. Bettahar, *J. Hazard. Mater.* **2009**, *165*, 206-217.

[29]   R. J. Ruano-Casero, M. E. Pérez-Bernal, V. Rives, *Z. Anorg. Allg. Chem.* **2005**, *631*, 2142-2150.

[30]   L. Trotochaud, J. K. Ranney, K. N. Williams, S. W. Boettcher, *J. Am. Chem. Soc.* **2012**, *134*, 17253-17261.

[31]   B. D. Ossonon, D. Bélanger, *Carbon* **2017**, *111*, 83-93.

[32]   M. Sun, D. Davenport, H. Liu, J. Qu, M. Elimelech, J. Li, *J. Mat. Chem. A* **2018**, *6*, 2527-2539.

[33]   S. Niyogi, E. Bekyarova, M. E. Itkis, H. Zhang, K. Shepperd, J. Hicks, M. Sprinkle, C. Berger, C. N. Lau, W. A. deHeer, E. H. Conrad, R. C. Haddon, *Nano Lett* **2010**, *10*, 4061-4066.

[34]   H. Lim, J. S. Lee, H. J. Shin, H. S. Shin, H. C. Choi, *Langmuir* **2010**, *26*, 12278-12284.

[35]   K. K. Upadhyay, N. Bundaleska, M. Abrashev, N. Bundaleski, O. M. N. D. Teodoro, I. Fonseca, A. M. de Ferro, R. P. Silva, E. Tatarova, M. F. Montemor, *Electrochim. Acta* **2020**, *334*, 135592.

[36]   R. Thimmasandra Narayan, *Indian. J. Eng. Mater. S.* **2015**, *2015*.

[37]   C. Tessier, P. Haumesser, P. Bernard, C. Delmas, *J. Electrochem. Soc.* **1999**, *146*, 2059-2067.

[38]   S. Deabate, F. Fourgeot, F. Henn, *Ionics* **1999**, *5*, 371-384.

[39]   D. Zhang, J. Shi, Y. Qi, X. Wang, H. Wang, M. Li, S. Liu, C. Li, *Adv. Sci.* **2018**, *5*, 1801216.

[40]   Q. Qin, L. Chen, T. Wei, Y. Wang, X. Liu, *Catal. Sci. Technol.* **2019**, *9*, 1595-1601.

[41]   A. N. Mansour, *Surf. Sci. Spectra* **1994**, *3*, 239-246.

[42]   D. Yang, A. Velamakanni, G. Bozoklu, S. Park, M. Stoller, R. D. Piner, S. Stankovich, I. Jung, D. A. Field, C. A. Ventrice Jr, *Carbon* **2009**, *47*, 145-152.

[43]   C. D. Wagner, L. E. Davis, M. V. Zeller, J. A. Taylor, R. H. Raymond, L. H. Gale, *Surf. Interface Anal.* **1981**, *3*, 211-225.

[44]   G. C. Anderson, B. S. Pivovar, S. M. Alia, *J. Electrochem. Soc.* **2020**, *167*, 044503.

[45]   A. K. Taylor, I. Andreu, M. Louie, B. D. Gates, *ACS Appl. Energy Mater.* **2019**.

[46]   Y. Gao, Y. Wei, Z. Lu, X. Chen, D. Wang, *J. Energ. Chem.* **2019**, *35*, 49-54.

[47]   S. Haschke, D. Pankin, V. Mikhailovskii, M. K. S. Barr, A. Both-Engel, A. Manshina, J. Bachmann, *Beilstein J. Nanotechnol* **2019**, *10*, 157-167.

[48]   A. Shatskiy, A. A. Bardin, M. Oschmann, R. Matheu, J. Benet-Buchholz, L. Eriksson, M. D. Karkas, E. V. Johnston, C. Gimbert-Surinach, A. Llobet, B. Akermark, *ChemSusChem* **2019**, *12*, 2251-2262.

[49]   Q. Liu, L. Wu, M. Chen, Y. Guo, T. Xie, P. Wang, *Catal. Commun.* **2019**, *122*, 38-42.

[50] A. C. Sander, S. Maji, L. Francas, T. Bohnisch, S. Dechert, A. Llobet, F. Meyer, *ChemSusChem* **2015**, *8*, 1697-1702.

[51] T. Qiu, Z. Liang, W. Guo, S. Gao, C. Qu, H. Tabassum, H. Zhang, B. Zhu, R. Zou, Y. Shao-Horn, *Nano. Ener.* **2019**, *58*, 1-10.

[52] S. S. Zance, S. Ravichandran, *Appl. Phys. A* **2019**, *125*, 456.

[53] G. Chen, Y. Zhu, H. M. Chen, Z. Hu, S. F. Hung, N. Ma, J. Dai, H. J. Lin, C. T. Chen, W. Zhou, Z. Shao, *Adv. Mater.* **2019**, *31*, e1900883.

[54] C. C. Wang, Y. Cheng, E. Ianni, B. Lin, *Electrochim. Acta* **2017**, *246*, 997-1003.

[55] S. N. Faisal, E. Haque, N. Noorbehesht, H. Liu, M. M. Islam, L. Shabnam, A. K. Roy, E. Pourazadi, M. S. Islam, A. T. Harris, *Sustain. Energy Fuels* **2018**, *2*, 2081-2089.

[56] S. Chen, J. Duan, J. Ran, M. Jaroniec, S. Z. Qiao, *Energy Environ. Sci.* **2013**, *6*, 3693-3699.

[57] L. Ai, T. Tian, J. Jiang, *ACS Sustain. Chem. Eng.* **2017**, *5*, 4771-4777.

[58] Z. Grubač, M. Metikoš-Huković, R. Babić, *Int. J. Hydrog. Energy* **2013**, *38*, 4437-4444.

[59] L. Fagiolari, F. Zaccaria, F. Costantino, R. Vivani, C. K. Mavrokefalos, G. R. Patzke, A. Macchioni, *Dalton Trans* **2020**, *49*, 2468-2476.

Chapter 9. Carbon-Nitrogen-Metal Material as a High Performing Oxygen Evolution Catalyst

9.0 Preface

Part of the work described in this chapter is under review as: Fruehwald, H. M.; Zenkina, O. V.; Easton, E. B., Carbon-Nitrogen-Metal Material as a High Performing Oxygen Evolution Catalyst. *Catal. Sci. Technol.* **submitted**.

In this chapter, the exploration of using the materials that were developed in Chapter 4 for the oxygen reduction reaction, now as an oxygen evolution catalyst. In Chapter 4, Vulcan carbon was modified with tpy using the diaonzium coupling reaction that was developed in Chapter 2. The success of the nickel-based catalyst for OER in Chapter 8, lead to the testing of the alternate metal materials for OER. In this work the V-tpy-Ni catalyst showed high activity in basic electrolyte that demonstrated low overpotentials and this catalyst was incredibly stable over 26 hours of harsh stability testing. Thus, showing the versatility of the material for both applications.

9.0 Abstract

Novel oxygen evolution catalysts were prepared through diazonium coupling chemistry to covalently modify Vulcan carbon via terpyridine (tpy) motifs followed by coordination of non-precious transition metal (Ni, Co) to the tpy-ligand on the surface support. This resulted in highly active catalysts that demonstrate low over potentials for the V-tpy-Ni catalyst of 313 mV at 10 mA cm^{-2}, and stable long-term performance over 26 hours of continual testing.

9.1 Introduction

Overwhelming efforts have been taken to reduce the use and consumption of fossil fuels and shift to more renewable alternatives. The technologies are rapidly being favoured for greener alternatives for worldwide energy production. One such technology is the splitting of water into hydrogen gas and oxygen gas using an electrolyzer[1-3]. This device relies on two reactions: at the cathode, the hydrogen evolution reaction (HER), and at the anode the oxygen evolution reaction (OER)[4]. Both of these reactions heavily rely on the catalyst materials based on Iridium (Ir), which is a very costly rare earth metal[1, 5]. Additionally, the OER at the anode suffers from efficiency issues and is kinetically hindered so it often requires high loadings of Ir[6-7]. Thus, to lower the cost and kinetic limitations, alternative materials for anode catalysts should be developed[8].

Current research to replace the Ir has focused on the development of catalysts that involve non-noble materials such as nickel, and iron. These metals are abundant and significantly less expensive than the classic Ir or Pt-based electrode materials[9]. However, one of the main issues with the non-noble based materials is that they suffer from stability issues and require high overpotentials. The common approach to solve those issues and to synthesize the low-cost catalysts is to dope carbon supports with heteroatoms as this aids in the formation of active sites on the surface and increases electrochemical performance[10-12]. One of the most common dopants used is nitrogen. Doping carbon support by nitrogen allows for the development of a non-noble catalyst with a porous network to provide many active sites and high activity[5, 10]. The carbon provides conductive support for the materials to anchor on, and the addition of nitrogen can help to stabilize the metal nanoparticles, coordinate to single metal sites, and increase the electroactive surface area[10, 13].

We had previously published work on graphene oxide support that was modified with nickel oxide nanoparticles (Ni@EGO) that showed high performance with low overpotentials (290 mV) and it was incredibly stable for alkaline OER for over 28 hours of continuous testing[14]. We had also recently developed catalysts that were synthesized by the covalent attachment of a terpyridine ligand onto a Vulcan carbon support. We had coordinated various metals (Ni, Co, Mn, and Sn) to the tpy ligand on the surface and assessed the ability of the materials to catalyze the oxygen reduction reaction[15]. In the work presented here we used the previously synthesized by us Vulcan carbon-based catalysts modified with a terpyridine ligand and various non-noble transition metals (Ni, Co, Sn) to assess their activity and stability for the oxygen evolution reaction (OER) in alkaline media as Ni and Co are known to show some favourable OER activity in alkaline media[16-17].

9.2 Experimental

9.2.1 Materials

Nickel (II) chloride hexahydrate, isopropyl alcohol, and potassium hydroxide were purchased from Sigma Aldrich. Nafion® was purchased from Ion Power Inc. TPG-H-090 Toray Paper 30% Wet Proofing Carbon fibre paper was purchased from Fuel Cell Earth LLC. Vulcan XC-72 was purchased from Cabot.

9.2.2 Catalyst Synthesis

The detailed synthesis of the catalysts has been published elsewhere[15, 18-19]. Briefly, the terpyridine (tpy) ligand was coordinated to the Vulcan carbon support using diazonium coupling chemistry where a 10 mM solution of the tpy was reacted with an equal volume of 1 M $NaNO_2$ and let react for 3 minutes. The resulting solution was added to ca. 800 mg of the Vulcan carbon and left stir in ambient conditions for 24 hours. After the reaction was complete the solid was vacuum filtered and washed 3 times with acetone, methanol, and deionized water before being placed in the oven to dry. The resulting V-tpy was then reacted with either a 10 mM solution of Ni^{2+} ($NiCl_2 \cdot 6H_2O$), Co^{2+} ($CoCl_2$), or Sn^{2+} ($SnCl_2$) stirring for 48 hours. The resulting catalysts were vacuum filtered and washed 3 times with methanol, acetone, and water to produce V-tpy-Ni, V-tpy-Co, and V-tpy/Sn. A portion of these materials were heat treated in a tube furnace at 700 ºC under N_2 atmosphere for 2 hours.

9.2.3 Physical Characterization

High-Resolution Transmission Electron Microscope (HRTEM) microscopy was performed at the Canadian Centre for Electron Microscopy (also supported by NSERC and other government agencies). Thermogravimetric analysis (TGA) using a TA instruments Q600 SDT thermal analyser. The catalysts were heated using a heating rate of 5°C min^{-1} from room temperature to 1000°C while under an air atmosphere flowing at 20 mL min^{-1}. Pore size analysis was performed using a Quantachrome NOVAe 1200 pore analyser using N_2 as an adsorbate. Scanning electron microscopy (SEM) measurements were obtained using a HITACHI FlexSEM 1000. The energy of the beam was 5 kV with a working distance of 5 mm and a spot size of 20. X-ray photoelectron spectroscopy (XPS) was performed on a Thermo Scientific K-Alpha Angle-Resolve that is equipped with a monochromated Al Kα (1486.7 eV) x-ray source and 180° double focusing hemispherical analyzer with effective charge compensation. A Shirley fit algorithm was used for background subtraction and Powell peak-fitting algorithm was used for data analysis. Detailed physical characterization has been previously reported in our last publication, see that work for more information[15].

9.2.4 Electrochemical Characterization

The oxygen evolution reaction was studied using a carbon fibre paper electrode in 1 M KOH that was purified based on literature procedures prior to use[1, 17, 20]. Catalyst inks were made by sonicating 10 mg of catalyst, 200 µL deionized water, 200 µL isopropyl alcohol, and 100 µL Nafion®. 10 µL of the catalyst was dropped onto a piece of carbon fiber paper and dried with heat (200 µg cm^{-2} catalyst loading). A mercury/mercury sulfate reference electrode was used, and a graphite rod was used as a counter electrode. The electrochemical measurements were performed using a Solartron Analytical 1470E potentiostat.

9.3 Results and Discussion

The synthesis of V-tpy-Ni, V-tpy-Co, and V-tpy/Sn catalysts for the oxygen reduction reaction is described in detail in our previous published works[15, 21]. Briefly, these materials were prepared at ambient temperature by covalent attachment of the terpyridine (tpy) ligand to the commercial Vulcan carbon support via diazonium coupling, followed by reaction with the Ni, Co or Sn precursor to obtain V-tpy-Ni, V-tpy-Co, and V-tpy/Sn

materials, respectively. The diazonium coupling reaction leads to the loss of N_2 gas and forms a carbon-carbon bond to the surface where the terminal NH_2 was. This leads to the exposure of the 3 pyridinic nitrogen functionalities on the surface of the support. To test the effect that heat-treatment had on the activity of the catalysts the materials were heat-treated at 700 ºC for 2 hours in a nitrogen atmosphere. The resulting catalysts are denoted as V-tpy-Ni-700, V-tpy-Co-700, and V-tpy/Sn-700. See Table 9.1 for the summary of physical characterization of the materials[15]. From our work we had determined that the Sn is not coordinating to the tpy-moities, and forms Sn oxides on the surface of the carbon support instead. This was confirmed through intensive XPS and STEM analysis of the catalysts. We performed TGA to determine an estimate of the metal loading and then further compared it to the results obtained by XPS. Interesting to note that the Ni loading in the V-tpy-Ni sample was much lower than that of the Ni@EGO. Using BET we were able to determine that the Vulcan-based catalysts had a higher surface area than the EGO and the higher surface area could create more active sites that would be beneficial for increased activity of the catalysts.

Table 9.1) Physical characterization of the catalysts.

Catalyst	TGA metal wt%	BET surface area / $m^2\,g^{-1}$	XPS / metal At %
Ni@EGO[14]	2.7 %	13.5	3 %
V-tpy-Ni[15]	5.2 %	119	0.80 %
V-tpy-Co[15]	4.7 %	127	-
V-tpy/Sn[15]	5.8 %	117	1.2%

We further analyzed these catalysts through High-Resolution Transmission Electron Microscopy (HRTEM). See representative TEM images for the V-tpy-Ni and V-tpy-Co samples at Figure 9.1A-B, D-E. The TEM images of V-tpy/Sn material is presented in the SI in Figure S9.1. HRTEM of V-tpy-Ni and V-tpy-Co reveal the porous nature of the nitrogen-doped carbon support with no presence of large metal agglomerates consistent

with homogenous dispersion of the metals within the surface of the support. Scanning Tunnel Microscopy (STEM) was also performed on the materials (Figure 9.1C and F). STEM results further confirm the homogenous dispersion of Ni and Co over the surface of the materials. We believe this is happening due to the coordinative interaction between the metal centers and tpy units in the material. Apparently, the formation of metal-tpy adducts is preferable for Ni and Co materials. In comparison, the V-tpy/Sn HRTEM images featured large metal agglomerates on the surface that were further confirmed through STEM analysis. This further confirms that tin tends to form metal/metal oxide agglomerates/nanoparticles on the surface of carbon instead of the formation of coordinative bonds with the tpy units on the support.
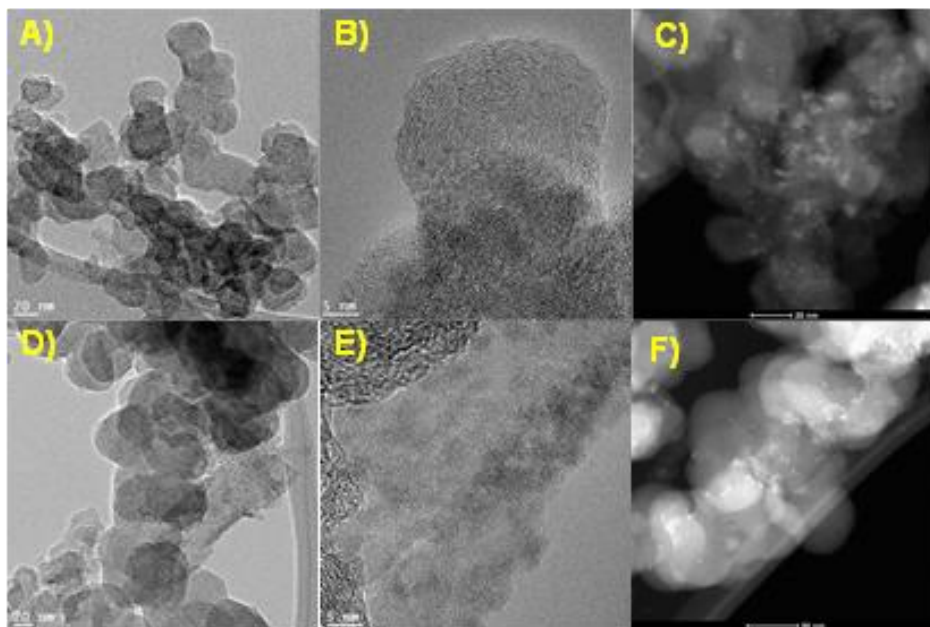
Figure 9.1) (A-B) HRTEM of V-tpy-Co (C) STEM image of V-tpy-Co (D-E) HRTEM of V-tpy-Ni (F) STEM image of V-tpy-Ni.

We compared our best catalysts (V-tpy-Ni and V-tpy-Co) in alkaline media to our previously synthesized Ni@EGO material which showed high activity for the OER and superior durability to see how the addition of the tpy ligand might affect the activity[14]. The results of the V-tpy/Sn are presented in the SI as this catalyst had the lowest activity for the OER. Cyclic voltammetry (CV) was performed in 1 M KOH at a scan rate of 20 mV s^{-1} (Figure 9.2). The Ni@EGO showed very prominent peaks in the CV which are characteristic of the conversion of Ni hydroxide to the more active β-NiOOH[1-2, 22-24]. With

the V-tpy-Co, V-tpy-Ni, V-tpy-Ni-700, and V-tpy-Co-700 no peaks are visible, this is partially due to lower loadings of the metals in these catalysts compared to the Ni@EGO, as well as the pH of the electrolyte that shifts the peak positions.
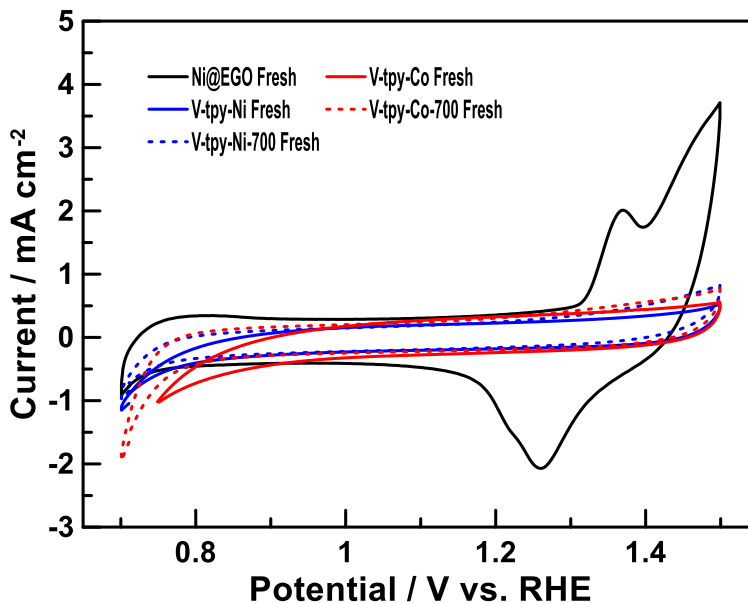
Figure 9.2) Cyclic voltammograms of the catalysts at a scan rate of 20 mV s^{-1} in 1 M KOH.

The catalysts were assessed for their activity towards the oxygen evolution reaction (OER) in 1 M KOH in the fresh state and after a 24-hour stability test at 1 mA cm^{-2} (Figure 9.3). The Ni@EGO was our best performing catalyst with an overpotential of 290 mV at 10 mA cm^{-2}. For the V-tpy-Co catalyst the activity was quite low, however some improvements in activity were seen after the heat treatment procedure which sightly increased the activity of the material. Astonishingly, the V-tpy-Ni was quite active for the OER in the fresh state with an overpotential of 313 mV at 10 mA cm^{-2}. In the case of the heat treatment the activity of the V-tpy-Ni-700 did not increase, the activity instead declined. The onset potentials and standard deviations for the catalysts are presented in Table 9.2.

Table 9.2) OER onset potentials of the catalysts in 1 M KOH at 5 mV s^{-1}.

Catalyst	Onset potential fresh at 10 mA cm^{-2}/ V	Onset potential after 24 hr hold at 10 mA cm^{-2} / V
Ni@EGO[14]	1.484 ± 0.008	1.470 ± 0.011
V-tpy-Ni	1.607 ± 0.009	1.432 ± 0.014
V-tpy-Co	1.772 ± 0.014	1.898 ± 0.006
V-tpy-Ni-700	1.830 ± 0.016	1.898 ± 0.010
V-tpy-Co-700	1.708 ± 0.013	1.686 ± 0.009

The fresh V-tpy-Ni catalyst showed remarkable activity, on par or higher than the best representatives of C-N-Ni catalysts reported in literature[6, 9]. More impressive, the activity of the V-tpy-Ni after the 24-hour stability testing showed a substantial increase in performance, even out performing our starring Ni@EGO catalyst. We believe that this is due to some further activation of the catalyst during the stability testing that leaves exposed more active forms of the Ni species[25]. To the best of our knowledge, this is some of the highest reported activity for C-N-Ni based system, while other works have reported overpotentials that are 320 mV or higher[5, 13, 26], where our systems show overpotentials of that below 320 mV. In comparison, the V-tpy-Co decreases in activity which we hypothesize could be due to the unstable nature of the cobalt-tpy complex.
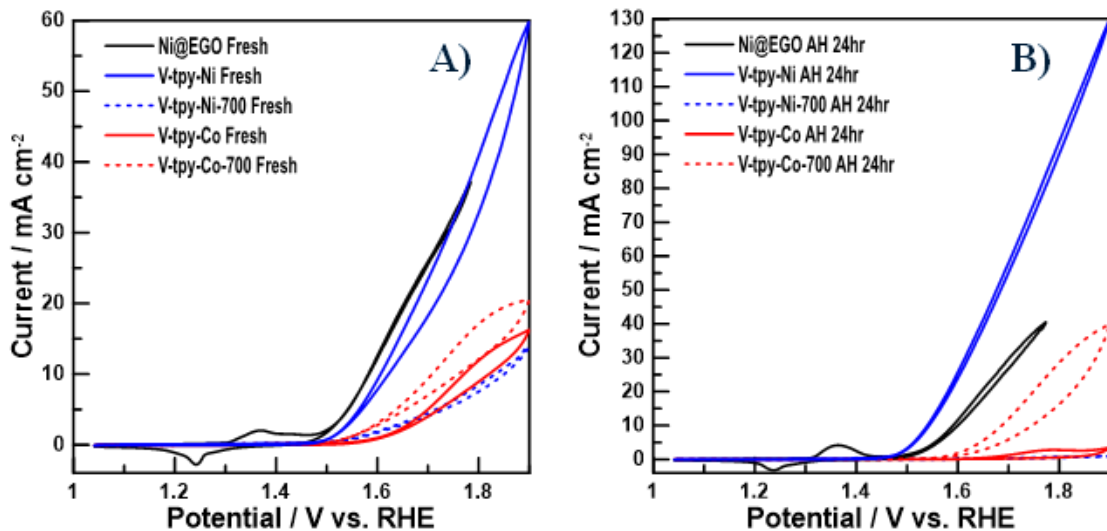
Figure 9.3) (A) OER activity of the fresh catalysts at a scan rate of 5 mV s^{-1} in 1 M KOH (B) OER activity of the catalysts after 24 hr stability tests at 1 mA cm^{-2} at a scan rate of 5 mV s^{-1} in 1 M KOH.

Galvanostatic polarization was performed on the catalysts using a current density of 1 mA cm^{-2} in 1 M KOH for 24 hours to assess the long-term stability of the catalysts (Figure 9.4A). The Ni@EGO reached the lowest overpotentials, with minor or no increases to the overpotential over the 24 hour period. The V-tpy-Ni performed quite well over the course of the stability tests. There was little to no increase in the overpotential over the 24 hours, in fact the potential stayed quite low. In comparison, the V-tpy-Co was not stable during the long-term testing protocol and a large increase in the overpotential was observed. We believe this could be due to the enhanced carbon corrosion with this material at the high potentials compared to the Ni, leading to higher overpotentials[27]. Finally, we subjected the catalysts to a significantly harsher stability test at 10 mA cm^{-2} for 1 hour (Figure 9.4B). The V-tpy-Ni catalyst demonstrated unprecedented stability in the overpotential we observed over the course of testing, which is a direct indication of the high stability of the catalyst. In comparison, the V-tpy-Co and V-tpy-Co-700 demonstrated large increases in the overpotential during the testing and were not stable during the long-term testing.
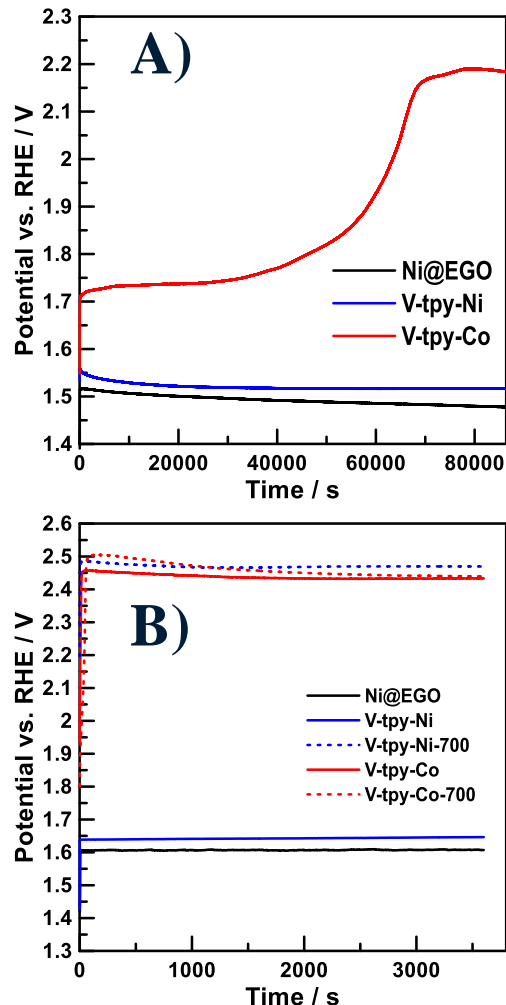
Figure 9.4) (A) Galvanostatic hold at 1 mA cm^{-2} for 24 hours (B) Galvanostatic hold at 10 mA cm^{-2} for 1 hour.

9.4 Conclusion

In conclusion, the synthesis of nitrogen-doped Vulcan support with a terpyridine-based molecule showed exceptional activity towards the OER in basic media, with a low overpotential of 313 mV. Notably, this catalyst was incredibly stable over 24 hours of galvanostatic polarization and at an even harsher 10 mA cm^{-2} testing protocol. The drastic boost of the material performance and stability could be attributed to the effect of the addition of the nitrogen groups that may facilitate the formation of active sites on the surface of the catalyst. Our synthetic approach also allows for these materials to be synthesized under low-cost and ambient conditions and utilize non-noble materials. This work highlights a promising route to ultra active OER catalysts that may work in the future

to replace costly materials such as iridium-based materials for alkaline OER. The addition of nitrogen to Ni/C-based catalysts shows promising results for the development of next generation of non-noble OER catalysts.

9.5 Supporting Information
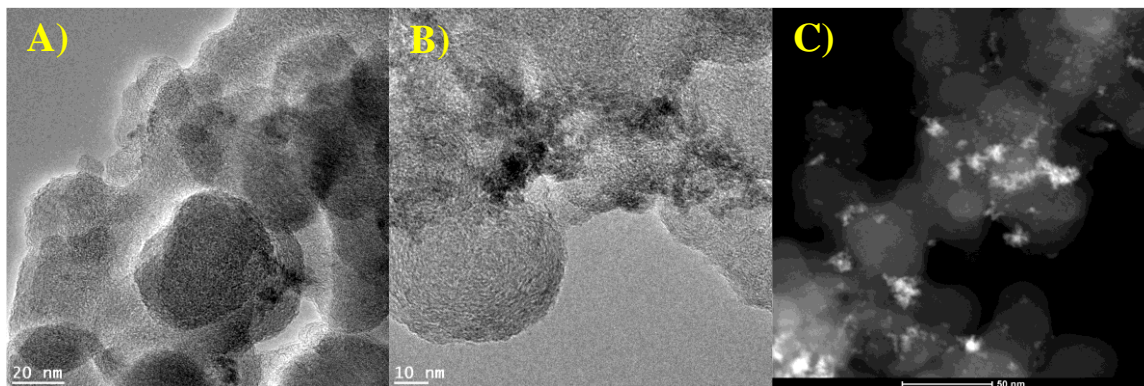
Supporting Information Figure S9.1) (A-B) HRTEM images of the V-tpy/Sn catalyst (C) STEM image of the V-tpy/Sn catalyst.
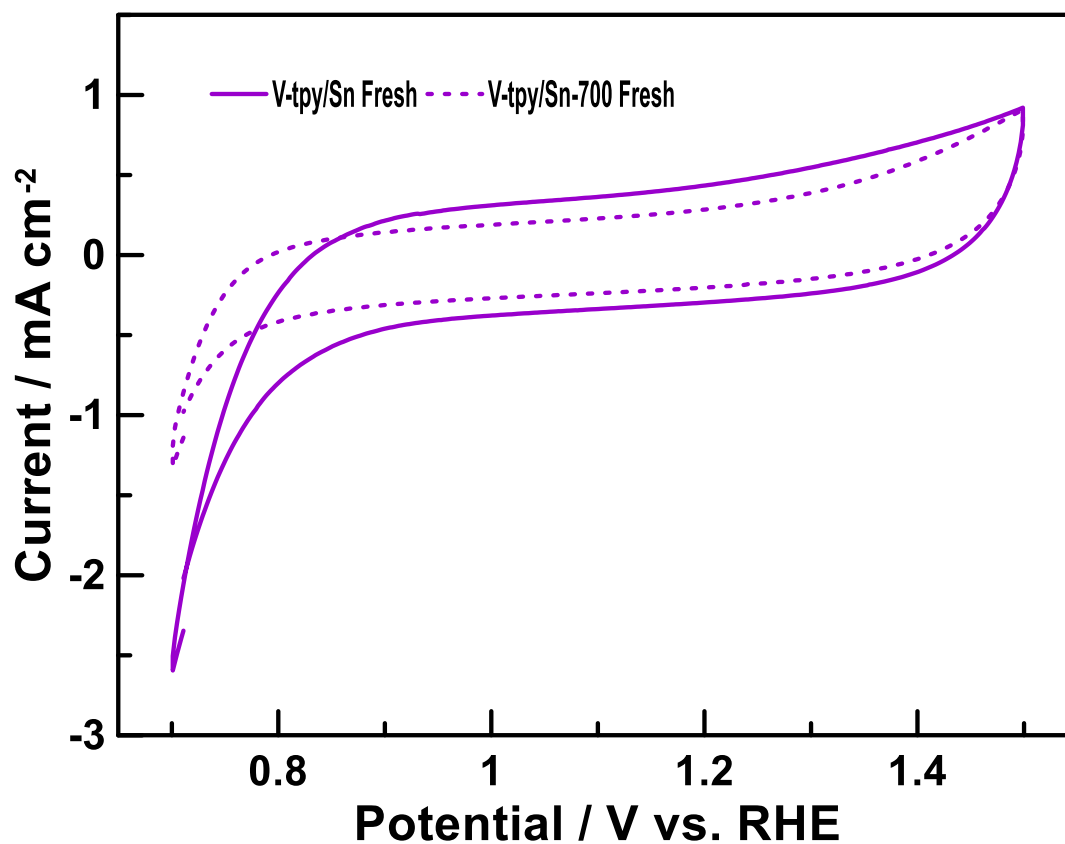
Supporting Information Figure S9.2) Cyclic voltammetry of V-tpy/Sn catalysts in 1 M KOH at a scan rate of 20 mV s^{-1}.
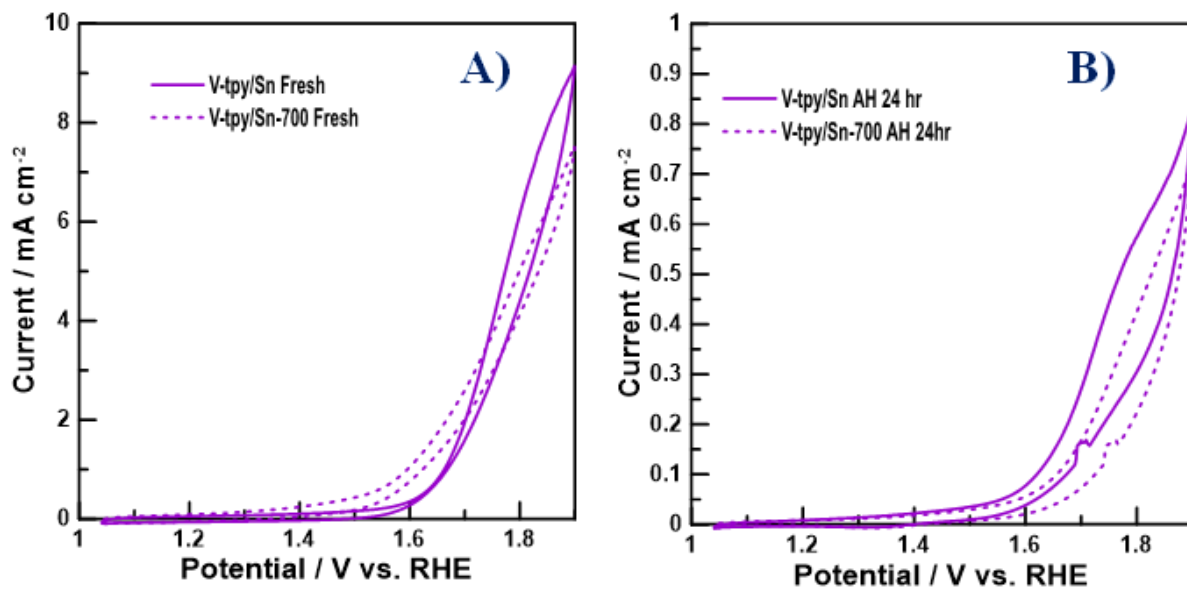
Supporting Information Figure S9.3) (A) OER activity of the fresh V-tpy/Sn catalysts at 5 mV s^{-1} in 1 M KOH (B) OER activity of the V-tpy/Sn catalysts after stability tests at 5 mV s^{-1} in 1 M KOH.
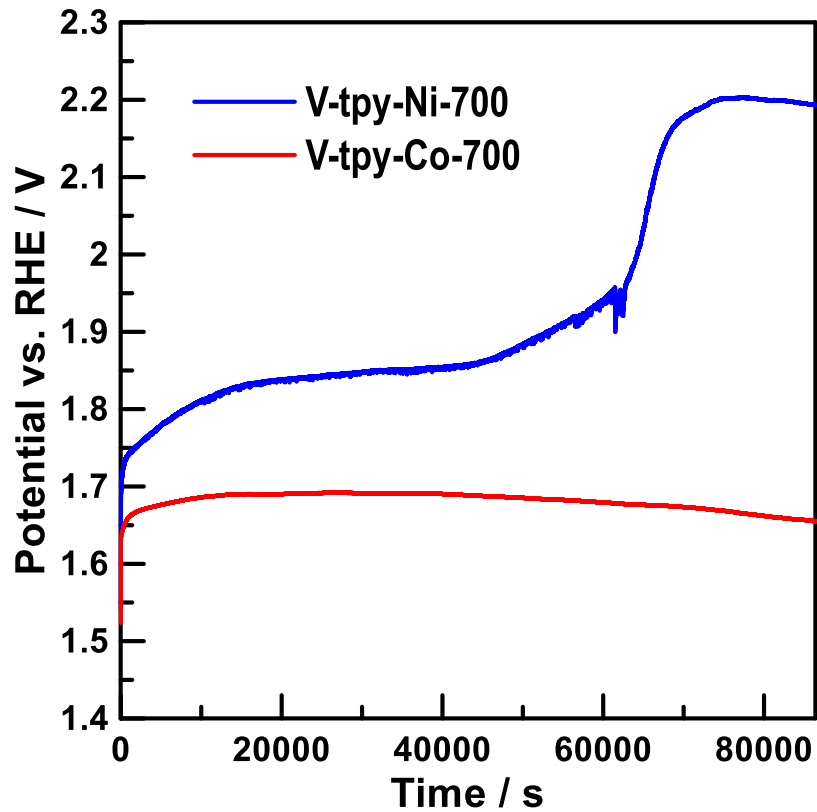
Supporting Information Figure S9.4) 24 hour galvanostatic hold at 1 mA cm^{-2} in 1 M KOH.

9.6 Acknowledgements

9.7 References

[1]   L. Trotochaud, J. K. Ranney, K. N. Williams, S. W. Boettcher, *J. Am. Chem. Soc.* **2012**, *134*, 17253-17261.

[2]   J. Juodkazytė, B. Šebeka, I. Savickaja, M. Petrulevičienė, S. Butkutė, V. Jasulaitienė, A. Selskis, R. Ramanauskas, *Int. J. Hydrog. Energy* **2019**, *44*, 5929-5939.

[3]   R. B. Moghaddam, C. Wang, J. B. Sorge, M. J. Brett, S. H. Bergens, *Electrochem. Commun.* **2015**, *60*, 109-112.

[4]   Z. Grubač, M. Metikoš-Huković, R. Babić, *Int. J. Hydrog. Energy* **2013**, *38*, 4437-4444.

[5]   S. Chen, J. Duan, J. Ran, M. Jaroniec, S. Z. Qiao, *Energy Environ. Sci.* **2013**, *6*, 3693-3699.

[6]   P. Li, R. Chen, S. Tian, Y. Xiong, *ACS Sustain. Chem. Eng.* **2019**, *7*, 9566-9573.

[7]   C. Wang, R. B. Moghaddam, M. J. Brett, S. H. Bergens, *ACS Sustain. Chem. Eng.* **2016**, *5*, 1106-1112.

[8]   J. Liu, C. Wang, F. Rong, S. Wu, K. Tian, M. Wang, L. He, Z. Zhang, M. Du, *Electrochim. Acta* **2020**, 1-14.

[9]   M. Ramadoss, Y. Chen, Y. Hu, W. Li, B. Wang, X. Zhang, X. Wang, B. Yu, *J. Power Sources* **2020**, *451*, 227753.

[10]   S. N. Faisal, E. Haque, N. Noorbehesht, H. Liu, M. M. Islam, L. Shabnam, A. K. Roy, E. Pourazadi, M. S. Islam, A. T. Harris, *Sustain. Energy Fuels* **2018**, *2*, 2081-2089.

[11] K. K. Upadhyay, N. Bundaleska, M. Abrashev, N. Bundaleski, O. M. N. D. Teodoro, I. Fonseca, A. M. de Ferro, R. P. Silva, E. Tatarova, M. F. Montemor, *Electrochim. Acta* **2020**, *334*, 135592.

[12] X. Meng, J. Han, L. Lu, G. Qiu, Z. L. Wang, C. Sun, *Small* **2019**, *15*, 1-10.

[13] L. Ai, T. Tian, J. Jiang, *ACS Sustain. Chem. Eng.* **2017**, *5*, 4771-4777.

[14] H. M. Fruehwald, R. B. Moghaddam, P. D. Melino, I. I. Ebralidze, O. V. Zenkina, E. B. Easton, *Catal. Sci. Technol.* **2021**, *11*, 4026-4033.

[15] H. M. Fruehwald, I. I. Ebralidze, O. V. Zenkina, E. B. Easton, *ChemElectroChem* **2020**, *8*, 53-61.

[16] Y. Chen, K. Rui, J. Zhu, S. X. Dou, W. Sun, *Chemistry* **2019**, *25*, 703-713.

[17] L. Trotochaud, S. W. Boettcher, *Scripta Materialia* **2014**, *74*, 25-32.

[18] H. M. Fruehwald, I. I. Ebralidze, P. D. Melino, O. V. Zenkina, E. B. Easton, *J. Electrochem. Soc.* **2020**, *167*, 084520.

[19] H. M. Fruehwald, O. V. Zenkina, E. B. Easton, *ECS Transactions* **2019**, *92*, 523-532.

[20] L. Trotochaud, S. L. Young, J. K. Ranney, S. W. Boettcher, *J. Am. Chem. Soc.* **2014**, *136*, 6744-6753.

[21] H. M. Fruehwald, I. I. Ebralidze, O. V. Zenkina, E. B. Easton, *ChemElectroChem* **2019**, *6*, 1350-1358.

[22] D. S. Hall, C. Bock, B. R. MacDougall, *J. Electrochem. Soc.* **2013**, *160*, F235-F243.

[23] G. C. Anderson, B. S. Pivovar, S. M. Alia, *J. Electrochem. Soc.* **2020**, *167*, 044503.

[24] A. K. Taylor, I. Andreu, M. Louie, B. D. Gates, *ACS Appl. Energy Mater.* **2019**.

[25] L. Fagiolari, F. Zaccaria, F. Costantino, R. Vivani, C. K. Mavrokefalos, G. R. Patzke, A. Macchioni, *Dalton Trans* **2020**, *49*, 2468-2476.

[26] L. Gu, C. Zhang, Y. Guo, J. Gao, Y. Yu, B. Zhang, *ACS Sustain. Chem. Eng.* **2019**, *7*, 3710-3714.

[27] P. Kanninen, B. Eriksson, F. Davodi, M. E. M. Buan, O. Sorsa, T. Kallio, R. W. Lindström, *Electrochim. Acta* **2020**, *332*, 135384.

[28] J.-J. Jhao, C.-H. Lin, T.-K. Yeh, H.-C. Wu, M.-C. Tsai, C.-K. Hsieh, *Surf. Coat. Technol.* **2017**, *320*, 263-269.

[29]   M. Ernst, W. Sloof, *Surface and Interface Analysis: An International Journal devoted to the development and application of techniques for the analysis of surfaces, interfaces and thin films* **2008**, *40*, 334-337.

[30]   D. J. Morgan, *Surf. Interface Anal.* **2015**, *47*, 1072-1079.

[31]   K. Krishnamoorthy, M. Veerapandian, K. Yun, S.-J. Kim, *Carbon* **2013**, *53*, 38-49.

Chapter 10. Summary and Future Directions

10.1 Conclusions

In this thesis, I demonstrated the use of using a molecularly defined surface modification approach to covalently modify carbon supports with various nitrogen-containing ligands. I showed that covalent imprinting a terpyridine group to the surface of the carbon support allows to fully expose active pyridinic nitrogen functionalities to facilitate the catalytic properties of materials. This thesis showed the tunability of the nitrogen functionalities on the surface depending on the ligand of choice. These nitrogenous motifs on the surface, upon coordination to transition metals demonstrated significant activity for the oxygen reduction reaction in both acidic and basic media, along with drastic improvements of the charge storage abilities of the materials.

First, a model catalytic system based on Vulcan carbon, tpy, and iron was explored as a proof of concept confirming the activity of the $Fe-N_3/C$ sites in the ORR. In Chapter 2, I demonstrated that diazonium coupling chemistry could be effectively utilized to attach the tpy ligand to the carbon support. Through XPS and TOF-SIMS analysis, the primary form of nitrogens on the surface were unambiguously identified as most catalytically active pyridinic nitrogens. Following room temperature coordination of the iron to the terpyridine- sites, the desired V-tpy-Fe was produced as our model catalyst. It was found through the electrochemistry that the V-tpy material alone showed some activity for the ORR, but the catalytic performance was significantly improved when Fe was incorporated into the material, showing the role that iron plays in the catalyst design. Interestingly, after a heat-treatment, the activity of the catalyst significantly declines. Before the heat-treatment, the catalyst followed the most effective and direct pathway (n=4) that involves the transfer heat of 4 electrons which reduces O_2 directly to water. After heat treatment the mechanism changed to the least effective indirect pathway (n=2), that involves the transfer of 2 electrons and leads to the formation of the side product H_2O_2, showing that for our model system the heat-treatment is not beneficial for catalyst design.

In Chapter 3, this thesis explored how changing the surface area and the porosity of the carbon support would alter the activity of the materials for the ORR. Using the same synthetic design from Chapter 2, the surface areas of the carbon support were altered from 2500-230 m^2 g^{-1} (Black Pearls, Ketjen Black, Multi-walled carbon nanotubes) and were

compared to our initial work on Vulcan. The results of this work showed that as the surface area of the carbon increases, the activity of the materials after the heat-treatment increases as well. So, the material based on the lowest surface area carbon support (Vulcan, 230 m^2 g^{-1}) demonstrated a higher onset potential for the ORR when the catalyst was not heat-treated, but the Black Pearls-based catalyst (material based on the carbon with the highest surface area) demonstrated a significant increase of the onset potential from 0.32 V to 0.63 V after heat-treatment. This is attributed to the different types of active sites that are formed on the carbons of different surface areas and porosities, thus affecting the activity of the material before and after heat-treatment.

Furthermore, after exploring the role of the carbon support in Chapter 3, the thesis explored how the nature of the transition metal coordinated into the pyridinic nitrogens of the tpy molecule on the Vulcan support affected the activity of the material in Chapter 4. In this chapter, I explored the potential of Co, Mn, Ni, and Sn to be coordinated to the tpy motif on the surface to create the catalytic active site(s) and assessed the activity of the resulting materials for the ORR. The deposition of Co, Mn, and Ni resulted in the formation of coordination adducts with N$_3$-functionalities on the surface support, as judged by SEM, TEM, and XPS, confirming the homogenous distribution of metal- and nitrogen- moieties within the material. No detectable grains, islands or aggregates were detected. Interestingly, in the TEM results, I saw that the Sn was forming large agglomerates on the surface of the material. XPS analysis on the V-tpy/Sn material further confirmed the formation of large agglomerates of Sn Oxides on the surface, indicating that the Sn was not coordinating to the tpy sites, rather it was physisorbed on the carbon support instead. Through the electrochemistry in acidic media, I determined that the trend of activity of the materials was Fe>Co>Mn>Ni>Sn. This was consistent with the trends reported in the literature for structurally related non-precious metal catalysts. Some previously reported computational studies were suggesting that Sn might be a good option to use in combination with nitrogen-enriched active sites but good activity for this tin-based material was not observed. With this work, I demonstrated the promise of the novel N$_3$/C active site in combination with different transition metals, most of which showed good activity for the ORR in both acidic and basic media.

After the development and optimization of the catalysts for ORR, I moved on and assessed the energy storage ability of the materials. First, in Chapter 5, I performed 3-cell electrode testing of the charge storage properties of the materials on Vulcan support. In this work, it was found that the surface functionalization approach to modify Vulcan carbon with tpy and tpy analogs results in significant increases in the capacitance when compared to the bare Vulcan support. More interestingly, I could compare the capacitance increases per molecule to assess the energy storage ability of different materials. For example, an increase of the capacitance per molecule was detected when the iron was added to nitrogen-enriched materials (from 1.308×10^{-9} µF molecule^{-1} to 1.479×10^{-9} µF molecule^{-1} for V-phen and V-phen-Fe, respectively) demonstrating the impact of the Faradaic contributions from the iron on the overall charge storage. In this work, I showed that after long-term testing for 6000 galvanostatic cycles the capacitance increased significantly, over ca. 100% of the initial capacity of the material. This was attributed to the electropolymerization of the ligands on the surface which further enhanced the charge storing capabilities. Notably, for our best system, V-phen, the capacitance remained quite high even in the full cell configuration showing the promise of our synthetic approach to prepare effective materials for charge storage. In Chapter 6, I explored the results from Chapter 2,3, and 5 to synthesize a dual-functioning material that could be used for both the ORR and charge storage. In this work, a phenazin ligand was incorporated via the diazonium coupling on various commercial carbon blacks (Vulcan, Ketjen Black, and Black pearls). The materials were tested for the ORR and it was found that the heat-treated materials showed higher activity for the ORR than their non-heat treated analogs. These observations were consistent with the results from Chapter 3, showing that increasing the surface area of the support result in the higher ORR activity for heat-treated systems. Moving on, the materials were then tested for their charge storing capabilities, and interestingly I observed that the heat-treatment, while beneficial for ORR was not beneficial for charge storage. This was in turn attributed to the decrease in the nitrogen surface functional groups which are important to increase the pseudocapacitance. The correlation between the surface area of the carbon support versus the specific capacitance of the resulting material was observed and it is apparent that the initially high surface area carbon support allows for the preservation and further improvement of charge storage even after the bulky nitrogen groups are added to the

264

material. In this work stability tests showed a similar trend to what was observed in Chapter 5, the specific capacitances also increased over ca. 110 % of the initial value for all materials. This Chapter highlights how this synthetic approach can be used to synthesize versatile materials that are suitable for multiple applications.

Finally, the oxygen evolution reaction (OER) was assessed. First, in Chapter 7, the initial synthetic approach was developed to prepare Ru-based catalysts for the OER. Notably, the high-performing catalysts for the OER were prepared under ambient conditions in a high yield. These catalysts were assessed for its OER activity in acidic media and the Ru(III)-based systems demonstrated high onset potentials of 0.2 V or less and ultra-high durability over long-term testing for over 24 hours. Building on this initial work in Chapter 8, I then explored the use of the same synthetic method to modify graphene oxide with Ni. In this work the Ni@EGO material showed superior activity in alkaline media with low loadings of Ni (2.7 wt%). Importantly, Ni-based catalyst demonstrated significantly improved OER activity after the stability test for over 24 hours, and this was attributed to the post-synthetic activation that was occurring on the material electrochemically triggering activity and exposure of previously passivated Ni nanoparticles. The overpotential for the material was 290 mV, which is much lower than any other Ni-carbon-based catalyst reported in the literature. Furthermore, the Ni@EGO catalyst was incredibly stable over 24 hours of continuous testing with little to no increases in the overpotential. More impressively, after an even harsher stability test at higher currents, the Ni@EGO catalyst still remained stable with no increases in the overpotential during the testing. Using the information from this work on the stability and high performance of the Ni@EGO catalyst, in Chapter 9 I explored the potential of some materials from Chapter 4 to be used as OER catalysts. In this work, the OER activity of the V-tpy-Ni and V-tpy-Co were explored. The V-tpy-Ni showed impressive activity for the OER, even outperforming the Ni@EGO catalyst material. The V-tpy-Co material showed increases in the OER activity after heat-treatment, however, the activity was still poor compared to the V-tpy-Ni. Low overpotential of the V-tpy-Ni (313 mV) was an impressive achievement for C-N$_3$-Ni based materials. The material was tested for long-term durability and showed incredible stability over the various harsh testing conditions with little to no increases in the overpotential during the testing. This work showed that a

molecularly defined multi-functional material was able to be synthesized that showed good activity for the ORR (Chapter 4) and the OER (Chapter 9).

The work in this thesis successfully demonstrated the capability of using a synthetic approach to create nitrogen and metal-doped materials as multi-functional systems. Diazonium coupling chemistry proved to be a successful method to covalently embed the desired nitrogen functionalities into the carbon surface to maximize the level of exposure of the nitrogen-enriched sites on the support for multiple applications. For the ORR applications, this synthetic approach allowed for the creation of mainly the most catalytically active pyridinic nitrogens to be formed on the surface. The chemical modification of the materials does not require energy-intensive heat-treatment procedures which significantly reduce the cost of materials production. These unique N_3/C catalysts with various metals demonstrated good ORR activity. In addition, our synthetic approach yielded materials with enhanced charge storing capabilities. Notably, tuning the surface area of the material leads to changes (either gains or losses) for the ORR and specific capacitances. Finally, this methodology could also be expanded into another clean energy application, OER. The fundamental synthesis of these non-noble metal-based materials that could be used for multiple applications within clean energy would significantly decrease the cost of the technologies without using rare and costly materials for the materials preparation.

10.2 Future Directions

Future directions for this work could include expanding on the use of alternate nitrogenous ligands and functionalities. Either more nitrogen groups in the molecule or tuning of the amount and ratios of pyridinic functionalities to other forms of nitrogen on the surface, such as pyrrolic nitrogen, could be explored to gain more detailed information on how the different forms of nitrogen might affect the activity of the active site(s) for both ORR and in supercapacitor applications. Some molecules of interest could be porphyrin or corrole ligands that adopt N_4 configurations.

Another direction for this research could explore other linkages to introduce desired functionalities to the support. With the diazonium reaction, there are some inherent challenges with the linkage. Most notably is that characterizing these linkages provide very difficult as carbon-carbon bonds are present throughout not only the linkage method, but

the entire carbon support as well. This makes it difficult to assess in detail the linkage to the surface and in some instances proving that there is in fact a chemical bond being formed on the surface. For example, other linkages could include a benzimidazole linkage to introduce different molecules to the support. This may provide information on how changing the linkage could impact the activity, stability, and charge storage of the materials. In addition, future work can explore the use of this modification technique on supports other than carbon. For example, using this modification approach to functionalize metal oxide supports with tpy and other metals.

Finally, using combinations of various non-noble metals could provide interesting outcomes due to some cooperative effects. For example, combing Fe and Co in various ratios for the ORR could provide the catalyst with enhanced activity based on synergetic effects from both metals. Assessing the different metals for charge storage could prove interesting results since the utilization of metals with multiple different oxidation states should lead to better charge storage capabilities. Lastly, combining various metals (Fe, Ni, Co, etc) for OER applications would be interesting to try with the novel synthetic approach as there are literature reports on Fe/Ni nanoparticle combinations, but not often are the metals immobilized on either a bare carbon support or carbon support modified with nitrogen.